UNIVERSITY OF SOUTHAMPTON

FACULTY OF PHYSICAL AND APPLIED SCIENCES

OPTOELECTRONICS RESEARCH CENTRE

PERIODIC FIBRE DEVICES FOR ADVANCED APPLICATIONS IN ALL-OPTICAL SYSTEMS

by

Jindan Shi

Thesis submitted for the degree of Doctor of Philosophy

September 2012

UNIVERSITY OF SOUTHAMPTON

ABSTRACT

FACULTY OF PHYSICAL AND APPLIED SCIENCES

OPTOELECTRONICS RESEARCH CENTRE

Doctor of Philosophy

Periodic Fibre Devices for Advanced Applications in All-Optical Systems

by Jindan Shi

The main objective of this work is to investigate advanced applications of fibre gratings with the combination of nonlinear fibre optical effects, including the stimulated Raman scattering (SRS), Kerr effects, four-wave mixing (FWM) and second-harmonic generation. A Raman distributed-feedback (R-DFB) fibre laser formed in a passive optical fibre by using Raman gain is considered as the most promising route to generate a single-frequency and narrow-linewidth laser source at any wavelength given a proper pump source.

In this thesis, the R-DFB fibre laser has been intensively studied both numerically and experimentally. Simulation results of centre π phase-shifted R-DFB fibre lasers show that the longer length of the DFB grating, the higher Raman gain coefficient and the lower background loss of the host fibre are always beneficial for achieving low threshold R-DFB fibre lasers. 30-cm long centre π phase-shifted R-DFB fibre lasers have been respectively demonstrated in two types of commercially available Ge/Si fibres of PS980 and UHNA4. Both un-polarised and linearly polarised CW Yb-doped fibre lasers at ~1.06 µm were used as the pump sources. The R-DFB fibre lasers are single-frequency operation at around 1.11 µm and have 3 dB linewidth less than 2.5 kHz; lasing thresholds down to sub-watt power levels; total output powers up to ~2 W; and total conversion efficiencies against incident pump power around 13%. Ultra-wide range (>110 nm) wavelength conversion by using FWM in these 30 cm-long R-DFB fibre lasers have been observed and up to ~-25 dB FWM conversion efficiency has been obtained.

The nonlinearities and photosensitivity of several high-index non-silica glasses and fibres are also studied in order to incorporate fibre Bragg gratings (FBGs) with the highly nonlinear fibres to form R-DFB fibre lasers with lower thresholds. In particular, the Raman gain coefficient of a house-made tellurite glass fibre has been found to be ~35 times higher than the silica fibre and a SRS-assisted supercontinuum from ~1.1-1.7 µm has been observed in the fibre with a length of ~1.35 m by pumping at ~1.06 µm in the normal dispersion region of the fibre.

Preliminary investigations into concatenating periodic poled silica fibres (PPSFs) to improve the frequency-doubling conversion efficiency are also presented.

Table of Contents

List of Figures

List of Tables

Declaration of Authorship

I, Jindan Shi declare that the thesis entitled *Periodic Fibre Devices for Advanced Applications in All-Optical Systems* and the work presented in the thesis are both my own, and have been generated by me as the result of my own original research. I confirm that:

- this work was done wholly or mainly while in candidature for a research degree at this University;
- where any part of this thesis has previously been submitted for a degree or any other qualification at this University or any other institution, this has been clearly stated;
- where I have consulted the published work of others, this is always clearly attributed;
- where I have quoted from the work of others, the source is always given. With the exception of such quotations, this thesis is entirely my own work;
- I have acknowledged all main sources of help;
- where the thesis is based on work done by myself jointly with others, I have made clear exactly what was done by others and what I have contributed myself;
- parts of this work have been published. (see *List of Publications*)

Signed: ……………………Jindan Shi…………………………………..

Date:………………………12th Nov. 2012   …………………………….

Acknowledgements

The thesis would not have been possible without the kind assistance and support of the organizations and the people around me. I would like to acknowledge China Scholarship Council (CSC) and Optoelectronic Research Centre (ORC) for providing financial support for my four years study in UK. I wish to convey thanks to Prof. Jintong Lin and Prof. Jian Wu who gave me the opportunity to be here.

I would like to express my sincere gratitude to my supervisor, Dr. Morten Ibsen, for his patient guidance and invaluable assistance throughout the course of this work. I am particularly thankful for his unwavering encouragement and timely comments throughout my studies. I thank Dr. Xian Feng for his invaluable support and guidance on the studies of novel glasses and fibres. Big thanks to Dr. Shaif-ul Alam for all his help and advice on the fibre lasers and for numerous useful technical discussions. A very special thank to Dr. Peter Horak for his theoretical support and simulation guidance on nonlinear fibre optics.

Many thanks to Dr. Neil G. R. Broderick and Dr. Youfang Hu for the simulation model of the Raman DFB fibre laser and many fruitful discussions. I thank Dr. Albert Canagasabey and Dr. Costantino Corbari for making the poling fibre samples and the helpful technical discussions about the second-harmonic generation in optical fibres. I thank Dr. Dejiao Lin, Dr. Kangkang Chen and Mr. Peh Siong Teh for all their help with the high power fibre laser sources and the optical components. I thank Dr. Gilberto Brambilla and Ms. Ming Ding for their help with the fibre tapering and the microscope measurements. I acknowledge Dr. Sakellaris Mailis, Dr. Ben Mills, Dr. Zhaowei Zhang, Dr. Junhua Ji, Dr. Yongjun Ying, Dr. Sheng Liu, Mr. Ee Leong Lim, Mr. Rafal Cieslak, Mr. Jae Daniel, Ms. Yi Liao and Ms. Tianfu Yao for all their assistance with the equipment and useful discussions throughout the studies.

I am most grateful to Mr. Simon Butler and Mr. Trevor Austin for their tireless technical support. I would like to thank our student mentors, Dr. Eleanor Tarbox and Dr. Peter Lanchester, for their helpful advice on my studies. I thank Mrs. Eveline Smith, Ms. Tanya Morrow, Mr. Kevin Sumner and Mr. David Olive for all their assistance. A special thank to my landlords, Mr. and Mrs. Anthony & Ela Robson for providing me long-term accommodation and proofreading my thesis. I am grateful to my housemates and my good friends for helping me get through the difficult times and for all the entertainment and care they have provided.

I would like to thank my parents, my elder sister and elder brother for their encouragement and support throughout my studies.

Principal Abbreviations

ASE	Amplified Spontaneous Emission
AOM	Acousto-Optic Modulator
ASC	Air-Suspended-Core
CW	Continuous-Wave
DBR	Distributed-Bragg Reflector
DFB	Distributed-Feedback
DSF	Dispersion Shifted Fibre
DSHI	Delayed Self-Heterodyne Interferometer
EYDFA	Erbium/Ytterbium-Doped Fibre Amplifier
FBG	Fibre Bragg Grating
FHW	Fundamental-Harmonic Wave
Fig.	Figure
FOM	Figure-of-Merit
FP	Fabry-Perot
FWHM	Full-Width-at-Half-Maximum
FWM	Four-Wave Mixing
GVD	Group Velocity Dispersion
HF	Holey Fibre
HNLF	Highly Nonlinear Fibre
HR	High Reflector
IR	Infrared
LD	Laser Diode
LIDAR	Light Detection And Ranging
LMA	Large Mode Area
LWA	Lightwave Analyser
MFD	Mode Field Diameter
MOF	Microstructured Optical Fibre
MOPA	Master-Oscillator Power Amplifier

NA	Numerical Aperture
NLCME	Nonlinear Coupled Mode Equations
OC	Output Coupler
OD	Outer Diameter
OSA	Optical Spectrum Analyser
PBG	Photonic Bandgap
PBS	Polarizing Beamsplitter
PC	Polarisation Controller
PCF	Photonic-Crystal Fibre
PER	Polarisation Extinction Ratio
PM	Polarisation Maintaining
PPSF	Periodic Poled Silica Fibre
PSP	π Phase-Shift Position
RBW	Resolution Bandwidth
R-DFB	Raman Distributed-Feedback
RE	Rare-Earth
RF	Radio-Frequency
rms	Root-Mean-Square
SCG	Supercontinuum Generation
TC	Temperature Controller
SEM	Scanning Electron Microscope
SHG	Second-Harmonic Generation
SHW	Second-Harmonic Wave
SMF	Single Mode Fibre
SMSR	Side Mode Suppression Ratio
SNR	Signal-to-Noise Ratio
SOA	Semiconductor Optical Amplifier
SON	Second-Order Nonlinearity
SPM	Self-Phase-Modulation
SRS/SBS	Stimulated Raman/Brillouin Scattering

SVEA	Slowly Varying Envelope Approximation
TC	Temperature Controller
TEM	Transverse Electromagnetic
TIF	Total Internal Reflection
TLS	Tunable Laser Source
TON	Third-Order Nonlinearity
TPP	Threshold Pump Power
TSE	Total Slope Efficiency
TWA	Travelling-Wave Amplifier
UV	Ultra-Violet
vs	Versus
WDM	Wavelength Division Multiplexer
XPM	Cross Phase Modulation
ZDW	Zero Dispersion Wavelength

Symbols

ε_0	Vacuum permittivity
c	The light speed in vacuum
$\chi^{(i)}$	i^{th} order of the nonlinear susceptibility tensor
n_0	Linear refractive index
n_2	Nonlinear refractive index
n_b	The Bose-Einstein thermal factor
α	Attenuation constant
g_r	Raman gain coefficient
h	Planck’s constant
I	Optical intensity
A_{eff}	Effective mode area
L_{eff}	Effective length
P_{th}	Threshold pump power
L	Length
L_c	Coherence length
L_W	Walk-off length
L_{tt}	Thermal tuning length
$\boldsymbol{P}$	Electric polarisation
$\boldsymbol{E}$	Electric field
β	Propagation constant
λ	Wavelength
Λ	Pitch of grating
A_i	Amplitude of wave i
γ	Nonlinear coefficient
γ_{eff}	Effective nonlinear coefficient
κ	Coupling coefficient of FBGs
κ_{dc}	Self-coupling coefficient of FBGs
$\delta\mathrm{k}, \Delta k$	Wave vector mismatch

To my Parents with love

Chapter 1 Introduction

1.1 Overview

1.1.1 ***Fibre Bragg gratings***

The *fibre Bragg grating* (FBG) has developed into a crucial and versatile component in the field of fibre optics. FBGs were first formed by means of launching highly intense visible light (Argon-ion laser) into Ge-doped core optical fibres by Hill et al. in 1978 [1]. Such ‘self-organised’ FBGs remained mysterious for nearly a decade until Meltz et al. demonstrated FBGs by a transverse holographic approach in 1989 [2]. Since then, FBGs have received significant attention and have progressed rapidly as a result of the breakthroughs and maturity of the FBGs fabrication techniques [3-8]. A variety types of high-quality FBGs, including chirped, phase-shifted, superstructured and titled FBGs, have been produced, and been widely made use of, in the areas of fibre amplifiers and lasers, optical communications, fibre sensing and so on [9-13].

The primary characteristics of FBGs include fibre compatibility with low insertion loss, compact design and precise control of the reflectivity as well as the Bragg wavelength, so they are ideal for the use as reflectors and/or narrow-band filters in the applications of amplifiers and lasers, and optical communications for example add/drop multiplexers [9, 10, 14]. Moreover, with the combination of additional advantages of high sensitivity to temperature and strains, FBGs play a key role in the field of fibre sensing [13, 15-17]. FBGs are also well-known as dispersive devices especially at the stop-band edge, which has been exploited in the nonlinear applications of pulse compression [11, 18], Bragg grating solitons [19], all-optical switching [20] and slow light [21-23]. Additionally, chirped FBGs enables tailoring the dispersion profiles for specific applications such as pulse broadening and/or compressing, chromatic dispersion compensation [12, 24-26].

The ultra-compact *distributed-feedback* (DFB) fibre laser was initiated in 1994 by Kringlebotn et al. [27] and developed in 1995 [28-30], by inserting a permanent π phase-shift into a unique FBG formed in a *rare-earth* (RE) doped fibre. Such a kind of DFB fibre laser has attracted great interest both in industry and academia because of its excellent features of single-frequency operation, narrow-linewidth, low noise characteristics and continuous wavelength tunability. Indeed, DFB fibre lasers have been demonstrated in a range of active single mode fibres, e.g., Yb-doped [31, 32], Er/Yb-doped [30, 33], Tm-doped [34, 35]. Very recently, multi-core DFB Er-doped fibre lasers [36], *Raman DFB* (R-DFB) fibre lasers [37-40] and Brillouin gain based DFB fibre lasers [41] have been reported. In particular, R-DFB fibre lasers overcomes the wavelength limitations of the RE-doped counterparts so that in principle, they can be designed to oscillate at any wavelength with a proper pump source [42].

Last but not least, most applications of FBGs demonstrated so far have been restricted to conventional silica-based optical fibres. The emergence of the non-silica glass fibres, which are considered as promising candidates for a range of nonlinear and/or *mid-infrared* (mid-IR) applications [43, 44], stimulates the desire for incorporating the FBGs into non-silica glass fibres to realize compact nonlinear devices. For instance, all-optical switching devices with low power threshold (~55 W) in FBG based (6 mm long) bismuth-oxide highly nonlinear fibre have been demonstrated [45]. However, high-index non-silica glasses have high *ultraviolet* (UV) absorption, the traditional UV light sources, i.e., 193 nm - 248 nm, are not suitable for writing FBGs into the core of the non-silica glass fibres. Instead, FBGs in non-silica glass fibres, based on tellurite, [46], fluoride [47], chalcogenide [48], bismuth [49] glasses, have been reported using femtosecond (fs) pulsed IR laser sources. However, the experimental setup of using fs IR lasers to fabricate FBGs is much more complex and more expensive than that of using UV light sources. Hence, it is highly desirable to find an alternative low-cost method to write FBGs into non-silica glass fibres.

1.1.2 High index-contrast, highly nonlinear non-silica glass fibres

The invention of non-silica glass *photonic-crystal fibre* (PCF) or *holey fibre* (HF) in 2000 [50], opens the way towards high index-contrast, highly nonlinear fibre using high performance non-silica glasses. In a PCF, the high index-contrast between the glass core and air-filled holey cladding allows the fibre to possess many novel optical performances, for example, an extremely small mode area and consequently high nonlinearity, a tailored dispersion profile within a broad wavelength range, and a very large mode area with single mode guidance (or the so-called endless single mode behaviour) [51, 52]. Non-silica glasses, including tellurite glasses, chalcogenide glasses and other heavy metal oxide glasses, have attractive optical properties including high linear and nonlinear refractive indices, high transparency from visible to the mid-IR region, and high rare-earth solubility [43, 52]. The PCF technology [53, 54] can reduce the core area down to micrometre level. As a result, the nonlinearities with the value of ~3-4 folds higher than conventional silica fibres have been achieved in lead silicate [44], bismuth oxide [55], tellurite [56], chalcogenide [57] glasses PCFs. Thus, they are promising candidates for the nonlinear applications, e.g., *supercontinuum generation* (SCG) [56, 58, 59] and wavelength conversion [51, 60]. The excellent nonlinear performance of the non-silica glass PCFs can be undoubtedly expected to be extended to mid-IR region, due to the excellent transparency of many high-index non-silica glasses such as tellurite and chalcogenide glasses. Additionally, a later exploration of non-silica glass based nonlinear fibre [51, 61] showed that the high index-contrast between the core and cladding can be obtained by a non-microstructural approach, which was to simply use two thermally compatible glasses with large index contrast ($\Delta n > 0.2$).

A main shortcoming of the non-silica glass fibre so far has been the high background loss (typically a few dB/m) and the difficulties in integrating them into the conventional silica glass fibre systems. Technically, the background loss can be improved by using high chemical purity glasses. And splicing method ought to be a good solution for connecting the non-silica glass fibres with silica glass fibres [62, 63].

*1.1.3 **Raman fibre lasers***

Raman fibre lasers were first observed with a *continuous-wave* (CW) source (Argon-ion) at 488 nm in 1976 by Hill et al. [64]. In that work, the Raman threshold was approximately 5 W for fibre lengths of 20 m to 100 m with core diameters of ~2.4 - 4 μm. Very different from the RE-doped counterparts, the operating wavelength of a Raman fibre laser depends on the pump wavelength and the Raman shift of the fibre material. For example, in silica glass fibres, the Raman shift with the peak Raman gain coefficient is typically ~440 cm^{-1} [65]. They can therefore in principle be designed to oscillate at any desired wavelength ranging from the visible to the infrared region, pending only the availability of a suitable pump source [65, 66]. However, the typical Raman fibre lasers with linear cavity configurations, which are formed with two FBGs, suffer from a large number of longitudinal modes because of the long cavity length. Until now the shortest *distributed-Bragg reflector* (DBR) Raman fibre laser is ~17 cm long formed in a high Raman gain fibre with a threshold of ~4.1 W [67]. Nevertheless, ~24 longitudinal cavity modes still exhibit within the ~60 pm bandwidth of the Stokes spectrum. With a shorter length cavity, the number of longitudinal modes will be reduced with the penalty of higher threshold pump power. On the other hand, DFB cavity structures rather than DBR designs enable single-frequency Raman fibre lasers with low threshold [40, 68]. Note that at the time when most of the work presented in the thesis was carried out, there had been no experimental demonstration of a R-DFB fibre laser yet.

*1.1.4 **Periodic poled silica fibres (PPSFs)***

The demonstration of *second-harmonic generation* (SHG) to visible light in *periodic poled silica fibres* (PPSFs) makes the PPSFs be a competitor to nonlinear crystals for second-order nonlinearity based wavelength conversion [69, 70]. A *figure of merit* (FOM) has been introduced for the comparisons between the poled fibres and nonlinear crystals [71].

$$\mathrm{FOM} = \frac{\left|\chi^{(2)}\right|^2 \cdot L^2 \cdot I}{\alpha {n_0}^3} \tag{1-1}$$

In which $\chi^{(2)}$, L, I, α and n_0 are the second-order susceptibility, the interaction length, the intensity of the pump beam, the propagation loss and the refractive index of the medium, respectively. Although, the $\chi^{(2)}$, induced through poling is relatively modest in optical fibres, PPSFs possess a much lower loss (0.2 dB/km) and much higher damage threshold (~2-3 folds higher) enabling them to withstand much higher intensities than the nonlinear crystals. The strongest point for PPSFs is that the interaction length of PPSFs can be much longer than the nonlinear crystals due to the intrinsically low chromatic dispersion of silica fibres. Besides, PPSFs are relatively cheaper, easier to be integrated with the high power fibre lasers and easier to fabricate than nonlinear crystals.

Frequency-doubling to red light (~771 nm) in 32-cm long PPSF has been realized using a high power pulsed-fibre laser source [72]. The average output power is ~236 mW for ~207 W of fundamental peak power, corresponding to an average conversion efficiency of ~15%. Over 50% conversion efficiency is theoretically possible by doubling the length of the PPSF device. However, the attainable length of the PPSFs is restricted by the thermal poling stage and the grating fabrication stage. It will be a high cost to extend the lengths of the poling stage and the grating fabrication stage. On the contrary, concatenating several PPSFs together is a relatively economic and simple way to achieve longer PPSFs for SHG application with higher conversion efficiency.

1.2 Motivations and key achievements

To extend the oscillation wavelength of a single-frequency DFB fibre laser to a new wavelength range, out of the range covered by the emission of RE ions in particular, it is desirable and of great interest to investigate DFB fibre lasers based on Raman gain from passive optical fibres instead of the active fibres providing RE gain.

In the thesis, the R-DFB fibre lasers have been explored thoroughly. This starts with building up the simulation model of the R-DFB fibre lasers by solving the coupled mode equations [73]. With the assistance of the simulation results, R-DFB fibre lasers have been successfully demonstrated in two types of standard optical fibres, which are PS980 (from Fibercore Ltd.) and UHNA4 (from Nufern) [39, 42]. The DFB gratings are 30 cm-long with a centre π phase-shift, fabricated in-house with phase-mask method. The lasing behaviour and the power scaling properties of the output R-DFB signal with respect to the incident pump source have been investigated with un-polarised and linearly polarised pump sources at ~1.06 μm, respectively. The lowest threshold of R-DFB fibre laser is observed to be ~440 mW with the linearly polarised pump source [40]. Besides, a truly uni-directional R-DFB fibre laser has been realized and characterized in this work [74]. Additionally, the linewidth of the R-DFB fibre lasers have been measured by using a delayed self-heterodyne method, with a value of <2.5 kHz limited by the delay line (~30 km). What is more, broadband wavelength conversion by using *four-wave mixing* (FWM) in these R-DFB fibre lasers has been observed and analysed both numerically and experimentally [75].

High-index non-silica glass fibres with high Raman gain coefficient and high nonlinear coefficient are promising host materials for R-DFB fibre lasers with low threshold. However, the prerequisites for realizing R-DFB lasers in high-index non-silica glass fibres are: (1) creating high-quality DFB gratings into non-silica glass fibres; (2) having the characteristics of the Raman gain spectra of non-silica glass fibres; (3) integrating the non-silica glass fibres with the conventional silica glass fibre systems.

In this context, the Raman gain spectrum of a non-silica glass, i.e., tellurite glass (made in-house), has been measured. A broadband *stimulated Raman scattering* (SRS) assisted SC has been demonstrated in a metre-length tellurite glass PCF with a pump source at ~1.06 µm, which is within the high normal dispersion region of the fibre [59]. Two types of high-index non-silica glass PCFs (lead silicate and tellurtite glass fibres) have been connected with standard silica glass fibres with low splice loss by means of arc-fusion splicing [63]. The ultraviolet photosensitivity of two types of non-silica glasses, i.e., lead silicate and tellurite, has been investigated with UV light sources at 325 nm, 344 nm and 355 nm, respectively. The challenges of fabricating FBGs into the non-silica glass fibres with UV light sources have been analysed.

All-fibre frequency-doubling in silica fibres are promising even though the induced second-order nonlinearity of the PPSFs is still low (~0.1 pm/V). In order to improve the SHG conversion efficiency in PPSFs, an experiment of concatenating two PPSFs has been conducted and the overall SHG conversion efficiency has been enhanced to more than 2.86 times of that of single PPSF device. Additionally, the effects of the connection loss at the fundamental and second-harmonic waves on the growth of the overall conversion efficiency of the concatenated PPSFs have been numerically analysed.

1.3 Outline of the thesis

Chapter 2 presents the basic background underlying the thesis. The fundamental knowledge of optical fibres is given in Section 2.1. Section 2.2 summarises the background of FBGs, including the coupled mode equations, the fabrication methods and the measurement of reflection and transmission spectra of FBGs. The third-order and second-order nonlinearities of optical fibres are introduced in Section 2.3. A conclusion is drawn in Section 2.4.

In Chapter 3, the studies of the R-DFB fibre lasers are given in detail. A brief review of the development of the DFB/DBR fibre lasers is summarised in Section 3.1. An overview of R-DFB fibre lasers is presented in Section 3.2. In Section 3.3, a numerical simulation model as well as the simulation results of R-DFB fibre lasers is discussed. Experimental demonstrations of R-DFB fibre lasers are presented in Section 3.4, including the experimental setup, the process of fibre selection, DFB gratings characterization and experimental data of (i) high power R-DFB fibre lasers with un-polarised pump source, (ii) low threshold R-DFB fibre lasers with linearly polarised pump source, and (iii) uni-directional output R-DFB fibre lasers. Section 3.5 summarises the linewidth measurement of the R-DFB fibre lasers. In Section 3.6, four-wave mixing in R-DFB fibre lasers have been studied both numerically and experimentally. Finally, Section 3.7 summarises the work of R-DFB fibre lasers.

Chapter 4 focuses on the investigation of the Raman gain of tellurite glass fibres and UV photosensitivity of the high-index non-silica glass fibres. A concise discussion about the nonlinear optical performance of high-index non-silica glasses fibres is given in Section 4.1. In Section 4.2, the calculation of the Raman gain spectrum of the tellurite glass and the experiment of generating SRS-assisted SC from metre-length tellurite PCFs have been provided. Fusion splicing non-silica glass fibres with standard silica fibres is concerned in Section 4.3. Besides, Section 4.4 summarises the studies on the photosensitivity of high-index non-silica glass fibres. Finally, a conclusion is drawn in Section 4.5.

Chapter 5 is the last chapter about the experimental work of the thesis, which is about the study on the concatenation PPSFs. The effects of connection loss on the overall conversion efficiency in concatenated PPSFs have been numerically studied in Section 5.1. Section 5.2 introduces the experimental setup for concatenating two PPSFs. The experimental results are presented in Section 5.3 and the work is concluded in Section 5.4.

Chapter 6 concludes the thesis and presents the potential future works.

Chapter 2 Background

2.1 Optical Fibres

An optical fibre is usually a thin cylindrical dielectric waveguide made of a low-loss material, e.g., silica or non-silica glass. The basic structure of an optical fibre is a circular core with a refractive index of n_{co} for guiding the light, embedded in an outer cladding of slightly lower refractive index, $n_{cl} < n_{co}$, (as seen in Fig. 2-1). According to the variation of the core index, optical fibres are usually classified as step-index or graded-index fibres. In a step-index fibre, the core and cladding indices, n_{co} and n_{cl}, are constant, whereas for a graded-index fibre, the core index varies with the radial distance from the core axis [76].

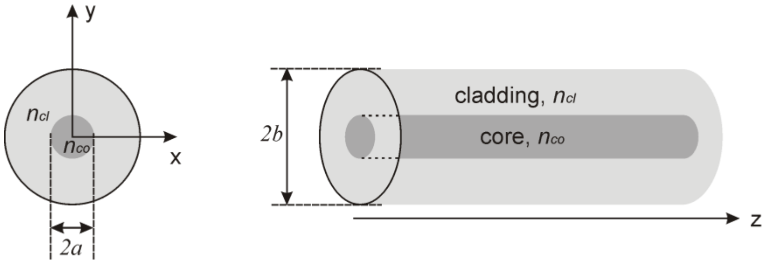

Fig. 2-1 Schematic diagram of an optical fibre.

2.1.1 *Step-index fibres*

The conventional optical fibres used in currently implemented optical communication systems are step-index *single-mode fibres* (SMFs) [77]. For example, SMF28 the standard Corning fibre, is made of fused silica glass with high chemical purity leading to the ultra-low loss at the transmission band of 1550 nm (~0.17 dB/km). Typically, the cladding diameter, *2b* (see Fig. 2-1) is 125 µm, while the core diameter, *2a*, varies from several micro-metre to tens of micro-metre to support different numbers of modes. The guidance mechanism in step-index fibres is known as *total internal reflection* (TIF) with the fact of $n_{co} > n_{cl}$. Such slight changes of the refractive indices (index contrast between the core and cladding) obtained by doping materials, e.g., germanium and boron, into the fibre core.

The *numerical aperture* (NA), expressed as Equation (2-1), is an important parameter for an optical fibre, which determines the divergence of the light emitted from the fibre.

$$NA = \sqrt{{n_{co}}^2 - {n_{cl}}^2} \tag{2-1}$$

To study the electric and magnetic fields of the guided waves in the step-index optical fibre, it is assumed that, as an approximation and for simplicity, the radius b of the cladding is infinitely thick and also the fibre is infinitely long in the axial direction (z axis in Fig. 2-1). For the case of monochromatic waves at λ_0, the guided modes are travelling in the z direction with propagation constant of β. As the index profile is ϕ-independent (ϕ is the azimuthal in the cylindrical coordinate system), the complex amplitude of the electric and magnetic field can be expressed as:

$$U(r,\phi,z) = u(r)e^{-jl\phi}e^{-j\beta z}, \qquad l = 0, \pm 1, \pm 2, \cdots \tag{2-2}$$

in which l is the azimuthal index and $u(r)$ is the radial profile.

In such a case, $U(r,\phi,z)$ obeys the Helmholtz equation [76, 78] and can be expressed as Equation (2-3) in a cylindrical co-ordinate system:

$$\frac{\partial^2 U}{\partial r^2} + \frac{1}{r}\frac{\partial U}{\partial r} + \frac{1}{r^2}\frac{\partial^2 U}{\partial \emptyset^2} + \frac{\partial^2 U}{\partial z^2} + n(r)^2 {k_0}^2 U = 0 \tag{2-3}$$

where $k_0 = 2\pi/\lambda_0$ is the vacuum wavenumber at λ_0. Substituting Equation (2-2) into Equation (2-3) leads to an ordinary differential equation for the $u(r)$:

$$\frac{\partial^2 u}{\partial r^2} + \frac{1}{r}\frac{\partial u}{\partial r} + (n(r)^2 {k_0}^2 - \beta^2 - \frac{l^2}{r^2})u = 0 \tag{2-4}$$

Since the wave is guided in the core of the optical fibre, the propagation constant must satisfy the relationship of:

$$n_{cl}k_0 < \beta = Nk_0 < n_{co}k_0 \tag{2-5}$$

in which *N* is the effective index of the guided wave. Herein, the *V*-parameter and generalized propagation constant *b* are introduced as:

$$V = NA \cdot a \cdot k_0 = \frac{2\pi}{\lambda_0} a \cdot NA \tag{2-6}$$

$$b = \frac{\beta^2 - {n_{cl}}^2 {k_0}^2}{{n_{co}}^2 {k_0}^2 - {n_{cl}}^2 {k_0}^2} = \frac{N^2 - {n_{cl}}^2}{{n_{co}}^2 - {n_{cl}}^2} \tag{2-7}$$

By using Equations (2-6) and (2-7), Equation (2-4) can be rewritten in the core and cladding separately as:

$$\frac{\partial^2 u}{\partial r^2}+\frac{1}{r}\frac{\partial u}{\partial r}+\left(\frac{V^2(1-b)}{a^2}-\frac{l^2}{r^2}\right)u=0,\ \ r<a\ (core)$$
$$\frac{\partial^2 u}{\partial r^2}+\frac{1}{r}\frac{\partial u}{\partial r}-\left(\frac{V^2 b}{a^2}+\frac{l^2}{r^2}\right)u=0,\ \ r>a\ (cladding) \tag{2-8}$$

The solutions of Equation (2-8) are the family of Bessel functions and can be expressed as:

$$u(r)\propto\begin{cases}J_l\left(\dfrac{V\sqrt{1-b}}{a}r\right), & r<a\ (core)\\ K_l\left(\dfrac{V\sqrt{b}}{a}r\right), & r>a\ (cladding)\end{cases} \tag{2-9}$$

in which $J_l(x)$ and $K_l(x)$ are the Bessel functions of the first kind and the modified Bessel function of the second kind of order *l*. With the help of Maxwell's equations and combining the boundary conditions, each of the components of electric and magnetic fields can be solved [78].

In general, most of the step-index fibres have the feature of $(n_{co}-n_{cl})/n_{co}\ll 1$, i.e., $n_{co}\approx n_{cl}$. When the core radius is, $a>\lambda_0$, the fibre can be treated as the case of weakly guiding and so the guided rays are approximately parallel to the fibre axis. Hence, the transverse components of the electric and magnetic fields are much stronger than the longitudinal components and the guided waves are approximately *transverse electromagnetic* (TEM) in nature. Additionally, the boundary conditions of transverse components can be approximately equivalent to the conditions that $u(r)$ in Equation (2-9) is continuous and has a continuous derivative at the core-cladding boundary ($r=a$). Such conditions will be satisfied if the *V*-parameter and *b* meet the characteristic equation as below:

$$V\sqrt{1-b}\frac{J_l{}'(V\sqrt{1-b})}{J_l(V\sqrt{1-b})}=V\sqrt{b}\frac{K_l{}'(V\sqrt{b})}{K_l(V\sqrt{b})} \tag{2-10}$$

where $J_l{}'$ and $K_l{}'$ are the derivatives of Bessel functions. Equation (2-10) can also be modified as:

$$V\sqrt{1-b}\frac{J_{l\pm1}(V\sqrt{1-b})}{J_l(V\sqrt{1-b})}\mp V\sqrt{b}\frac{K_{l\pm1}(V\sqrt{b})}{K_l(V\sqrt{b})}=0 \tag{2-11}$$

The characteristic Equation (2-11) can be solved numerically [76, 78]. Given a *V* and *l*, there may be none, one or more solutions for *b*, yielding discrete propagation constants $\beta_{lm}, m=1,2,\cdots$. Each solution, if it exists, represents a linearly polarised mode, as LP_{lm} mode, of which, *l* describes the azimuthal mode whereas *m* characterizes the radial distribution of transverse field. When $V < 2.405$, all modes apart from the fundamental mode, LP_{01}, are cut off such that the fibre operates as a single-mode waveguide. For $V > 2.405$, multiple modes can propagate in the fibre.

Since a propagating mode is confined into the core of the fibre, the ratio of the power delivered in the core to the total power can be evaluated as [78]:

$$\Gamma = \frac{P_{core}}{P_{core} + P_{clad}} = 1 - (1 - b)[1 - \frac{{K_l}^2(V\sqrt{b})}{K_{l+1}(V\sqrt{b})K_{l-1}(V\sqrt{b})}] \tag{2-12}$$

Fig. 2-2 illustrates the relations between b and Γ with respect to the V-parameter of the fundamental mode, LP_{01}, in step-index SMFs. As seen from Fig. 2-2, the power becomes more confined in the core with the increase of the V-number.

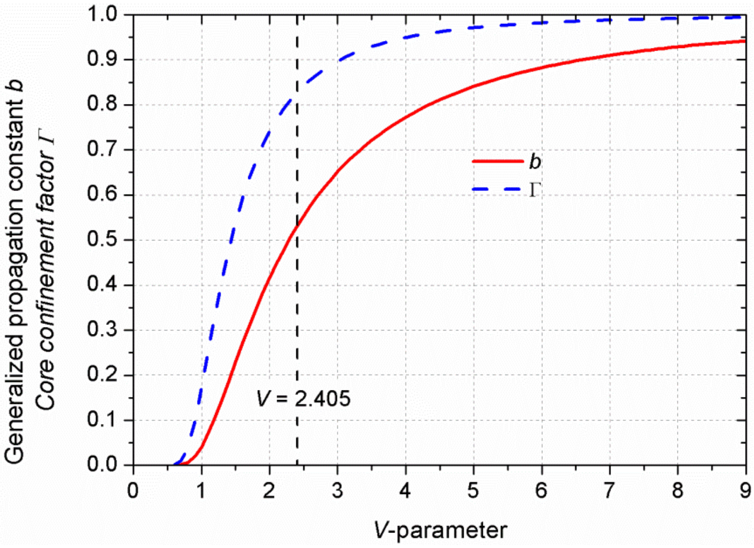

Fig. 2-2 *b and* Γ vs *V*-parameter of LP_{01} in weakly guiding step-index fibres.

2.1.2 *Photonic-crystal fibres (PCFs)*

In addition to the conventional step-index fibres (as seen in Fig. 2-1) discussed above, photonic-crystal fibres, also called *microstructured optical fibres* (MOFs) or HFs, have gained great attention and attained considerable technological maturity since 1996 [54]. PCF is made of a single-material with a built-in transverse air-filled microstructured cladding, e.g., as shown in Fig. 2-3. The guidance mechanisms of PCFs are distinct from the step-index SMFs, including (i) effective TIF, when the core-cladding index contrast is positive (e.g., as seen in Fig. 2-3 (a)(b)) (ii) *photonic bandgap* (PBG) guidance, e.g., PCF with a hollow core, as illustrated in Fig. 2-3 (c)(d). In the case of index guided PCF, the index contrast between the core and cladding can be varied from low values (for a PCF with extremely low air-filling fraction) to extremely high values (for a PCF with an air-suspended core). The combination of the high index-contrast and the wavelength-scaled microstructure allows the PCFs to have many remarkable advantages at the control of some key parameters of optical fibres, such as dispersion and nonlinearity, via playing the size and structure of the air-filled holes in the cladding.

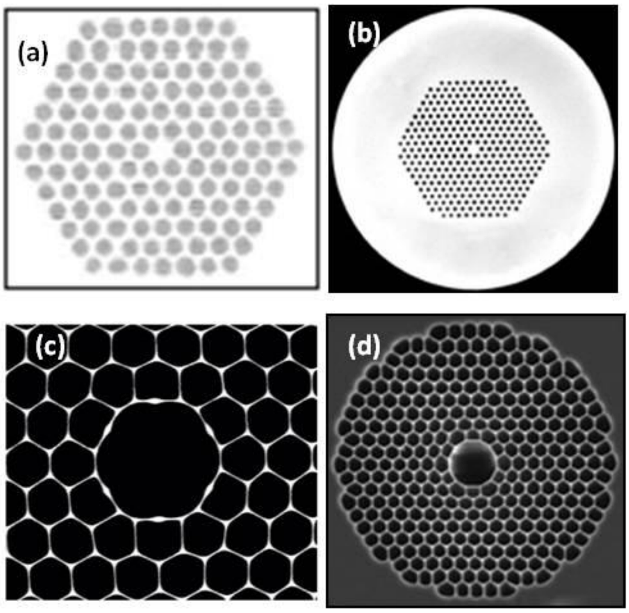

Fig. 2-3 Transverse images of (a) (b) effective TIF guided PCF and (c) (d) optical bandgap guided PCF. (After Ref. [79])

In particular, high-index non-silica glass PCFs, like lead silicate PCFs [44, 51], tellurite glass PCFs [59, 80], chalcogenide glass PCFs [50, 57], possess much higher nonlinearity due to the high refractive indices of the non-silica glasses, which will be discussed more detail in Chapter 4. Based on the excellent high nonlinear properties of the high-index non-silica glass PCFs, they are promising host fibres for FBGs to form compact (short length) nonlinear applications devices. However, the FBGs fabrication technique in the high-index non-silica glass PCFs is still at its early stage and the investigation of writing FBGs into the high-index non-silica glass PCFs with UV light sources will be presented in Chapter 4.

2.2 Fibre Bragg gratings

2.2.1 *Fundamentals of fibre Bragg gratings*

Fibre gratings are important fibre components for coupling light between different modes and are usually formed by a periodic or quasi-periodic index modulation in the core of optical fibres [5, 9, 11]. The most basic fibre grating generates coupling between forward- (β_1) and backward- ($-\beta_2$) propagating modes and is referred to as a fibre Bragg grating (FBG), which is widely used as a reflector or filter in fibre lasers or fibre communication systems [5, 9].

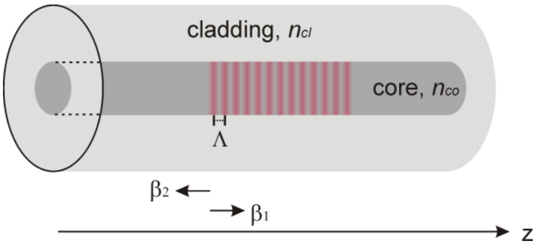

Fig. 2-4 Schematic diagram of a FBG.

Fig. 2-4 illustrates the schematic diagram of a FBG with a uniform index modulation period of Λ. Since the first-order diffraction dominates in a FBG, a phase-mismatch factor between the counter-propagation modes in the FBG can be expressed as:

$$\Delta\beta = \beta_2 + \beta_1 - \frac{2\pi}{\Lambda} \tag{2-13}$$

The Bragg resonator wavelength, λ_{FBG}, occurs at the phase-matching point of $\Delta\beta = 0$ for the coupled modes, i.e.,

$$\frac{2\pi}{\Lambda} = \frac{2\pi N_1}{\lambda_{FBG}} + \frac{2\pi N_2}{\lambda_{FBG}} \tag{2-14}$$

in which N_1 and N_2 are the effective indices at the two modes, respectively. For identical or nearly identical modes, $N_1 = N_2 = n_{eff}$, the Bragg grating condition can be expressed as:

$$\lambda_{FBG} = 2n_{eff}\Lambda \tag{2-15}$$

The theory of FBGs can be developed by solving the wave propagation equations in optical fibre with the consideration of the refractive index perturbation along the z axis of the optical fibres (as indicated in Fig. 2-4) [11]. For instance, a FBG with a sinusoidal periodic index modulation with a nominal period of Λ, the spatial variation of the index profile can be expressed as:

$$\Delta n(z) = \overline{\Delta n}(z)\left\{1 + \nu \cdot cos[\frac{2\pi}{\Lambda} z + \theta(z)]\right\} \tag{2-16}$$

where $\overline{\Delta n}(z)$ is the average index change over a single period of grating, ν is the visibility of the fringes and $\theta(z)$ represents grating chirp [9]. Typically, the amplitude of Δn is in the range of 10^{-5} to 10^{-3} for FBGs [4, 11] so that they could be considered as weak-perturbations along the optical fibres. In such a situation, coupled-mode theory is normally applied to obtain solutions for the forward- and backward-propagation waves involved in FBGs [11]. The derivation of the coupled-mode equations for FBGs has been given out in a number of references [11], and the equations obtained are:

$$\begin{aligned}&\frac{dR(z)}{dz}+i\delta\cdot R(z)+i\kappa^{*}\cdot S(z)=0\\&\frac{dS(z)}{dz}-i\delta\cdot S(z)-i\kappa\cdot R(z)=0\end{aligned}\qquad(2\text{-}17)$$

in which $R(z)=A_1(z)\exp\left(-i\frac{\Delta\beta\cdot z-\theta(z)}{2}\right)$ and $S(z)=A_2(z)\exp\left(i\frac{\Delta\beta\cdot z-\theta(z)}{2}\right)$, (where $\Delta\beta$ is obtained as Equation (2-13), describing detuning phase-mismatch factor), represent the amplitude profiles of forward (input) and backward propagation (reflected) modes. The coefficient in the second term of Equation (2-17) is as follows [11]:

$$\delta=\kappa_{dc}+\frac{1}{2}\left(\Delta\beta-\frac{d\theta(z)}{dz}\right)\qquad(2\text{-}18)$$

where κ_{dc} is self-coupling coefficient due to average index change ($\overline{\Delta n}$). Whilst, κ, in the third term of Equation (2-17), is the coupling constant between the coupled modes and $\kappa=v\cdot\frac{\kappa_{dc}}{2}$.

For a uniform FBG formed in a single-mode fibre, $\overline{\Delta n}$(z) is constant along the FBG and $\frac{d\theta(z)}{dz}=0$. Also, $\kappa_{dc}=\frac{2\pi}{\lambda}\overline{\Delta n}$ is constant and $\kappa=\kappa^{*}=v\cdot\frac{\pi}{\lambda}\overline{\Delta n}$. For a FBG with a length of L, and it is assumed that the amplitude of the incident wave is launched from the left-side, as seen in Fig. 2-4, as $R(z=0)=1$ and that the backward propagation wave $S(z=L)=0$, the power reflection coefficient at the input site of the fibre is obtained as [9, 11]:

$$r=\left|\frac{S(z=0)}{R(z=0)}\right|^{2}=\left|\frac{\kappa\cdot sinh\,(\sqrt{|\kappa|^{2}-\delta^{2}}L)}{\delta\cdot sinh\left(\sqrt{|\kappa|^{2}-\delta^{2}}L\right)-i\cdot\sqrt{|\kappa|^{2}-\delta^{2}}cosh\,(\sqrt{|\kappa|^{2}-\delta^{2}}L)}\right|^{2}\qquad(2\text{-}19)$$

The peak reflectivity, r_B, occurs at the condition of $\delta=0$. For a uniform FBG, Equation (2-18) reduces to:

$$\kappa_{dc}+\frac{1}{2}\Delta\beta=0\qquad(2\text{-}20)$$

Hence, the peak reflectivity at the Bragg wavelength for a uniform FBG can be simplified from Equation (2-19) as:

$$r_B=\tanh^{2}(\kappa L)\qquad(2\text{-}21)$$

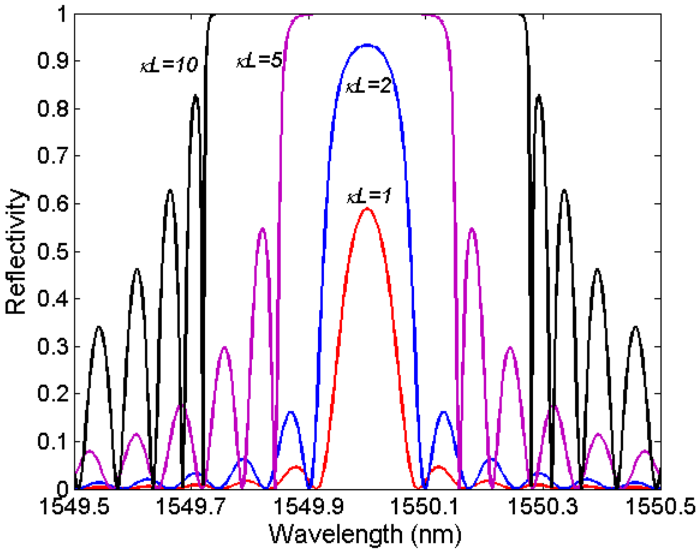

Fig. 2-5 Reflection spectra of four uniform FBGs with constant length of 10 mm but varied strength (κL) of 1, 2, 5, and 10.

Fig. 2-5 illustrates the reflection spectra of four 10 mm-long uniform FBGs at 1550 nm with varied grating strength (κL) of 1, 2, 5, and 10. It can be seen clearly that the peak reflectivity increases with the FBGs' strength, κL. Besides, the side-lobes in the reflection spectra are due to the abrupt start and end to a finite length grating. Furthermore, as seen in Fig. 2-5, the full bandwidth ($2\Delta\lambda$) between the first zero on either side of Bragg wavelength at the stronger grating strength of $\kappa L = 10$ is much broader than that of $\kappa L = 1$. This is because $2\Delta\lambda$ relates to the coupling constant as [9, 11]:

$$2\Delta\lambda = \frac{\lambda_{FBG}}{\pi n_{eff} L}\sqrt{(\kappa L)^2 + \pi^2} \tag{2-22}$$

Additionally, for non-uniform FBGs, such as chirped, apodized or phase-shifted FBGs, the reflection and transmission spectra of them can also be studied through solving the coupled-mode Equation (2-17), numerically or with a transfer matrix technique, which has been described in detail in the references of [9, 11, 81].

2.2.2 Phase-shifted distributed-feedback fibre gratings

The DFB fibre grating incorporating a phase-step within the length of the grating is the basic structure for a DFB fibre laser. The induced phase-step opens up a narrow transmission band in the stop-band of a FBG, leading to a *Fabry-Perot* (FP) cavity with a gap of less than one Bragg wavelength. The wavelength and the position of the transmission band is influenced by the position and the size of the phase-step [11, 82]. Typically, a single π phase-shifted DFB grating is used for a single-frequency DFB fibre laser [28, 31, 34]. And the single π phase-shifted DFB grating is usually formed by comprising a $\Lambda/2$ (or $(1/2+m)\Lambda$, m is an integer) gap in the FBG with the nominal pitch of Λ, as illustrated in Fig. 2-6, which could be effectively viewed as combining two single uniform FBGs together with half of the original length. Fig. 2-7 shows the reflection spectra from a uniform FBG and a centre π phase-shifted DFB grating, which has a narrow transmission band at the centre of the stop band of grating and the reflectivity from each side of the transmission band is identical.

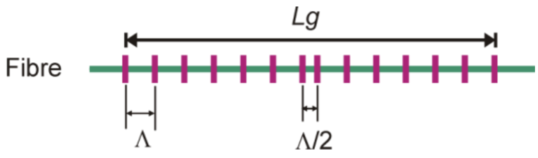

Fig. 2-6 Schematic diagram of a centre π phase-shifted DFB fibre grating. L_g is the length of the grating.

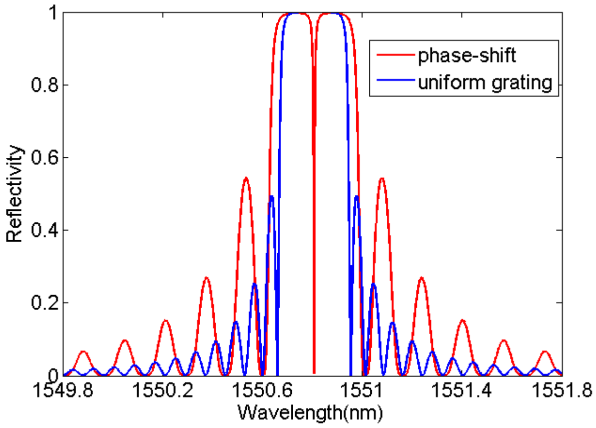

Fig. 2-7 Calculated reflection spectra of a uniform FBG (blue) and a centre π phase-shifted (red) DFB grating with a length of 10 mm and a coupling constant, $\kappa = 456\ m^{-1}$, respectively.

By shifting the phase-step from the centre of the grating, the reflectivity from one side of the transmission band will be higher than the other, effectively resulting in an *high reflector* (HR) and *output coupler* (OC) cavity for establishing a unidirectional output DFB fibre laser [83]. Furthermore, integrating/cascading multiple phase-steps into a fibre grating could open multi-transmission bands simultaneously, which is also referred to as superstructured FBGs [84, 85].

2.2.3 *Fabrication methods of FBGs*

The methods for fabricating FBGs fall simply into two categories: holographic methods by dual-beam interferometers or phase mask interferometers and point-by-point techniques [5, 8, 11].

2.2.3.1 Dual-Beam holographic method

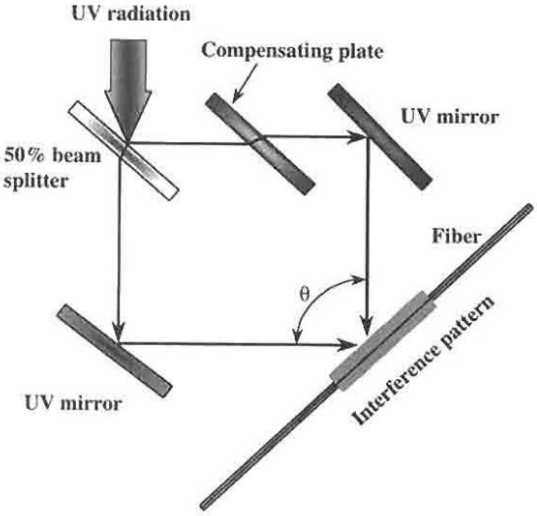

Fig. 2-8 Schematic diagram of FBGs fabrication with a dual-beam holographic technology. (After Ref. [11])

Fig. 2-8 shows the schematic diagram of the dual-beam holographic method to write FBGs from the side of the optical fibres, which was first demonstrated by Meltz et al. [2]. The UV beam is divided into two beams with equal intensity by a beam splitter and then recombined at a mutual angle of θ to produce an interference pattern in the core of the fibre. The compensating plate on one of the beam arms is used to compensate the length difference of the optical path so that the interference pattern can be optimized. The pitch, Λ, of the FBG is calculated as:

$$\Lambda = \frac{\lambda_{UV}}{2 \cdot \sin(\theta/2)} \tag{2-23}$$

From Equation (2-23), it can be seen that the pitch can be tuned over a wide range by adjusting the angle of θ ($0 < \theta < \pi$) for a fixed UV beam. Therefore, from the Bragg condition of Equation (2-15), a wide range of Bragg wavelength can be obtained with this method. Moreover, a flexible length of FBGs is feasible with this method via mounting the fibre on a translation stage and moving the fibre during the exposure. However, in this interferometer setup, two coherent beams are required. Also, any mechanical vibrations or environmental perturbations would influence the interference fringes. Hence, in practice, this method requires a very stable environment and the alignment is very complex.

2.2.3.2 Phase mask fabrication method

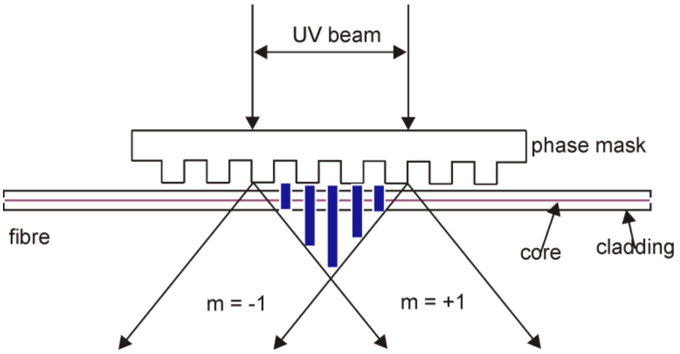

Fig. 2-9 Schematic diagram of FBGs fabrication by Phase mask method with a UV beam.

The phase mask fabrication method is considered as the most effective method for writing FBGs with UV light (for UV photosensitive optical fibres) [11] or fs-IR laser (for both UV photosensitive and non-photosensitive optical fibres) [86]. A phase mask is used as a component of the interference and has grooves etched into one surface of a high-quality fused silica glass plate transparent to the UV light beam. Fig. 2-9 illustrates the schematic of the phase mask technique for a FBG fabrication with a normal incident UV beam. At the output side of the phase mask, the normal incident UV beam is diffracted into ±1 orders and the zeroth-order is suppressed by the phase mask. Then a near-field fringe pattern is produced by the interference of the two diffracted beams. The fibre is placed in close proximity immediately with the phase mask but not in contact. The period of a FBG (Λ) is determined by the period of phase-mask (Λ_{pm}) in use, and has the following relationship:

$$\Lambda = \frac{\Lambda_{pm}}{2} \tag{2-24}$$

The phase mask technique has been broadly used for fabricating FBGs due to its advantages of a compact and robust writing system. A stable interference pattern is formed by the phase mask and the mechanical vibrations are also minimised by means of placing the fibre directly behind the phase mask. Additionally, with the assistance of a translation system for fibre or phase mask, complex index modulation profiles as well as varied length of FBGs can be easily produced by this approach.

2.2.3.3 Point-by-point method

The point-by-point scheme for writing a periodic refractive index grating is produced by illuminating a single spot at a time along the fibre. The refractive index of the irradiated core changes locally and the fibre is then translated through a distance to repeat the step again. This method has the main advantage of flexibility at selecting the radiation laser source, ranging from UV light to near-IR fs-laser sources [6, 7]. However, the radiation beam has to be focused tightly to form a first-order FBG in the fibre core because the pitch of the FBG at 1550 nm is in the order of ~0.5 µm [87, 88]. Therefore, a high-resolution translation stage is required to control the fibre position during the fabrication process [7, 88]. Since the spot size is diffraction-limited, higher-order (2nd or 3rd) FBGs are usually implemented with a near-IR fs-laser source [7]. Besides, oil immersion techniques are commonly implemented to overcome the beam distortion in the core of the fibre due to the fibre surface geometry [7, 89]. In addition, since the core diameter of single-mode fibres is typically less than ~10 µm, the point-by-point method is usually applied to fabricate short-length FBGs because of the difficulties of controlling the radiation beam accurately enough to be maintained in the core of the fibre along the whole length of the grating.

2.2.4 Measurement of reflection and transmission spectra of FBGs

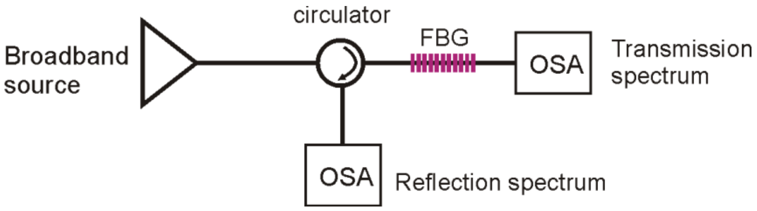

Fig. 2-10 Schematic diagram of the FBGs measurement.

The transmission and reflection spectra of FBGs are typically straightforwardly measured with an *optical spectrum analyser* (OSA) using a setup shown in Fig. 2-10. A broadband source, e.g., *Ytterbium*/*Erbium-doped fibre amplifier* (YDFA/EDFA) or *amplified spontaneous emission* (ASE) source or supercontinuum (SC) source, is connected to a circulator (or a coupler [11]). The output is then connected to the FBG under test. As a result, the transmission spectrum of the FBG can be measured at the output end of the FBG, whilst the reflection spectrum is detected at another output of the circulator, as seen in Fig. 2-10. From the transmission and reflection spectra, the Bragg wavelength, the maximum reflectivity, the full bandwidth of the grating and the *side mode suppression ratio* (SMSR) can be obtained. However, special care needs to be taken when measuring FBGs with the reflectivity higher than ~99.9%, corresponding to the transmission dips exceeding ~30 dB, or DFB gratings with an ultra-narrow pass-band, i.e., less than ~1 GHz, due to the resolution limitation of the OSA. For example, the highest resolution for an OSA is 0.01 nm, which is corresponding to ~1.24 GHz at 1550 nm. This problem can be solved with several other approaches, such as replacing the broadband source with a narrow-bandwidth tunable laser source or characterising the power reflection spectrum of the FBGs with a side-diffraction method [90]. In Addition, the phase and dispersion response of the FBGs can only be measured from the grating's complex amplitude reflectivity

[91], but it is beyond the scope of this work to consider these in detail. However, a number of methods for measuring the phase as well as the dispersion profiles of FBGs have been summarised in Chapter 9 of Ref. [11].

2.3 Nonlinearities of optical fibres

When radiation is incident upon a medium, the oscillating electromagnetic field interacts with electric dipoles in the molecules of the medium and causes them to oscillate. This results in a time-varying local electric polarisation in the medium. The oscillating electric field then re-radiates the electromagnetic field and the incident wave is considered to propagate through the medium via a series of such absorption and re-radiation process. The induced polarisation, $\boldsymbol{P}$, by the applied electric field, $\boldsymbol{E}$, can be expressed as [65]:

$$\boldsymbol{P} = \varepsilon_0 \chi^{(1)} \boldsymbol{E} + \varepsilon_0 \chi^{(2)} \boldsymbol{E}^2 + \varepsilon_0 \chi^{(3)} \boldsymbol{E}^3 + \cdots \tag{2-25}$$

where ε_0 is the electric permittivity in vacuum, and $\chi^{(i)}, (\ i = 1,2,3, \cdots)$ is the i^{th} order of the nonlinear susceptibility tensor of the medium. Specifically speaking, $\chi^{(1)}$ is the linear susceptibility tensor term, which represents the dominant contribution to $\boldsymbol{P}$ and affects the linear refractive index of the medium (n_0) and the absorption attenuation coefficient (α). If the induced polarisation has a purely linear dependence on the applied electric field then the re-radiated electric field will be identical to the incident field. While the second- or higher-order susceptibility terms are non-zero, harmonics begin to appear in the radiated field which were not present in the incident field. For media having symmetrical molecular structures, for example fused silica (SiO_2) glass (the basic constituent of the optical fibres), the susceptibility of these materials contains only odd expansion terms. Consequently, $\chi^{(2)}$ vanishes and the second-order nonlinear effects are not normally observed in optical fibres. On the contrary, the materials having anti-symmetric molecules, e.g., quartz and crystals, the even terms such as $\chi^{(2)}$ may be non-zero.

2.3.1 *Third-order nonlinear effects in optical fibres*

The inherent lowest order of nonlinear effect in optical fibres emerges from the *third-order nonlinearity* (TON), $\chi^{(3)}$, which is responsible for nonlinear behaviour such as *self-phase-modulation* (SPM), *cross-phase-modulation* (XPM), FWM as well as stimulated Raman/Brillouin scattering (SRS/SBS) [65, 76].

2.3.1.1 Kerr effect

SPM and XPM originate from the Kerr effect, which refers to the phenomenon of the refractive index change in proportion to the optical intensity as:

$$n(\omega, |E|^2) = n_0(\omega) + n_2 \cdot |E|^2 \tag{2-26}$$

in which $n_0(\omega)$ is the linear part of the refractive index and $|E|^2$ represents the applied optical intensity in the fibre. n_2 is the nonlinear-index coefficient, which can be evaluated from the real part of $\chi^{(3)}$ as $n_2 = \frac{3Re(\chi^{(3)})}{8n_0}$ [65]. In SMF28, n_2 is measured to be ~$2.2 \times 10^{-20}\ m^2/W$ [65]. Such a kind of optical intensity induced refractive index change leads to the nonlinear phase shift of an optical field propagating in the optical fibre, which is known as the phenomenon of SPM when the phase shift is self-field induced, or XPM when the phase shift is induced by another optical field.

2.3.1.2 Four-wave mixing (FWM)

FWM refers to the nonlinear process to generate radiation at new frequencies through the interaction between optical fields at two or three different frequencies. The nonlinear response of a nonlinear medium to the applied electric field relating to the TON can be expressed as [65]:

$$\boldsymbol{P}_{NL} = \varepsilon_0 \chi^{(3)} \boldsymbol{E}^3 \tag{2-27}$$

Giving that three optical waves are at the angular frequencies of $\omega_j, j = 1,2,3$, and propagate simultaneously in the same direction with propagation constants of $\beta_j, j = 1,2,3$, and are linearly polarised along the same axis, the amplitude of the total electric field can be written as:

$$E(t) = \frac{1}{2}\sum_{j=1}^{3}\{E_j exp\left[i(\beta_j z - \omega_j t)\right] + c.c.\} \tag{2-28}$$

Substituting Equation (2-28) into Equation (2-27), the nonlinear polarisation P_{NL} is found to be the sum of harmonic components of angular frequencies $\omega_1, \cdots, 3\omega_1, \cdots, 2\omega_1 \pm \omega_2, \cdots, \pm\omega_1 \pm \omega_2 \pm \omega_3$, in which the new frequencies of $\omega_l + \omega_m - \omega_n, (l, m, n = 1,2,3; l \neq m \neq n)$ are considered as the outcome of FWM process and are also known as idler waves or conjugate waves [65]. The amplitude of $P_{NL}(\omega_l + \omega_m - \omega_n)$ can be determined as:

$$\begin{gathered} P_{NL}(\omega_l + \omega_m - \omega_n) \propto E(\omega_l)E(\omega_m)E^*(\omega_n) \\ \sim E_{lmn}\exp\left[i(\beta_l + \beta_m - \beta_n)z - (\omega_l + \omega_m - \omega_n)t\right] \end{gathered} \tag{2-29}$$

If the idler waves oscillate at angular frequency of ω_{lmn} with propagation constant of β_{lmn}, the phase matching conditions for FWM can be obtained from Equation (2-29) as:

$$\begin{aligned} \beta_{lmn} &= \beta_l + \beta_m - \beta_n \\ \omega_{lmn} &= \omega_l + \omega_m - \omega_n \end{aligned} \tag{2-30}$$

If the initial three frequencies are unique, i.e., $\omega_1 \neq \omega_2 \neq \omega_3$, a large number of extra frequencies are possible via different permutations of ω_l, ω_m and ω_k, according to Equation (2-30). In this situation, the FWM process is referred to as a non-degenerate case. Alternatively, if two of the three waves have the same frequencies, the incident pump waves are degenerated to oscillate at two distinct frequencies of ω_1 and ω_2. Thus, according to the phase matching conditions in Equation (2-30), one of the incident waves acts the role of both ω_l and ω_m, such as $\omega_l = \omega_m = \omega_1$ or $\omega_l = \omega_m = \omega_2$. As a result, there are only two new frequencies (ω_{112} and ω_{221}) generated in such FWM process, which is known as the partially degenerated FWM (PDFWM). Fig. 2-11 illustrates the frequencies relations in non-degenerate FWM and PDFWM processes, respectively.

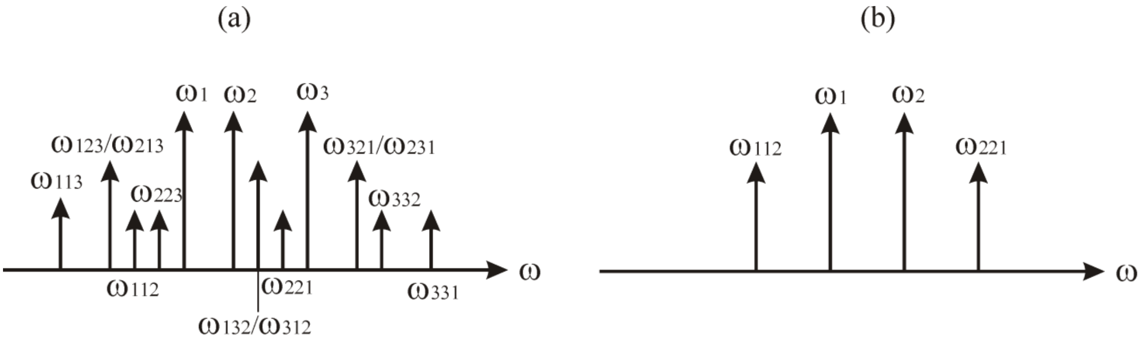

Fig. 2-11 New frequencies generated through FWM processes in (a) non-degenerate case and (b) partially degenerate case. (After Ref. [92])

The FWM effect converts energy from the pump waves to the new frequencies and the conversion efficiency depends on the phase matching conditions in Equation (2-30) as well as the nonlinear coefficient of the medium. Since the optical fibres are dispersive waveguides, the wavenumber mismatch $\Delta\beta = \beta_{lmn} + \beta_n - \beta_l - \beta_m$ is relatively easy to be satisfied in the condition of $\Delta\beta = 0$ in PDFWM case, as displayed in Fig. 2-11(b). Therefore the PDFWM is more relevant for optical fibres. In the PDFWM case, if only a single pump wave is incident into an optical fibre, FWM may occur between the pump wave and the noise since the phase-matching conditions are satisfied. On the other hand, as seen in Fig. 2-11(b), if a weak signal at ω_{112} or ω_{221} is launched into the fibre with the combination of the strong pump waves (ω_1 and ω_2) and the phase-matching conditions are met, the signal will be amplified through the FWM effect while a new frequency (ω_{221} or ω_{112}) is generated simultaneously. This process is referred to as parametric amplification [65, 93, 94]. The intensity evolution of the interaction waves during FWM process is usually investigated by means of solving the coupled amplitude equations, which have been studied in detail in other documents [65, 95].

2.3.1.3 Stimulated Raman scattering (SRS)

SRS originates from the atomic vibrations of glass lattice in response to an incident light beam and is an inelastic scattering process in which optical phonons are involved [65]. If the vibrations are associated with acoustical phonons, the effect is called stimulated Brillouin scattering (SBS). In either SRS or SBS process, the scattered light with frequencies shifted down are called the Stokes waves and those with frequency shifted up are named the anti-Stokes waves [96, 97]. In optical fibres, the SBS only occurs in backward directions due to the dispersion relation whilst the SRS can occur in both directions.

In the case of a CW or a quasi-CW incident light beam propagating through an optical fibre, the Raman Stokes wave initially grows exponentially as [65, 96, 98]:

$$\frac{dI_s}{dz} \propto g_r I_p I_s \tag{2-31}$$

where I_s, I_p are the Stokes intensity and pump wave intensity, respectively. g_r is the Raman-gain coefficient of the optical fibre, which depends usually on the composition of the fibre core and relates to the cross section of spontaneous Raman scattering [65, 98]. Fig. 2-12 illustrates the Raman gain spectrum normalized to its peak at 440 cm^{-1} for silica-core SMF as a function of Raman frequency shift [99]. It is evident that the Raman gain coefficient, g_r, is maximum for the frequency component that is downshifted from the pump frequency by ~440 cm^{-1} (corresponding to ~13.2 THz), which is herein noted as peak Raman shift. According to Equation (2-31), such a frequency component builds up most rapidly through the SRS process. In practice, the peak Raman shift is often used to calculate the Stokes frequency when the frequency of the pump wave is given. As also seen from Fig. 2-12, the full bandwidth of Raman gain of silica SMF is as large as ~1400 cm^{-1} (corresponding to ~40 THz) due to the amorphous nature of silica glass [65]. The g_r is inversely proportional to the pump wavelength [99] and the peak Raman gain is around 0.93 x 10^{-13} m/W for a pump wave at 1064 nm in silica-core SMF.

According to Equation (2-31), if a weak probe beam is launched together with the strong pump wave at the fibre input, the probe beam will be amplified at the output of the fibre via SRS process if the frequency difference between the probe beam and the pump wave is within the Raman gain spectrum, as shown in Fig. 2-12. Alternatively, if only the strong pump beam is incident into the fibre, the spontaneous Raman scattering generating from the noise acts as a probe and is amplified with the propagation in the fibre [65]. As a result, SRS has been widely used in the applications of optical amplifiers and lasers [64, 65, 100-102].

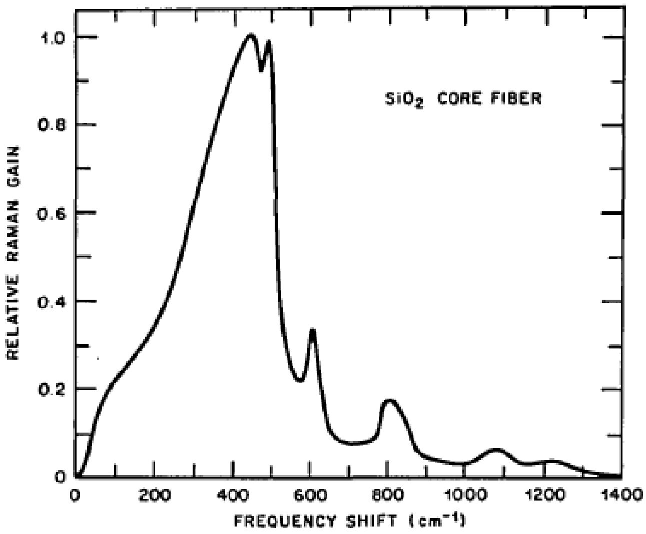

Fig. 2-12 Raman gain spectrum normalized to its peak at 440 cm^{-1} of a silica-core SMF. The Raman gain scales inversely with pump wavelength (λ_p). (After Ref. [99])

Raman threshold is a very useful parameter for designing a Raman amplifier or Raman laser. In general, Raman threshold is referred to as a certain pump power level, exceeding which the pump energy converts to the Stokes energy significantly [65]. As in a SMF with a length of L, for the forward Stokes, a good approximation of the Raman threshold, P_{th}, is given as Equation (2-32) [65, 103], with the assumption of a Lorentzian shape for the Raman gain spectrum and the polarisation states of the pump and Stokes waves are maintained along the fibre. Note that such Raman threshold is defined as the input pump power at which the forward Stimulated Stokes power becomes equal to the pump power at the fibre output (i.e., at $z = L$).

$$P_{th} \cong 16 \frac{A_{eff}}{g_r \cdot L_{eff}} \tag{2-32}$$

in which A_{eff} is the effective mode area of the waves in the fibre and g_r is the Raman gain coefficient at the Stokes wavelength. The effective interaction length, $L_{eff} = (1 - \exp(-\alpha L))/\alpha$, where α is the linear propagation loss of the pump and Stokes waves. For the backward Stokes, the Raman threshold is defined to be that input power for which the backward Stimulated Stokes power equals the input pump power at the fibre input (i.e., at $z = 0$). Similarly, the Raman threshold for backward Stokes can be expressed as Equation (2-32) by replacing 16 with 20 instead [65, 103]. The slightly higher Raman threshold for backward Stokes than the forward Stokes is due to counter-propagation between the pump and Stokes waves. The detail derivation of the Raman threshold is presented in Appendix A. Thus, the Raman threshold for forward SRS is reached first at a given input pump power and backward SRS is normally not observed in fibres.

Based on Equation (2-32), for a silica-core SMF with a length of 1 m, $A_{eff} = 30\ \mu m^2$ and propagation loss of ~10 dB/km, the Raman threshold is calculated to be ~ 5.2 kW for a pump wave at 1064 nm by using the peak Raman gain coefficient of 0.93 x 10^{-13} m/W. Lower Raman threshold can be achieved by using an optical fibre with longer length, higher Raman gain coefficient and smaller core diameter. It is worth noting that the Raman gain coefficient is polarisation dependent [98, 104]. If the polarisation of the pump and Stokes waves are not maintained along the fibre, the Raman threshold will be increased by a factor of between 1 and 2 [65].

Additionally, the Stokes wave can be used as a new pump wave to generate the higher order Stokes when the Stokes power is high enough to reach the Raman threshold for the higher order Stokes. Multiple Stokes lines have been observed in silica and non-silica optical fibres [65, 99, 105, 106]. By using this feature, cascaded Raman fibre lasers with very large wavelength shifts from pump source (up to ~ 400 nm) have been demonstrated as well [107, 108]. For example, with a pump source at 1.06 μm, ~1.48 μm can be realized by making use of the sixth order Raman Stokes in silica optical fibres. Therefore, in principle, Raman fibre lasers can oscillate at any wavelength with a proper pump source.

2.3.2 Second-harmonic generation (SHG) in optical fibres

SHG or called as frequency-doubling is a nonlinear phenomenon, in which an incident pump wave interacts with a nonlinear medium to generate a new wave with a frequency twice that of the pump wave [76], as shown in Fig. 2-13. As indicated in Equation (2-25), the *second-order nonlinearity* (SON), $\chi^{(2)}$ of the nonlinear medium is responsible for SHG and affects the conversion efficiency.

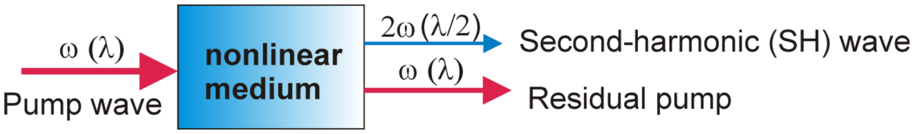

Fig. 2-13 Schematic diagram of the SHG process.

With the exception of the SON of the nonlinear medium, the phase mismatch factor between the SH and the fundamental waves also influences the output power of SH wave and conversion efficiency from a finite length (L) of the nonlinear medium. The phase mismatch between the SH wave and the corresponding fundamental wave can be expressed as:

$$\Delta k = \frac{4\pi}{\lambda_p} |n_{2\omega} - n_{\omega}| \tag{2-33}$$

where λ_p is the fundamental wavelength and $n_{2\omega}$, n_ω are the refractive indices at the SH and fundamental waves, respectively. To consider the special case of the nonlinear medium with one-dimensional interaction volume and the contributions of different points in the interaction volume are added as phasors, Fig. 2-14 illustrates the variations of phasors along the interaction length in the cases of (a) phase matched, (b) phase mismatched and (c) quasi-phase matched. It is evident that if $\Delta k = 0$, the maximum conversion efficiency can be attained and the SH power grows quadratically with the length (L) of the nonlinear medium [76]. However, if $\Delta k \neq 0$, the SH power increases within the length of $\pi/\Delta k$, which is known as the coherence length, l_c. However, it reduces back to zero when the length increases to $2\pi/\Delta k$, twice the coherence length. Hence, in the presence of a phase-mismatch and the length of nonlinear medium is much longer than the coherence length, *quasi-phase matching* (QPM) technique is required to improve the SH conversion efficiency [76, 109]. QPM is accomplished by introducing a periodic structure to compensate the phase-mismatch. For instance, the simplest QPM pattern can be periodically reverse the nonlinear coefficient by every coherence length l_c, as illustrated in Fig. 2-14(c) [76]. Such a periodicity introduces an opposite phase each coherence length to bring back the phases of the radiation elements into better alignment.

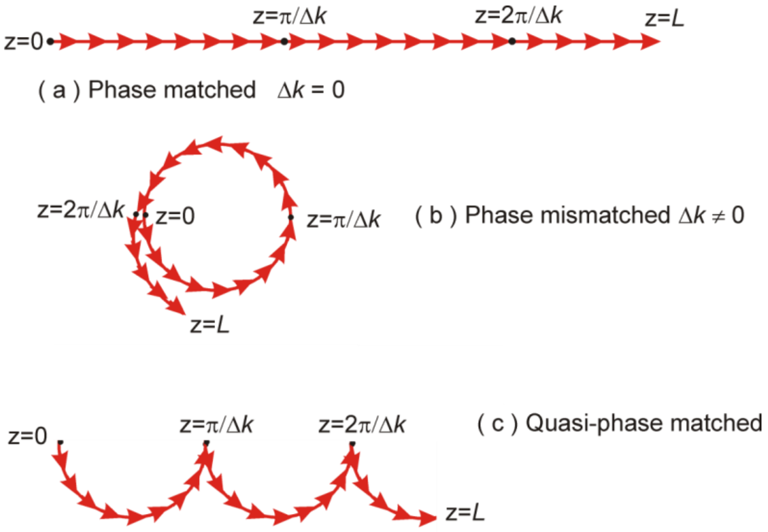

Fig. 2-14 Schematic diagram of phasors of the waves radiated by incremental elements at different positions z in the nonlinear medium. (a) In the case of phase matched, the phasors are all aligned; (b) In the presence of a phase mismatched, the phasors are misaligned; (c) In quasi-phase matched case. (After Ref. [76])

Even though the SON ($\chi^{(2)}$) is zero in glass optical fibres as mentioned above, efficient SHG in phosphor-doped glass fibres with up to 5% conversion efficiency was reported by Österberg and Margulis in 1987 [110]. In that particular work, the green light at 532 nm was observed from the fibres less than a metre long, which were illuminated by a high intensity pump source of 1064 nm (Nd:YAG) for several hours. In the same year, Stolen and Tom hypothesized that the SHG in the fibres was a permanent photo-induced change analogous to the photorefractive Hill gratings and also they demonstrated that the SHG buildup time can be reduced to a few minutes by means of seeding the SH light along with the 1064 nm pump source [111]. The mechanism for such self-organized photoinduced SHG in optical fibres is very complex and it was suggested that the interaction between the optical fields (fundamental and SH) with the TON of the fibres gave rise to an effective SON [111]. Although the effective SON was quite low (~10^{-3} *pm/V*) in optical fibres, the long interactive length and low-cost of the optical fibres made them very attractive for the applications of SHG.

Subsequently, phase-matched electric-field induced SHG in periodically poled optical fibres was first demonstrated by Kashyap [112, 113]. That technique required a high voltage (~120 V) and a high pump power to observe the SHG. And the periodic effective SON was induced by a simple interdigitated electrode structure [112]. However, the maximum conversion efficiency obtained was ~$4x10^{-4}$% limited by the interaction length and the accuracy of the electrode fabrication [112].

Since the demonstration of a permanent $\chi^{(2)}$ with a value of ~1 pm/V in silica glass by Myers et al. in 1991 [114], the thermal poling approach is widely used for SHG in optical fibres. In 1995, frequency-doubling to the blue light in a QPM thermally poled optical D-shaped fibre was first reported by Kazansky et al. in Optoelectronics Research Centre (ORC), University of Southampton [69]. In that case, the fibre samples were subjected to a periodic electric field (~4-5 kV) generated by the anodic electrode which had been photolithographically defined on the flat side of the D-shape fibres. With the same periodic thermal poling technique, SHG to 766 nm light with a maximum average efficiency of ~21% was demonstrated in 75 mm long Ge/Si D-shaped fibres with a ~2 ns Q-switched fibre laser source (@ ~1531 nm) at ~4 kW peak power by the same research group in ORC in 1999 [115].

As the photolithographic process limited the poled device length to ~10 cm, a new QPM technique, point-by-point periodic erasure of the uniformly thermal poled fibre by using a UV light (244 nm), forming a QPM grating to compensate the phase-mismatch, was realized in 2000 [116]. Such a QPM grating is easy to implement for achieving a longer length PPSF for SHG and the period of the QPM grating is flexible for any fundamental wavelength ranging from visible to IR [72]. With periodic UV erasure QPM approach, ~11.5 cm long PPSF was demonstrated in 2005, with a maximum average conversion efficiency of ~2.4% for a peak pump power of ~100 W [117]. In that work, a specially designed twin-hole Ge/Si fibre was used, as shown in Fig. 2-15. Two Metal wires functionally as electrodes were manually inserted into the two holes for poling [118]. One hole was placed closer to the core than the other. In the case of positive poling, a positive voltage was applied within the anode hole which was closer to the core. For negative poling, a negative voltage was applied within this hole. The typical voltage applied for thermal poling was 10-11 kV at the temperature of ~210 ºC. The details of the fabrication PPSFs for SHG have been described in the references of [71, 118].

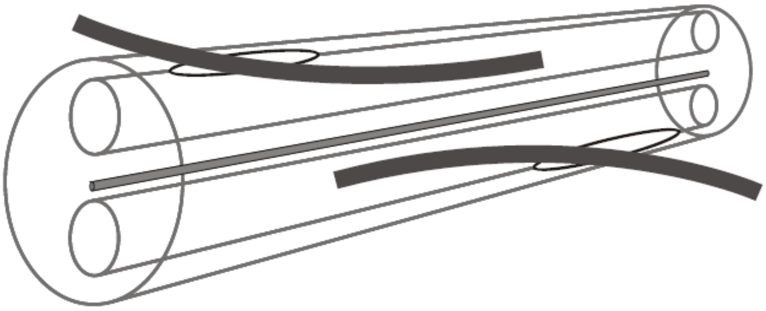

Fig. 2-15 A specialty twin-hole fibre device with two electrodes inserted through side-polished holes. (After Ref. [118])

The inducible effective SON from the intrinsic SON of the optical fibre through thermal electric-poling with the applied dc electric field (E_{dc}), can be evaluated as:

$$effective\ \chi^{(2)} \cong 3\chi^{(3)}E_{dc} \tag{2-34}$$

In silica, the TON ($\chi^{(3)}$) is ~2 x 10^{-22} m^2/V^2 [71] and the electrical breakdown field at room temperature is ~2 x 10^9 V/m [114, 118]. As a result, the effective SON based on thermal poling technique is limited to the maximum of approximately 1 pm/V. However, this value has not been achieved in silica fibres, due to the lower nonlinearity experienced by the core of the fibre which is typically a few microns away from the anode hole in the fibre as seen in Fig. 2-15 [118]. The typical inducible effective SON in thermal poled twin-hole fibres is ~0.11 pm/V in ORC [118]. And the maximum normalized SHG conversion efficiency of ~8.61 x 10^{-2} %/W has been reported in 32-cm long PPSFs by Canagasabey et al. in 2009 [72]. It is predictable that higher conversion efficiency can be achieved by extending the interaction length of PPSFs.

2.4 Conclusions

In this chapter, the basic knowledge of the background underlying the thesis has been presented. This includes: (i) the fundamentals of the optical fibres, focusing on the commonly used step-index SMF together with an outline to the PCF; (ii) an overall introduction to the fibre Bragg gratings (FBGs), which consists of the theory of the FBGs based on the coupled mode equations, the formation of the phase-shifted DFB gratings, the fabrication methods of FBGs and the characterization of FBGs; and (iii) a brief introduction of several nonlinear effects in optical fibres, i.e., Kerr effects, FWM, SRS and SHG.

Chapter 3 Raman distributed-feedback fibre lasers

A R-DFB fibre laser is formed with a single DFB fibre grating in a passive optical fibre utilizing the Raman gain. It could be a strong competitor to the well-known RE-doped DFB fibre lasers [27, 29] and semiconductor DFB lasers [119]. This work focuses on the area of optical fibre lasers and therefore bypasses the discussions about semiconductor DFB lasers.

DFB fibre lasers are one of the most favourite methods to generate laser radiation with several excellent optical properties, including (i) singe frequency operation [29, 30], (ii) very low noise characteristics, including low intensity noise as well as low phase noise [28, 30, 83, 120, 121], and (iii) continuous tuning over a wide wavelength range [122]. As a result, they are highly useful sources for a wide range of applications, such as in telecommunications, fibre sensing, high resolution interferometry, *Light Detection and Ranging* (LIDAR) etc. [34, 83, 84, 123]. However, for a RE-doped DFB fibre laser, the core of the fibre has to be doped with high-concentration of RE ions to facilitate high lasing efficiency. The high concentration of the doped RE ions not only limits the oscillation wavelengths of the DFB fibre lasers to regions characteristic to the specific RE material used, but can also cause the output power instability due to the ion-pair quenching leading to inefficient pump energy transfer and excessive thermal loading. Therefore, DFB fibre lasers based on Raman or Brillouin gain media [65], instead of the RE gain media, are of great interest to make single frequency and narrow linewidth light sources at new frequencies, especially those that cannot be achieved by RE-doped DFB fibre lasers.

Raman amplification is vastly superior to Brillouin amplification in terms of the frequency shift and bandwidth of the gain spectrum [65]. In general, for standard silica fibres, Raman gain extends over a large frequency range (up to 40 THz) with a broad peak located near 13.2 THz frequency detuning from the pump wave [98], whilst the Brillouin frequency shift is of the order of 10-20 GHz with a narrow-band gain spectrum <100 MHz [65]. As a result, a narrow-band optical source is typically required for pumping a Brillouin fibre laser. Raman gain based fibre lasers therefore have the advantages of much more flexibility in choosing pump sources and wide tunability over a wide wavelength range.

Hence, the major motivation of this work is to demonstrate and characterize a R-DFB fibre laser, which can not only overcome the limitations from the RE-doped counterparts, but also maintain all the attractive optical properties of a DFB fibre laser. If achieved, this would open up the prospect of generating single-frequency and narrow linewidth oscillation at any desired wavelength ranging from the visible to the infrared region, depending on only the availability of a suitable pump source.

In this chapter, the investigation of the R-DFB fibre lasers is presented in detail. In the first section, a review of the development of the DFB/DBR fibre lasers is given. Following that, an overview of the R-DFB fibre laser is introduced in Section 3.2. A numerical simulation model of the R-DFB fibre laser is examined in Section 3.3 which includes the simulation results as well. Section 3.4 shows the experimental data of R-DFB fibre lasers with an un-polarised pump source and a linearly polarised pump source, respectively. Section 3.5 concerns the linewidth measurement of the R-DFB fibre lasers. Ultra-wide range wavelength conversion by using FWM in R-DFB fibre lasers are studied experimentally and numerically in Section 3.6 and this work is concluded in Section 3.7.

3.1 Review of development of DFB/DBR fibre lasers

A DFB fibre laser typically consists of a single π phase-shifted Bragg grating formed in the fibre core with laser gain [28, 30], while a DBR fibre laser is typically a linear cavity laser established by using two FBGs attached at the ends of the gain fibre [14, 67, 124, 125].

The first DBR fibre laser using FBGs was demonstrated in a Er^{3+} doped Ge/Si fibre at ~1548 nm by Ball et al. in 1991 [14], because of the progress of FBGs' fabrication techniques [4, 8, 9]. In that work, the two FBGs were written directly into the gain fibre without splicing to form a resonator cavity with a length of 0.5 m, so that the laser was made as a compact all-fibre design. With this design, continuously tunable fibre lasers (with tunable wavelength ranges up to ~16.7 nm) have been realized [124, 126]. Additionally, the DBR fibre lasers have shown the performances of single frequency operation, low noise and narrow linewidth, high wavelength stability and accuracy, and have attracted great interest both in the industry and academia [125, 127-130].

The cavity length for conventional RE-doped DBR fibre lasers is typically in the range of 1 millimetre to tens of centimetre [14, 124-126, 128]. As the longitudinal mode spacing scales inversely with the cavity length, a shorter cavity length is required to obviate the possibility of mode hopping from any external perturbations and therefore resulting in a reliable DBR fibre laser. Besides, the DBR laser cavity is formed with two separate FBGs, whose Bragg wavelengths have to be carefully synchronized to make oscillation. This could lead to the experimental setup and packaging complicated.

In 1994, Kringlebotn et al. first demonstrated a compact all-fibre design, more reliable and mode-hopping free, single frequency and narrow-linewidth fibre laser with the DFB configuration [27]. In that work, the lasing cavity was formed by locally heating a Bragg grating to introduce the required optical phase-shift. One year later, DFB fibre lasers with permanent phase-shift around 1047 nm were reported by Asseh et al. [28]. These results have proven that the DFB fibre lasers have all the advantages of the DBR counterparts. What is more, in the former case, the lasing wavelength is uniquely determined by the single Bragg grating, which is much more robust against external perturbations. Since then, DFB fibre lasers have been studied intensively and a number of DFB fibre lasers at varied wavelengths in different RE-doped gain fibres have been demonstrated, as shown in Fig. 3-1 [29-35, 131-135].

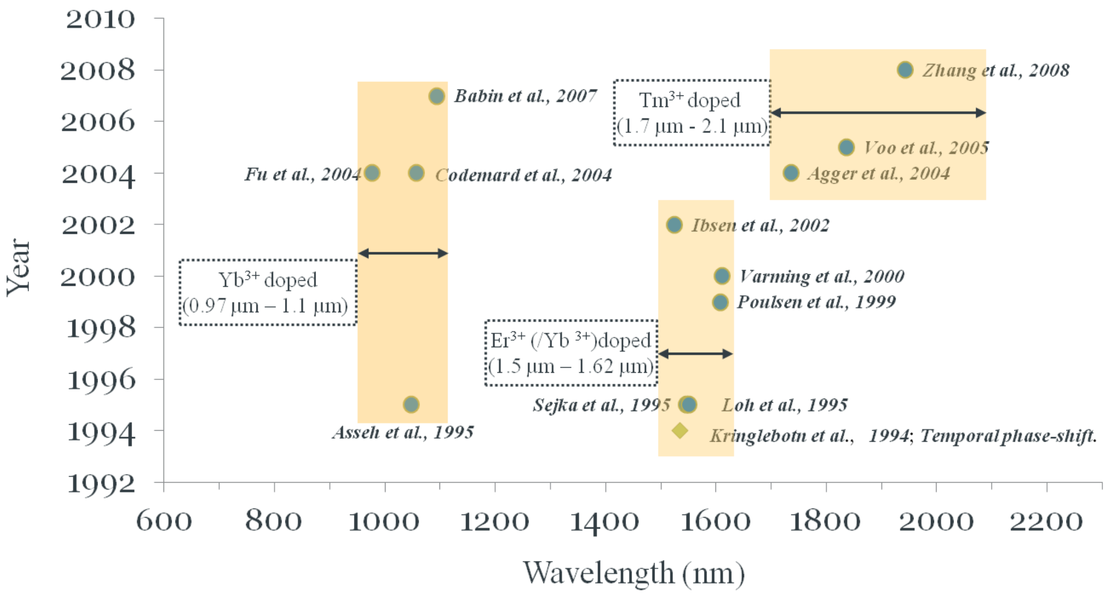

Fig. 3-1 Diagram of reported RE-doped DFB fibre lasers at different wavelengths so far.

Specifically, 1 µm region DFB fibre lasers have been reported in Yb^{3+}-doped fibres. In 1995, Asseh et al. first demonstrated a 10 cm-long Yb^{3+} DFB fibre laser at 1047 nm, of which the threshold pump power and the one-way slope efficiency with respect to the launched pump power were <230 µW and ~ 44%, respectively [28]. Almost a decade later, Fu et al. reported a 5 cm-long DFB fibre laser operating at 977 nm, with a maximum output power of 38.2 mW (for a lunched pump power of 150 mW at 910 nm), a threshold pump power of ~60 mW and a slope efficiency against launched pump power of ~61%, respectively [31]. By increasing the pump power to ~1.5 W (at 976 nm), ~400 mW of output power at ~1056 nm from a uni-directional Yb^{3+} DFB fibre laser was obtain by Codemard et al. [32]. In 2007, ~1093 nm DFB fibre lasers were observed by Babin et al. [135], in which, the maximum output power was ~1.5 mW for a pump power of 105 mW. Furthermore, the C- and L-band DFB fibre lasers have been realized in Er^{3+}-doped or Er^{3+}/Yb^{3+} co-doped fibres. In 1995, Sejka et al. and Loh et al. reported single-frequency DFB fibre lasers oscillating at ~1.55 µm with threshold pump powers of ~10 mW and narrow-linewiths in the order of 10 kHz [29, 30]. DFB fibre lasers at ~1.61 µm were achieved by Poulsen et al. [33] and Varming et al. [131] in Er^{3+}-doped fibres. Additionally, broadband continuous tunable DFB fibre lasers with wavelengths ranging from ~1524 nm to ~1551 nm were demonstrated with the combination of extension and compression technique by Ibsen et al. in 2002 [122]. Besides, ~2 µm regime DFB fibre lasers have been generated in Tm^{3+}-doped fibres. Agger et al. first reported a single-frequency 5 cm-long 1735 nm Tm-doped DFB fibre laser pumping at 790 nm, with a pump threshold power of 59 mW, a maximum output power of 1 mW for a launched pump power of ~600 mW and a slope efficiency of ~0.2% against the launched pump power [132]. Afterwards, operating at 1836 nm, a single-frequency DFB fibre laser with an output power of ~5 mW (for an absorbed pump power of 550 mW) was realized by Voo et al. in 2005 [34]. In that work, the DFB fibre laser was in-band pumped at 1565 nm and the Tm-DFB fibre laser was amplified to ~345 mW for an absorbed pump power of ~1.5 W with the aid of a 1 m-long Tm-doped gain fibre. By pumping at the same wavelength, a Tm-DFB fibre laser at 1943 nm with an output power of 875 mW was reported by Zhang et al. in 2008 [35], which has recorded the highest output power from a RE-doped DFB fibre laser so far.

The shade boxes in Fig. 3-1 represent the wavelength domains obtainable with the specific RE-ions. The limitation of RE-doped DFB fibre lasers in terms of their wavelength coverage is clearly seen from Fig. 3-1. For example, the radiation wavelengths between 1.62 µm and 1.7 µm, cannot be reached by RE ions gain media. What is more, the cavity length of a DFB fibre laser is the length of single distributed Bragg grating and usually in the order of several cms, which is much more convenient and robust for frequency tuning over a wider range than the DBR counterparts [122].

The output power of a DFB/DBR fibre laser depends on the composition of the gain fibre, available pump power, pumping scheme and the design of the DFB grating [82, 83]. Usually, RE-doped DFB fibre lasers restrict the output powers in the sub-watt regime owing to the thermal effect and the short cavity length which results in low conversion efficiency (<50%) [32, 35, 129, 136, 137]. However, higher output power can be easily scaled by recycling the unabsorbed pump power to form a *master-oscillator power amplifier* (MOPA) configuration [34].

On the other hand, high conversion efficiency (>80%) and high output power (up to 150 W of CW power) Raman fibre lasers with the DBR configuration have been demonstrated, as a result of the progress of the high power fibre lasers [107, 138]. Due to the low Raman gain coefficient of standard silica fibres, the cavity length of a lumped Raman fibre laser is typically >10 m, which could be reduced to 3 m [139] with high Ge-doped silica fibres, and even to 17 cm with a *polarisation maintaining* (PM) Raman fibre [67]. In the last case, the short cavity length helped to reduce the number of the longitudinal modes to ~24 modes at the expense of increasing the lasing threshold to ~4.1 W [67]. The longitudinal modes and the threshold pump power of a Raman fibre laser could be further reduced by applying a DFB grating in a Raman fibre to establish a R-DFB fibre laser [68], which will be discussed in detail below.

In addition, a Brillouin gain-based DFB fibre laser with single frequency oscillation has also been demonstrated by Abedin et al. recently [41]. A narrow-linewidth (~150 kHz) CW pump source at ~1583 nm was used and the threshold of the Brillouin DFB fibre laser was ~30 mW in a 12.4 cm long DFB grating with a π phase-shift 8% offset from the centre. However, the frequency shift was only ~10 GHz and the spectral bandwidth of SBS was very narrow (in the order of ~10 MHz in silica optical fibres). The narrow bandwidth nature of SBS limits its applications.

3.2 Overview of R-DFB fibre lasers

The concept of a R-DFB fibre laser was first proposed by Perlin and Winful in 2001 [68]. In that work, the R-DFB fibre laser was made up of a uniform intracore FBG in a standard silica fibre as shown in Fig. 3-2. The Bragg wavelength was designed to be equal to the first-order Raman Stokes wavelength of the fibre for a given pump wave, in order to ensure the lowest threshold oscillation condition. It was theoretically predicted that (i) the threshold pump power is inversely proportional to the effective length of DFB grating cubed; (ii) about 0.7 W of threshold pump power is required for a ~1 m-long uniform DFB cavity formed in a standard silica fibre with κL = 100; and (iii) the competition between the lowest two modes (symmetric about the Bragg wavelength) may occur when the threshold is reached, which could lead to an unstable output [140].

Fig. 3-2 Schematic diagram of the Raman DFB fibre laser in a uniform FBG.

In order to reduce the threshold and eliminate the mode competition, a R-DFB fibre laser in a π phase-shifted DFB grating was studied numerically by Hu and Broderick [141]. They showed that watt-level threshold R-DFB fibre lasers were possible from 20 cm long centre π phase-shifted DFB gratings.

The results of R-DFB fibre lasers mentioned above were based on the ideal noiseless Bragg gratings. In a practical system however, some level of random noise is likely to occur on the grating profile. This is due to the fibre non-uniformities (cladding variations along the length of the fibre due to the fabrication) and the imperfections of the FBGs, for example, arising from the power fluctuations of the UV writing beam, the mechanical vibration and so on. Taking these into consideration, the effects of phase and amplitude noise on π phase-shifted R-DFB fibre lasers have been numerically studied in order to evaluate the impact of grating noise and the feasibility of an experimental demonstration of such a R-DFB fibre laser [73]. The details about this simulation will be presented in the Subsection 3.3.4 and the simulation results have shown that π phase-shifted R-DFB fibre lasers are resilient against phase and amplitude *root-mean-square* (rms) errors up to ~5%, with negligible deterioration of the threshold and slope-efficiency of the lasers. It is indeed helpful to make R-DFB fibre lasers come true.

In 2011, R-DFB fibre lasers at 1.58 μm was demonstrated experimentally for the first time in an OFS Raman fibre (NA: 0.23, effective area: 19 μm^2, and Raman gain efficiency: 2.5 /W/km) and an OFS *highly nonlinear fibre* (HNLF) (NA: 0.29, effective area: 12 μm^2, and Raman gain efficiency: 5 /W/km), respectively [37, 38]. In that work, the FBG was 12.4 cm long with uniform profile and incorporated an 8% off-centred π phase-shift. The threshold powers for the R-DFB fibre lasers were observed to be ~39 W and ~4.3 W in the Raman fibre and the HNLF, respectively. The maximum output power was ~350 mW for an incident pump power of 34 W, indicating that the conversion efficiency was as low as ~1%. The linewidth was measured to be in the low MHz range. Almost at the same time, R-DFB fibre lasers at ~1.12 μm have been reported in this work, and with several advanced properties of (i) high output power (with up to 2 W) [39, 42], (ii) low threshold pump power (around 0.44 W) [40], and (iii) very narrow linewidth (<2.5 kHz) [40]. The details of the R-DFB fibre lasers are discussed in the following subsections.

3.3 Numerical simulation of R-DFB fibre lasers

This section presents the numerical model of R-DFB fibre lasers and simulation results in terms of the lasing behaviour, lasing threshold properties and the effects of phase and amplitude noises on the threshold.

3.3.1 Model setup

The schematic diagram of a π phase-shifted R-DFB fibre laser is shown in Fig. 3-3. In this configuration, a CW pump source is launched from the left side (z = 0) of a DFB grating with a length of *L*. A π phase-shift is placed at the length of $z = z_\pi$ of the DFB grating. The Bragg wavelength, i.e., the laser wavelength, is assumed to be identical to the first-order Raman Stokes

(λ_S), which possesses the peak Raman gain coefficient thereby ensuring the lowest threshold for lasing. As a result, the generated Stokes is coupled within the π phase-shifted DFB grating cavity, which is nearly transparent for the pump wave.

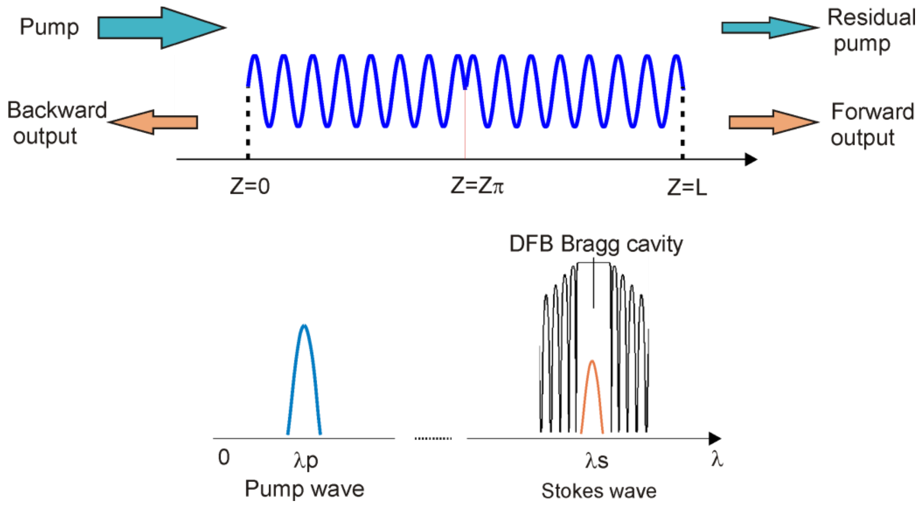

Fig. 3-3 Schematic diagram of a π phase-shifted Raman DFB fibre laser. Top illustrates the index modulation profile of the DFB grating and the bottom shows the relation between the pump wave (λ_p), Bragg wavelength and Raman Stokes (λ_S).

The dynamics of the R-DFB fibre lasers are normally described by the *nonlinear coupled mode equations* (NLCMEs) for the amplitudes of the pump (A_p), forward Stokes (A_f) and backward Stokes (A_b) [68, 141-143]. Herein, single-mode fibres are only considered for the R-DFB fibre lasers, which is valid for this work. Thus, the effective mode area of each wave can be assumed approximately identical with a value of the effective core area of the fibre. As a simplification, it is assumed that the pump wave as well as the Stokes is CW single-frequency operation, therefore the *group velocity dispersion* (GVD) effect is negligible and also the *slowly varying envelope approximation* (SVEA) is effective with the waves of pump and Stokes.

With the above assumptions, the time- and length-dependent NLCMEs can be expressed as Equations (3-1(a-c)) [141]:

$$\frac{\partial A_p}{\partial z} + \frac{1}{v_p}\cdot\frac{\partial A_p}{\partial t} = -\frac{g_p}{2}\left(\left|A_f\right|^2 + |A_b|^2\right)A_p + i\gamma_p\left(\left|A_p\right|^2 + 2\left|A_f\right|^2 + 2|A_b|^2\right)A_p - \frac{\alpha_{lp}}{2}A_p \quad \text{(3-1a)}$$

$$\frac{\partial A_f}{\partial z} + \frac{1}{v_s}\cdot\frac{\partial A_f}{\partial t} = \frac{g_s}{2}\left|A_p\right|^2 A_f + i\gamma_s\left(2\left|A_p\right|^2 + \left|A_f\right|^2 + 2|A_b|^2\right)A_f + i\kappa A_b + i\delta_\beta A_f - \frac{\alpha_{ls}}{2}A_f \quad \text{(3-1b)}$$

$$-\frac{\partial A_b}{\partial z} + \frac{1}{v_s}\cdot\frac{\partial A_b}{\partial t} = \frac{g_s}{2}\left|A_p\right|^2 A_b + i\gamma_s\left(2\left|A_p\right|^2 + 2\left|A_f\right|^2 + |A_b|^2\right)A_b + i\kappa^* A_f + i\delta_\beta A_b - \frac{\alpha_{ls}}{2}A_b \quad \text{(3-1c)}$$

where v_p and v_s are the group velocities of pump and Stokes waves, respectively. Due to the short length of the laser cavity (<1 m), the dispersion and walk-off effects of the pump and

Stokes waves are ignored in this case so that their velocities are considered to be identical. The first terms on the right-hand side of Equation (3-1) show the SRS coupling process between the Stokes (forward and backward) and pump waves with Raman gain coefficients of $g_s = g_r$, (g_r is the peak Raman gain coefficient of the fibre with a pump wave), and g_p, corresponding to $g_p = g_s \cdot \lambda_s/\lambda_p$, respectively. The second terms represent the nonlinearities of SPM and XPM, in which the nonlinear coefficients are defined as $\gamma_p = 2\pi n_2/\lambda_p$ and $\gamma_s = 2\pi n_2/\lambda_s$, where n_2 is the nonlinear refractive index of the fibre. The last set of terms in Equation (3-1) simulates the linear propagating losses of the pump (α_{lp}) and Stokes (α_{ls}) in the fibre. The other two terms left in Equations (3-1b) and (3-1c) describe the effects of Bragg grating resonance, which include the coupling between the forward and backward signals with a coupling coefficient of κ and the detuning effect of δ_β. Similar to the numerical model in [68], the slowly varying amplitudes equal to the intensities of the corresponding wave: $\left|A_{p,f,b}\right|^2 \equiv I_{p,f,b} \equiv P_{p,f,b}/A_{eff}$, where A_{eff} is the effective mode area of the fibre. The boundary conditions are expressed as below:

$$\begin{aligned} A_p(z=0,t) &= \sqrt{I_0} = \sqrt{P_0/A_{eff}} \\ A_f(z=0,t) &= 0 \\ A_b(z=L,t) &= 0 \end{aligned} \tag{3-2}$$

where P_0 is the initial pump power at the input side of the DFB grating.

The NLCMEs of Equations (3-1) and (3-2) are solved numerically by implementing C-language with a fourth-order implicit Runge-Kutta algorithm proposed by de Sterke [143]. The original C-code was programmed by Dr. Hu and Dr. Broderick [141]. However, the code has been further developed and the interface of the model has been optimized in this work. The simulation results of $A_{p,f,b}(z,t)$ are generated in the Unix programming environment on iSolutions servers, University of Southampton. Afterwards, the amplitude profiles of pump and Stokes waves are analysed with MATLAB.

The step-size of the simulation grid is 200-800 points per grating. This gives a space resolution of 0.15-0.0375 cm/step for a 30 cm-long DFB grating. These are much larger than the Bragg grating pitch (~0.5 μm for a Bragg wavelength of 1.55 μm), indicating that the SVEA is valid. Meanwhile, it has been verified that the simulation results are consistent with varied step-sizes in the range of 200 - 800, so the setp-sizes are sufficient to give accurate results. But with a bigger step-size, the simulation time will be significantly increased, and 201 step-size is applied for the simulations discussed in this part. Since the laser signal is built-up from the noise, at the beginning of the simulation, the amplitudes of the fields at the grid points are initialized with a certain level of random noise, i.e., a mean power of ~ 1 x 10^{-12} W (corresponding to ~ -90 dBm). After a number of round trips in the DFB grating, the Stokes signal reaches a stable output and the time window for each simulation scenario is >3 µs, corresponding to ~1033 round trips.

Table 3-1 Detail parameters used in the model for numerical simulations.

Parameters	Value	Unit
Length (L)	30	cm
Effective mode area (A_{eff})	~12	μm^2
Nonlinear refractive index (n_2)[144]	$\sim 3.2 \times 10^{-20}$	m^2/W
Peak Raman gain coefficient (g_r)[145]	$\sim 7 \times 10^{-14}$	m/W
Pump wavelength (λ_p)	~1540	nm
Signal wavelength (λ_s)	~1652	nm
Propagation loss (α)	~ 0.1	dB/m
Coupling coefficient (κ)	>20	/m
Detuning coefficient (δ_β)	0	-
Length step points (N_L)	>200	-
Round trip number (N_t)	>1000	-

Regarding the parameters of the optical fibre used for the simulation, the optical fibre is referred to a practical high NA (NA = 0.28) Ge/Si fibre, with an effective mode area of ~12 µm^2, n_2 of ~3.2 x 10^{-20} m^2/W and Raman gain coefficient, g_r, of ~7 x 10^{-14} m/W with a pump source at 1540 nm, as listed in Table 3-1. It has been noticed that the nonlinear refractive index n_2 and the Raman gain coefficient vary slightly with different concentration of Ge in the fibre core [65]. However, in this work, for further simplification, n_2 and g_r are quoted from a standard Ge/Si fibre [65]. Given the pump wavelength is 1540 nm, according to the Raman shift of 440 cm^{-1}, the first Stokes wavelength (also the R-DFB signal) is calculated to be ~1652 nm. Table 3-1 also shows the parameters of the DFB grating, including the length with a value of 30 cm, which is the longest Bragg grating can be written in lab at the time of this work, and the coupling coefficient with a value of >20 m^{-1}. The linear propagation losses at the pump wave,

α_{lp}, and signals, α_{ls} (as seen in Equations (3-1(a-c)) are assumed to be identical with a value of α = 0.1 dB/m with the consideration of the extra losses induced by the cladding modes and UV exposure during the FBG fabrication [42]. Additionally, the detuning coefficient δ_β of the grating is ignored in the simulations below.

3.3.2 *Lasing behaviour of a R-DFB fibre laser*

Fig. 3-4 shows the lasing behaviour of centre π phase-shifted R-DFB fibre lasers with varied pump powers from 15 W to 30 W based on a constant coupling coefficient of 30 /m (in Fig. 3-4(a)) and with coupling coefficients of 28 /m and 30 /m for an fixed incident pump power of 25 W (in Fig. 3-4(b)), respectively. The R-DFB laser grows exponentially from the spontaneous Raman noise and reaches steady state when the pump power reaches or exceeds the *threshold pump power* (TPP), at which point, the gain overcomes the total cavity loss [68, 141]. In terms of the *startup time,* which is defined here as the time required for R-DFB laser to reach steady state, it is evident that the startup time reduces as the increase of the pump power in the same DFB grating as indicated in Fig. 3-4(a). Also as seen in Fig. 3-4(b), the startup time is smaller when $\kappa = 30\ /m$ than if $\kappa = 28\ /m$ at the same incident pump power, predicting that the lasing threshold is lower in the former DFB grating than that in the latter. This is because the total cavity loss is lower when the κ is stronger, due to the higher reflectivity.

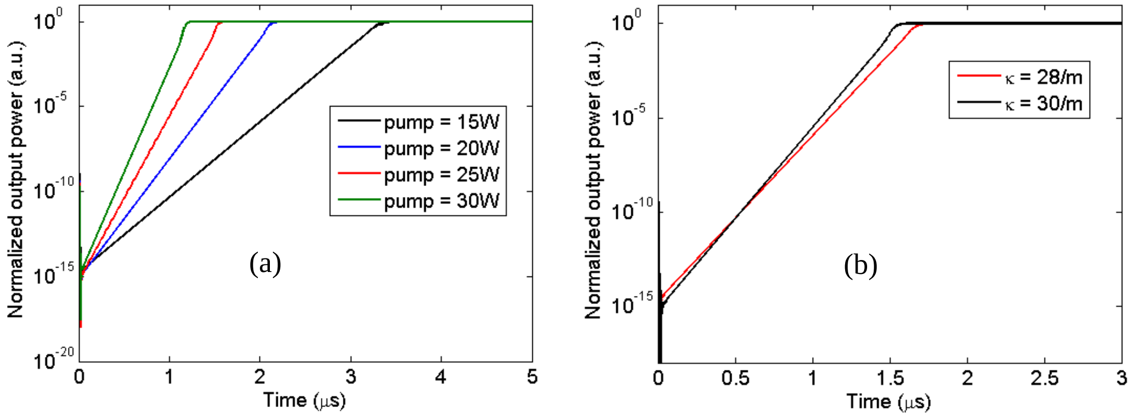

Fig. 3-4 (a) Normalized output power vs elapsed time with the parameters listed in Table 3-1, with $\kappa = 30\ /m$; (b) Normalized output power vs elapsed time at a pump power of 25 W with κ = 28 /m and 30 /m, respectively.

In the context of the fibre laser, the centre π phase-shifted structure DFB fibre laser can be functionally equivalent to a FP cavity laser [11] and the effective cavity length (L_{eff}) of the DFB fibre laser can be estimated from the coupling coefficient (κ) of the DFB grating [121]. In a uniform centre π phase-shifted DFB grating, L_{eff} can be approximated to be $L_{eff} = |r_B|/|\kappa|$, in which r_B is the reflectivity of the grating. Therefore, in the case of $\kappa = 30\ /m$, L_{eff} is about 3.33 mm.

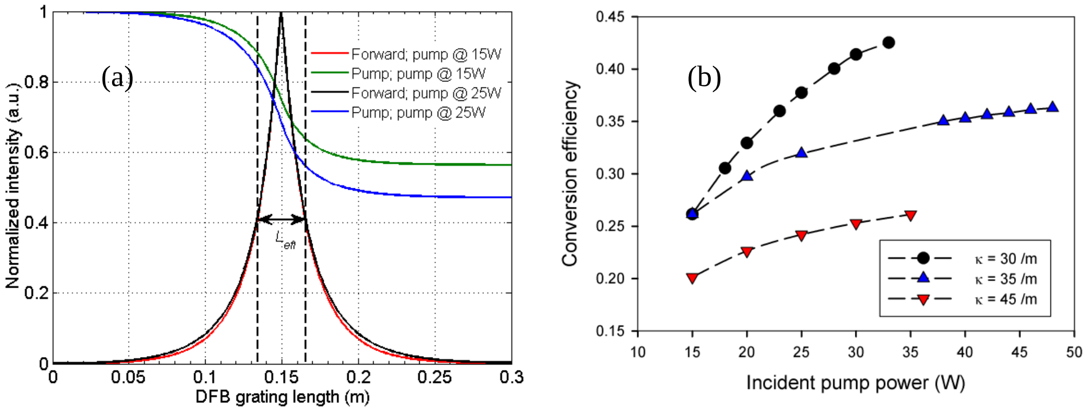

Fig. 3-5 (a) Normalized intensity distribution profile of pump and forward R-DFB signal inside DFB grating cavity with $\kappa = 30\ /m$. The dashed vertical lines indicate the effective length of the laser cavity. (b) Conversion efficiency of total R-DFB signal output powers vs incident pump powers. Note that other parameters are listed in Table 3-1.

Fig. 3-5(a) shows the normalized intensity distribution profile of the pump and forward R-DFB signal inside the DFB cavity with $\kappa = 30\ /m$ at the steady state and the vertical dashed lines indicate the edges of the effective FP cavity with an effective cavity length of L_{eff}. It can be seen clearly that the intensity of the R-DFB signal dominates in the effective cavity area of the grating and the distribution profile is similar to the RE counterparts [82, 136], in which the peak intensity locates at the π phase-shifted position. However, this behaviour is different from that of the uniform DFB Raman fibre laser as discussed in Ref. [68], in which the field distribution flattens and takes a more constant value along the length in the cavity when the laser reaches steady state.

On the other hand, as seen the traces (blue and green curves) of the pump wave intensity distribution in the cavity in Fig. 3-5(a), the pump power is significantly converted to the signal within the effective cavity length area. In addition, the slope of the pump depletion is steeper at higher pump power level which is confirmed by the shorter startup time with higher pump power as shown in Fig. 3-4(a). Also, the higher pump power above the lasing threshold, the pump is more strongly depleted, which agrees well with that in the uniform R-DFB fibre laser in Ref. [68].

Consequently, it can be deduced that by increasing the L_{eff} of the laser, the conversion efficiency of the output signal power with respect to the incident pump power can be increased since the length of the region with Raman gain is extended. This can be confirmed by further simulation results of conversion efficiency (signal output power divided by the incident pump power) as a function of the incident pump power, as shown in Fig. 3-5(b). With the same incident pump powers, the conversion efficiencies are higher when the κ is smaller, owing to the longer effective cavity length (L_{eff}). In addition, for a constant κ of the DFB grating, the conversion efficiency increases with the incident pump powers because of the stronger pump depletion at the higher pump power level. Hence, the coupling coefficient, κ, of the DFB grating is a key parameter in determining the conversion efficiency of the R-DFB fibre laser.

3.3.3 Threshold pump power with respect to the κ, A_{eff}, g_r, α, L, and phase-shift position

The TPP can either refer to the incident or absorbed pump power [146]. This work discusses the TPP deduced from the incident pump power. As shown in Fig. 3-6, the TPP is obtained by extending the slope curve of the total output power against the incident pump power to cross the x-axis. Obviously, TPP is a very useful parameter for experimental demonstration. Also, for a practical laser, a low threshold pump power is always desirable. Hence, it is important and very useful to find out the relationship between the TPP and the κ, A_{eff}, g_r, α, L, and phase-shift position, so as to lower down the threshold by means of optimizing these parameters.

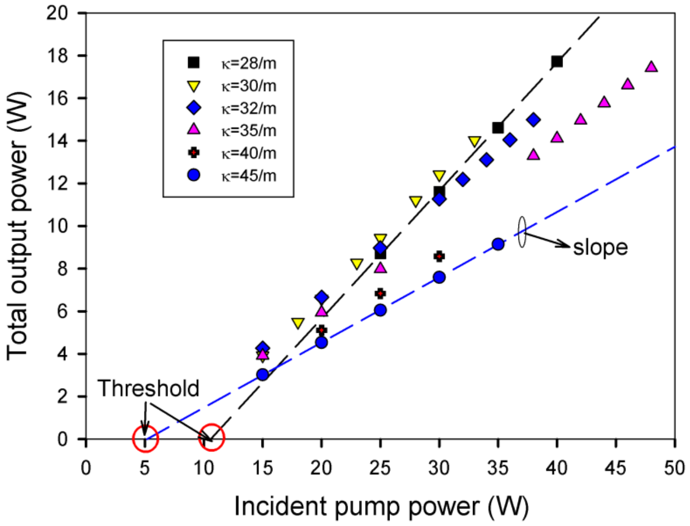

Fig. 3-6 Total output power of R-DFB signal vs incident pump power with constant length (30 cm) by varied κ of DFB grating. Note that other parameters are listed in Table 3-1.

Fig. 3-7 shows the TPP and the *total slope efficiency* (TSE) with respect to the κ. Note that the other parameters are given in Table 3-1. Please mind that the TSE is obtained from the relation of the total output power against the incident pump power, as shown in Fig. 3-6. As demonstrated in Fig. 3-7, the TPP drops down from ~40 W (κ = 20 m^{-1}) to ~ 5.8 W (κ = 32 m^{-1}) and that it reaches a constant level of ~ 5.2 W for higher grating strengths. However, the TSE is reduced from ~ 60% to ~ 31% with the increase of κ from 28 m^{-1} to 45 m^{-1}. This is probably due to the reduction of the effective cavity length [73].

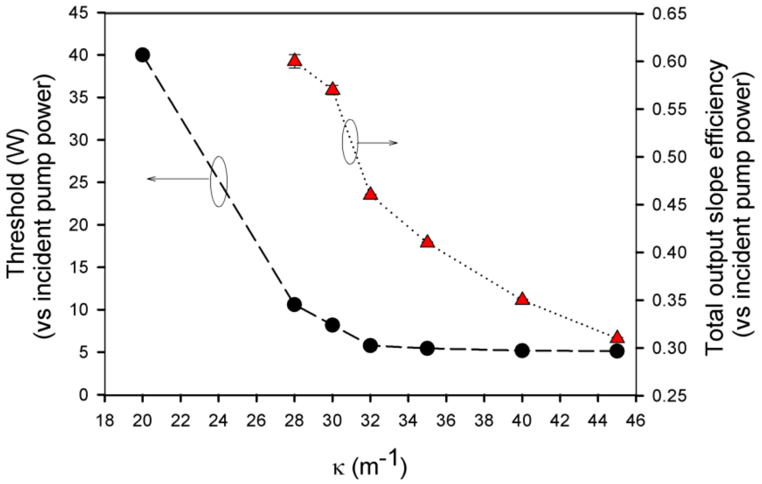

Fig. 3-7 Threshold (left axis) and TSE (right axis) vs coupling coefficient with constant length (30 cm) of DFB grating. Note that other parameters are listed in Table 3-1.

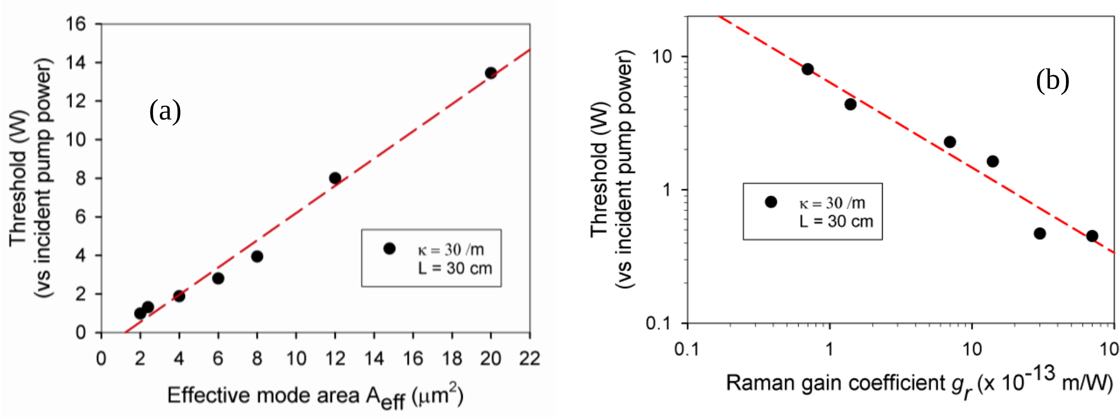

Fig. 3-8 Threshold vs (a) effective mode area and (b) Raman gain coefficient, respectively.

Fig. 3-8 shows the trends of TPP with respect to the A_{eff} (Fig. 3-8 (a) with a linear scale) and g_r (Fig. 3-8 (b) with a logarithmic scale) with constant κ (30 m^{-1}) and length (30 cm) of DFB grating. The TPP is linearly proportional to the A_{eff} whilst inversely proportional to the g_r. This behaviour is the same as the Raman threshold in a conventional Raman fibre laser [65], and it is understandable since the field intensity scales inversely with the A_{eff} and the higher Raman gain the laser resonator has, the less pump power required to overcome the resonator loss.

Apart from the κ, A_{eff} and g_r, the linear propagation loss, α, of the cavity, and the length of the DFB grating, L, associated with the laser resonator length, are the other two essential parameters in any laser. It is self-evident that lasing only occurs when the total gain in the cavity exceeds the total loss of the cavity. This loss includes the intrinsic propagation loss of the host fibre together with any losses introduced by components utilised in the laser system. Even though the cavity length is very short for Raman DFB fibre laser, the signal propagation length is significantly longer because of the multiple cavity roundtrips required for the laser to reach threshold and thereupon start oscillating. The influence of α is thus an important parameter that cannot be neglected. In the case of a R-DFB fibre laser, α is composed of the intrinsic fibre loss, the cavity reflection loss determined by κL, together with losses potentially imposed by the inscription process of the grating itself, including for example hydrogen or deuterium loading treatments to enhance the level of photosensitivity, and the choice of laser source used to inscribe the grating and create the refractive index changes [37].

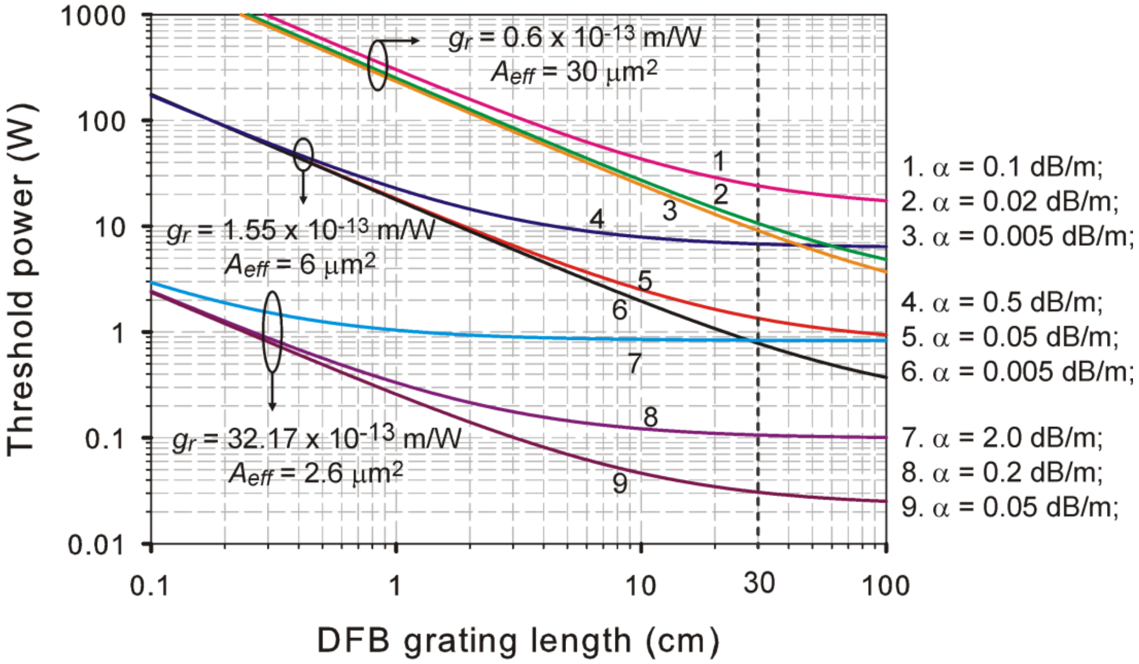

Fig. 3-9 Threshold vs DFB grating length with varied linear propagation loss (α). The vertical dashed line indicates the DFB grating length of 30 cm.

Fig. 3-9 describes the calculated TPP as a function of the length (L) of a centre π phase-shifted DFB grating for three types of optical fibres that conceivably could be used as the host for R-DFB lasers pumping with a 1.06 μm CW source. Here, the grating strength, κL, is kept constant at 9 in all the simulated cases. This value is chosen because it both ensures a relatively low threshold power whilst retaining the slope efficiency relatively high, as demonstrated in Fig. 3-7 [73]. The total linear loss, α, is varied across a range of values denoted in Fig. 3-9, typical to what could be expected in each of the chosen fibres depending on which grating inscription process is used to form the DFB gratings. The simulation results in Fig. 3-9 clearly demonstrate that for low levels of linear loss, the reduction of the threshold power follows the expected inverse relationship with the length. Unsurprisingly, the results also indicate that the linear loss ultimately sets the limit of the threshold, irrespective of the grating length. There is a clear trend in that it is seen to be almost always favourable to increase the length when possible.

Generally speaking, for standard single mode silica fibre for 1 µm, referring to HI-1060 in this specific case, with an un-polarised peak Raman gain coefficient of g_r = 0.6 x10^{-13} m/W and effective area of A_{eff} = 30 µm^2, more than 10 W of incident pump power is required to reach the threshold when the loss is larger than 0.02 dB/m for DFB grating lengths less than 30 cm, as indicated by the vertical dashed line intersecting with line 2 in Fig. 3-9. The 30 cm long DFB grating is highlighted here only as an example and it is the length applied for further experimental demonstrations. In this case, the lowest possible threshold power is ~9 W when only the intrinsic fibre loss, ~0.005 dB/m, is taken into account, as seen at the point of the intersection between trace 3 and the vertical dashed line. As also seen from trace 3, the threshold could be reduced to ~4 W for an 1 m long DFB grating. When considering a fibre with slightly higher Raman gain, such as for example UHNA4 (from Nufern), which has a nominal un-polarised peak Raman gain coefficient of g_r = 1.55 x10^{-13} m/W and an effective mode area of A_{eff} = 6 µm^2, the threshold is reduced by almost an order of magnitude to ~1 W for a 30 cm long device as long as the losses in the grating are kept below ~0.05 dB/m as illustrated by lines 5 and 6 of Fig. 3-9. For higher loss value of ~0.5 dB/m (line 4), although still relatively modest considering certain types of grating inscription methods, the threshold approaches that of the HI-1060 fibre. However, the threshold reaches a plateau of ~7 to 8 W from ~10 cm grating length (line 4), a level that in this case cannot be reduced further by increasing the grating length. In reality, increasing the length whilst maintaining κL constant will almost always be beneficial in terms of reducing the threshold power, since the value of κ will decrease accordingly. A reduction in the value of κ would typically imply a reduction in the grating inscription induced loss and thus a reduction in the overall cavity loss. As confirmed by line 6 in Fig. 3-9, the theoretical minimum threshold for a 30 cm long DFB grating in this case is ~800 mW. Note that all these threshold powers are achieved based on an un-polarised Raman gain coefficient. If polarised Raman gain is considered the level would scale accordingly as referred to above in Fig. 3-8 [147].

Due to the emergence of a variety of low-loss non-silica glass fibres with higher values of both nonlinearity and Raman gain coefficient, it is also been simulated what the likely performance of R-DFB lasers would be in these types of fibres. Tellurite glass fibres, for example, have recently shown promising potential for efficient Raman amplification [59, 148]. Combined with higher values of Raman gain, interestingly, these fibres also exhibit a level of photosensitivity that would facilitate the formation of sufficient strength gratings for the applications of R-DFB fibre lasers [46]. Propagation losses in these fibres tend to be slightly higher than those in silica based fibres, so for the simulated examples considered in this work, practical losses are selected to represent what currently is achievable (Fig. 3-9, lines 7-9). The Raman gain coefficient is g_r = 32.17 x 10^{-13} m/W, estimated by measuring the spontaneous Raman spectrum from a tellurite glass bulk sample [59]. For consistency, the grating design parameters are kept similar to the cases discussed above. In order to simulate a fibre which also would be transverse single-mode at the operating wavelength considered here, an effective mode area of A_{eff} = 2.6 μm^2 is used in the simulation. As the results illustrated in Fig. 3-9, even with a relatively high loss value of 2 dB/m (line 7), ~1 W threshold power can be achieved using only a 2 cm long DFB grating. Similar to the case of the higher loss in the UHNA4 example given above, the threshold is seen to reach a plateau of ~900 mW for increasing grating length rendering a longer length futile. Since the achievable losses in tellurite fibres in reality are somewhat lower at the ~0.05 dB/m level [149], in part depending on the purity of the materials used and the fibre design (solid vs. air-suspended core designs), the simulations suggest that threshold levels in the 300 mW regime should be possible from only 1 cm long devices. As indicated by lines 8 and 9, this level could even be brought down to the 100 mW level and even lower, by implementing R-DFB gratings of around 10 cm in length.

Having pump power requirements as low as ~100 mW would open up for these sources to be pumped using existing fibre-pigtailed laser diode technology as opposed to higher power pump lasers. Centimetre-length lasers in non-silica fibre with DFB level performance such as low intensity and phase noise together with narrow linewidth, would potentially be very attractive for a large range of applications in for example, point sensing, interferometry and extended wavelength transmission band telecommunications where transmission beyond 2 μm currently is being considered.

With the exception of placing the π phase-shift at the centre of the DFB grating, the effects of the π phase-shifted position on the TPP have been concerned in this part. Fig. 3-10(a) shows the sketch of a R-DFB fibre laser with a step-like offset π phase-shifted DFB grating, in which the π phase-shift is placed offset the centre of the grating at $z = z_\pi$, meanwhile, the strengths of the two sides of the laser resonator are maintained to be identical, i.e., $\kappa L_{(left)} = \kappa L_{(right)}$. This indicates that the coupling coefficient is stronger at the shorter length side than that of the longer length side. Note that such an index modulation profile differs from that of the conventional unidirectional DFB fibre lasers, in which the π phase-shift is offset from the centre but the coupling coefficient is constant throughout the DFB grating [83, 150]. In this circumstance, the field penetration depths to the two sides of the cavity are different from each other, which have been illustrated in Fig. 3-10(b). For convenience, the location of the π phase-shift is noted as PSP, which means the ratio of phase-shifted position to the entire grating length, (z_π/L). Therefore if PSP is between 0 and 0.5, the π phase-shift is at the left half of the grating, as illustrated in Fig. 3-10(a).

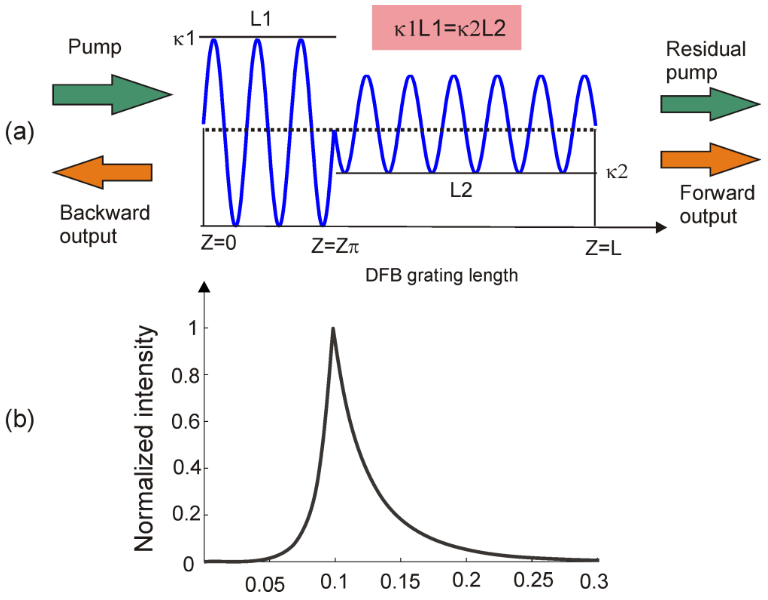

Fig. 3-10 Schematic diagram of a Raman DFB fibre laser with step-like offset π phase-shifted DFB grating (a) and corresponding normalized intensity distribution of the R-DFB fibre laser inside the laser cavity (b).

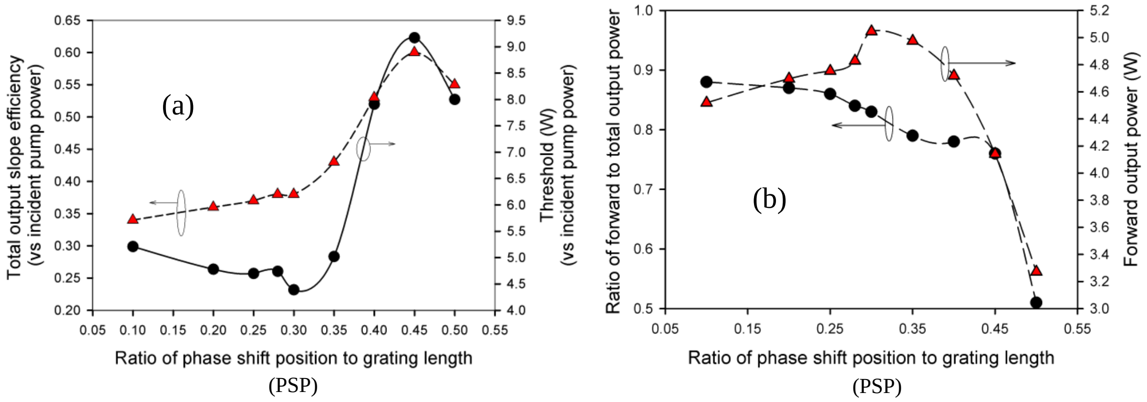

Fig. 3-11 (a) Threshold and TSE vs PSP with total $\kappa L = 9$; (b) Power ratio of the forward to total output and forward output power for an incident pump power of 20 W vs PSP. Note that other parameters are listed in Table 3-1.

Fig. 3-11(a) shows the TPP and the TSE vs the variation of the PSP in the range of 0.05 to 0.5 while maintaining the total $\kappa L = 9$ given $L = 30$ cm. It is interesting to see that the lowest TPP (about 4.5 W) occurs when PSP is about 0.3, after which, the TPP grows quickly to reach the maximum point, around 9.2 W for a PSP of 0.45. The TPP of the centre π phase-shifted design (PSP = 0.5) is about 1.8 times higher than that of the π phase-shift placed at 30% of the total grating length. For the TSE, as seen from the left-axis in Fig. 3-11(a), it increases by moving the π phase-shift closer to the centre of the grating and reaches to the top of ~60% when the PSP is 5% offset from the centre.

The simulation results also revealed that the forward output power of R-DFB signal is greater than that from the backward when $0 < \text{PSP} < 0.5$, indicating that the output power predominates from the smaller κ side of the DFB grating. Fig. 3-11(b) displays the power ratio of the forward output power to the total output power as well as the forward output powers with an incident pump power of 20 W. The power ratio drops from about 87% down to 50% when moving the PSP closer to the centre. With a constant incident pump power of 20 W, the forward output power gradually increases to the maximum (about 5 W) corresponding to the PSP is ~32%, and then decreases to about 3.3 W in the centre π phase-shifted DFB grating.

The basis for this behaviour in this type of step-like offset π phase-shifted R-DFB fibre laser has not yet been completely understood. It is likely to be relative to the effective cavity length, the field intensity distribution profile in the DFB cavity and the corresponding nonlinear effects. Even though, it is very promising to realize that the laser threshold could be reduced further via simply shifting the π phase-shift to ~20% away from the centre while retaining the grating strengths of the two sides identical. Apart from this strong point, un-directional output feature has also been recognized in the step-like offset π phase-shifted R-DFB fibre laser.

3.3.4 Effects of phase and amplitude noise on the grating index modulation profile

It is worth noting that the simulations which have been conducted above are based on ideal DFB gratings, which possess noiseless coupling coefficient characteristics. However, in a practical system, some level of random noise or imperfection on the Bragg grating profile is unavoidable. This noise could arise from non-uniformities of the optical fibres [151]; the mechanical vibration of the translation stages or even intensity variations of the UV beam during FBGs' writing process. In this section, the effects of phase and amplitude noise both on centre (as seen in Fig. 3-3) and step-like offset 30% π phase-shifted DFB Raman fibre lasers (as seen in Fig. 3-10) have been theoretically investigated, for the purpose of estimating the impact of grating imperfections and the feasibility of experimentally demonstrating these types of lasers. Note that, the imitated noise upon the amplitude and/or phase of the DFB grating is assumed to be uncorrelated in all the simulation grid points. Accordingly, white noise sequences with normal distribution are generated in MATLAB (with the function of *rand()*) and added onto the amplitude and/or phase term of the coupling coefficient of the DFB grating. The magnitude of the deviation is measured by the level of rms in each simulation scenario.

Fig. 3-12 shows the variations of TPP (a) and TSE (b) in 30 cm-long centre π phase-shifted DFB grating with κ = 30 /m, by increasing the level of rms phase and amplitude noise from 0% to 12%, respectively. It is evident that the influence of the amplitude noise on the TPP and TSE of the laser is low up to the maximum rms noise level considered here, since they both remained almost constant within the uncertainties of ± 0.5 W and ± 3% respectively. In contrast, the TPP is seen to rise quickly for rms phase-noise levels above 5%. This could be due to the degradation of wave confinement in the cavity. It is interesting to observe that for rms amplitude-noise levels up to 12%, the TPP increases slightly from ~8.2 W to ~9.2 W. Additionally, the slope-efficiency remains almost constant at about 55% for rms noise levels below 10%.

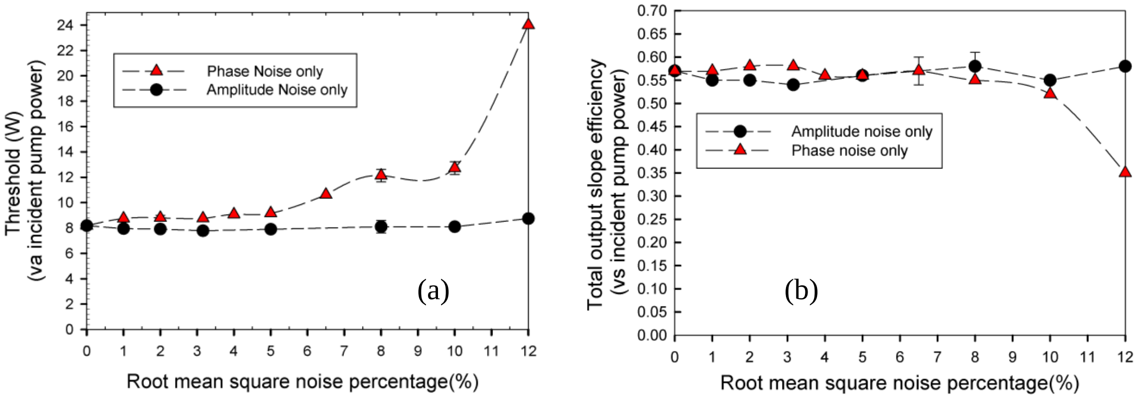

Fig. 3-12 Threshold vs individual phase and amplitude noise (a) and the slope efficiency vs individual phase and amplitude noise (b) in a centre π phase-shifted DFB Raman fibre laser with $\kappa = 30\ m^{-1}$. Note that other parameters are listed in Table 3-1.

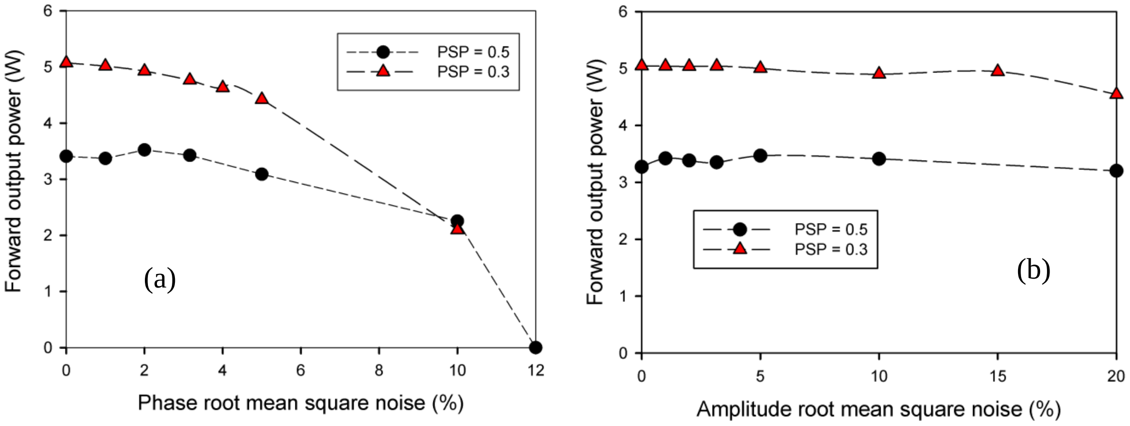

Fig. 3-13 Forward output power vs phase noise only (a) and amplitude noise only (b) with an incident pump power of 20 W both in the centre and PSP at 30% R-DFB fibre lasers, respectively. The uncertainties of the output power and the slope efficiency are ± 0.5W and ± 3%.

Fig. 3-13 illustrates the evolutions of forward Stokes output power for an incident pump power of 20 W, both in the 30 cm-long centre and step-like with PSP at 30% π phase-shifted R-DFB fibre laser models by individually introducing the rms phase and amplitude noise from 0% to 12%. The simulation results behave in similar manners to the above that the phase noise degrades the performance of the laser much more significantly than the amplitude noise. Moreover, when the rms phase-noise increases from 0% to 12%, the forward output power decreases faster in the 30% offset model than that in the centre phase-shifted model, as seen in Fig. 3-13 (a), which is probably due to the asymmetric cavity structure in the former laser.

To simulate a more realistic grating profile, both phase and amplitude noise should be considered simultaneously. Table 3-2 lists the total output power for an incident pump power of 24 W for 7 different combinations and levels of phase and amplitude noise in centre π phase-shifted R-DFB fibre laser model. The total output power remains almost constant when the rms phase and amplitude noise is within a level of 5%, this is consistent with the results obtained with either phase or amplitude noise only. However, once the rms phase and amplitude noise is enhanced up to 10%, the output power is significantly reduced to about one third of the noiseless case.

Table 3-2 Total output power with 24 W incident pump power in the centre π phase-shifted R-DFB model with $\kappa = 30/m$. η_a and η_p are the rms noise coefficients of amplitude and phase, respectively.

η_a	η_p	Pump power (W)	Total output power (W)
0.00	0.00	24	8.9 ± 0.2
0.00	2.00	24	8.9 ± 0.2
1.00	2.00	24	8.6 ± 0.2
1.00	5.00	24	8.3 ± 0.5
2.00	5.00	24	8.3 ± 0.5
5.00	5.00	24	8.1 ± 0.5
5.00	10.00	24	3.1 ± 0.5
10.00	10.00	24	2.9 ± 0.5

This result is somewhat surprising since a 5% rms noise level normally is considered fairly substantial on long-length gratings. To investigate this point further, the reflection spectrum of the DFB grating with the combination of white noise (both on phase and amplitude) levels of 0%, 5% and 10% is respectively calculated and shown in Fig. 3-14, in which the top (Fig. 3-14(a)) is the zoom in figure for the pass-band of the DFB grating. The calculated reflection spectra of the DFB grating have demonstrated that with the rms noise level of 5%, little change induced on the Bragg wavelength indicating that the feedback characteristics of the structure were maintained almost unaffected. However, as seen as the red curve in Fig. 3-14(a), when the rms noise is increased up to 10%, the Bragg wavelength is shifted away from the centre which is noiseless and the strength of the Bragg resonance is obviously decreased. As a result, at this level of noise (rms 10%), the performance of the R-DFB fibre laser is significantly deteriorated and the output power is thereby reduced by about two thirds of that of the noiseless.

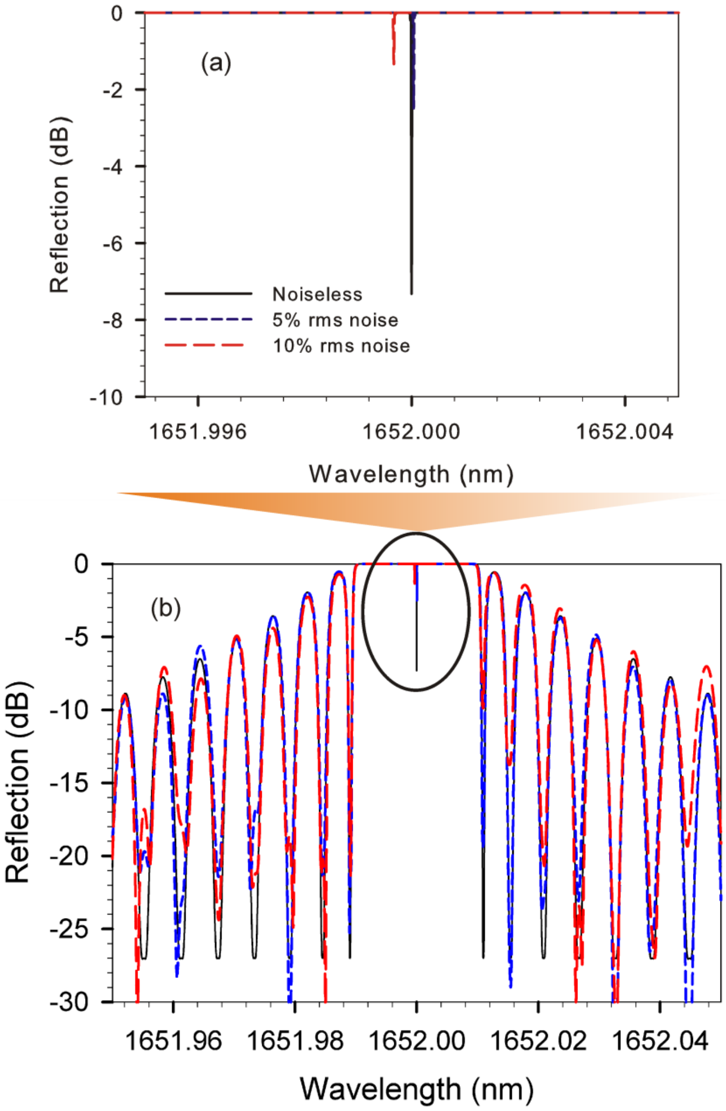

Fig. 3-14 Calculated reflection spectra of 30 cm-long centre π phase-shifted DFB gratings with 0%, 5% and 10% rms phase and amplitude noise. Top zooms in the pass-band of the DFB grating. (These data were generated by my supervisor, Dr. Morten Ibsen.)

3.3.5 Operating wavelength of R-DFB fibre lasers

Obviously, the wavelength of the R-DFB fibre laser is determined by the DFB grating, as illustrated in Fig. 3-3. And the Bragg wavelength of the DFB grating is typically designed based on the pump wavelength and the Raman gain spectrum of the host fibre. As similar as the lumped Raman fibre lasers, higher-order R-DFB fibre lasers are possible if the lower-order Raman Stokes fibre laser could reach the threshold for higher-order Raman Stokes. Accordingly, the wavelength of R-DFB fibre laser can be calculated by using the Raman shift of the host fibre and the pump wavelength. For example, Table 3-3 illustrates the calculated wavelength of 1st to 5th order R-DFB fibre lasers with pump sources at 1064 nm, 1550 nm and 2000 nm in conventional silica based optical fibres and tellurite glass based optical fibres, respectively. For the conventional silica based optical fibres, the peak Raman gain coefficient occurs at the Raman shift of 440 cm^{-1}, as shown in Fig. 2-12. It is clearly seen from Table 3-3 that R-DFB fibre lasers in silica based fibres can cover all the wavelengths ranging from ~1.11 µm to ~ 2.35 µm, which is close to the mid-IR absorption edge of the silica fibre, with the commercial high power Yb-doped fibre lasers at 1064 nm and Er/Yb-codoped fibre lasers at 1550 nm [152]. On the other hand, for the tellurite glass based optical fibres, which are good candidates for mid-IR applications, possess much higher and broader Raman gain spectra than that of the silica fibres. The Raman gain spectra of tellurite glass fibres will be discussed in detail in Chapter 4 and they are indeed promising candidates as host fibres for R-DFB fibre lasers. As clearly seen in Table 3-3, with the high power fibre lasers of 1064 nm (Yb-doped), 1550 nm (Er/Yb-codoped) and 2000 nm (Tm-doped) [153], R-DFB fibre lasers in tellurite glass fibres could cover all the wavelengths ranging from near-IR to mid-IR of ~ 5 µm, which is only limited by the mid-IR absorption edge of the material.

Table 3-3 Calculated wavelength of R-DFB fibre lasers by using 1st to 5th order Raman Stokes with different pump wavelength in silica based and tellurite glass based fibres.

Pump (nm)	Raman shift (cm^{-1})	R-DFB fibre laser (nm)					Fibre
		1st	2nd	3rd	4th	5th	
1064	440	1116	1174	1238	1309	1389	silica based
1550		1663	1795	1949	2131	2352	
2000	433	2193	2427	2717	3086	3571	tellurite glass based
2000	741	2348	2843	3601	4912	7722	
1550		1751	2012	2365	2867	3641	
1064		1155	1263	1394	1554	1756	

Regarding to the higher-order R-DFB fibre lasers, it can be realized with the configurations of intra-cavity R-DFB fibre lasers and cascaded DBR-DFB Raman fibre lasers. For example, Fig. 3-15 shows the schematic diagrams of experimental setup for generating 3rd order (a) intra-cavity R-DFB fibre laser and (b) cascaded DBR-DFB Raman fibre laser, in which the 1st- and 2nd-order FBGs are used to form corresponding DBR Raman fibre lasers with a certain length of Raman fibre. Given a pump source, the Bragg wavelength of the R-DFB grating is written at the 3rd-order Raman Stokes, which can be calculated with the Raman shift frequency, as seen in Table 3-3. In the intra-cavity R-DFB configuration, as seen in Fig. 3-15 (a), the R-DFB grating is inserted in the cavity of the 2nd-order DBR Raman fibre laser. In the other setup, the 2nd-order DBR Raman fibre laser is applied as the pump source for the 3rd-order R-DFB fibre laser. The pump power required for higher-order R-DFB fibre lasers depends on the conversion efficiencies of the DBR Raman fibre lasers and the threshold of R-DFB fibre laser. In typical, the conversion efficiency for first order Raman fibre can be obtained as high as 80%. Assuming the threshold of the R-DFB fibre laser is ~2 W, which is predicted by line 5 in Fig. 3-9 with 30 cm long DFB grating in small core silica glass fibre, only ~4 W pump power is required given 80% conversion efficiency of DBR Raman fibre lasers and ideally no insertion loss of the pump source. The connection loss between the silica glass optical fibres is quite low, however, for the tellurite glass fibres, the connection loss could be high, which will discussed in Chapter 4. With the development of the higher power fibre laser, >100 W CW pump sources at 1064 nm (Yb-doped fibre lasers), 1550 nm (Er/Yb-codoped fibre lasers) and ~2 μm (Tm-doped fibre lasers) are available already. Hence, there is no technical problem for demonstrating higher-order R-DFB fibre lasers.

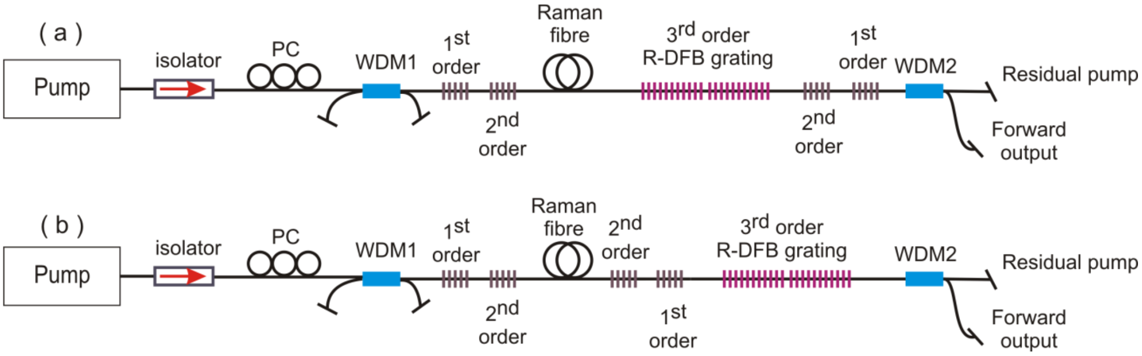

Fig. 3-15 Schematic diagram of experimental setup for 3rd order (a) intra-cavity R-DFB fibre laser and (b) cascaded DBR-DFB Raman fibre laser.

3.3.6 *Summary of the simulations*

In summary, R-DFB fibre lasers both with centre and step-like offset π phase-shifted DFB gratings have been studied numerically by solving the NLCMEs. The properties of lasing behaviour, TPP (with respect to the incident pump power), TSE (against the incident pump power) and the influences of the random noise on Bragg grating profiles, have been presented in this part.

The TPP is found to be approximately inversely proportional to the coupling coefficient (κ) and the Raman gain coefficient, and linearly proportional to the effective mode area of the fibre. A longer length of the DFB grating and lower background loss of the optical fibre is suggested to be always desirable to achieve a R-DFB fibre laser with low TPP. Sub-watt lasing threshold in 10’s cm long R-DFB fibre laser is predictable by using a HNLF, tellurite glass holey fibre, as an example. On the other hand, the simulation results have also revealed that a weak strength of the DFB grating is required to achieve a high TPP R-DFB fibre laser. Thereupon, by balancing the TPP and the TSE, $\kappa = 30\ \mathrm{m}^{-1}$ for 30 cm long DFB grating is selected for most of the simulation scenarios and the results show that at least 8.2 W CW pump power at 1540 nm is required to demonstrate a R-DFB fibre laser with a centre π phase-shifted DFB grating in a high NA (0.28) silica glass fibre with a Raman gain coefficient of ~ 7×10^{-14} m/W, an effective core area of ~ 12 $\mu\mathrm{m}^2$ and a linear loss of 0.1 dB/m. With the same configuration of the DFB grating, the simulation results also predict that only low-watt level CW pump power at 1.06 μm is needed to generate a R-DFB fibre laser in UHNA4 fibre with a linear loss below 0.05 dB/m. This threshold pump power could be reduced further by simply shifting the π phase-shift to 20% away from the centre to form a step-like offset π phase-shifted DFB structure laser, together with a single-side output performance.

In terms of the effects of the phase and amplitude noise on the fibre laser, the results have shown that R-DFB fibre lasers are resilient against the noise up to about 5%, with negligible degeneration of the threshold and slope-efficiency of the lasers.

Thus, with the assistance of the simulation, it is highly feasible to experimentally demonstrate the R-DFB fibre laser in lab.

3.4 Demonstration of R-DFB fibre lasers

This section describes the experimental demonstrations of the Raman DFB fibre lasers, including the experimental setup, fibre selection, characteristics of the DFB gratings and the features of R-DFB fibre lasers.

3.4.1 *Experimental setup*

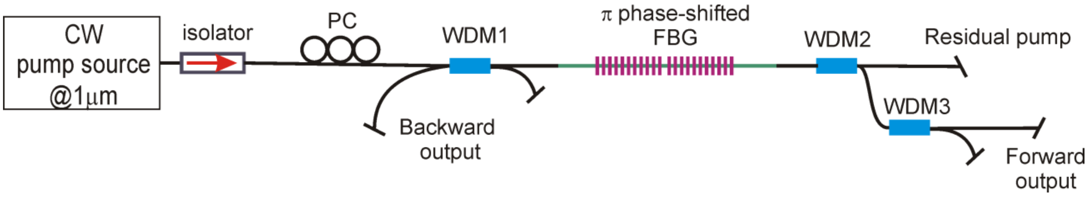

Fig. 3-16 Schematic diagram of the experimental setup for Raman DFB fibre lasers.

Fig. 3-16 shows the schematic diagram of the experimental setup for R-DFB fibre lasers. A CW fibre laser source at ~1.06 μm is used as the pump source. The output of the pump is spliced to a non-PM high power isolator and then a *polarisation controller* (PC), which is exploited to adjust the state of polarisation of the pump light. 1064 nm/1117 nm *wavelength division multiplexer*s (WDM 1/2/3), from Gooch & Housego, are used to separate the R-DFB signal from the pump both at the backward and forward output ends of the DFB grating. All fibre ends are angle-cleaved to prevent end-feedback, and the WDMs and the DFB grating are mounted on heat sinks, which are made up of copper plates, Peltier coolers and temperature controller, to help maintaining uniform temperature distributions along the DFB grating, and to better remove any generated heat. The DFB gratings are very sensitive to the temperature and the environment fluctuation, such that they are covered with thermal paste in order to not only improve the thermal conductivity with the heat sink but also eliminate the effects of environmental fluctuations on them.

The reasons for using ~1.06 µm pump source to demonstrate the R-DFB fibre lasers in this work are because: (i) they are the available high power fibre laser sources in lab; (ii) as predicted from the simulation, low-watt level threshold R-DFB fibre lasers is possible to be realized with commercial optical fibres, such as UHNA4 from Nufern. This is partially due to the higher Raman gain coefficient of the fibre with shorter wavelength pump source of ~ 1.06 µm than that with a longer wavelength pump source, e.g., ~1.54 µm, since the Raman gain coefficient is inversely proportional to the pump wavelength [99]; and (iii) the projected R-DFB laser wavelength, ~1.12 µm is out of the wavelength regime demonstrated by RE-doped counterparts and also this wavelength is useful for the application of visible light source generation implementing frequency-doubling technique [117].

Accordingly, two pump sources at ~1.06 µm have been setup as the pump sources for the R-DFB fibre lasers. Fig. 3-17 shows the photos of the two pump sources: (a) an un-polarised CW Yb-doped all fibre MOPA at ~1068 nm; and (b) a linearly polarised CW Yb-doped PM fibre MOPA at ~1064 nm. In both pump sources, a linearly polarised fibre pigtailed *laser diode* (LD) at 1.06 µm is used as the seed, which is stabilized by the self-seeding with the reflection from the FBG at the output of the seed. For the un-polarised pump source, the seed is amplified with a two-stage YDFA MOPA chain, which was provided by Dr. Shaif-ul Alam. For the linearly polarised pump source, the seed is amplified with a 10 m long PM Yb-doped fibre (from Nufern), which is pumped with 50 W LD at 975 nm (from JDSU). A high power isolator is connected at the output of the pump source to protect the pump source (as seen in Fig. 3-17). Note that all the passive components in the un-polarised pump source (as seen in Fig. 3-17(a)) are non-PM, whilst all PM components, except the final high power isolator, are used in the linearly polarised pump source. As seen in Fig. 3-17, all the components as well as their fibre pigtails are fixed stationary on the optical bench in order to minimise the influence of the environmental fluctuations on the polarisation state of the pump source.

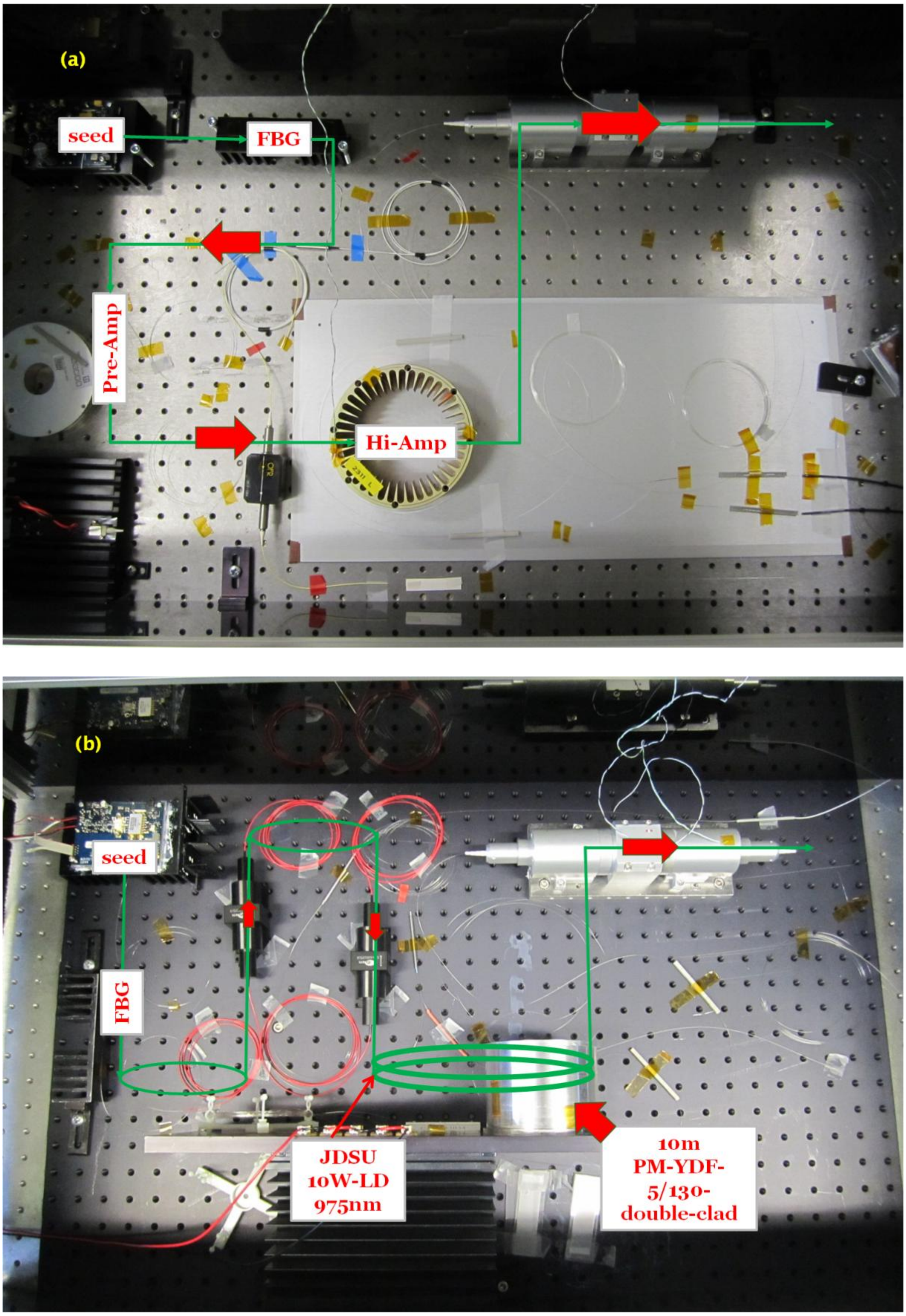

Fig. 3-17 Photos of (a) un-polarised CW Yb-doped all fibre MOPA and (b) linearly polarised CW Yb-doped PM-fibre MOPA.

Fig. 3-18 shows the optical spectra of the pump sources measured at the low power with an OSA, Advantest Q8384, at a *resolution bandwidth* (RBW) of 0.01 nm. It can be seen that both pump sources operate with multiple longitudinal modes.

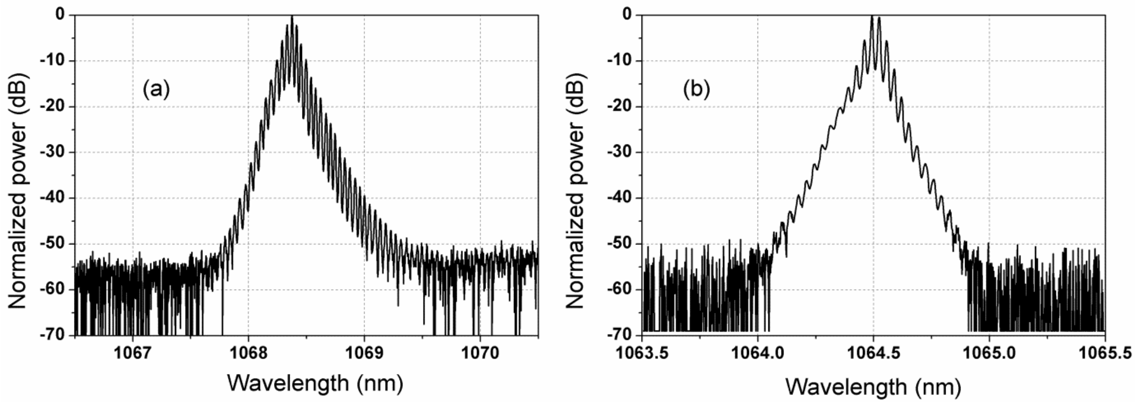

Fig. 3-18 Output spectra of the un-polarised pump source (a) and the linearly polarised pump source (b).

The main parameters of the pump sources are summarized in Table 3-4. The maximum output power of the un-polarised pump source is ~20 W and ~5 W for the linearly polarised pump source, restricted by the available pump diode power for the MOPA. The *full-width-at-half-maximum* (FWHM) bandwidth for both pump sources is ~0.1 nm.

Table 3-4 Main parameters of the pump sources.

Pump sources	Wavelength (nm)	Polarisation status	Maximum output power (W)	FWHM (nm)	Spectrum (RBW:0.01nm)	CW
#1	~1068	un-polarised	~20	~0.1	Fig. 3-18(a)	yes
#2	~1064	linearly polarised	~5	~0.1	Fig. 3-18(b)	yes

The degree of linear polarisation is often quantified with a *polarisation extinction ratio* (PER), which is defined as the ratio of optical powers in the two polarisation directions. Fig. 3-19 (a) shows the setup for measuring the PER of the pump sources. The output of the pump source from WDM1 is collimated and then passed through a *Polarizing Beamsplitter* (PBS) cube (PBS25-1064-HP from Thorlabs). P-polarised light of the collimated incident beam is transmitted while S-polarised light is reflected at a 90^{o} angle with respect to the incident beam. By adjusting the PC, the power ratio between the P-light and S-light is varied. Therefore, the PER can be obtained as the ratio of maximum and minimum powers of P-light or S-light. For the linearly polarised pump source (#2), the PER is measured to be ~16 dB for all operational power. It is worth noting that in Fig. 3-19, the fibre pigtail as well as the passive components, e.g., PC and WDM1, is non-PM, which indicates PER of the pump source might be slightly degenerated by them. In order to minimise the influence of the fluctuations (both mechanical or thermal) of the fibre and WDM1 on the polarisation state of the pump source, all the fibres are set stationary on the optical bench with adhesive tape; and the WDM1 is mounted on the heat sink maintaining constant temperature during the measurement. Additionally, it is found that the output of the un-polarised pump source (#1) is partially polarised due to the linearly polarised seed was used. However, the polarisation state of the pump source (#1) keeps rotating with respect to operation time, which might deteriorate the stability of the R-DFB fibre lasers. Therefore, instead of polarising the output of the high power source #1 to produce a linearly polarised pump source for R-DFB fibre laser generation, the linearly polarised all-PM fibre MOPA source has been built up in this work.

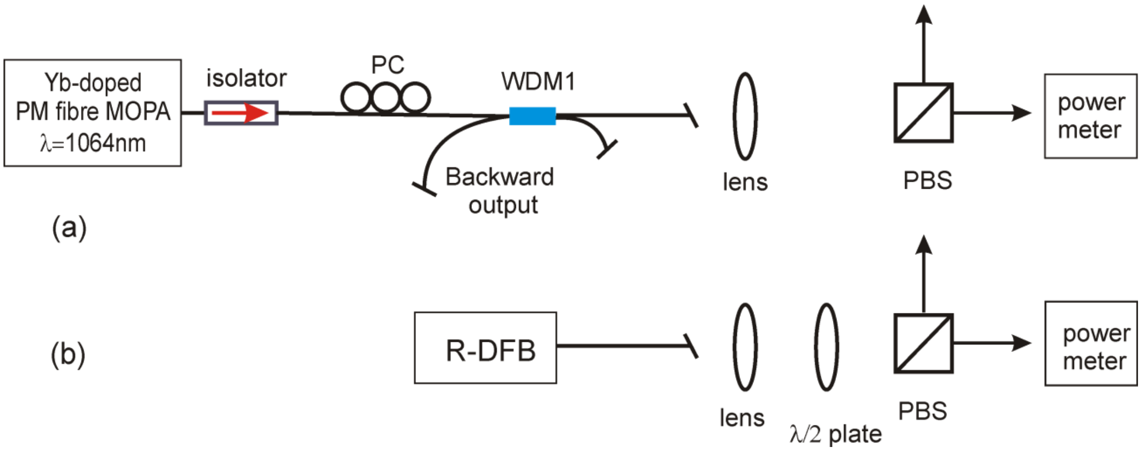

Fig. 3-19 Schematic diagram of the measurement setup for polarization extinction ratio of pump source (a) and R-DFB fibre lasers (b).

Fig. 3-19 (b) illustrates the setup for measuring the PER of R-DFB fibre lasers, in which a half-wave plate is used instead of a PC in Fig. 3-19(a). Herein, the half-wave plate is used as a polarization rotator and with the combination of the PBS, the PER of the R-DFB signal can be characterized with this approach.

Note that the OSA of Q8384 can tolerate a low power input but with very high resolution (0.01 nm). Another OSA, Agilent 18640B, has also been used for measuring the spectra at higher power levels throughout this work. The optical power is measured by a power meter (TPM-300) with a thermal detector of UP25N-100H-H9-D0 when the power is above 2 W, below which, the power is measured with another thermal detector of 13PEM001.

3.4.2 Fibre selection

From the simulation results in Section 3.3, in order to achieve a R-DFB fibre laser with low laser threshold, one requirement is that the fibre needs a high intrinsic Raman gain coefficient. Fig. 3-20 (a) shows the relative Raman cross section spectra of the high-purity bulk samples of vitreous (v-) SiO_2, v-GeO_2, v-P_2O_5 and v-B_2O_3 [145]. Among these glass formers, the peak Raman cross section of v-GeO_2 is the strongest and is 7 - 8 times higher than that of v-SiO_2.

This clearly indicates that high Ge-doped silica glass fibres are good candidates for Raman applications [40, 67, 154]. What is more, Fig. 3-20 (b) illustrates the measured relative reduced Raman intensity spectra of fused silica, Schott SF57 glass (SiO_2-PbO-R_2O, in which PbO > 47% (mol.%), and R_2O is alkali oxides), 75TeO_2-20ZnO-5Na_2O (mol.%) (TZN, made in-house) glass and 87.5TeO_2-12.5Nb_2O_5 (mol.%) (TNb, made in-house) glass, of which the Raman intensity is normalized to the peak Raman intensity of pure silica glass (SiO_2) at 440 cm^{-1}. It has been found that the reduced Raman intensity spectrum is very close to the Raman gain profile [155] and the details of Raman gain coefficient calculation will be discussed in Chapter 4. As seen in Fig. 3-20 (b), the tellurite glass based optical fibres, e.g., TZN or TNb, possess about 30 – 50 times stronger peak Raman gain coefficient than that of silica optical fibres. Hence, tellurite glass based fibres are promising host media for R-DFB fibre lasers with low threshold pump power, as predicted by the simulation in Fig. 3-9.

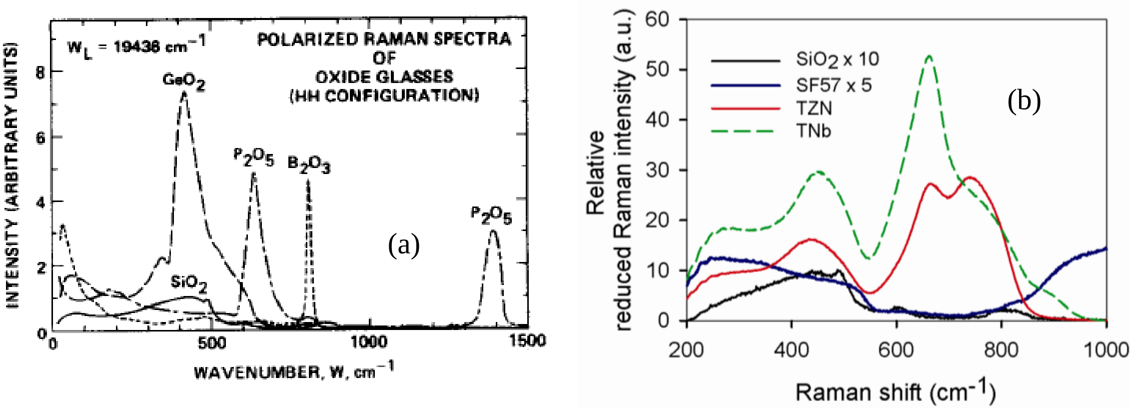

Fig. 3-20 (a) The relative HH Raman spectra of the primary glass formers SiO_2, GeO_2, B_2O_3 and P_2O_5. (After Ref. [145]) (b) Relative reduced Raman intensity of fused silica, SF57 glass, TZN and TNb at a pump wavelength of 1.06 μm.

In addition to the Raman gain coefficient of the fibre, photosensitivity is equally important for achieving a R-DFB fibre laser with a low lasing threshold [40]. The simulation results, as presented in Fig. 3-9, suggest that >10 cm long DFB grating is required to achieve a R-DFB fibre laser in silica-based optical fibres with watt-level threshold pump power. Also learnt from the simulation, high quality DFB gratings (with error less than 5%) and optical fibres with low background loss are favorable for realizing low threshold R-DFB fibre lasers. Consequently, DFB gratings that are written (1) in photosensitive fibres without pre-treating with hydrogen/deuterium gas, such that the background loss of the DFB gratings will be minimised; (2) with phase-mask method exposed to a UV light, which is the most reliable method to establish Bragg gratings so as to minimise the noise on the DFB grating profiles, are the most appropriate samples for demonstrating R-DFB fibre lasers.

Taking into account the two facts discussed above, silica fibres doped with a high concentration of Ge and/or Boron (B) are good candidates as Raman-gain media for R-DFB fibre lasers. Therefore, two commercially available fibres, which are PS980 (from Fibercore Ltd.) and UHNA4 (from Nufern) are selected for experimental demonstration. Table 3-5 summarises the main parameters of these two fibres. It is worth noting that PS980 fibre is a boron co-doped Ge/Si fibre and the UHNA4 is Ge-doped only. The addition of boron aids the photosensitivity and also increases the Raman gain coefficient marginally compared to a Ge/Si only fibre with similar NA. The *mode field diameter* (MFD) at ~1.1 µm is calculated to be ~6.2 µm for PS980 and ~2.6 µm for UHNA4, respectively. PS980 fibre has a cut-off wavelength of ~0.9 µm so that it is single mode at the pump wavelength (~1.06 µm) as well as the projected R-DFB fibre lasers. For the UHNA4 fibre, the cut-off wavelength is ~1.1 µm, indicating that it is singe mode for R-DFB fibre lasers and the *V*-number is ~2.48 at the pump wavelength (~1.06 µm), which ensures only the fundamental mode of pump source is dominant in the fibre [78]. The peak Raman gain coefficient in Table 3-5 is estimated by taking into account the Ge concentration only with the approximation equation given in Ref. [154]. The background loss is ~20 dB/km for PS980 and ~5 dB/km for UHNA4 at projected Raman DFB operating wavelength.

Table 3-5 Main parameters of PS980 and UHNA4 fibres

Parameter	PS980	UHNA4
NA	0.12-0.14	0.35
MFD @1100nm (µm)	6.2 ± 0.3	2.6 ± 0.3
Cut-off wavelength (nm)	900	1100
g_r@1.06 µm (x 10^{-13}m/W)	~0.86	~1.55

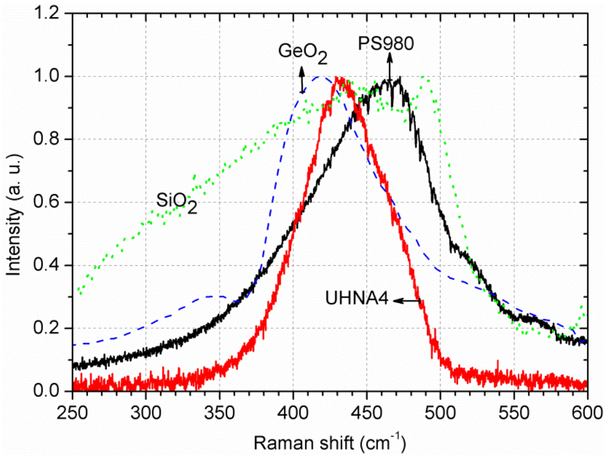

Fig. 3-21 Measured Raman gain spectra of PS980, UHNA4, fused silica (SiO_2) and GeO_2 (The curves of SiO_2 and GeO_2 are after Ref. [145]).

Fig. 3-21 shows the SRS spectra of PS980 (black solid curve) and UHNA4 (red solid curve) measured with the linearly polarised pump source at ~1.06 µm (source #2 in Table 3-4). They were generated by replacing the DFB grating in Fig. 3-16 with ~295 m long PS980 fibre and

~49 m long UHNA4 fibre, respectively. Note that all the fibre ends must be angle-cleaved to avoid forming any resonator cavity. Fig. 3-21 also shows the Raman gain spectra of fused silica (SiO_2) and *v*-GeO_2 for comparison. It is found that the bandwidth of the Raman gain spectra of PS980 and UHNA4 are narrower than that of fused silica, owing to the Ge and/or B co-doping [156]. The peak Raman gain coefficient of PS980 occurs at a longer Raman shift (460-470 cm^{-1}) than that of UHNA4 (430 cm^{-1}), which is also wider than that of *v*-GeO_2 (420 cm^{-1}). This is due to the different concentration of Ge in these samples.

Therefore, with the pump source of 1064 nm, DFB grating with Bragg wavelength at around 1120 nm (corresponding to 470 cm^{-1} Raman shift) or 1115 nm (corresponding to 430 cm^{-1} Raman shift) will take advantage of the maximum Raman gain coefficient in PS980 or UHNA4, respectively, so as to generate low threshold R-DFB fibre lasers.

3.4.3 Transmission spectra of DFB gratings

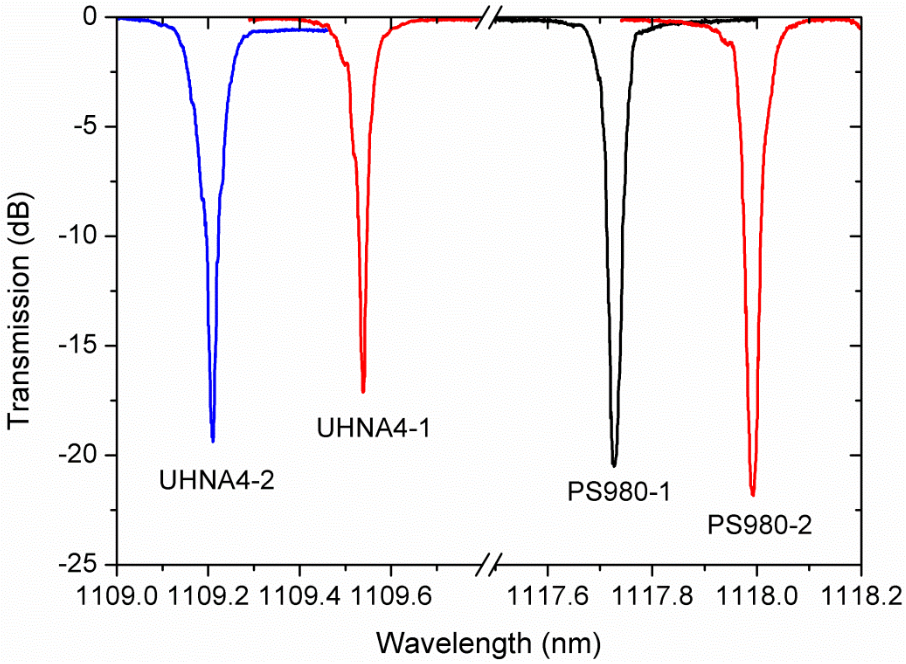

Fig. 3-22 Passive cold transmission spectra of 30 cm long centre π phase-shifted DFB gratings.

A set of 30 cm long DFB gratings with centre π phase-shift have been fabricated in-house in PS980 and UHNA4 fibres, respectively. Note that they were fabricated by my supervisor, Dr. Morten Ibsen. The DFB gratings were written directly into the fibres without the aid of hydrogen loading with 244 nm CW UV light using the continuous grating writing technique [85]. Fig. 3-22 shows the passive cold transmission spectra of the DFB gratings measured with a SC source. The Bragg wavelengths are found to be ~1117.7 nm for PS980-1, ~1118 nm for PS980-2, ~ 1109.5 nm for UHNA4-1 and ~1109.2 nm for UHNA4-2, respectively. Note that the Bragg wavelengths are slightly away from the ideal Raman peak Stokes for a pump source at

~1064 nm. This is only restricted by the available phase-mask for this wavelength region. From uniform test gratings written prior to the π phase-shifted DFB gratings, the coupling coefficient, κ, of the set of DFB gratings are estimated to be between 30 m^{-1} and 37 m^{-1}. Such weak DFB gratings are designed based on the simulation results discussed in Sections 3.3.2 and 3.3.3, in order to ensure low lasing threshold and also high conversion efficiency. The amplitude of the refractive index modulation of the DFB grating is very low at the level of 10^{-5}. Consequently, the UV-induced loss in the DFB gratings is minimal and so the total propagation loss is therefore maintained very close to the linear loss of the pristine fibres. Note that the π phase-shifted cavity notch cannot be solved by the OSA, which is only limited by the RBW.

3.4.4 High power R-DFB fibre lasers with un-polarised pump source

With the un-polarised pump source at ~1068 nm, R-DFB fibre lasers have been demonstrated in all of these DFB grating samples. It is found that the threshold pump power varies slightly among these samples, due to the slightly different values of the coupling coefficient (κ) of these gratings and the different Raman gain coefficient between the two types of fibres. However, the R-DFB output spectra as well as the output power characteristics are revealed to be similar for the DFB gratings formed in the same optical fibre. As a result, the experimental data of the R-DFB fibre lasers generated in DFB grating samples of PS980-1 and UHNA4-1, as the representative of DFB gratings formed in each fibre, have been discussed in detail in this part.

Table 3-6 summarises the main parameters of the DFB gratings of PS980-1 and UHNA4-1. For convenience, the R-DFB fibre laser formed in PS980-1 DFB grating is named as R-DFB1, and R-DFB2 represents the R-DFB fibre laser formed in UHNA4-1 DFB grating.

Table 3-6 Key parameters of the fibres and DFB gratings used for demonstrating the Raman DFB fibre lasers.

R-DFB	**DFB grating**	**Fibre**	**A_{eff} @1100 nm (μm^2)**	**λ_B (nm)**	**κ (m^{-1})**	**L_{DFB} (cm)**	**L_{total} (incl. pigtails) (cm)**
1	PS980-1	PS980	30.3 ± 2.9	~1117.7	~ 37	30	38
2	UHNA4-1	UHNA4	5.4 ± 1.2	~1109.5	~ 30	30	57

Fig. 3-23 (a) and (c) show the forward and backward DFB output spectra just below and just above the lasing threshold of R-DFB1 and R-DFB2, respectively. Note that the power displayed in Fig. 3-23 represents the incident pump power, which has been corrected with the splicing loss at the input end of the DFB grating, as seen in Fig. 3-16. The forward output spectra traces shown in Fig. 3-23(a) and (c), have clearly demonstrated that the threshold incident pump power is close to ~2.1 W for R-DFB1 and close to ~1.1 W for R-DFB2, respectively. This is because no signal above the noise floor instead of a dip at the Bragg wavelength has shown up when the incident pump is below this power level. For instance, when the incident pump power was ~1.3 W in R-DFB1 (as seen Fig. 3-23 (a)), a dip at ~1117.7 nm is clearly seen from the forward output spectrum. Also it is evident that the lasing occurs exactly at the Bragg wavelength of the DFB grating as expected from a π phase-shifted grating structure.

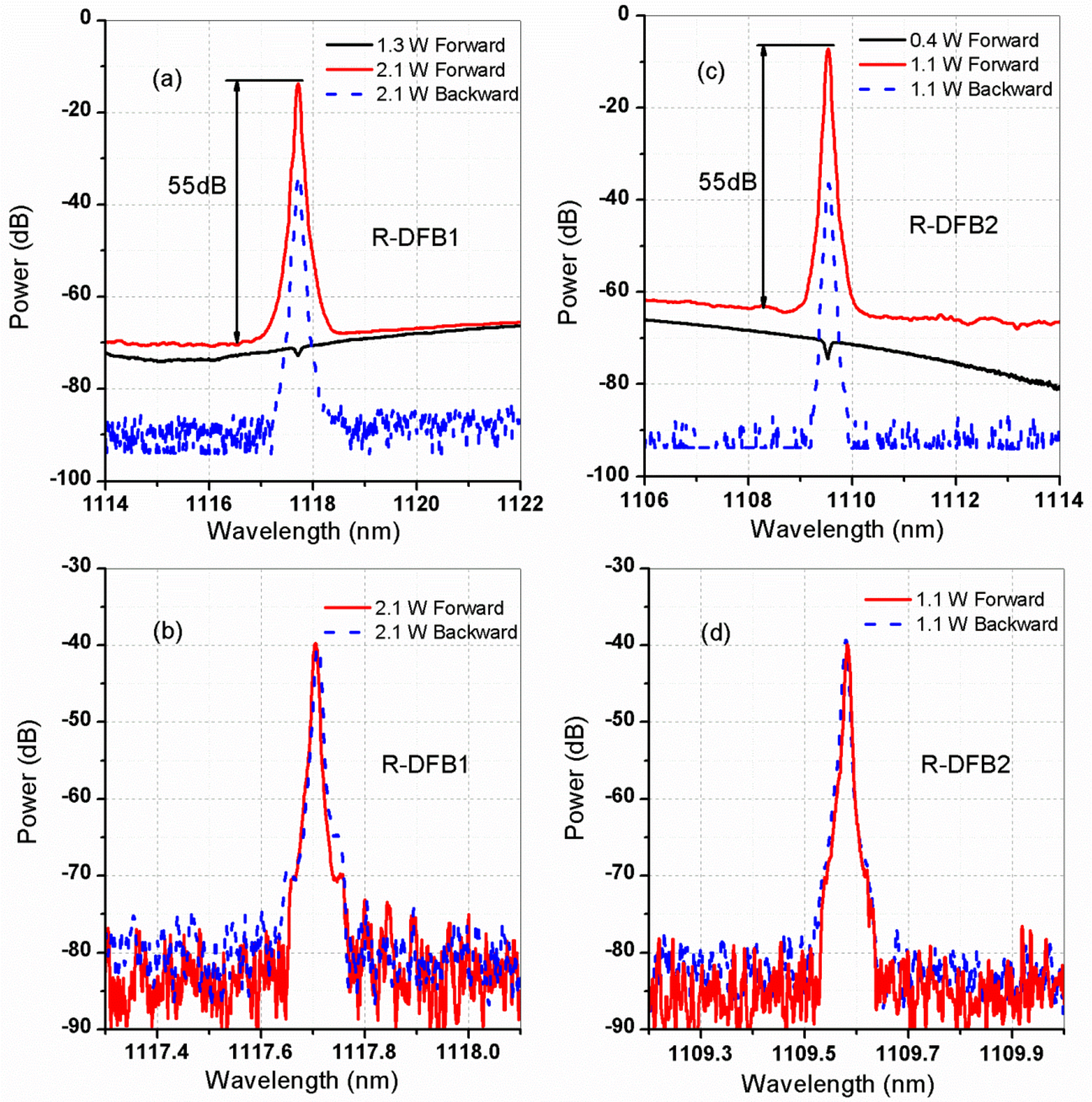

Fig. 3-23 R-DFB output spectra just below and just above threshold of R-DFB1 with 0.1 nm RBW (a) and 0.01 nm RBW (b), and R-DFB2 with 0.1 nm RBW (c) and 0.01 nm RBW (d). The power shown in the figure is the incident pump power.

The threshold of R-DFB2 is found to be ~52% of that of R-DFB1. As the DFB gratings in R-DFB1 and R-DFB2 are very similar, the different threshold is mainly due to the difference of the Raman gain coefficient (g_r), effective area (A_{eff}) and propagation loss (α) between the two types of host fibres, i.e., PS980 and UHNA4. According to the simulation in the above section, the threshold is linearly proportional to the effective area whilst inversely scale to the Raman gain coefficient, i.e., $P_{th} \propto A_{eff}/g_r$. Table 3-7 shows the estimated Raman gain coefficient at the R-DFB wavelength in R-DFB1 and R-DFB2 by using the peak Raman gain coefficient in Table 3-4, corresponding frequency shift from the pump source and the normalized Raman gain profiles in Fig. 3-21. Thus, the threshold of R-DFB2 can be calculated to be ~69% of that of R-DFB1 by using the Raman gain coefficient in Table 3-7 and effective area in Table 3-6, without the consideration of the disparity in propagation loss in PS980 and UHNA4. Taking into account the slightly higher loss in PS980 than that in UHNA4, the experimental result matches well with the calculation. Please remind that there is uncertainty in estimating the peak Raman gain coefficient and the MFD of the fibre.

Table 3-7 Estimated Raman gain coefficient at the R-DFB wavelength in R-DFB1 and R-DFB2.

R-DFB	Fibre	g_r @ *peak* (x 10^{-13} *m/W*)	Frequency shift (cm^{-1})	g_r @ *R-DFB* (x 10^{-13} *m/W*)
1	PS980	~0.86	~415	~0.6
2	UHNA4	~1.55	~350	~0.16

Both lasers exhibit ~55 dB *signal-to-noise ratio* (SNR) with 0.1 nm RBW soon after lasing has started. Fig. 3-23 (b) and (d) show the DFB output spectra of R-DFB1 and R-DFB2 at just above the threshold pump power with a high resolution of 0.01 nm in a 0.8 nm wavelength span. It can be seen clearly that the 3 dB linewidth is no more than 0.01 nm, limited only by the resolution of OSA. More accurate linewidth measurements can be carried out by using, for example, delayed self-heterodyne or self-homodyne methods [157]. Results of the linewidth measurements will be presented in the next section (Section 3.5).

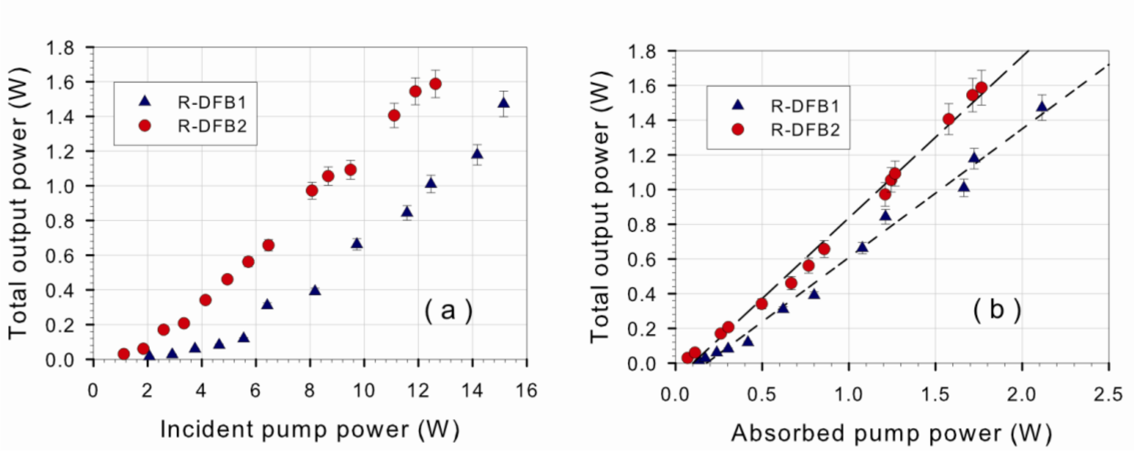

Fig. 3-24 Total R-DFB output power against incident pump power (a) and absorbed pump power (b).

Fig. 3-24 (a) illustrates the relationship between the total R-DFB output power and the incident pump power for R-DFB1 and R-DFB2, respectively. The uncertainty in the measured output power is about ± 5%, due to the use of a thermal power meter and the power variation of the pump source. The incident pump power has been corrected with the splicing loss at the input end of the DFB grating, as seen in Fig. 3-16, which is about 0.16 dB for R-DFB1 whilst is about 0.64 dB for R-DFB2. The higher splicing loss for UHNA4 fibre is because of the mismatch of the MFDs between the UHNA4 and the Hi1060 fibre, which was used as the pigtail of WDMs.

As seen in Fig. 3-24 (a), the R-DFB output power grows slowly for low incident pump powers but gradually increases as the pump power is increased. Although not a particularly good measure of the efficiency due to the nonlinear nature of the growth of the output power with respect to the incident pump power, the output powers are seen to increase with a slope efficiency of ~13% in both lasers for pump powers of ~3 W above their threshold. This efficiency is slightly lower than that was predicted by simulations. This discrepancy could in part be explained by the presence of minor phase and/or amplitude errors in the gratings [73]. However, this efficiency is still ~x12 times higher than the R-DFB fibre lasers reported by OFS Laboratory [38].

Indeed, viewing the slope efficiency of the output power against absorbed pump power will give a better picture of the conversion efficiency. The absorbed pump power is obtained by comparing the incident pump power with the residual pump power, which has been corrected with the insertion loss of WDM2 and the splice loss at the output end of the DFB grating, as shown in Fig. 3-16. In the case of R-DFB 1 (the low-NA R-DFB fibre laser in PS980), the slope efficiency is found to be ~74%, and in the case of R-DFB2 (the high-NA R-DFB fibre laser in UHNA4) it is ~93% as shown in Fig. 3-24 (b). The reason for the lower slope-efficiency from R-DFB1 might be due to the slightly higher propagation loss in this fibre and also slightly longer R-DFB wavelength indicating lower quantum conversion efficiency. However, the 93% in R-DFB2 is very close to the theoretical quantum conversion efficiency, which matches well with the numerical simulations.

The maximum output powers of R-DFB1 and R-DFB2 were measured to be ~1.5 W for an incident pump power of ~15.1 W and ~1.6 W for an incident pump power of ~12.6 W, respectively. With the DFB grating sample of UHNA4-2, ~2 W R-DFB output power has been observed with the same pump source [39], which is the highest reported output power for a DFB fibre laser source.

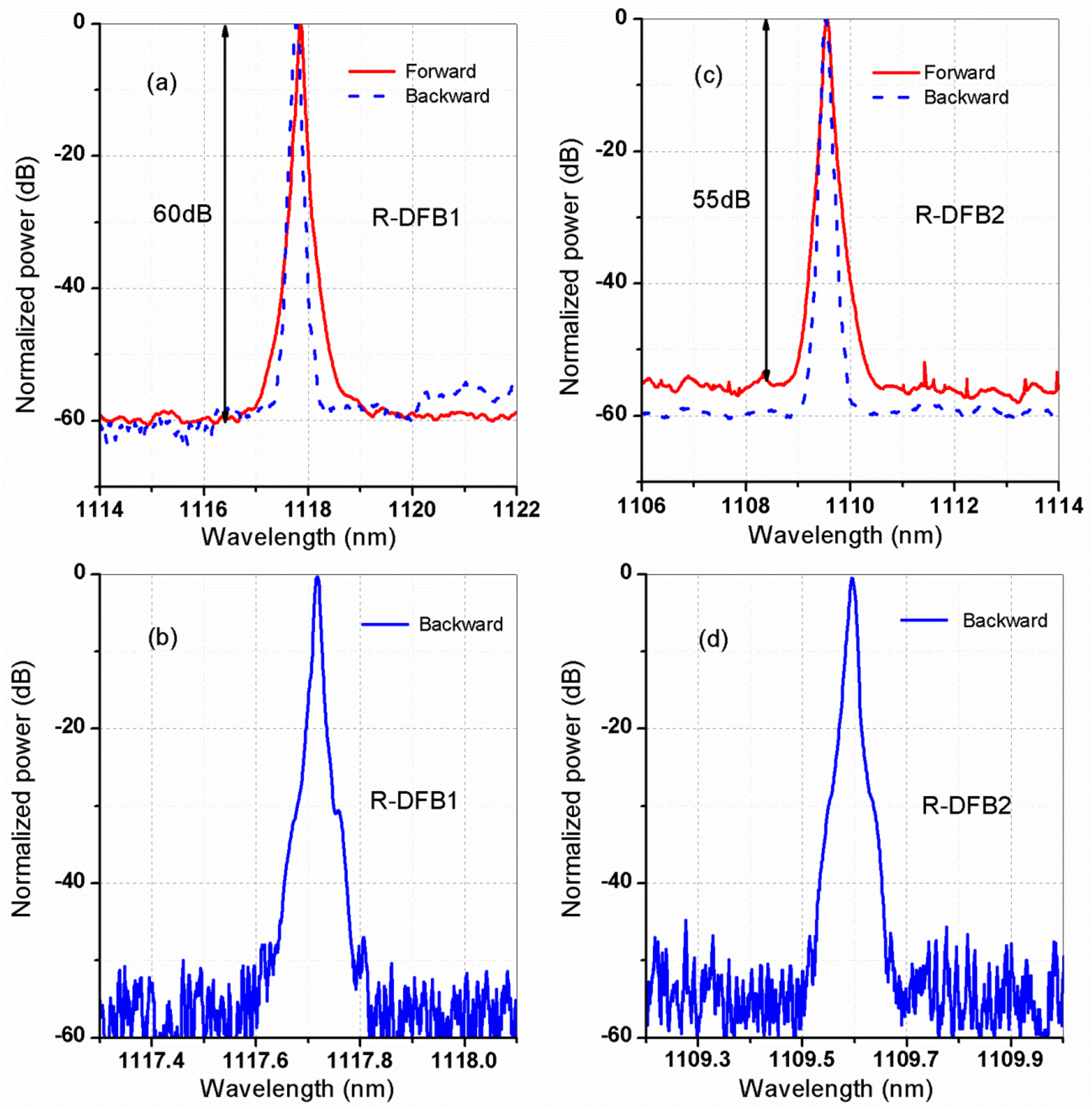

Fig. 3-25 R-DFB output spectra at the maximum output power of R-DFB1 with 0.1 nm RBW (a) and 0.01 nm RBW (b), and R-DFB2 with 0.1 nm RBW (c) and 0.01 nm RBW (d), respectively.

Fig. 3-25 (a) and (c) show the forward and backward output spectra with 0.1 nm RBW at the maximum output power of R-DFB1 and R-DFB2, respectively. Additionally, Fig. 3-25 (b) and (d) illustrate the backward DFB output with 0.01 nm RBW of R-DFB1 and R-DFB2 at this power level, respectively. The spectra demonstrate that the high SNR (above 55 dB) and narrow-bandwidth properties are maintained even at this power level. A slight bandwidth broadening is observed when comparing the forward output spectra with those of the backward spectra. The reason for such a broadening is likely due to the interplay between the forward signal and the co-propagating pump wave [42, 139].

3.4.5 Sub-watt threshold R-DFB fibre lasers with a linearly polarised pump source

Since the Raman gain is highly depending on the light polarization [65, 67, 98], it is anticipated that the threshold of the R-DFB fibre laser could be further reduced by employing a linearly polarised pump source. Besides, as seen in Table 3-7, with the pump source at 1068 nm, the Raman gain coefficient at R-DFB wavelength is much smaller than the peak Raman gain coefficient, especially in the case of R-DFB2 fibre laser. Since the peak Raman gain coefficient occurs around 440 cm^{-1} Raman shift, shifting the pump source to shorter wavelength could enhance the Raman gain coefficient at the R-DFB wavelength. By replacing the un-polarised pump source (#1 @ 1068 nm) with the linearly polarised pump source (#2 @ 1064 nm), the laser thresholds of all these four DFB grating samples (as shown in Fig. 3-22), have been reduced by a factor of ~2. In other words, the threshold pump power of the R-DFB fibre lasers formed in PS980 fibre (PS980-1 and PS980-2 DFB grating samples) is observed to be ~1 W with the linearly polarised pump source at 1064 nm instead of ~2.1 W with the un-polarised pump source at 1068 nm. So do the R-DFB fibre lasers formed in UHNA4 fibre. Sub-watt threshold R-DFB fibre lasers have been demonstrated in UHNA4 DFB grating samples with the linearly polarised pump source.

This part presents the experimental data of the R-DFB fibre laser generated in UHNA4-1 DFB grating sample by using the linearly polarised pump source at ~1064 nm.

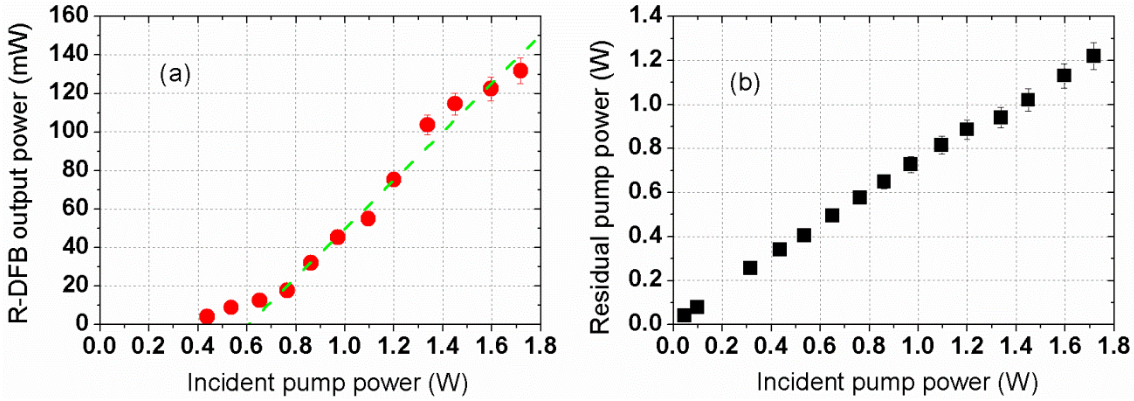

Fig. 3-26 R-DFB output power (a) and residual pump power (b) against incident pump power.

Fig. 3-26(a) shows the measured total R-DFB output power with respect to the incident pump power, which has been corrected with the splice loss (0.64 dB) between the WDM1 and the UHNA4 fibre at the input end of the DFB grating. The uncertainty in the measured power is estimated to be around ± 5%, due to the use of the thermal detector as well as the slight intensity fluctuation of the pump source. It is found that the threshold pump power in this case is only ~440 mW, which is ~48% of that with the pump source at 1064 nm (corresponding to a reduction factor of ~2.5), as seen in Fig. 3-24 (a). Such a low threshold pump power is attributed to the combination of the linearly polarised pump source with slightly shorter pump wavelength (~1064 nm) than the previous un-polarised pump source (~1068 nm). Note that the pump source #1 is partially polarized as discussed in the Section 3.4.1, hence the reduction factor on the threshold would be between 1 and 2 by employing the linearly polarised pump source #2. On the other hand, Table 3-8 summarises the frequency shift, normalized Raman gain coefficients and the quantum conversion efficiencies of R-DFB1 and R-DFB2 with these two pump sources. Such normalized Raman gain coefficients are evaluated with the SRS spectra (as seen in Fig. 3-21) and corresponding frequency shift. It can be seen clearly that the frequency shift becomes closer to the peak Raman shift with the 1064 nm pump source, so that the Raman gain coefficient at the R-DFB wavelength would be higher. As seen in Table 3-8, the enhancement factor on the Raman gain coefficient is estimated to be ~1.34 and ~2.7 in R-DFB1 and R-DFB2, respectively. Accordingly, the threshold of R-DFB1 and R-DFB2 would be reduced with a factor of ~1.34 and ~2.7, respectively. Therefore, it could be concluded that in the case of R-DFB2, the low threshold is mainly due to the shorter pump wavelength of the linearly polarised pump source (#2) than the previous pump source (#1). Furthermore, even lower threshold R-DFB fibre lasers could be achieved in these DFB gratings by using shorter-wavelength pump source, e.g., at or close to 1060 nm for UHNA4 DFB gratings. The lower threshold would lead to higher conversion efficiency at a certain pump power. In addition, the quantum conversion efficiency will be decreased while enlarging the frequency shift, as shown in Table 3-8.

Table 3-8 Frequency shift, normalized Raman gain coefficients and quantum conversion efficiencies of R-DFB1 and R-DFB2 with two pump sources.

R-DFB	Pump (nm)	R-DFB(nm)	Frequency shift (cm^{-1})	g_r @ *R-DFB* normalized	Quantum conversion efficiency (%)
1	1068	1117.7	415	~0.7	95.6
	1064		450	~0.94	95.2
2	1068	1109.5	350	~0.1	96.3
	1064		385	~0.27	95.9

As also seen in Fig. 3-26(a), the R-DFB output power increases nonlinearly for increasing incident pump power, and the slope efficiency is measured to be ~13% as indicated by the dashed line. This is found to be in a similar manner to that with un-polarised pump source shown in Fig. 3-24 (a). The maximum R-DFB output power obtained was ~132 mW for an incident pump power of ~1.72 W, corresponding to a conversion efficiency of ~7.6%. Regarding the residual pump power, Fig. 3-26(b) illustrates the measured residual pump power (at the output of WDM2, shown in Fig. 3-16) against the incident pump power. It is found that almost 70% of the input pump power is transmitted through the system, implying that a better overall conversion efficiency may be possible by using an even longer R-DFB and/or by recycling of the unconverted pump power.

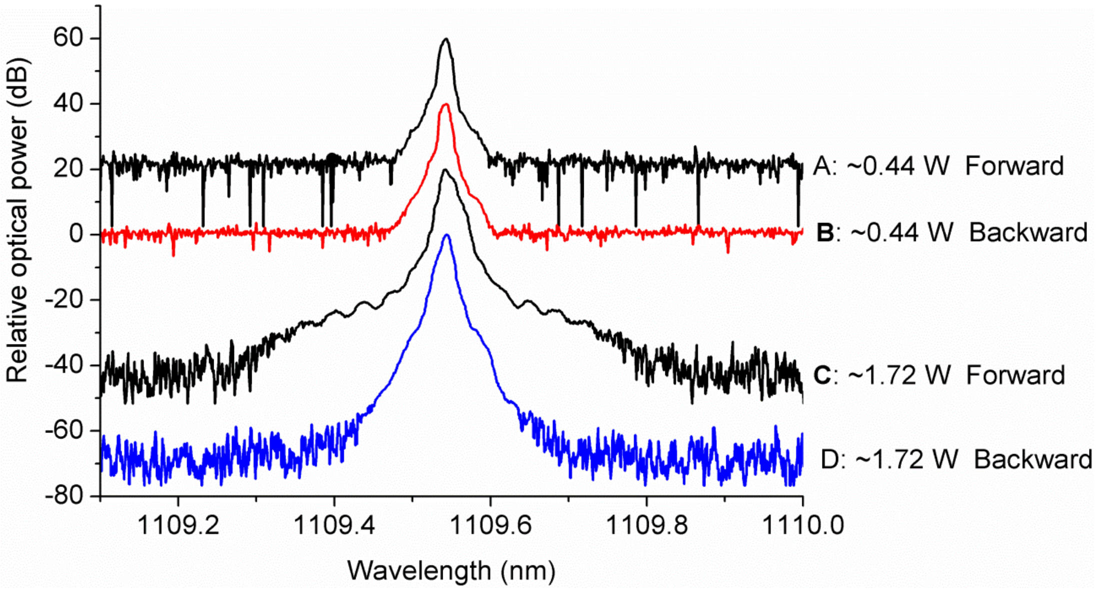

Fig. 3-27 Forward and backward R-DFB output spectra (RBW: 0.01 nm) just above threshold and at the maximum incident pump power, respectively. The power in the figure is the incident pump power.

Fig. 3-27 shows the observed forward and backward lasing spectra just above the lasing threshold and at the maximum incident pump power, respectively. Traces A and B are the forward and backward signal spectra just above the lasing threshold and demonstrate a SNR of ~40 dB with the RBW of 0.01 nm. Unlike the results with the un-polarised pump source shown in Fig. 3-23 ((a) & (c)), the DFB grating transmission spectra below the threshold cannot be observed. This is due to a more optimized design of the pump source being used resulting in very low levels of spontaneous emission at the R-DFB operating wavelength. Traces C and D show the forward and backward signal spectra at the maximum incident pump power of ~1.72 W. As seen, the R-DFB signal wavelength is maintained at ~1109.54 nm, and the 40 dB bandwidth is almost constant for all the power levels, indicating the negligible thermal effect in the laser within the observed power levels. Trace C shows slight broadening below the -40 dB level of the forward output compared to the backward output, which was also observed with the un-polarised pump source, as shown in Fig. 3-25. This is believed to be due to the interplay between the DFB output signal and the co-propagating pump wave.

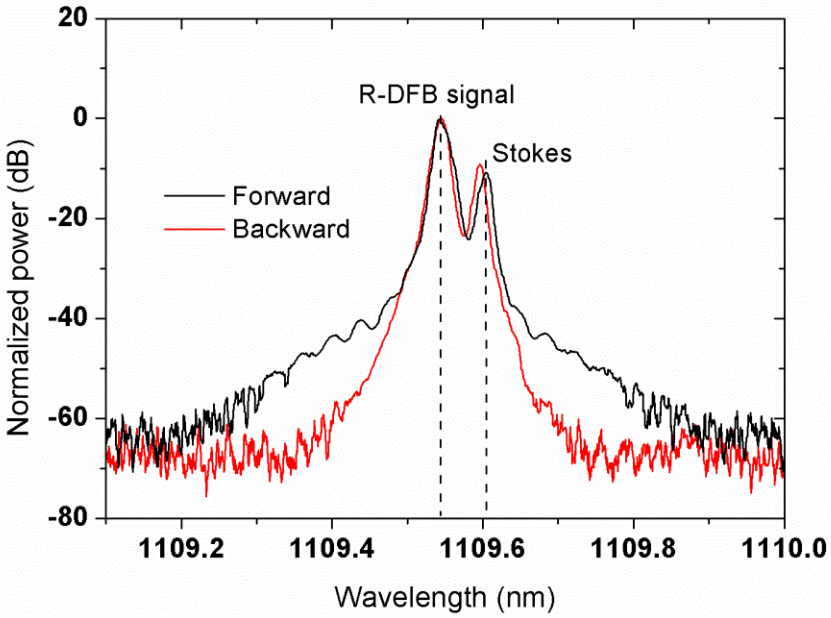

Fig. 3-28 Forward and Backward output spectra at incident pump power of ~2.0 W. The dashed vertical lines indicate the two peaks of R-DFB signal and Stokes, respectively.

It is worth pointing out that the maximum output power reported here is limited by the emergence of an unanticipated Stokes under high incident pump power. When the incident pump power was increased above ~1.72 W, Stokes have been observed both in the forward and backward output directions, as shown in Fig. 3-28 (with RBW of 0.01 nm) for an incident pump power of ~ 2.0 W. Note that the bidirectional Stokes are due to the bidirectional R-DFB output. The strong Stokes appears with a redshift of ~0.06 nm from the R-DFB signal, corresponding to the frequency shift of ~15.6 GHz with the pump wave at ~1109.54 nm. This is in very good agreement with the theoretical predicted Brillouin Stokes shift by $v_B = 2n_0 v_A/\lambda_p$ (where v_B is the Brillouin shift, n_0 is the refractive index, v_A is the acoustic velocity in optical fibre and λ_p is the pump wavelength, respectively), provided n_0 = 1.45, v_A= 5.96 km/s and λ_p = 1109.54 nm [65]. However, the mechanism for such efficient SBS generation in this circumstance has not yet been wholly understood. It might be associated with (i) the ultra-narrow linewidth of the R-DFB signal, which will be characterized in detail in Section 3.5; (ii) the high splicing loss (~0.64 dB/joint) at both ends of the DFB grating with the pigtail fibre (Hi-1060), indicating a resonator cavity is unexpectedly established for the Stokes wave thereby the SBS threshold is reduced; and (iii) the external pigtail fibre beyond the DFB grating in the experimental setup as shown in Fig. 3-19, including the PC and WDM1 pigtail fibre in the backward direction (~3-4 m) and WDM2 and WDM3 pigtail fibre in the forward direction (~3-4 m) of the R-DFB fibre laser, is likely to help to reduce the SBS threshold as well. However, such SBS phenomenon is the first observation and more work is required to quantify the threshold of the SBS in R-DFB fibre lasers.

3.4.6 *Uni-directional output R-DFB fibre lasers with a linearly polarised pump source*

In the above discussion, the total R-DFB output power (including the forward and backward) is used for characterising the overall conversion efficiency with respect to the incident pump power. However, the performance of the output power from the single side, e.g., forward or backward, is also very important for a practical R-DFB fibre laser. Typically, for a centre π phase-shifted DFB fibre laser with the combination of symmetric index modulation profile about the π phase-shift, the forward output power is found to be identical to the backward counterpart. Uni-directional output RE-doped DFB fibre lasers have been realized by shifting the π phase-shift away from the centre to comprise an asymmetric DFB grating cavity, leading to the reflectivity of one side is bigger than the other [11, 82, 83].

In this experiment, the forward and backward output power of the R-DFB fibre lasers in these four centre π phase-shifted DFB grating samples (as discussed in Section 3.4.3), are measured individually. The experimental data confirm that the forward and backward output powers are almost identical for R-DFB fibre lasers in UHNA4 DFB grating samples of UHNA4-1 and UHNA4-2 within the operational power range. However, truly uni-directional output phenomenon is observed in R-DFB fibre lasers formed in PS980 DFB grating samples, both in PS980-1 and PS980-2, with the linearly polarised pump source. Besides, it is found that the output power ratio between the forward and backward is very sensitive to the environmental conditions on the DFB gratings, such as the uniformity of temperature and/or stress distribution along the whole length of the grating. This is understandable since the DFB gratings are very sensitive to the temperature and the stress [4, 10, 15]. Thus, the DFB gratings are kept under nearly the same conditions to ensure the results are comparable. The mechanism and the performance of such uni-directional output R-DFB fibre lasers are analysed in this section.

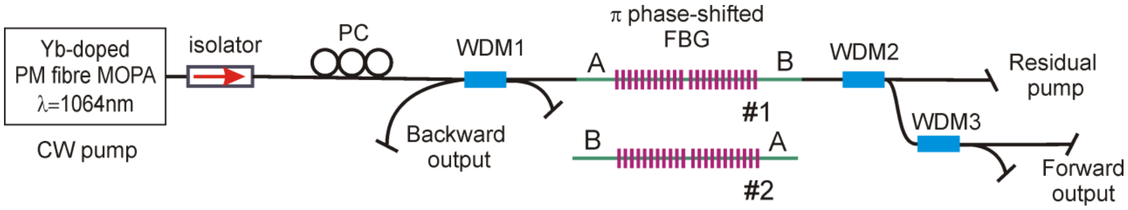

Fig. 3-29 Schematic diagram of the experimental setup for uni-directional R-DFB fibre lasers.

Fig. 3-29 illustrates the schematic diagram of the experimental setup, which is very similar to that in Fig. 3-16, apart from indicating the inscription orientation of the DFB grating. The DFB grating is originally written from side A to side B, indicated in Fig. 3-29, and has a π phase-shift at the centre of the grating. Due to the uni-directional output demonstrated from side A of the DFB grating, the reflectivity of the right half of the grating must be higher than that of the left half counterpart. Differing from the conventional design of a uni-directional DFB fibre laser, which is produced by shifting the π phase-shift offset from the centre, in this particular case, the refractive index modulation profile of the DFB grating has been linearly tapered up from A to B, as illustrated in Fig. 3-30. Also the coefficient of the tapering is estimated to be ~20% due to the alignment during the grating inscription process. Still, more work is required to characterize the precise index profile of the DFB grating.

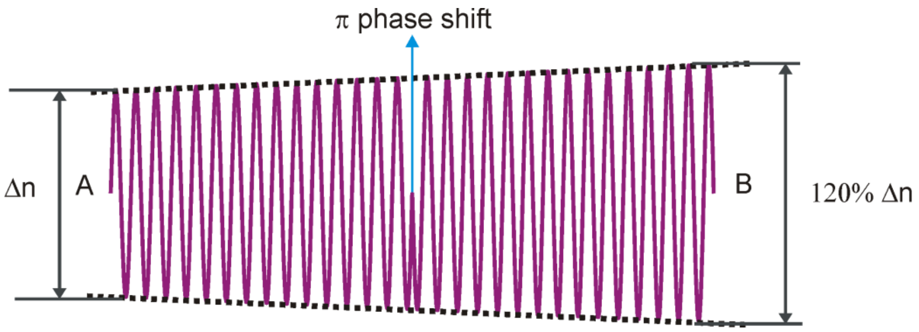

Fig. 3-30 Schematic diagram of the tapering index modulation profile of DFB grating.

The R-DFB fibre laser has been both characterized by pumping from side A (denoted AB), to form a counter-pumping scheme, and side B (denoted BA), to form a co-pumping configuration, as shown in Fig. 3-29. The data show below is based on the sample of PS980-1, which has an average coupling coefficient of ~37 /m.

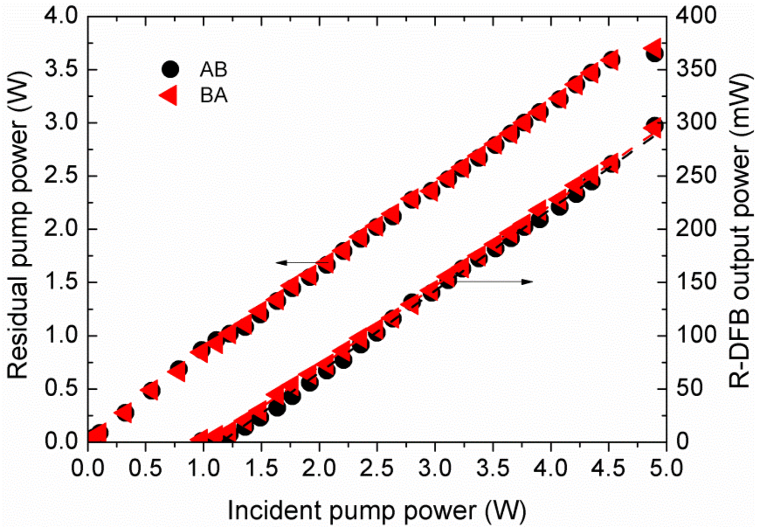

Fig. 3-31 R-DFB uni-directional output power (right axis) and residual pump power (left axis) vs incident pump power.

Fig. 3-31 shows the relationship between the R-DFB output power and the relevant residual pump power against the incident pump power of the linearly polarised pump source in both configurations of co-pumping (expressed as BA) and counter-pumping (expressed as AB). It is evident from Fig. 3-31 that the R-DFB fibre laser behaves in a consistent manner using either pumping scheme (co-pumping or counter-pumping). This proves that the uni-directional output feature is not relevant to the pumping direction but only to the index modulation profile of the DFB grating itself.

The incident pump power has been corrected with the splicing loss (~0.16 dB) between the WDM pigtail and the PS980 DFB grating. The threshold power is observed to be ~980 mW, which is about half of the value of that using the un-polarised pump source (see Section 3.4.4 [42]). As also seen in Fig. 3-31, the slope efficiencies of R-DFB output power with respect to the incident pump power, with the layouts of AB and BA, are identical at ~7.7%. However, it is smaller than that of bidirectional R-DFB fibre lasers (~13%, as discussed in the above section), which is due to: (i) the slightly higher total cavity loss in this case, which is due to the asymmetric reflectivity of the DFB cavity, as indicated in Fig. 3-30. This leads to increase net output power from one end to form unidirectional output R-DFB fibre laser; (ii) there might be additional phase and/or amplitude error on the DFB grating in this case, which decreases the conversion efficiency as discussed in Section 3.3.4. The maximum output power obtained is about 296 mW for an incident pump power of 4.9 W. Almost 70% of the input pump power was transmitted through the system. This is very similar to the results obtained in other DFB grating samples discussed in the above sections.

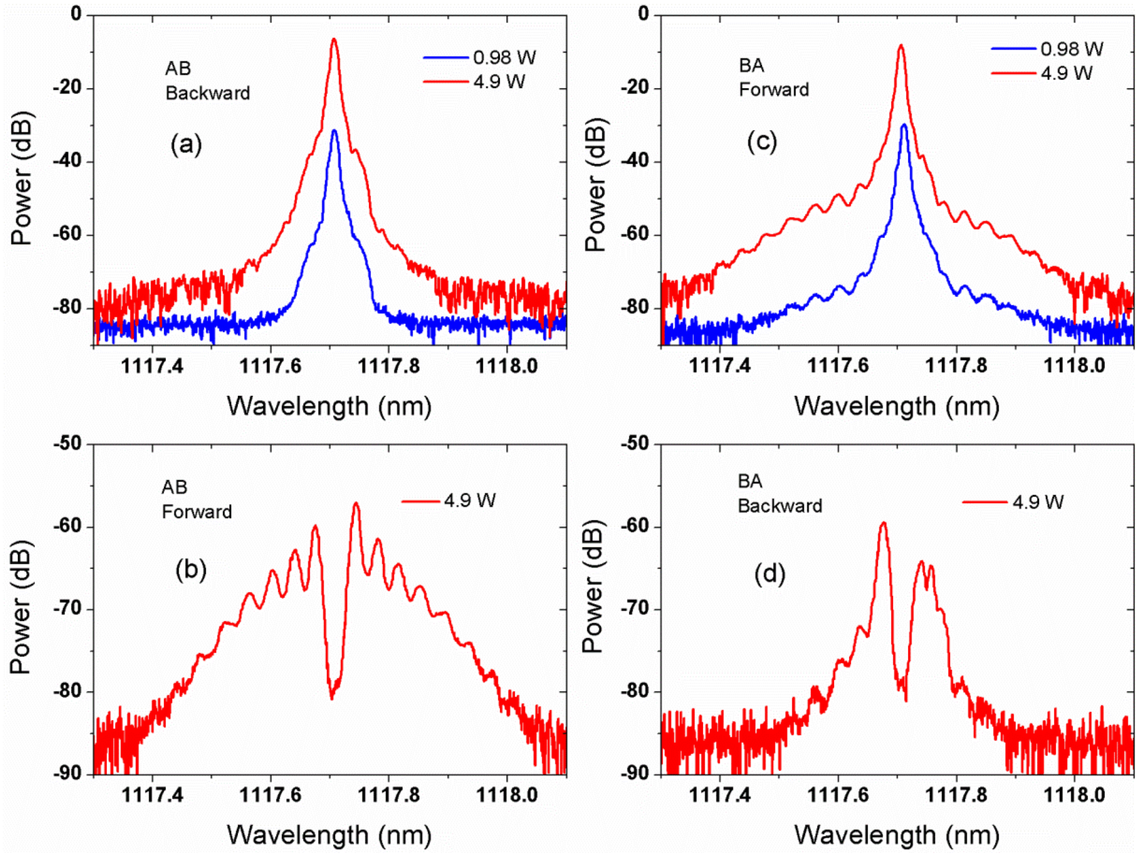

Fig. 3-32 Output spectra of the R-DFB fibre laser with RBW of 0.01 nm.

Fig. 3-32 illustrates the R-DFB output spectra at just above the laser threshold and the maximum incident pump power (~4.9 W) from both sides of the grating. When the incident pump power is ~0.98 W, the R-DFB signal is clearly detected from side A of the DFB grating either in counter-pumping, AB (Fig. 3-32 (a)) or co-pumping, BA (Fig. 3-32 (c)) configurations. Also the SNR of the R-DFB signal at this power level is as high as ~60 dB in both pumping schemes. However, there is no signal at all from side B of the DFB grating. The output spectra are monitored with the increase of the incident pump power. The signal wavelength of the R-DFB is seen to remain constant at ~1117.7 nm throughout the entire power range. This suggests that the thermal effect in this laser is negligible, which agrees with the results obtained in other DFB grating samples, e.g., UHNA4-1 and UHNA4-2. The maximum incident pump power is ~4.9 W, and the output spectra from both sides of the DFB grating are shown in Fig. 3-32. The SNR of the R-DFB signal is seen to be retained at ~60 dB, while no lasing signal at the signal wavelength is observed from the other side, side B, of the DFB grating. This clearly demonstrates that the R-DFB fibre laser indeed is operating with true single-side output. A slight tapering of the refractive index profile, as shown in Fig. 3-30, implies that one half of the structure will have a higher reflectivity compared with the other half thereby creating an effective HR, i.e., side B of PS980-1, and OC, i.e., side A of PS980-1, but the effects of this were more dramatic than anticipated. In terms of the slightly broadening spectra at the wavelengths on both sides of the R-DFB signal wavelength from the co-propagation side than that from the other side, this phenomenon has been observed in the other DFB grating samples as well.

The PER of the R-DFB fibre laser is measured with the experimental setup showing in Fig. 3-19(b). Fig. 3-33 shows the evolution of the measured power of the transmitted light (P-polarised light) by rotating the half-wave plate, at the output power of the R-DFB fibre laser at 53 mW, 73 mW and 143 mW, respectively. It can be seen clearly that the PER of the R-DFB fibre laser is >18 dB in this power range. Therefore R-DFB fibre laser is a high linearly polarised laser source.

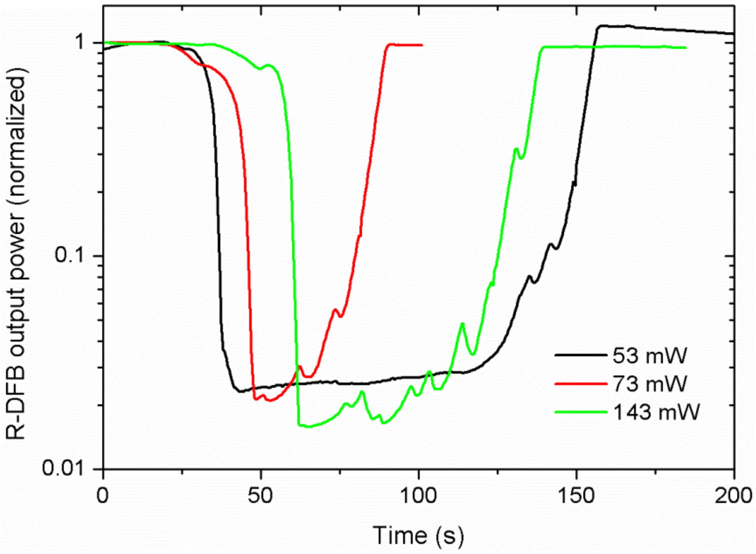

Fig. 3-33 PER of the R-DFB fibre laser at varied output power levels.

3.5 Linewidth measurement of R-DFB fibre lasers

As seen from the R-DFB output spectra presented in Fig. 3-23, Fig. 3-25, Fig. 3-27 and Fig. 3-32, it is evident that the linewidth of the R-DFB fibre laser is out of the resolution of the OSA, which has the highest frequency resolution of ~2.65 GHz at 1064 nm, corresponding to a RBW of 0.01 nm. It is well-known that DFB lasers, e.g., semiconductor DFB laser or RE-doped DFB fibre lasers, have ultra-narrow linewidth and low noise characteristics [29, 30, 121]. In particular, the linewidth of a RE-doped DFB fibre laser is in the scope of a few kHz to the low range of MHz. Therefore, a high resolution (up to ~10 kHz) linewidth measurement technique, such as heterodyne interferometer, delayed self-homodyne interferometer or *delayed self-heterodyne interferometer* (DSHI) [158], is required for measuring the ultra-narrow linewidth of the R-DFB fibre lasers. Each of these methods has advantages and limitations upon the linewidth measurement. Taking into account the available apparatus in lab and the required accuracy of the linewidth measurement, herein the linewidth of the R-DFB fibre lasers are demonstrated by using the DSHI.

3.5.1 Linewidth measurement setup

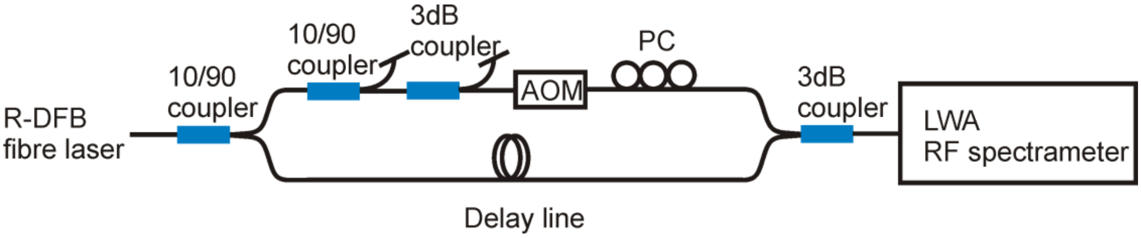

Fig. 3-34 Schematic diagram of the linewidth measurement setup. LWA denotes Lightwave analyser.

Fig. 3-34 shows the experimental setup for measuring the linewidth of R-DFB fibre lasers implementing DSHI, which was first reported in 1980 [158, 159]. The output of the R-DFB fibre laser is divided into two arms. One arm of the laser beam is sent through a ~29.75 km long delay line (single mode fibre, Hi1060) which provides a time delay, τ_d, ~144 μs (given the refractive index of the fibre is 1.45). The other arm is sent through a fibre pigtailed *acousto-optic modulator* (AOM) with a carrier frequency shift of 110 MHz whereby all the optical frequency components are shifted by 110 MHz with respect to the other arm. Before combining the two arms together, (i) a PC is placed on one arm to align the polarization state of the laser beam to that of the other arm and (ii) a 10/90 and 3 dB couplers (optimized for 1117 nm applications) are used as a function of fibre attenuator, so as to optimize the visibility of the interference beat tone.

The linewidth of the laser is usually retrieved from the beat note centred at the AOM frequency (110 MHz) measured with a *radio-frequency* (rf) spectrum analyser. In order to achieve an accurate linewidth measurement of a laser with a Lorentzian lineshape (typically most of the lasers are), the delay line must be much longer than the coherence length of the laser such that the beat signal is effectively as from two mutually incoherent sources. In such a case, the validity is often expressed as:

$$\tau_d \gg \tau_c \tag{3-3}$$

where τ_c is the coherence time, which varies inversely with laser linewidth, Δv. For a laser spectrum with Lorentzian lineshape, the coherence time is often defined as:

$$\tau_c = \frac{1}{\pi \Delta v} \tag{3-4}$$

Thus, when τ_d/τ_c=1, the shape of the beat note is approximately that of the original Lorentzian laser lineshape [158]. At this point, given the τ_d = 144 μs for the delay line of 29.75 km in this experiment, with the aid of Equation (3-4), the frequency resolution of DHSI is calculated to be ~2.5 kHz. But usually there are still small ripples appearing at this boundary condition for the effective incoherence interferometer, a large delay time of at least several times longer than the laser coherence time is suggested for an accurate linewidth measurement. Alternatively, when τ_d/τ_c < 1, the delay is insufficient so that the measurement will be under partial coherence regime leading to the effects of phase between the interfering waves becoming more significant and ripples appearing in the beat spectrum.

The beat note is examined with two independent *electric spectrum analyser*s (ESA): (1) with a HP lightwave analyser, which consists of a high-speed InGaAs photo-detector and rf spectrum analyser, and (2) with the combination of a high-speed InGaAs photodiode (New

Focus 1611) and rf spectrum analysers (Tektronix, RSA3303A 3GHz and Marconi 2382). The beat spectra obtained from the two methods are found to be consistent with each other. Also, the experimental data confirms that the linewidth of the forward R-DFB signal is identical to that of backward counterpart.

3.5.2 Linewidth properties of R-DFB fibre lasers

The DHSI rf-spectra of the R-DFB fibre laser formed in the DFB grating samples of PS980-1 and UHNA4-1 are shown in Fig. 3-35(a) and (b) respectively. They are measured at the output power of ~9 mW. As seen clearly from the figure, the R-DFB fibre lasers generated from two types of fibres exhibit a very similar manner in the linewidth property. In the frequency span of 100 kHz centred at ~110 MHz, the experimental data of DHSI beat notes within ~20 dB full-bandwidth, are well reproduced by Lorentzian lineshapes (dashed red lines) in both these two DFB grating samples, as indicated in Fig. 3-35(a) and (b), respectively. The Lorentzian linewidth strongly suggests that the noise predominantly arises from the intrinsic laser noise, e.g., spontaneous emission, which is frequency independent in nature (white noise). This result is different from that in the RE-doped counterparts, which typically have additional Gaussian components leading to the linewidth broadening [121, 160, 161]. The contribution to the Gaussian components in RE-doped DFB fibre lasers is primarily attributed to thermal effects [161]. Accordingly, it can be again concluded that the thermal effect is negligible in the R-DFB fibre lasers, based on the linewidth distribution.

For the particular spectrum shown in Fig. 3-35(a), the full-bandwidth of the beat signal at 20 dB down from the peak is found to be ~10.5 kHz, which corresponds to a Lorentzian FWHM of the laser linewidth of only ~527 Hz. However, the distinguishable sidelobes (ripples) reveal that the effects of long coherence lengths of the R-DFB fibre lasers are significant [128, 158]. Due to the presence of these, the true linewidth of the R-DFB fibre laser is believed to be substantially less than the resolution of the measurement setup. The Lorentzian lineshape suggests that the linewidth of this laser is sub-kilohertz, which is very difficult to be measured with the DHSI method because otherwise the required fibre delay line would become impractically long. Thus, an improved DSHI, for example, replacing the delay line with a loss-compensated fibre recirculation loop [162], is needed for measuring the precise linewidth of the R-DFB fibre laser. It is hoped that more accurate linewidth data of the R-DFB fibre laser will be presented sometime in the future.

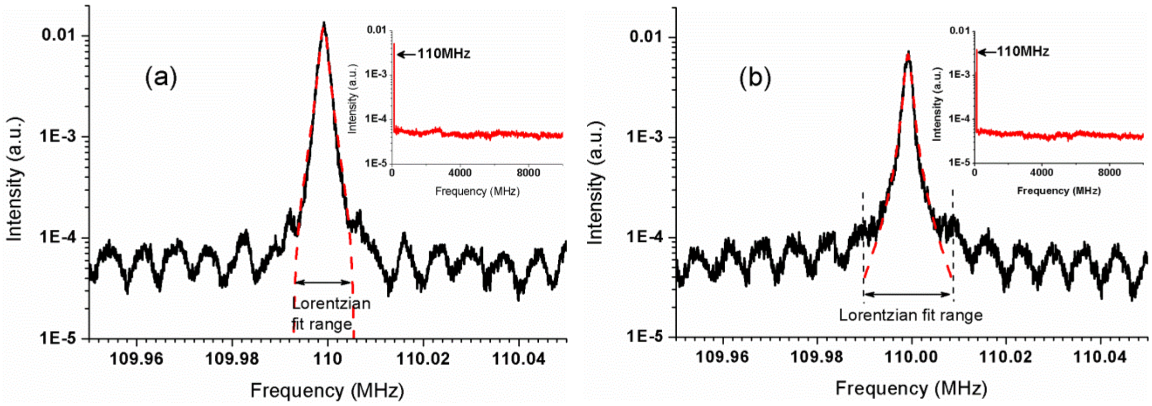

Fig. 3-35 Delayed self-heterodyne rf-spectra in the span of 100 kHz and 10 GHz (insets) of R-DFB fibre lasers with DFB grating samples of PS980-1 (a) and UHNA4-1 (b), respectively.

The DSHI rf-spectra have also been examined in a wider frequency span ranging from 10 MHz to 10 GHz. If any side modes or higher-order longitudinal-modes exist in the R-DFB fibre laser, a beat signal with the main mode at the AOM modulation frequency of 110 MHz should appear. As seen in the insets of Fig. 3-35, no such beat signal is observed down to the noise floor level, and as a result, the R-DFB fibre lasers are indeed with single-frequency operation.

3.6 Four-wave mixing in R-DFB fibre lasers

3.6.1 Introduction

FWM phenomenon has attracted considerable attention in nonlinear optics [65] and has been demonstrated as a promising approach for wavelength conversion, because of (i) the identical features between the converted signal and the original, (ii) the continuous tuning range, (iii) transparent in terms of modulation format, and (iv) simultaneous conversion of multiple signals [163-165]. Wavelength conversion implementing FWM technique has been realized in several nonlinear media, such as semiconductor-based *travelling-wave amplifier* (TWA) [165], *semiconductor optical amplifier* (SOA) [166], DFB lasers [167-169], silicon wire waveguides [170, 171], and optical fibres [172, 173]. Amongst the nonlinear media, optical fibre is uniquely advantageous in the sense that it offers low propagation loss, long interaction length and is naturally compatible to the optical transmission systems with low insertion loss. Therefore, optical fibre based FWM is a key route to achieve broadband wavelength conversion for the applications in optical transmission systems.

The conversion efficiency of FWM strongly depends on the phase-matching condition, described as formula (2-29). In optical fibres, the phase-matching parameter is typically determined by the chromatic dispersion of the fibres [163]. Thus, in general, a long length of a dispersion tailored fibre or *dispersion shifted fibre* (DSF) is adopted as the mixer for the

PDFWM generation and a strong wave with the wavelength at the *zero dispersion wavelength* (ZDW) or *near*-ZDW is injected as the pump wave. Accordingly, -24 dB PDFWM conversion efficiency for a wavelength conversion range of 7.6 nm (wavelength difference between the idler and the probe) was demonstrated in a 10-km-long DSF by pumping at ZDW region of the fibre (~1550 nm) in 1992 [172]. Furthermore, it was found that the wavelength conversion range could be expanded with shorter length optical fibres [163, 173] or rearranging the dispersion profile of the optical fibres [174]. The former results have revealed that the wavelength conversion range was expanded from ~4 nm with 24.5 km long high nonlinear DSF to ~91 nm with 100 m instead. This is because that the FWM conversion bandwidth in optical fibres is mainly limited by (i) group velocity dispersion variation along the fibre length, (2) birefringence of the optical fibre, and (iii) phase-mismatch factor ($\Delta\beta L$), which is relative to the length of the fibre [173]. Thereupon, these effects could be minimised with a shorter length of optical fibre, in which, the SBS threshold is also increased. By using high nonlinear PCFs, the 3 dB bandwidth of the wavelength conversion with ~-16 dB PDFWM conversion efficiency has been reported to be ~100 nm in a 20 m long silica-based PCF [175] and a bandwidth of ~ 60 nm with ~0 dB PDFWM conversion efficiency has been even demonstrated in a 2.2 m long lead silicate PCF [51]. In addition to the PDFWM discussed above, non-degenerated FWM or Bragg scattering FWM has been realized in optical fibres as well [176]. In that particular scheme, two pump waves are launched into the optical fibre simultaneously, and ~180 nm wavelength conversion range has been achieved by tuning the signal wavelength to satisfy the phase-matching condition between the interaction waves [176]. Overall, the FWM conversion efficiency as well as the conversion range intensely depends on the dispersion profile of the optical fibre and the applied pump wavelength.

A more compact and flexible method to realize wide range FWM in optical fibres is highly desirable. Ultra-wide bandwidth wavelength conversion by using FWM in the 30 cm-long R-DFB fibre lasers has been studied both numerically and experimentally in this work. As far as this research’s current knowledge, this is the first time of reporting the FWM in a DFB fibre laser, even though the context has been demonstrated in semiconductor DFB lasers for about two decades [168, 177].

3.6.2 Experimental setup

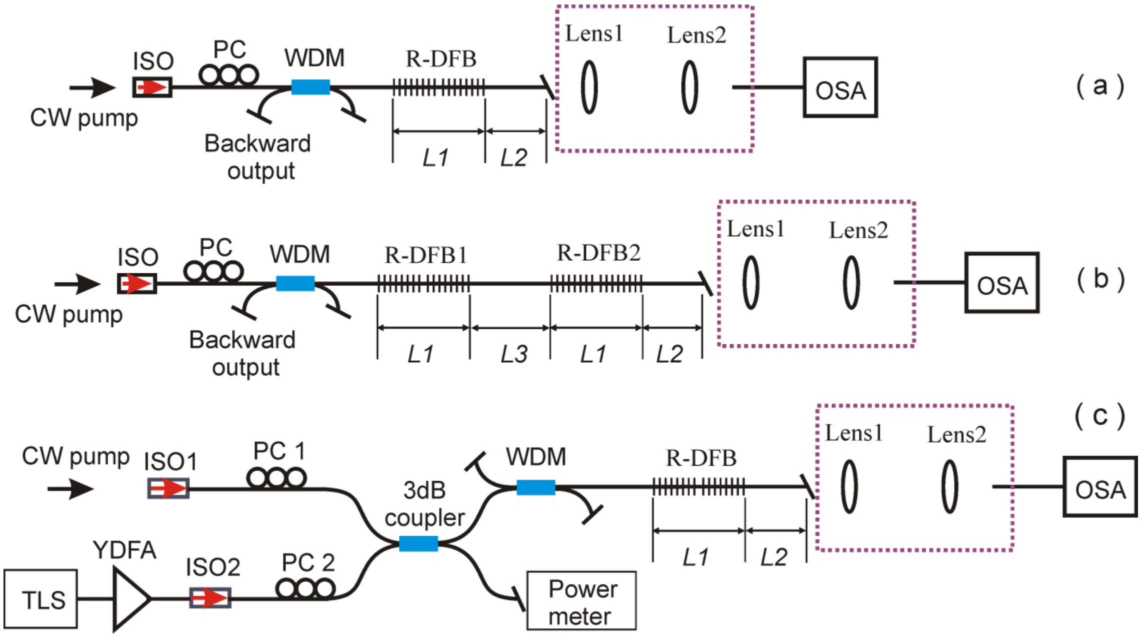

Fig. 3-36 Schematic diagram of the experimental setup for FWM generation in (a) a single R-DFB device, (b) cascaded R-DFB devices and (c) with a tunable laser source (TLS).

Fig. 3-36 illustrates the schematic diagram of the experimental setup for FWM generation in (a) a single R-DFB fibre laser, (b) two cascaded R-DFB fibre lasers and (c) with a tunable laser source as the probe wave, respectively. The pump source used to generate the R-DFB signal is a CW, linearly polarised, Yb-doped PM fibre MOPA at ~1064 nm. The output of the pump source is spliced to a high power isolator whilst a PC was used to adjust the polarization state of the pump source. A WDM designed at 1064 nm/1117 nm was used to monitor the backward output signal from the system. The WDM is directly connected to the R-DFB grating via fusion splicing technique. And the forward output from the R-DFB grating is directly coupled into OSA via a wavelength-independent free-space attenuator, which is established by a pair of lenses. All fibre end-facets are angle-cleaved to prevent end-feedback whilst all R-DFB gratings and WDMs are mounted on heat sinks to precisely control the temperature and effectively remove any generated heat. In Fig. 3-36(b), the two R-DFB devices are spliced together and the gap between them (*L3*) is ~55 cm. In Fig. 3-36(c), a linearly polarised *tunable laser source* (TLS) centred at ~1060 nm (DL pro, Toptica Photonics) is used as a probe signal, which is amplified by a PM Yb-doped fibre amplifier (YDFA). The CW pump wave and the TLS signal are coupled into the R-DFB grating sample via a 3 dB coupler (designed for 1064 nm). A WDM is inserted between the R-DFB grating and the 3 dB coupler in order to filter out the backward R-DFB signal. Note that, inasmuch as all the passive components used in this work are non-PM, all the components are mounted statically on the optical bench to reduce the influence of the environmental vibrations.

The R-DFB gratings are 30 cm (*L1*) long with centre π phase-shift and the transmission spectra are shown in Fig. 3-22. Hereafter, the experimental data of FWM generation in the R-DFB grating samples of PS980-1 (referred to as R-DFB1) and UHNA4-1 (referred to as R-DFB2) is discussed in detail. The pigtail between the R-DFB samples and the OSA is PS980 with a length of *L2*, which is 1.8 m or 11.8 m.

3.6.3 Experimental results

Fig. 3-37 shows the calculated GVD profiles of the fibres of PS980 and UHNA4. It is worth noting that these GVD traces exclude the effects of the DFB grating structure. However, the fact is that the dispersion at the DFB signal wavelength has been highly tailored by the DFB grating structure [178]. As seen from Fig. 3-37(a), the ZDW of PS980 is around 1.49 μm while it is around 2.56 μm in UHNA4 fibre, which is indicated by the dashed red lines in the figure. In this work, the pump wave for R-DFB generation is, λ_i = ~1064.5 nm, and the designed R-DFB signal wavelength in R-DFB1 (formed in PS980-1) is λ_{j1} = ~1117.8 nm, whilst it is λ_{j2} = ~1109.7 nm in R-DFB2 (formed in UHNA4-1), respectively. The conjugate wave, observed in the single R-DFB sample, is λ_{k1} = ~1176.6 nm in R-DFB1 and λ_{k2} = ~1158.7 nm in R-DFB2, respectively. These interaction waves have been highlighted by the vertical dashed lines in Fig. 3-37(b). Obviously, all these wavelengths are in the normal dispersion range of the employed fibres.

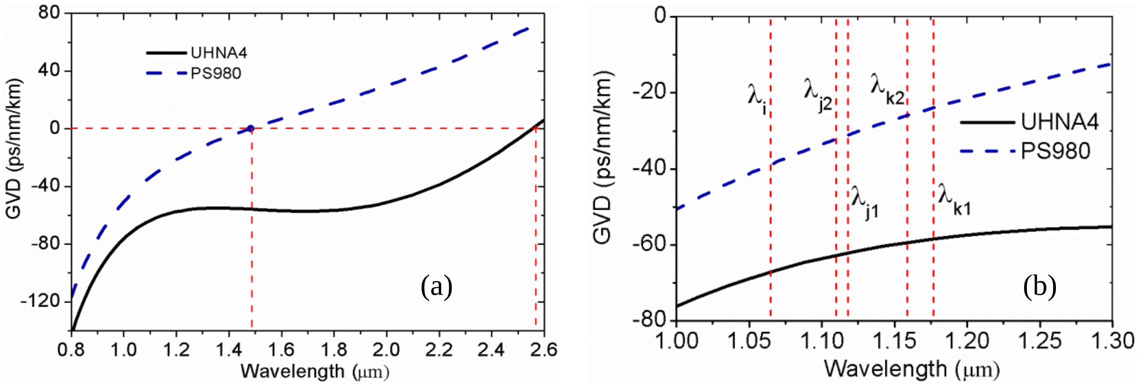

Fig. 3-37 Calculated GVD profiles of PS980 and UHNA4 in the wavelength range of 0.8-2.6 μm (a) and 1.0-1.3 μm (b), respectively. The vertical dashed lines indicated in (b) are the waves of probe, pump and conjugate. (These data were generated by my supervisor, Dr. Morten Ibsen)

3.6.3.1 FWM in single R-DFB device

The typical FWM output spectra from single R-DFB grating samples of R-DFB1 and R-DFB2 are plotted in Fig. 3-38, which includes the forward output spectra from R-DFB1 with L2 = 1.8 m (trace 1) and L2 = 11.8 m (trace 2), respectively, and forward output (trace 3) and backward output (trace 4) spectra from R-DFB2 with L2 = 1.8 m. The incident pump power (@1064.5nm) for this set of outputs is ~4.1 W. Note that the incident pump power has been corrected with the insertion loss between the CW pump and the R-DFB device.

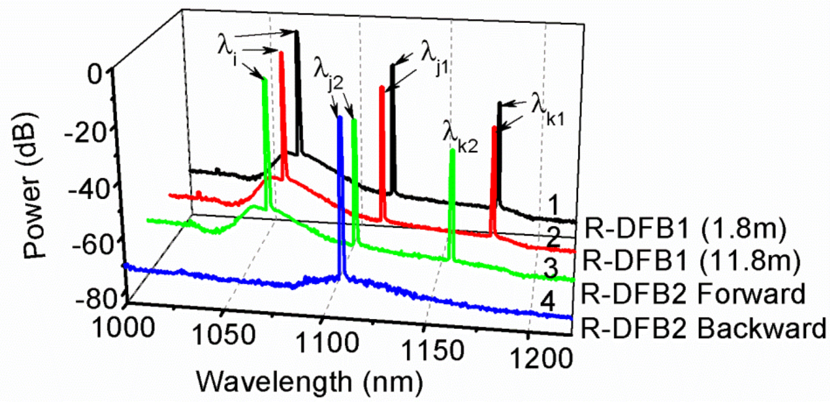

Fig. 3-38 Output spectra from R-DFB1 and R-DFB2 with RBW of 1 nm, respectively.

The forward output spectra (as traces 1, 2 and 3) in Fig. 3-38 evidently demonstrate the PDFWM-based wavelength conversion from R-DFB samples. On the contrary, only the R-DFB signal is detected from the backward output (as trace 4). This indicates that the FWM originates from the interaction between the pump wave and the co-propagated R-DFB signal. The conjugate waves with >40 dB above the noise floor, as expected, appear at ~1176.6 nm (λ_{k1}) from R-DFB1 and ~1158.7 nm (λ_{k2}) from R-DFB2, respectively. Here, the conjugate waves are indeed generated from FWM process rather than the Raman Stokes, because:

(1) The waves satisfy the PDFWM frequency relationship, simplified from Equation (2-29) as:

$$\frac{c}{\lambda_{kn}} = 2\frac{c}{\lambda_{jn}} - \frac{c}{\lambda_i} \quad (n = 1,2) \tag{3-5}$$

where c is the light speed in vacuum. This indicates that in the PDFWM process in the R-DFB cavity, the CW pump (~1064.5 nm) and R-DFB signal act as the probe signal and pump for PDFWM, respectively;

(2) The frequency shifts between the conjugate waves and the R-DFB signals are ~13.4 THz in R-DFB1 and ~11.4 THz in R-DFB2, respectively. This frequency shift is either larger or smaller than that of the Stokes shift from Raman scattering effect, which is normally ~13.2 THz in standard silica fibres.

What is more, the FWM output spectra have been verified with two different lengths of *L2*, with values of 1.8 m and 11.8 m, both for R-DFB1 and R-DFB2, and the experimental data confirms that the output spectra are identical with these two lengths, for example as the traces 1 and 2 in Fig. 3-38 from R-DFB1. Therefore, it can be concluded that the FWM is generated entirely inside the R-DFB fibre laser cavity (with the length of *L1* = 30 cm) but not in or partially in the pigtail L2 as shown in Fig. 3-36. Compared to the conventional FWM in optical fibres, such FWM in R-DFB fibre laser is: (i) ultra-compact, inasmuch as it is only 30 cm-long standard silica based optical fibre, which minimises the effects of non-uniformity and birefringence of the fibre resulting in broadband wavelength conversion range; (ii) the pump wave for FWM process is generated inside the R-DFB cavity, and consequently the coupling loss of the pump wave is nil so that the conversion efficiency can be maximised; and (iii) the pump wavelength is flexible to the ZDW of the optical fibre relieving the wavelength-bond in conventional FWM in optical fibres, in which the pump wavelength should be in the ZDW region of the fibres [163, 172, 179].

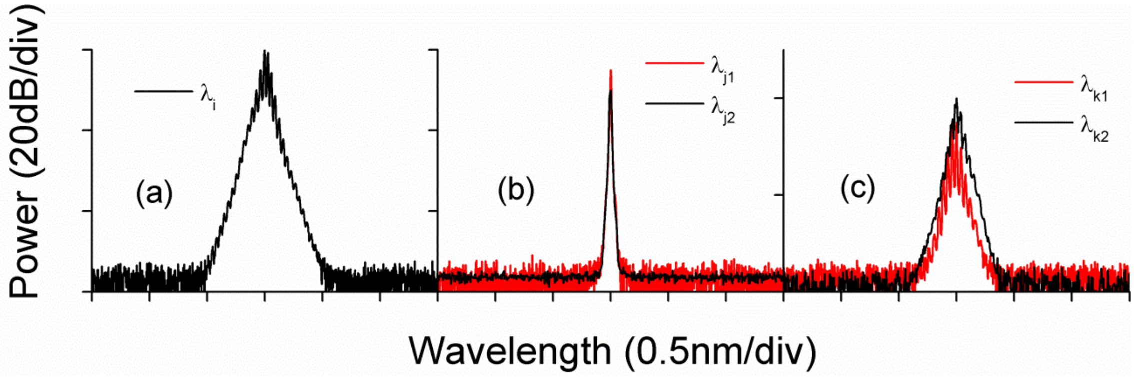

Fig. 3-39 Normalized OSA spectra of the probe (a), R-DFB signals (b) and conjugate waves (c) with a RBW of 0.01nm.

The spectra of the probe wave (~1064.5 nm), the pump wave for FWM, which is the R-DFB signal and the conjugate waves have been examined with a high resolution of 0.01 nm implementing the OSA of Advantest Q8384 and have been shown in Fig. 3-39. By comparing the conjugate waves (displayed in Fig. 3-39 (c)) to their probe waves (displayed in Fig. 3-39 (a)), it is evident that the conjugate waves perform the same lineshapes as that of the probe waves. This is understandable since the FWM process preserves the phase and amplitude of the wavelength-converted probe signal. Hence, this behaviour further confirms that in the FWM process in the R-DFB cavity, the CW pump (~1064.5 nm) and R-DFB signal indeed act as the probe signal and the pump respectively in the FWM process. The conversion wavelength range between the conjugate wave and the probe signal, is ~112 nm (corresponding to a frequency shift of ~26.8 THz) in R-DFB1 and ~94.2 nm (corresponding to a frequency shift of ~22.8 THz) in R-DFB2, respectively.

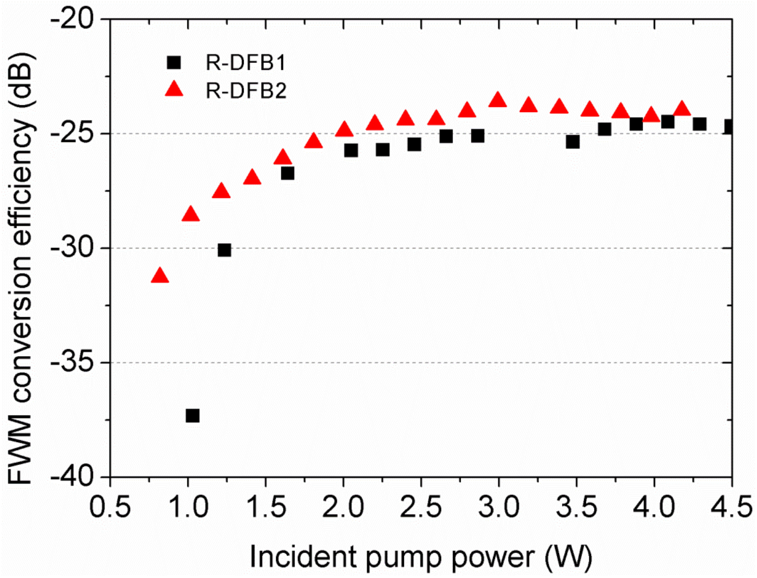

Fig. 3-40 FWM conversion efficiency vs incident pump (@~1064.5 nm) power.

The FWM-to-signal conversion efficiencies of the conjugate waves (@ λ_{k1} and λ_{k2}) to the probe wave (λ_i) with respect to the incident CW pump power (at ~1064.5 nm) in R-DFB1 and R-DFB2, are shown in Fig. 3-40 respectively. Note that the FWM conversion efficiency is measured as the FWM power ratio between the conjugate wave and its probe signal at the output of the R-DFB sample from the OSA traces with RBW of 1 nm. It is very interesting to see that the FWM occurs almost immediately as the R-DFB fibre laser has been generated [40]. The conversion efficiency grows as the increase of the CW pump power, in which case, the R-DFB signal increases as well. However, when the incident pump power exceeds ~2 W, the conversion efficiencies roll off at around -25.1 dB and -24.2 dB for R-DFB1 and R-DFB2 respectively. It is worth noting that a comparable high conversion efficiency has been reported when FWM occurs in a 10 km-long single-mode fibre by pumping at the ZDW of the fibre but the wavelength conversion range is only 7.6 nm [172]. Indeed, this sort of short R-DFB cavity is a remarkable FWM generator with broad wavelength conversion range and high conversion efficiency.

3.6.3.2 FWM in cascaded R-DFB devices

One of the attractive properties of FWM is that it is capable of converting multiple signals simultaneously. Here, the experiment of cascading the R-DFB1 and R-DFB2 together has been conducted so as to verify the wavelength conversion behaviour with multi-probe waves in the R-DFB cavity.

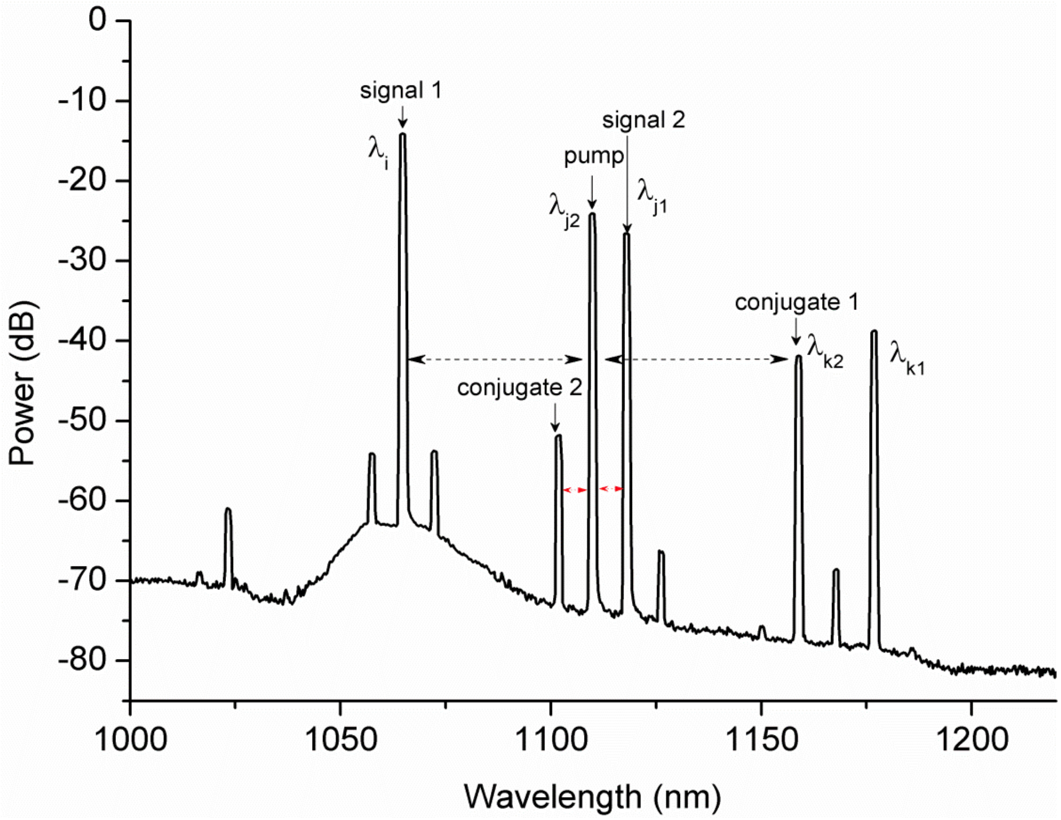

Fig. 3-41 FWM output spectrum from cascaded R-DFB samples.

The sequence for the cascaded R-DFB samples is shown in Fig. 3-36(b), in which, the generated R-DFB1 signal acts as the other probe signal for the FWM process in R-DFB2 cavity. Fig. 3-41 depicts the output spectrum at the incident pump power of ~3.87 W. As seen in Fig. 3-41, a number of conjugate waves are generated from non-degenerated and/or PDFWM processes in R-DFB2 cavity simultaneously. Two pairs of PDFWM processes have been identified and highlighted in the output spectral trace in Fig. 3-41, based on the conditions of (i) each pair satisfies the frequency relationship of Equation (3-5) and (ii) each pair has nearly identical optical spectra between the conjugate wave and probe wave. One is conjugate 1 from signal 1 indicated in Fig. 3-41, which is the same as the FWM process in the single R-DFB2 cavity. Another one is conjugate 2 from signal 2, which is generated by using the R-DFB1 signal as the probe and mixed with the R-DFB2 signal, as indicated in Fig. 3-41. The FWM conversion efficiency or FWM power ratio, measured from the OSA trace is about -27.77 dB and -25.22 dB for conjugate 1 and 2, respectively. However, the exact reasons for such a discrepancy are not clear at this stage. It could be related to the chromatic dispersion profile of the R-DFB device.

3.6.3.3 FWM with TLS in R-DFB devices

In addition, the conjugate wave from FWM can be continuously tuned, which could be achieved by tuning the pump wave or probe wave. In this particular design, the pump wavelength for the FWM is determined by the Bragg grating wavelength and in principle, it can be continuously tuned by thermal heating or stress [122, 124]. On the other hand, a TLS could be applied as the probe source for FWM generation. Because the TLS around 1.12 µm not being available at the time when the work was carried out, a TLS at ~1.06 µm was used as the probe source and coupled into the R-DFB device, as seen in Fig. 3-36(c).

It is well-known that the range of wavelength conversion that can be realized in a FWM process is restricted by the phase-mismatch factor between the waves. In the PDFWM process and given that the wavenumber at probe, pump and conjugate wavelengths is $k_{3,}$ k_1 and $k_{4,}$ respectively, the phase-mismatch factor, δk, can be approximated as:

$$\delta k = k_3 + k_4 - 2k_1 \approx \beta_{2(f=pump)}\Delta\omega^2 + \frac{1}{12}\beta_{4(f=pump)}\Delta\omega^4 + \frac{2}{6!}\beta_{6(f=pump)}\Delta\omega^6 \dots \quad (3\text{-}6)$$

in which $\beta_i, (i = 2,4,6,\cdots)$ is the i^{th} order derivative of the propagation constant β with respect to angular frequency. $\Delta\omega = \omega_{signal} - \omega_{pump}$ is the angular frequency separation between the probe signal and pump wave. From Equation (3-6), it is evident that the phase-mismatch factor becomes larger as the probe wavelength tunes away from the pump wave. Consequently, in general, the FWM conversion efficiency decreases as the increase of the phase-mismatch factor providing a constant length of FWM mixer.

By tuning the TLS from ~1040 nm to ~1080 nm and maintaining the FWM conversion efficiency above -37 dB, the wavelength conversion range, which is the wavelength separation from the conjugate wave to its original wave (the probe), is obtained around 167 nm from R-DFB1 and around 113 nm from R-DFB2 respectively. In other words, the frequency detuning range, which is the frequency separation between the pump frequency and the probe frequency, is achieved to be ~19.9 THz from R-DFB1 and ~13.8 THz from R-DFB2 respectively. This is so far the broadest FWM-based wavelength conversion that has been completed in sub-metre length of a standard optical fibre.

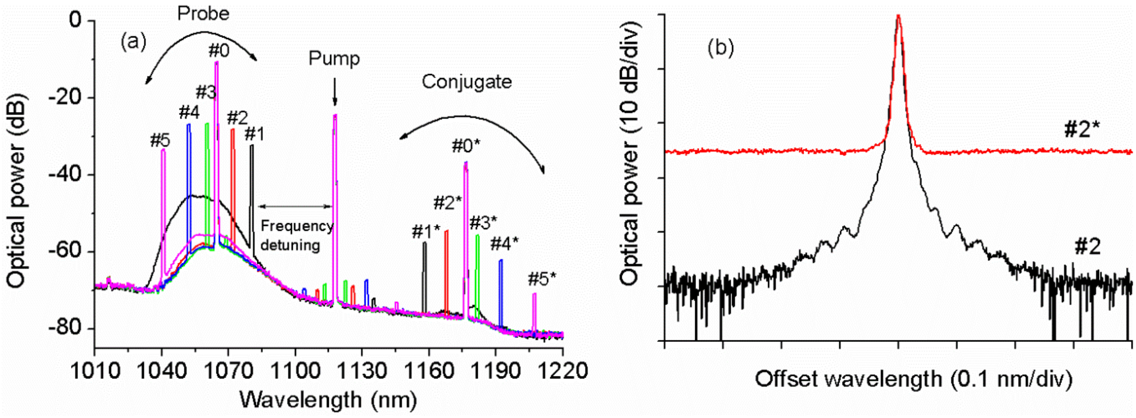

Fig. 3-42 FWM output spectra with a TLS with RBW of 1 nm (a) and normalized overlapping spectra of the probe #2 and conjugate wave #2* with RBW of 0.01 nm (b), from R-DFB1 cavity.

Fig. 3-42 (a) shows the typical FWM output spectra with TLS from R-DFB1 device with a RBW of 1 nm. As discussed in the above content, in the FWM process, the pump wave is the R-DFB signal, which is indicated in the figure, and the conjugate wave #0* is converted from its original wave of #0, which is the original ~1064 nm pump wave for R-DFB signal generation. When the TLS is continuously tuned from ~1080.4 nm to ~1040.8 nm, the corresponding idles from ~1158 nm to ~1207.3 nm appears clearly above the noise floor. For example, as seen in Fig. 3-42(a), the conjugate wave of #i* (i = 1,2,3,4,5) is individually converted from its original probe wave of #i. In terms of the specific spectra of the probe and conjugate waves, they have been measured with a high resolution of 0.01 nm and it has been found that the conjugate wave matches very well with its original wave within the 25 dB bandwidth. Note that the SNR of the conjugate wave is limited by the noise floor in the measurement. As an example, Fig. 3-42(b) illustrates the normalized overlapping spectra of the probe #2 for a frequency detuning of ~11.3 THz and its conjugate wave #2* with a high RBW of 0.01 nm. Note also that the noise floor of the traces of #2 and #2* is limited by the sensitivity of the OSA.

The wavelength tunable range of the TLS applied in this measurement is restricted by the output power of the PM YDFA, as seen in Fig. 3-36(c). The incident power of the probe wave (from TLS) into the R-DFB device is in the range of 10 to 70 mW over the wavelength range of 1060 ± 20 nm. Fig. 3-43 depicts the incident powers of the probe waves measured by a power meter and OSA traces from the FWM output spectra as seen in Fig. 3-42(a), respectively. The uncertainty of the power is due to the variation of the diode pump for the YDFA and the thermal detector of the power meter. Within the experimental uncertainty, the power measured from the OSA traces matches well with that measured by the power meter.

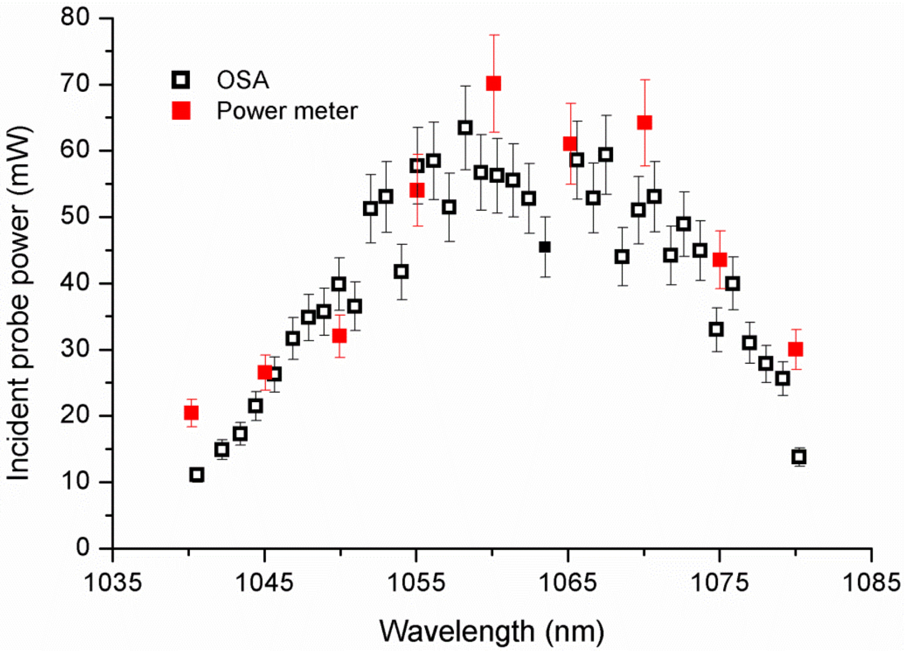

Fig. 3-43 Comparison of the incident powers of the probe waves measured via OSA traces and a power meter.

In addition, the incident pump power of ~1064 nm is maintained constantly at 2 W ± 5% during all the measurements of tuning the TLS from ~1080 nm to ~1040 nm with a step of ~1 nm. This pump power is selected due to the limitation of the maximum power provided by the pump source, and also, at this pump power level, the FWM conversion efficiency can be obtained at a relatively high level, as seen in Fig. 3-40.

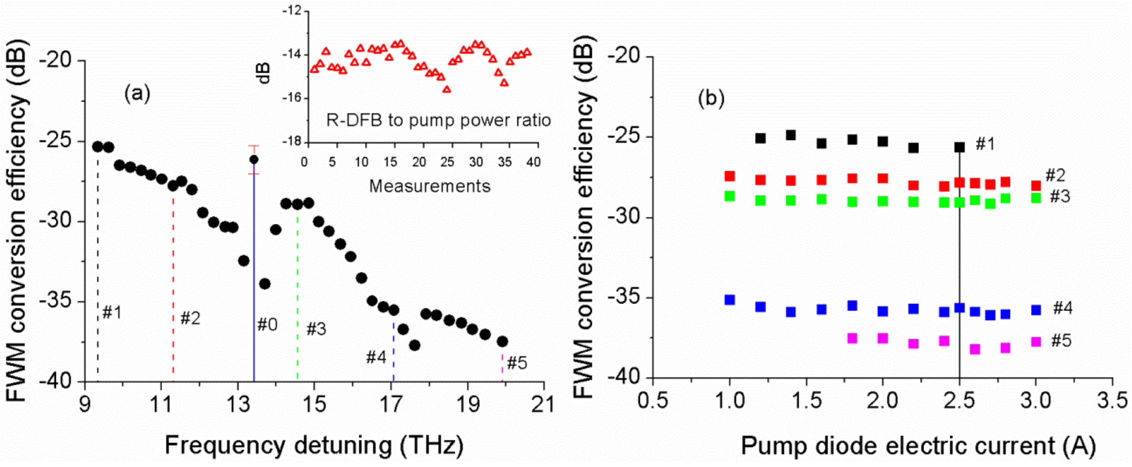

Fig. 3-44 (a) FWM conversion efficiency vs frequency detuning and the inset is the R-DFB to pump power ratio during the measurement. (b) FWM conversion efficiency vs pump diode electric current of YDFA.

Fig. 3-44(a) shows the FWM conversion efficiency with respect to the frequency detuning, which is the frequency separation between the probe wave and R-DFB signal. The vertical lines indicated in the figure are FWM conversion efficiency measured at the probe waves of #i (i = 0,1,2,3,4,5), as shown in Fig. 3-42(a). Moreover, the inset figure in Fig. 3-44(a), shows the conversion efficiency of R-DFB signal to its CW pump wave of ~1064 nm in each measurement, measured by the OSA traces as seen in Fig. 3-42(a). Note that the experiment is conducted by increasing frequency detuning from ~9.3 THz to ~19.9 THz, indicating an increased sequence number for the measurement plotted in the inset of Fig. 3-42(a). As seen in Fig. 3-44(a), the FWM conversion efficiency decreases from ~ -25 dB to ~ -37.5 dB while increasing the frequency detuning from ~9.3 THz to ~19.9 THz. It is unsurprising since the phase-mismatch factor increases while increasing the frequency detuning, as shown in Equation (3-6). Moreover, it is found that the overall profile of FWM conversion efficiency against the frequency detuning is similar to that of the R-DFB signal conversion efficiency with respect to the pump power (~1064 nm), as seen from Fig. 3-42(a) and its inset, respectively. However, it can be noted that there are two dips occurring at the probe waves near #0 and #4 as seen in Fig. 3-44(a). This might be due to the reduction of the R-DFB signal, indicated in the inset of Fig. 3-44(a). The reasons for such reduction could be attributed to the power variation of the pump diode for the MOPA source, the environmental fluctuations and the slight drifting of the polarization state, which could be eliminated by applying all-PM fibre components.

On the other hand, it is revealed that the FWM conversion efficiency remains constant while varying the probe wave powers. Fig. 3-44(b) illustrates the FWM conversion efficiency against the pump diode electric current of YDFA at selected probe waves of #i (i = 1,2,3,4,5), which have been indicated in Fig. 3-42(a) and Fig. 3-44(a), respectively. The incident probe wave power increases with the pump diode electric current of YDFA for a constant input power of the probe wave. It can be seen clearly that the FWM conversion efficiency remains constantly within ± 0.7 dB fluctuation. Note that the vertical line indicated in Fig. 3-44(b) is the YDFA pump diode electric current (2.5 A) applied to all the probe waves during the measurement in Fig. 3-43 and Fig. 3-44(a). Therefore, the reduction of the conversion efficiency in Fig. 3-44(a) is predominantly due to the frequency detuning and the variation of the R-DFB signal, but not because of the power variation of the probe waves.

The FWM property of integrating the TLS with the R-DFB2 device is characterized as similar to that of the R-DFB1 device discussed above. The incident pump power at ~1064 nm is retained at 1.7 W ± 5% during the measurement. The slightly lower incident pump power is due to the slightly higher connection loss between the pigtail fibre of the WDM and the UHNA4, which is due to the mismatch of the MFDs of these two fibres.

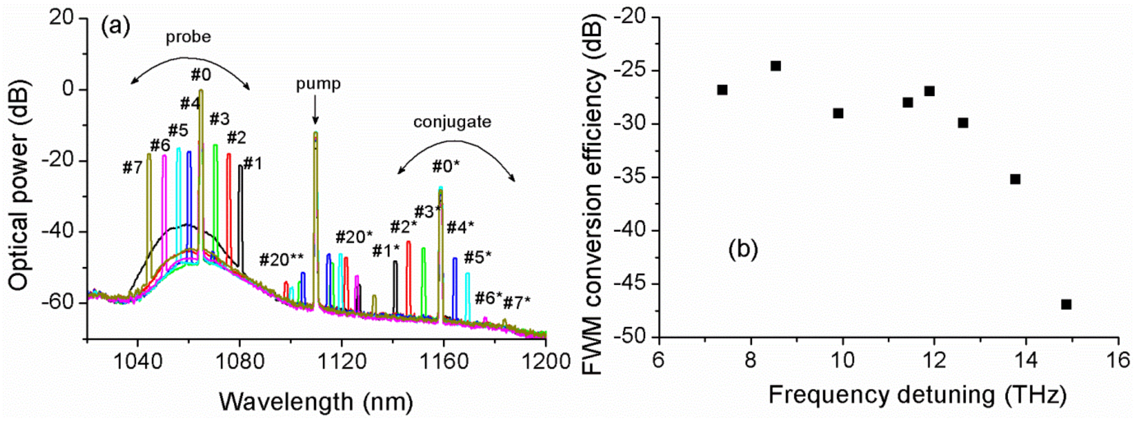

Fig. 3-45 Typical FWM output spectra with a RBW of 1 nm (a) and FWM conversion efficiency vs frequency detuning (b) from R-DFB2 cavity, respectively.

Fig. 3-45(a) describes the FWM output spectra with the TLS from R-DFB2 device with the RBW of 1 nm. Very similar to the FWM from R-DFB1 device, the conjugate waves at #i* (i = 0,1, ···,7) are converted from their original waves at #i. Fig. 3-45(b) shows the FWM conversion efficiency with respect to the frequency detuning. The FWM conversion efficiency is the power ratio of the conjugate wave, #i* (i=0,1, ···,7) to its original wave, #i, which is continuously tuned from ~1080.1 nm to ~1044.4 nm. It behaves in the same manner as that of the R-DFB1 device. Also, it can be seen that the FWM conversion efficiency is decreased to ~ -47 dB when the frequency detuning is increased to ~14.9 THz. Hence, the wavelength conversion bandwidth of R-DFB1 is much wider than that of R-DFB2. Such a difference is due to the varied dispersion profiles of PS980 and UHNA4 fibres as well as the slightly varied coupling coefficients of the DFB grating samples of PS980-1 and UHNA4-1.

Additionally, in the case of R-DFB2, there are extra idles appearing besides the R-DFB signal, as seen in Fig. 3-45(a), which are not obvious in the FWM process from the R-DFB1 device, shown in Fig. 3-42(a). This is due to the non-degenerated FWM process between the interaction of the probe wave, the pump wave at ~1064 nm and the R-DFB signal. For example, idles of #20* and #20** (as shown with the same colour) are the FWM generation from the interaction of the waves of #2, #0 and the pump (R-DFB signal), indicated in Fig. 3-45(a). This feature could be identified by examining the phase-matching conditions and the optical spectrum of each wave with a high resolution.

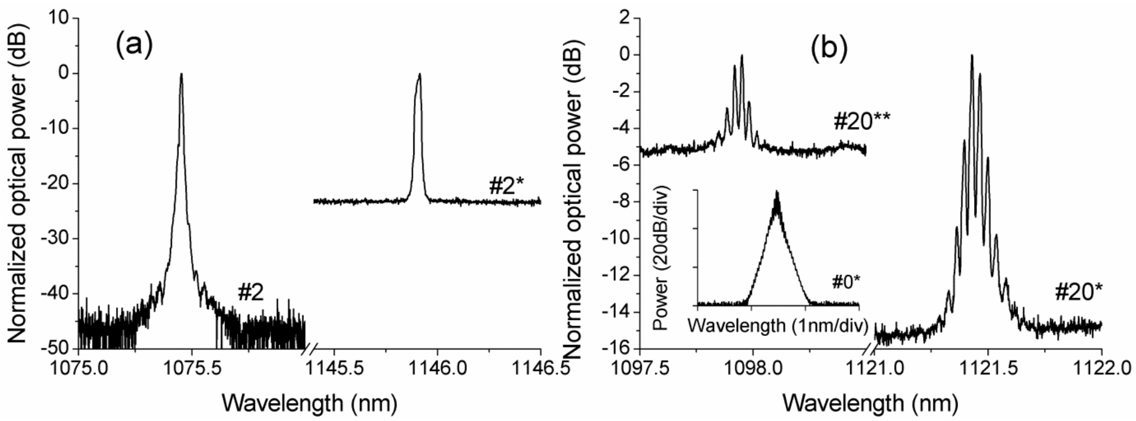

Fig. 3-46 High resolution spectra of probe #2 and conjugate wave #2* (a) and conjugate waves of #0*, #20* and #20 (b), respectively.**

Fig. 3-46 illustrates the spectra of probe wave at #2 and idlers at #2*, #0*, #20* and #20** with a high resolution of 0.01 nm. As seen in Fig. 3-46(a), the spectrum of #2* is almost identical as that of #2 within 20 dB bandwidth. This indicates that the conjugate wave at #2* is converted from the probe wave at #2 via the PDFWM process, which has the characteristic of preserving the optical features of the conjugate wave from its original probe wave. Moreover, as mentioned above, the conjugate wave of #0* is converted from the probe wave of #0, which has multi-longitudinal modes. As seen in Fig. 3-46(b), the idlers at #20* and #20** also have multi-longitudinal modes. Obviously, the idlers beside the R-DFB signal, such as #20* and #20**, are generated between the interaction of the waves of #0 (@1064 nm), probe wave of #2 and the R-DFB signal via the non-degenerated and/or PDFWM process.

3.6.4 *Model setup*

The experimental data, presented above, have demonstrated that the wavelength conversion by using FWM in the R-DFB fibre laser is with the high conversion efficiency up to -25 dB from 30 cm long DFB grating in standard optical fibre, and also the wavelength conversion bandwidth is ultra-wide, around 167 nm in the PS980 R-DFB fibre laser. In order to understand the fundamental mechanism for the FWM process within the R-DFB fibre laser, a theoretical model has been built up and solved numerically.

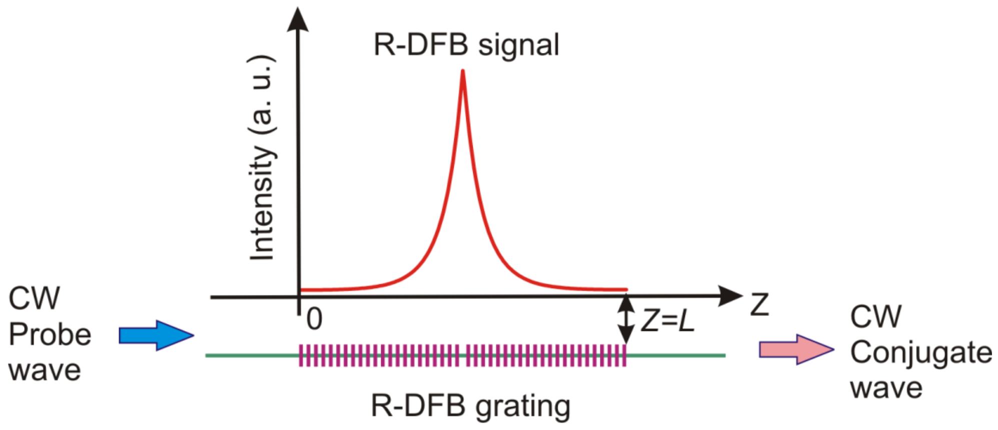

Fig. 3-47 Schematic diagram of the model setup for FWM in the R-DFB fibre laser.

The schematic diagram of the model setup for simulating the FWM process in the R-DFB fibre laser is shown in Fig. 3-47. In the model, the design of the R-DFB grating is based on the experimental data, which has a discrete π phase-shift at the centre of the grating with a length of *L*. A CW probe wave is launched into the R-DFB grating from the left side of the grating, at which z = 0, as seen in Fig. 3-47, the corresponding conjugate wave is emitted from the right side of the R-DFB grating at which z = *L*. Alternatively, the R-DFB signal possesses a nonlinear intensity distribution profile in the R-DFB cavity, which matches the profile obtained from the simulation of R-DFB fibre laser as discussed in Section 3.3.

The amplitude of the forward, $A_{1f}(z)$, and backward, $A_{1b}(z)$, R-DFB signals for a centre π phase-shifted DFB grating, can be expressed as the formulas of (3-7a) and (3-7b) [180], respectively, where κ is the coupling coefficient of the DFB grating. It is found that the amplitude of the R-DFB signal (both forward and backward) has the maximum field at the π phase-shift position at z = *L/2*, as depicted in Fig. 3-47. For simplification, several approximations are adopted for the simulation:

(1) Single-mode fibre is utilized and all the overlap integrals of the waves are assumed to be identical to $1/A_{eff}$, where A_{eff} is the effective mode area [65].

(2) The amplitude of the pump wave, which is the R-DFB signal, is assumed to be much stronger than the probe and conjugate wave within the effective cavity region of the R-DFB cavity centred at the π phase-shift position.

(3) The pump wave as well as the probe wave is assumed to be undepleted during the FWM parametric interaction. This is valid since the FWM conversion efficiency is below -20 dB from the experimental demonstration.

(4) The Raman scattering nonlinear effect is ignored during the FWM process.

(5) The propagation losses for the involved waves are assumed to be identical.

$$A_{1f}(z) = \begin{Bmatrix} A_{1f}(z=L)\cdot\sinh(\kappa z) & z<\frac{L}{2} \\ A_{1f}(z=L)\cdot\cosh[\kappa(L-z)] & z>\frac{L}{2} \\ A_{1f}(z=L)\cdot\frac{[\sinh(\kappa L/2)+\cosh(\kappa L/2)]}{2} & z=\frac{L}{2} \end{Bmatrix} \tag{3-7a}$$

$$A_{1b}(z) = \begin{Bmatrix} A_{1b}(z=0)\cdot\cosh(\kappa z) & z<\frac{L}{2} \\ A_{1b}(z=0)\cdot\sinh[\kappa(L-z)] & z>\frac{L}{2} \\ A_{1b}(z=0)\cdot\frac{[\sinh(\kappa L/2)+\cosh(\kappa L/2)]}{2} & z=\frac{L}{2} \end{Bmatrix} \tag{3-7b}$$

$$\frac{dA_3}{dz} = i\gamma_3\left[(|A_3|^2+2\left|A_{1f}\right|^2+2|A_{1b}|^2+2|A_4|^2)A_3+A_{1f}{}^2A_4{}^*e^{-i(\delta k)z}\right] -\frac{1}{2}\alpha_3A_3 \tag{3-8a}$$

$$\frac{dA_4}{dz} = i\gamma_4\left[(|A_4|^2+2\left|A_{1f}\right|^2+2|A_{1b}|^2+2|A_3|^2)A_4+A_{1f}{}^2A_3{}^*e^{-i(\delta k)z}\right] -\frac{1}{2}\alpha_4A_4 \tag{3-8b}$$

As a result, the coupled amplitude equations for the PDFWM in the R-DFB fibre laser is obtained, as described by the Equations (3-8 (a-b)), in which A_3, A_4 are the amplitude of probe wave and conjugate wave, respectively, and $A_j \equiv \sqrt{P_j/A_{eff}}, (j = 1f, 1b, 3{,}4)$. The first four terms on the right side of the Equation (3-8) describe the refractive index nonlinearities of SPM and XPM, in which $\gamma_i = 2\pi n_2/\lambda_i, (i = 3{,}4)$ is the nonlinear coefficient at the wavelength of probe (λ_3) or conjugate wave (λ_4). The last set of terms in the Equation (3-8) represent the linear background losses of the probe wave (α_3) and conjugate wave (α_4) in the R-DFB cavity. The remaining set of terms in the Equation (3-8) represents the parametric FWM interaction, in which δk is the phase mismatch parameter, defined as Equation (3-6).

$$\begin{gathered} A_{1f}(z=L) = A_{1b}(z=0) = \sqrt{P_{1f}(z=L)/A_{eff}} \\ A_3(z=0) = \sqrt{P_3(z=0)/A_{eff}} \\ A_4(z=0) = 0 \end{gathered} \tag{3-9}$$

The group Equations (3-7) and (3-8) are *ordinary differential equations* (ODEs) and therefore ODE45[1] (a MATLAB function) is implemented to solve these equations. The boundary conditions are shown as the Equation (3-9), in which $P_{1f}(z = L)$ is the output power of the R-DFB signal and $P_3(z = 0)$ is the incident power of the probe wave, respectively.

3.6.5 Simulation results

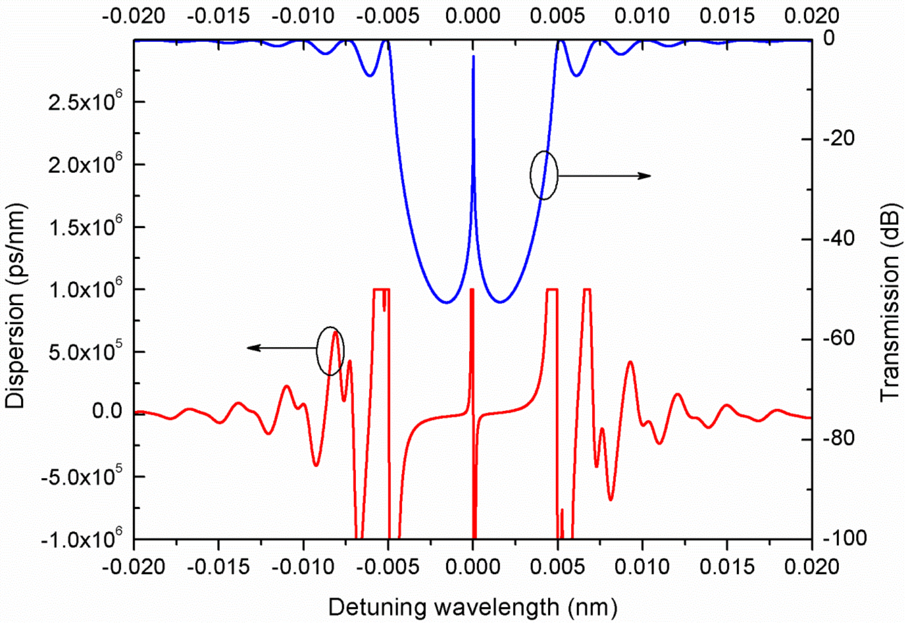

Fig. 3-48 Calculated transmission spectrum and dispersion profile of the 30 cm long centre π phase-shifted DFB grating. (These data were generated by my supervisor Dr. Morten Ibsen)

It has been pointed out that the GVD near the stop-band edge and the Bragg grating wavelength is strongly affected by the DFB grating structure. Fig. 3-48 shows the calculated transmission spectrum of the 30 cm-long centre π phase-shifted DFB grating (right axis) and also the estimated grating dispersion of the transmission wave (left axis). As clearly seen the GVD reaches very high values within the pass-band of the grating around the R-DFB wavelength, whilst the grating dispersion is negligible for the waves far outside the stop-band. Thus, in this specific configuration of the FWM process, the phase mismatch factor, δk, is the outcome of the combination of the fibre dispersion and the DFB grating dispersion since the pump wave for FWM parametric interaction is the R-DFB signal. Moreover, the pass-band of the R-DFB grating is extremely narrow, in the order of kHz, as seen in Fig. 3-48, so it is difficult to quantify the dispersion ($\beta_{2(f=pump)}$) at the R-DFB signal wavelength from the grating dispersion profile. Thus, hereafter, the δk is deduced with the aid of the experimental data.

Table 3-9 summarises the main parameters applied in the model for the FWM simulation from R-DFB1 and R-DFB2 fibre lasers. They are based on the practical fibres implemented in

---

[1] OED45 is based on the 4th order of explicit Runge-Kutta formula.

the experiments. Note that the output power of the R-DFB signal, $P_{1f}(z = L)$, is measured from the FWM spectrum in the single R-DFB device for an incident pump power (@1064 nm) of around 2 W from Fig. 3-40. In reality, the nonlinear refractive index, n_2, varies slightly with the different concentrations of Ge in the core of the optical fibre [65]. The same value is adopted for these two types of fibres for the simplification and also due to the lack of the practical data about n_2.

Table 3-9 Main parameters applied for FWM simulation in R-DFB1 and R-DFB2 fibre lasers.

Parameter	R-DFB1 (PS980)	R-DFB2 (UHNA4)
$P_{1f}(z = L)$ (mW)	~60	~100
$P_3(z = 0)$ (mW)	50	50
κ (m^{-1})	~37	~30
A_{eff} (μm^2)	~35	~5.3
n_2 (m^2/W)	~3.2 x 10^{-20}	~3.2 x 10^{-20}
L (cm)	30	30
α (dB/m)	0.02	0.005

In order to be consistent with the experiment, the FWM conversion efficiency is calculated as:

$$FWM\ conversion\ efficiency = P_4(Z = L)/\ P_3(Z = L) \tag{3-10}$$

3.6.5.1 FWM conversion efficiency with respect to δk

The evolution of the calculated FWM conversion efficiency with respect to the phase mismatch factor, δk, from R-DFB1 and R-DFB2 is shown in Fig. 3-49(a) and (b), respectively. Additionally, the FWM conversion efficiency against the phase mismatch factor from 30 cm long bare fibres of PS980 and UHNA4 with constant FWM pump power is also calculated and illustrated in Fig. 3-49 for comparison. Specifically, in PS980 fibre, as seen in Fig. 3-49(a), the maximum FWM conversion efficiency obtained is around -17.6 dB from R-DFB fibre laser whilst it is only -80 dB from the same length bare fibre. Similarly, in the UHNA4 fibre as seen in Fig. 3-49(b), the maximum FWM conversion efficiency achieved is about -13.3 dB from the R-DFB fibre laser whilst it is only -60 dB from the bare fibre with the same length. Obviously, the FWM parametric gain has been significantly enhanced in the R-DFB fibre cavity, which is exactly the reason that FWM in R-DFB fibre laser is extremely promising as a candidate for a compact fibre wavelength converter.

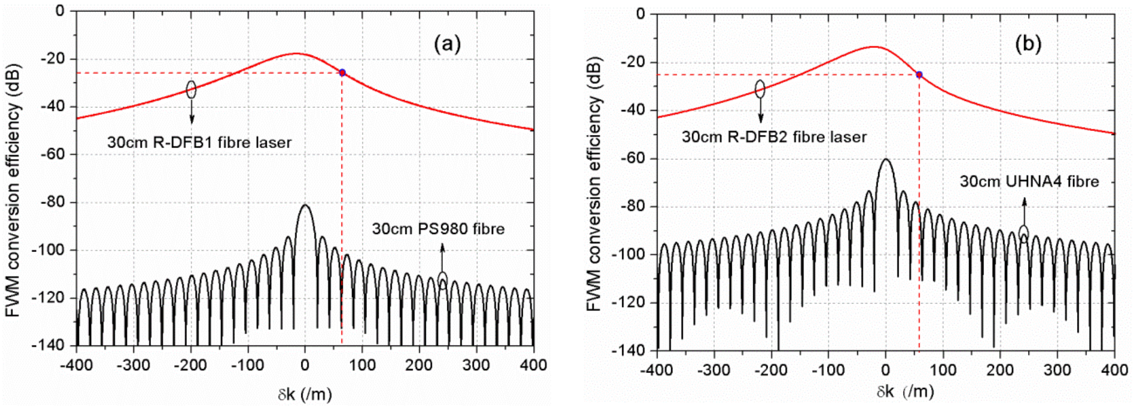

Fig. 3-49 Simulated FWM conversion efficiency vs δk in the 30 cm long R-DFB1 fibre laser and the same length of PS980 bare fibre (a) and in the 30 cm long R-DFB2 fibre laser and the same length of UHNA4 bare fibre (b), respectively.

3.6.5.2 FWM conversion efficiency with respect to the frequency detuning

From the experimental results of FWM generation conducted in the single R-DFB device at this power level (~2 W for 1064.5 nm pump wave), the FWM conversion efficiency obtained is around -25.6 dB for the frequency detuning of ~13.4 THz and -25.1 dB for the frequency detuning of ~11.4 THz in R-DFB1 and R-DFB2, respectively, as seen in Fig. 3-40. Therefore, since the pump wave for FWM (R-DFB signal) is in the normal dispersion region of the applied optical fibres, as seen in Fig. 3-37, the δk can be deduced to be ~65 /m (for the frequency detuning of ~13.4 THz) and ~60 /m (for the frequency detuning of ~11.4 THz) in R-DFB1 and R-DFB2, respectively, as indicated as the red broken lines in Fig. 3-49(a) and (b), respectively. As mentioned above, the value of $\delta k = \delta k_F + \delta k_{FBG}$, is the result of the dispersions from the fibre (δk_F) and the DFB grating (δk_{FBG}). When only the fibre dispersion is taken into account, by using the GVD curves of the fibres, as seen in Fig. 3-37, δk_F is calculated to be ~146 /m and ~213 /m for the set of FWM waves generated from single R-DFB1 and R-DFB2, respectively. Hence, the DFB grating contributes a negative phase mismatch factor on the FWM generation in the R-DFB device.

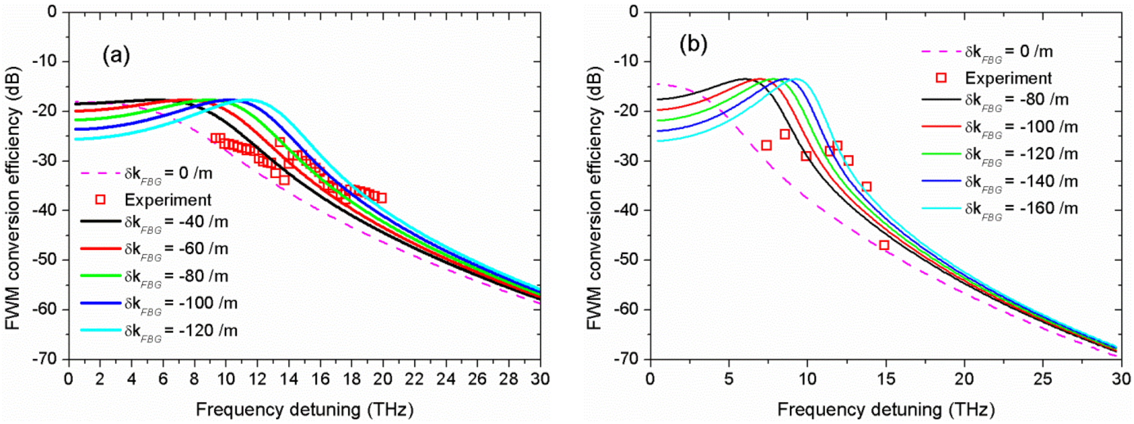

Fig. 3-50 Comparison of experimental and simulated FWM conversion efficiency vs frequency detuning in R-DFB1 (a) and R-DFB2 (b), respectively.

Considering the dispersions of the fibre and DFB grating together, the FWM conversion efficiency, with varied δk_{FBG} against the frequency detuning (the frequency separation between the probe wave and R-DFB signal) from R-DFB1 and R-DFB2, is simulated and shown in Fig. 3-50 (a) and (b), respectively. For comparison, the experimental data of the FWM conversion efficiency are plotted in Fig. 3-50 as well. Overall, the experimental data follow a similar trend to that of simulation. Also, the experimental data match well with the calculation results given δk_{FBG} varying within the range of 0 to -120 /m and 0 to -160/m in R-DFB1 (a) and R-DFB2 (b), respectively. Furthermore, with the reduction of the δk_{FBG}, the peak FWM conversion efficiency shifts to the larger frequency detuning and the detuning frequency range also increases. For example, when the $\delta k_{FBG} = -80/m$, the frequency detuning range with a -40 dB bandwidth obtained is around 19 THz and 13 THz in R-DFB1 and R-DFB2 respectively. This difference of the wavelength conversion range between R-DFB1 and R-DFB2 is due to the difference of the nonlinearities between the two fibres as well as the grating strength between R-DFB1 and R-DFB2.

3.6.5.3 FWM conversion efficiency with respect to the power of probe wave

With the total phase mismatch factor of ~65 /m and ~60 /m in R-DFB1 and R-DFB2 respectively, and with the same R-DFB output power listed in Table 3-9, the FWM conversion efficiency is calculated with respect to the variation of the incident power of P_3 from 0 W to 5 W, in R-DFB1 and R-DFB2, respectively, as shown in Fig. 3-51. It is evident that the FWM conversion efficiency remains constant within 0.1 dB variation, which is in good agreement with the experimental results illustrated in Fig. 3-44 (b).

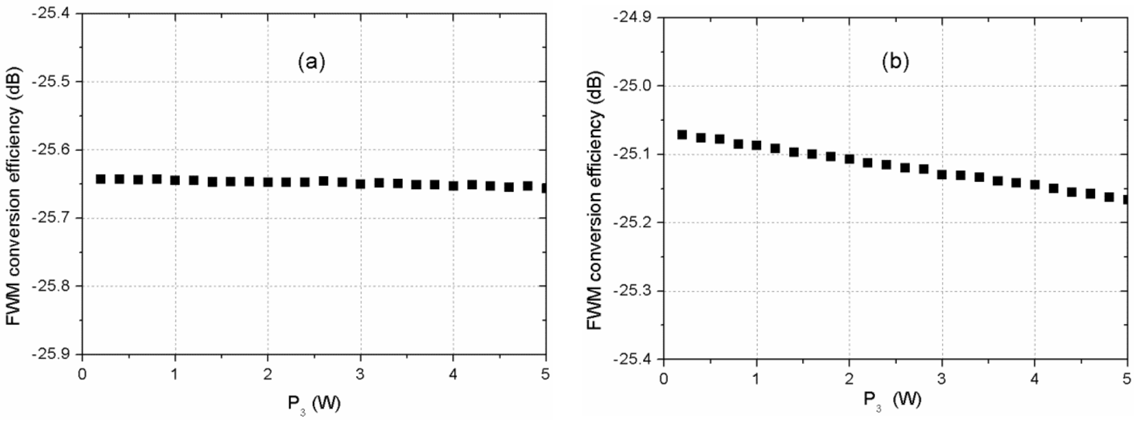

Fig. 3-51 Simulated FWM conversation efficiency vs P_3 in (a) R-DFB1 and (b) R-DFB2, respectively.

3.6.5.4 FWM conversion efficiency with respect to the pump power (R-DFB signal)

In addition, Fig. 3-52 demonstrates the experimental and calculated FWM conversion efficiency with varied phase mismatch factors with respect to the R-DFB output power ($P_{1f}(z = L)$) from 0 W to 0.4 W in (a) R-DFB1 and (b) R-DFB2, respectively.

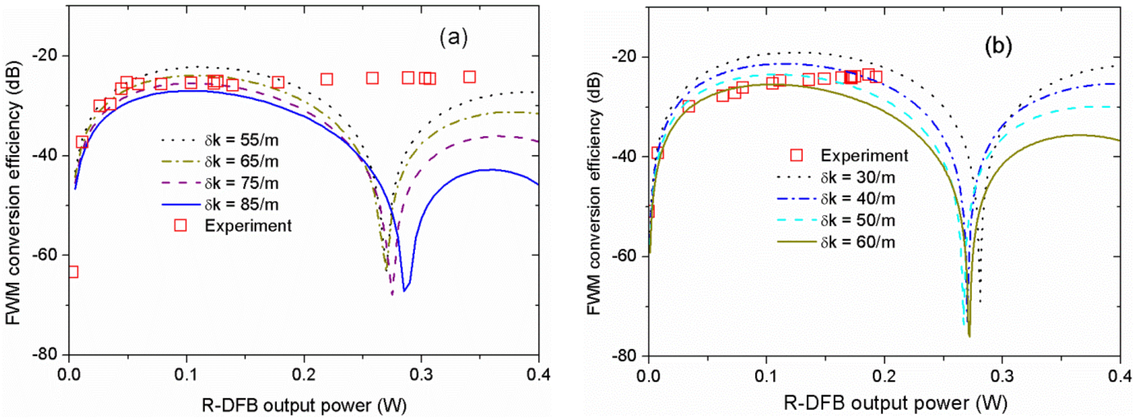

Fig. 3-52 Comparison of experimental and simulated FWM conversion efficiency vs R-DFB output power in (a) R-DFB1 and (b) R-DFB2, respectively.

For the FWM in the R-DFB1 device, as seen in Fig. 3-52(a), the experimental data match well with the simulation with the phase mismatch factor of 65 /m when the R-DFB output power is less than 0.2 W, beyond which, the experimental data remain nearly constant whilst there is a drop at around 0.27 W of R-DFB output power from the simulation. In the case of the R-DFB2 sample, the FWM conversion efficiency behaves in the same manner as that of R-DFB1. At this stage, this discrepancy between the experiment and simulation for the R-DFB output power (the pump power for FWM) above ~0.2 W cannot be explained. However, it might be due to the nonlinear effects at the high power level of the R-DFB signal and a sufficient explanation may require knowledge of the effects as yet unclarified, such as dynamic evolution of the filed distribution in the R-DFB cavity with respect to the increase of the pump power, nonlinear effects, such as two-photon absorption [181] and Raman scattering on the conjugate wave.

3.6.5.5 FWM conversion efficiency with respect to the κ and length of the DFB grating

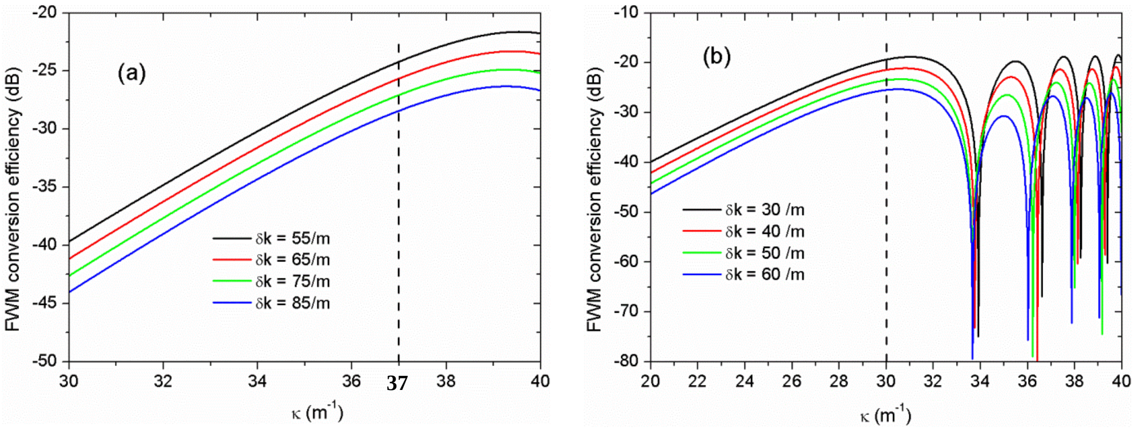

Fig. 3-53 Calculated FWM conversion efficiency vs κ of DFB grating in (a) R-DFB1 and (b) R-DFB2, respectively.

DFB grating is the essential structure for the FWM generation in the R-DFB fibre laser. Fig. 3-53 illustrates the evolution of the calculated FWM conversion efficiency with respect to the coupling coefficient of the DFB grating for R-DFB1 (a) and R-DFB2 (b), respectively. The coupling coefficients for the practical R-DFB1 and R-DFB2 used in the experiment are indicated by the vertical dashed lines in Fig. 3-53. In general, the FWM conversion efficiency increases with the reduction of the phase mismatch factor from 85 /m to 55 /m. In the case of R-DFB1, as seen in Fig. 3-53(a), the FWM conversion efficiency grows as the coupling coefficient increases up to ~39 m^{-1}, after which the FWM conversion efficiency appears slightly decreasing. On the other hand, in the situation of the R-DFB2, as seen in Fig. 3-53(b), the FWM conversion efficiency keeps increasing until the coupling coefficient reaches ~31 m^{-1}, beyond which it starts oscillating, i.e., first dropping down to < -60 dB and then growing back up to the maximum level.

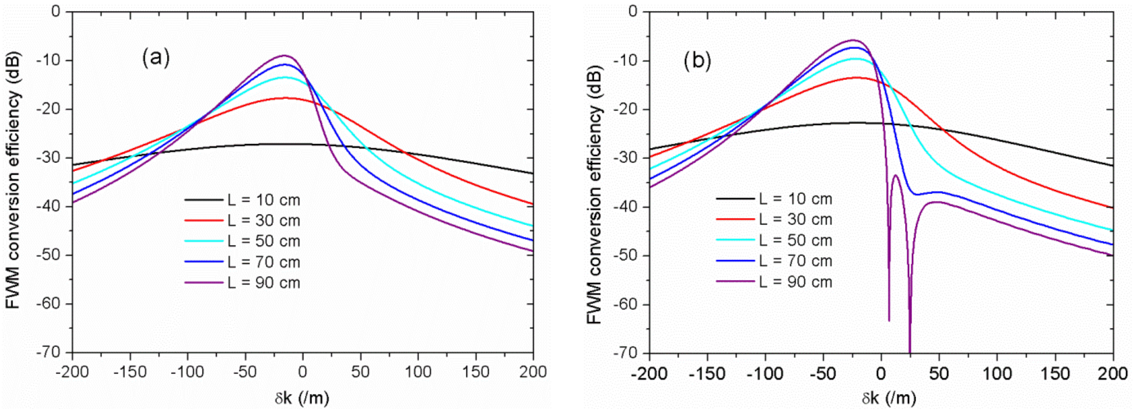

Fig. 3-54 Calculated FWM conversion efficiency vs the length of (a) R-DFB1 and (b) R-DFB2, respectively.

Finally, Fig. 3-54 shows the calculated FWM conversion efficiency with respect to the variation of the length of the DFB grating for (a) R-DFB1 and (b) R-DFB2, respectively. For the R-DFB1 sample, as displayed in Fig. 3-54(a), the peak FWM conversion efficiency increases from around -30 dB to around -10 dB when the length increases from 10 cm to 90 cm. Similarly, For R-DFB2, the peak FWM conversion efficiency increases from around -25 dB to around -5 dB by extending the grating length from 10 cm to 90 cm, as seen in Fig. 3-54(b). However, the wavelength conversion range is inversely proportional to the length of the DFB grating. This feature is the same as that in optical fibres [173].

3.7 Conclusions

In summary, the R-DFB fibre lasers have been studied numerically and experimentally in this chapter. Single-frequency R-DFB fibre lasers have been demonstrated both in the standard NA (PS980) and high NA (UHNA4) Ge/Si optical fibers with an un-polarised pump and a linearly polarised pump, respectively. The DFB gratings are 30 cm-long incorporating a π phase-shift at the centre of the gratings and the coupling coefficients of the DFB gratings are within the range of 30 m^{-1} to 37 m^{-1}. The lowest lasing threshold, the maximum total output power, the slope efficiency against the incident pump power, the linewidth and the PER of the R-DFB fibre laser are demonstrated to be sub-watt (440 mW in UHNA4 R-DFB fibre laser), up to 2 W (with high power un-polarised pump source), ~13% (total output power vs the incident pump power), less than 2.5 kHz (with 29.75 km delay line) and ~18 dB, respectively. With the linearly tapered index modulation profile of the DFB grating, truly uni-directional output R-DFB fibre laser has been observed and the slope efficiency of the single side output power against the incident pump power has been measured to be ~7.7 %. In all the R-DFB fibre laser samples, the R-DFB signal demonstrates high SNR (> 40 dB) immediately it starts lasing and the signal wavelength remains nearly constant within all the operational pump power range, attributing to the negligible thermal effect in the lasers.

The simulation results show that an even lower laser threshold could be realized using either longer length DFB gratings or by applying the highly nonlinear Raman fibres, for example, tellurite glass fibre, as the host fibre for the R-DFB generation. In addition, with a step-like offset π phase-shifted DFB grating structure, the threshold could be reduced almost by a factor of 2 by placing the π phase-shift at 20% offset from the centre whilst holding the strengths of the two sides of the grating to be identical.

Last but not least, wavelength conversion by using the FWM in the R-DFB fibre laser has been investigated both numerically and experimentally. Both the simulation and the experimental data demonstrate that the R-DFB fibre lasers are promising candidates for the FWM generation with the advantages of: (i) ultra-compact (only in the length of tens of cms), (ii) ultra-wide wavelength conversion range (~167 nm in PS980 R-DFB fibre laser and ~113 nm in UHNA4 fibre), (iii) high FWM conversion efficiency in passive Ge/Si fibres, (~ -25.1 dB for the frequency detuning of ~13.4 THz in PS980 R-DFB fibre laser and ~ -24.2dB for the frequency detuning of ~11.4 THz in UHNA4 R-DFB fibre laser), and (iv) extremely large freedom on the selection of the pump sources for FWM (the pump wave is determined by the R-DFB structure and flexible to the ZDW of the host fibre).

Chapter 4 Nonlinearities and photosensitivity of high-index non-silica glass fibres

The primary motive of this chapter is to inscribe FBGs into non-silica glass fibres for realizing compact fibre devices through the combination of the unique properties of FBGs with the high nonlinearities of high-index non-silica glass fibres.

The non-silica glasses, also known as soft-glass, due to their significantly lower processing temperature than that of silica glass. Since the nonlinear refractive index (n_2) of many high-index non-silica glasses is typically higher than that of silica glass by one to three orders of magnitude, non-silica glasses are considered as promising candidate hosts for HNLF. In addition, as mentioned in the last chapter, the Raman gain coefficient of tellurite glass is ~35 times higher than that of silica glass. Thus, compact nonlinear fibre devices can be realized by using short-length of highly nonlinear non-silica glass fibre with low pump power [45, 179, 182]. Also, it is extremely interesting to write FBGs into the core of the soft-glass fibre for compact centimetre-long FBG-based devices, such as, short cavity fibre lasers, e.g., R-DFB fibre lasers, wavelength converters [51], compact all-optical switching [45], and so on.

This chapter begins with the nonlinear optical performance of the non-silica glass fibres (in Section 4.1). The measurement of the Raman gain coefficient of tellurite glass as well as SRS-assisted SCG from a metre-long tellurite glass fibre is presented in Section 4.2. The splicing technique between the non-silica glass fibres and the standard silica fibres is discussed in Section 4.3. The photosensitivity of the non-silica glass fibres is given in Section 4.4, including the preliminary work of the FBGs fabrication in these fibres. In the last section, a conclusion is drawn.

4.1 Nonlinear optical performance of high-index non-silica glasses and fibres

The effective nonlinear coefficient γ_{eff} of a fibre is the primary indicator for its nonlinear device applications, and can be expressed as [65]:

$$\gamma_{eff} = \frac{2\pi}{\lambda} \cdot \frac{n_2}{A_{eff}} \qquad (4\text{-}1)$$

in which λ is the wavelength of light, A_{eff} is the effective mode area of the fundamental guided mode and n_2 is the nonlinear refractive index, respectively. The Equation (4-1) indicates that a HNLF with high γ_{eff} can be obtained by choosing a host material with a high n_2 [43, 50, 52], or by reducing the effective mode area A_{eff} of the fibre [51, 183, 184], or both.

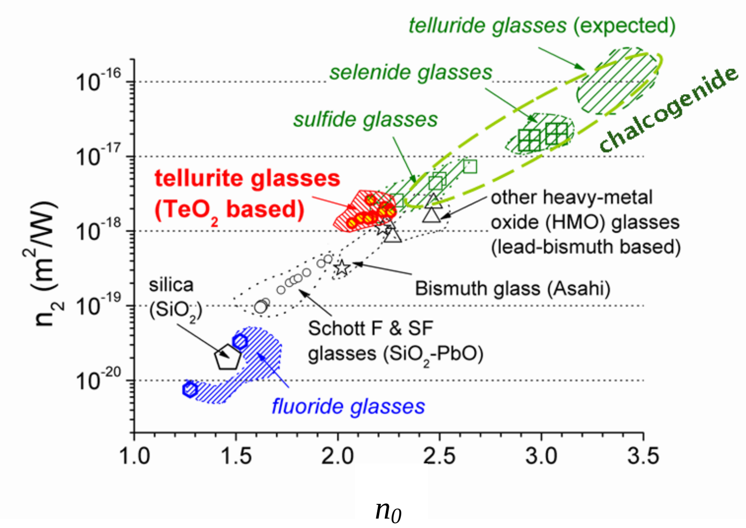

Fig. 4-1 Relation between linear (n_0) and nonlinear refractive index (n_2) of various optical glasses. (After Ref. [51])

Fig. 4-1 illustrates the relation between linear (n_0) and nonlinear refractive index (n_2) of various optical glasses, including fluoride (BeF_2-, and ZrF_4 based) glasses [185], lead silicate (SiO_2-PbO) glasses [61, 184], bismuth (SiO_2-B_2O_3-Bi_2O_3) glasses [186], tellurite (TeO_2-based) glasses [80, 187], and chalcogenide (chalcogen elements S, Se, and Te based) glasses [50, 52]. It can be seen that the nonlinear refractive index n_2 increases with the linear refractive index n_0, in good agreement with the empirical prediction of Miller's rule [52]. In particular, high-index oxide and chalcogenide glasses, with the refractive indices (n_0) of 1.8-3.5, possess high nonlinear refractive indices (n_2), which are about 1-4 orders of magnitude higher than that of pure silica glass (2.2×10^{-20} m^2/W). This indicates that a HNLF based on a high-index non-silica glass will have an enhanced fibre nonlinearity, γ_{eff}.

Reducing effective mode area (A_{eff}) is another effective route to achieve a high γ_{eff}. Since reducing A_{eff} requires a large index contrast (large NA) between the core and cladding materials to ensure a high light confinement inside the core, thermal mismatch between the pair of very dissimilar core and cladding glasses becomes a physical barrier limiting the ultimate index contrast that one can find. The silica glass PCF technology [43, 52], which introduces an microstructured air-filled cladding around a solid core in the fibre structure, the thermal mismatch issue for a solid core/cladding fibre does not exist for this sort of 'single material' fibre. The effective index contrast between the air-filled cladding and the solid glass core can be largely tailored by controlling the air-filling fraction and its position. Using a high-index non-silica glass rather than low-index silica glass as the host of a PCF, an even higher index contrast and consequently a smaller mode area can be achieved in the same PCF design. For example, at 1.55 µm, the conventional single mode silica fibre, SMF28 has a n_2 of 3 x 10^{-20} m^2/W in the core and an $A_{eff} = 90\ \mu m^2$, so the γ_{eff} is only ~1 $(W \cdot km)^{-1}$. Theoretically, the highest γ_{eff} which can be achieved in the silica-based PCF is ~70 $(W \cdot km)^{-1}$, given that the effective mode area can go to its minimum of ~1.5 μm^2 [52, 183]. However, for a commercial high-index lead silicate glass, Schott SF57, that has n_0 of ~1.80 and n_2 of ~41 x 10^{-20} m^2/W at 1.55 µm, the theoretical highest γ_{eff}, which can be achieved is ~1860 $(W \cdot km)^{-1}$ [52, 183]. The extra enhancement on this maximum γ_{eff} is from the contribution of the high-index background material on the strong light confinement inside the core.

Table 4-1 Summary of the properties of different non-silica glass fibres

Glass type	Main composition	n_0 (at 1550 nm)	n_2 (m^2/W)	γ_{eff} $(W \cdot km)^{-1}$	Reference
Lead silicate	Schott SF57	~1.80	~4.1 x 10^{-19}	1860 (at 1550 nm)	[44, 51]
Bismuth oxide	Bi_2O_3	~2.22	~1.1 x 10^{-18}	1360 (at 1550 nm)	[55]
Tellurite	$76.5TeO_2$-$6Bi_2O_3$-$11.5Li_2O$-6ZnO (mol%)	~2.03	~5.9 x 10^{-19}	5700 (at 1064 nm)	[56]
Chalcogenide	As_2Se_3	~ 2.44	~1.1 x 10^{-17}	9.34 x 10^4 (at 1550 nm)	[188]

Table 4-1 summarises the highest effective nonlinear coefficients (γ_{eff}) that have been reported in high-index non-silica glass fibres. It can be seen that high-index non-silica glass fibre can have a γ_{eff} of 10^3-10^4 times higher than the conventional silica fibre (~1 $(W \cdot km)^{-1}$). Thus, the use of non-silica glass fibres opens up the possibility for achieving efficient and compact nonlinear devices based on a metre to centimetre long highly nonlinear fibre.

4.2 Raman gain coefficient characterization and applications of tellurite glass fibres

Tellurite glass fibres not only have a much higher nonlinear coefficient than the conventional silica fibre, but also possess much stronger Raman gain coefficient and wider transmission window than silica glass fibres [148, 189, 190]. In this section, the characterization of Raman gain spectrum of a home-made tellurite glass fibre is presented with some details. Additionally, by using the high Raman gain property of tellurite glass fibre, SRS-assisted broadband SCG has been demonstrated in a metre-long fibre with a pump source at the high normal dispersion regime of the fibre. In this work, the tellurite bulk glass and tellurite glass fibre were made by Dr. Xian Feng, from the soft-glass group in ORC.

4.2.1 Preparation of bulk tellurite glass

The tellurite glass studied here was made in-house based on the composition of $75TeO_2$-$20ZnO$-$5Na_2O$ (mol.%) (TZN). The glass has a refractive index of 2.0 at 1.06 μm and a glass transition temperature T_g of 300°C. High purity commercial chemicals of tellurium oxide (TeO_2, purity: 99.9995%, Alfa Aesar), zinc oxide (ZnO, purity: 99.9995%, Alfa Aesar), and sodium carbonate (Na_2CO_3, purity: 99.997%, Alfa Aesar) were used as raw materials for the glass melting. A batch of ~30 grams was well-mixed first and then melted in a gold crucible at 800ºC for 45 minutes. Pure oxygen gas was purged into the furnace during the melting to prevent the reduction of tellurium oxide. The melt was then cast into a stainless steel mold which was preheated around the glass transition temperature (T_g). The glass and the mold were held around T_g for 2 hours to remove the thermal stress inside, and then cooled down to room temperature. The glass sample was grounded down to the dimensions of 20 x 10 x 3 mm and the two largest parallel faces were polished to optical quality.

4.2.2 Calculation of Raman gain coefficient of bulk glasses

The depolarised spontaneous Raman scattering spectra of the TZN glass and a reference of pure silica glass were measured by a micro-Raman spectrometer (RENISHAW Ramanscope) using a 10 mW He-Ne laser (633 nm) as a pump source. With the assistance of a CCD camera, it was ensured that the laser beam was focused on the top surface of the sample. The Raman spectra were recorded from 200 cm^{-1} to 1000 cm^{-1} with a resolution of 1 cm^{-1}. This measurement was carried out by Dr. Xian Feng from the soft-glass group in ORC.

The reduced Raman intensity spectra are obtained by dividing the spontaneous Raman spectra by a thermal population factor of $(1+n_b)$, where n_b is the Bose-Einstein thermal factor

[155, 191] ($n_b = \left[\exp\left(\frac{h\nu}{kT}\right) - 1\right]^{-1}$, where h is Planck's constant, ν is the Raman shift frequency, T is the absolute temperature for the measurement, and k is Boltzmann's constant). The reduced Raman intensity spectrum exhibits a line-shape close to that of stimulated Raman scattering [155]. In order to evaluate the Raman gain coefficient of the tellurite glass, the reduced Raman intensity is normalized by the peak Raman intensity of pure silica glass at 440 cm^{-1}.

Fig. 4-2 shows the relative reduced Raman intensity spectra of TZN and fused silica. The Raman vibration at 433 cm^{-1} is associated with the glass Te-O-Te chain unit's symmetric stretching mode, and the spectral features at 665 cm^{-1} and 741 cm^{-1} are due to the vibration of the TeO_4 bipyramidal structural arrangement and the TeO_{3+1} (or distorted TeO_4) unit, respectively [148].

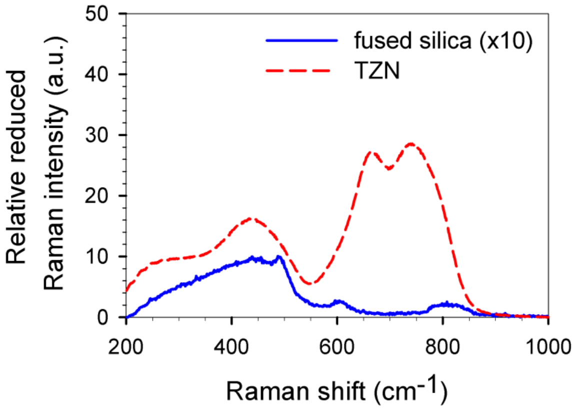

Fig. 4-2 Relative reduced Raman intensities of TZN glass and referenced pure silica glass, normalized to the peak intensity of silica at 440 cm^{-1}.

As Raman gain coefficient g_r is related to the differential cross section as: $g_r = \sigma\lambda_S{}^3/(c^2 h n_0{}^2)$ (σ is the differential cross section, λ_S is the Stokes wavelength, and n_0 is the linear refractive index of the glass at 633 nm) [98], the Raman gain coefficient of the tellurite glass can be obtained as:

$$g_{TZN} = g_{p\_SiO_2} \cdot \sigma_{TZN\_rel} \cdot \left(\frac{n_{SiO_2}}{n_{TZN}}\right)^2 \cdot \left(\frac{\lambda_{S\_TZN}}{\lambda_{S\_SiO_2}}\right)^3 \qquad (4\text{-}2)$$

where $g_{p\_SiO_2}$ is the peak Raman gain coefficient of the silica glass and σ_{TZN_rel} is the ratio of the differential cross section of the TZN to that of silica. n_{SiO_2} and n_{TZN} are the linear refractive indices of silica and TZN at 633 nm, respectively. The relative differential cross section, σ_{TZN_rel}, can be obtained by multiplying the relative reduced Raman intensity with a correction factor F, which takes into account the changes in the scattering geometry and the intensity related to the refractive index of the samples [145]. The F factor is calculated to be ~2.15 for TZN glass by using the method presented in Ref. [155] (see Appendix B).

Table 4-2 summarises the Raman gain coefficient of TZN glass for pump wavelengths of 633 nm and 1064 nm, respectively. The Raman gain coefficient is calculated via Equation (4-2) by using the relative differential cross section, the Raman gain coefficient of silica, and the refractive indices at 633 nm of the silica and the tellurite glasses. The reference peak gain of silica with pump wavelengths of 633 nm and 1064 nm, was converted from the gain coefficient of ~1.86 x 10^{-11} cm/W with 532 nm pumping by using its dependence on the pump wavelength as $1/\lambda_p$ [98]. It is seen that with the pump of 1064 nm the g_r of TZN glass at the 741 cm^{-1} Raman shift is ~35 times higher than the peak g_r of pure silica glass at 440 cm^{-1}.

Table 4-2 Refractive index n_0 at 633 nm, correction factor F, peak wave number, peak relative reduced Raman intensity, peak relative differential cross section and peak Raman gain coefficient g_r of investigated glasses with pumps at 633 nm and 1064 nm.

Glass	n_0 @633nm	F	Peak wavenumber (cm^{-1})	Relative reduced Raman intensity	Relative differential cross section	g_r @633 nm (x10^{-11} cm/W)	g_r @1064 nm (x10^{-11} cm/W)
SiO_2	1.45	1	440	1	1	1.56	0.93
TZN	2.03	~2.15	433	16	34.46	27.69	16.47
			665	26.9	57.94	50.29	29.92
			741	28.2	60.74	54.07	32.17

In principle, inasmuch as Raman scattering is a polarization-dependent effect, the polarised spontaneous Raman spectrum rather than the depolarised spontaneous Raman spectrum should be utilized for the calculation of the Raman gain coefficient of the bulk glass. However, for both tellurite and silica glasses, the intensity of the Raman scattering is dominated by the parallel polarization (VV or HH) and the intensity of the perpendicular polarization (VH) is typically no more than 5% of the former intensity [98]. As a result, the depolarised spontaneous Raman spectrum gives a relatively reduced Raman intensity almost identical to the one obtained from the polarised spontaneous Raman spectrum.

4.2.3 Fabrication and fundamental properties of the tellurite glass photonic-crystal fibre

With the same composition of TZN glass, an *air-suspended-core* (ASC) single-mode tellurite glass PCF was fabricated in-house (by Dr. Xian Feng, in soft-glass group in ORC) using the glass extrusion method [80]. Fig. 4-3(a) shows the *scanning electron microscope* (SEM) microphotographs of the cross-section of the fibre. It is seen that in the fibre with an outer diameter (OD) of 250 μm, a triangular core with an effective mode area (A_{eff}) of ~2.6 μm^2 is effectively suspended in the air with the support from three 7.4 (± 0.2) μm long and 180 (± 20) nm thin supporting struts. Given the nonlinear refractive index $n_2 = 2.5 \times 10^{-19}\ m^2/W$ [80], the effective nonlinear coefficient γ_{eff} of this fibre is calculated to be ~570 $(W \cdot km)^{-1}$ at 1.06 μm. Fig. 4-3(b) shows the near-field images from the output end of the tellurite glass ASC PCF at 1.06 μm. Robust single-mode guidance has been observed at 1.06 μm [80]. The propagation loss of the PCF was measured to be 2.3 (± 0.2) dB/m at 1.06 μm and 1.9 (± 0.2) dB/m at 1.55 μm, respectively by the cutback method.

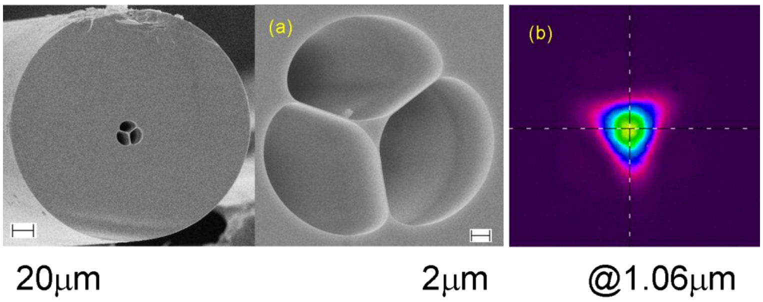

Fig. 4-3 (a) SEM photographs of the fabricated tellurite ASC PCF with 2.6 μm core diameter; (b) Observed near-field images from the output end of the ASC tellurite glass PCF at 1.06 μm. (This figure was provided by Dr. Xian Feng).

Fig. 4-4 shows the GVD profiles of the tellurite glass ASC PCF (calculated) and of the bulk tellurite glass and the vertical line indicates the pump wavelength selected for the Raman induced SC in this work. In comparison with the ZDW of the bulk at ~2.15 μm, the ZDW of the PCF is shifted to ~1.38 μm because of the large waveguide dispersion of the small ASC. The GVD of the PCF is ~ -320 ps/nm/km at 1.06 μm.

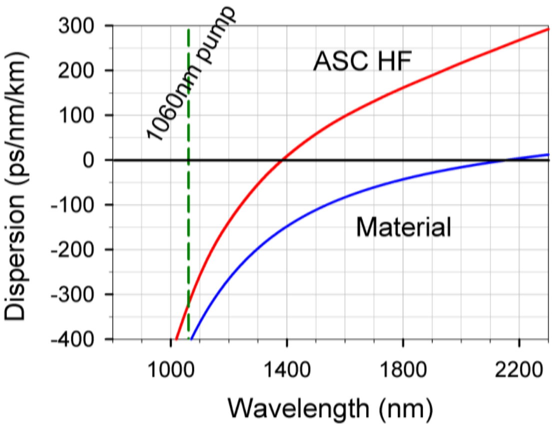

Fig. 4-4 Dispersion curves of the fabricated tellurite ASC PCF (calculated) and of the bulk material. The vertical line indicates the pump wavelength of 1.06 μm. (This figure was provided by Dr. Xian Feng).

4.2.4 SRS-assisted SCG from a metre-length of tellurite glass PCF

Fig. 4-5 Schematic diagram of the experimental setup for SCG generation from tellurite glass PCF.

Fig. 4-5 shows the experimental setup for generating the SRS-assisted SC in the tellurite ASC PCF. A linearly polarised 1.06 μm Yb-doped all-fibre MOPA with pulse duration of ~20 ps (with approximate Gaussian profile) and repetition rate of ~14.4 MHz [192] is used as the pump source. (The pump source is developed by Pulsed Fibre Lasers group in ORC and operated by Peh Siong (Simon) Teh during this experiment.) The set of half-wave plate, $\lambda/2$ (first $\lambda/2$ from left), and PBS cube (PBS25-1064-HP from Thorlabs) is applied to adjust the pump power for the ASC tellurite glass PCF by rotating the $\lambda/2$. The other $\lambda/2$ (second $\lambda/2$) is used to rotate the polarization plane of the linearly polarised pump light in order to investigate the birefringence effect of the fibre. With the free-space lens coupling method, the pump source is coupled into the small core of the tellurite glass PCF. A CCD camera is used to monitor the near-field image of the output end of the tellurite glass PCF to ensure that the pump light has been coupled into the core. Water-cooling is applied at the input end of the PCF to remove the generated heat. The generated output spectra from the fibre are recorded by the OSA of Agilent 86140B with a resolution bandwidth of 0.5 nm. A thermal power meter is used to measure the average power of the SC at the output end of the fibre for each value of the launched average pump power.

4.2.4.1 Experimental results of SRS-assisted SCG in tellurite glass PCF

In the experiment, the fibre initially has a length of 1.35 (± 0.02) m, and then the fibre is cut down to a length of 0.50 (± 0.02) m. For both situations, the generated SC spectra are observed with the incident average pump powers over the range of several mW to 128.7 mW, respectively. The effective length, $L_{eff} = (1 - \exp(-\alpha L))/\alpha$ (where α is the propagation loss of the fibre) has been fallen into consideration for evaluating the Raman gain of the fibre. At 1.06 μm, the effective lengths, L_{eff}, of the fibre with actual lengths of 1.35 m and 0.50 m are calculated to be ~0.96 m and ~0.42 m, respectively. Besides, the walk-off length can be calculated via:

$$L_w = \frac{T_0}{|\beta_1(\lambda_p) - \beta_1(\lambda_s)|} \tag{4-3}$$

where T_0 is the duration of the pulse (~20 ps), $\beta_1(\lambda_p) = (v_g(\lambda_p))^{-1}$, and $\beta_1(\lambda_s) = (v_g(\lambda_s))^{-1}$, in which v_g is the group velocity at pump wavelength (λ_p) or Stokes wavelength (λ_s). With the dispersion curve of the tellurite glass fibre, as shown in Fig. 4-4, the walk-off length between the pump, ~1060 nm, and the first-order Raman Stokes, ~1150 nm, (corresponding to the Raman shift of 741 cm^{-1}) is calculated to be ~0.75 m. Inasmuch as the L_{eff} of the used fibre is comparable to the L_W between the first-order Raman Stokes and pump waves, the walk-off effect will have some impact on the SRS generation, especially for the case of longer length. Additionally, it is found that the output remains almost constant when rotating the second $\lambda/2$, indicating the birefringence of the fibre in this experiment can be ignored.

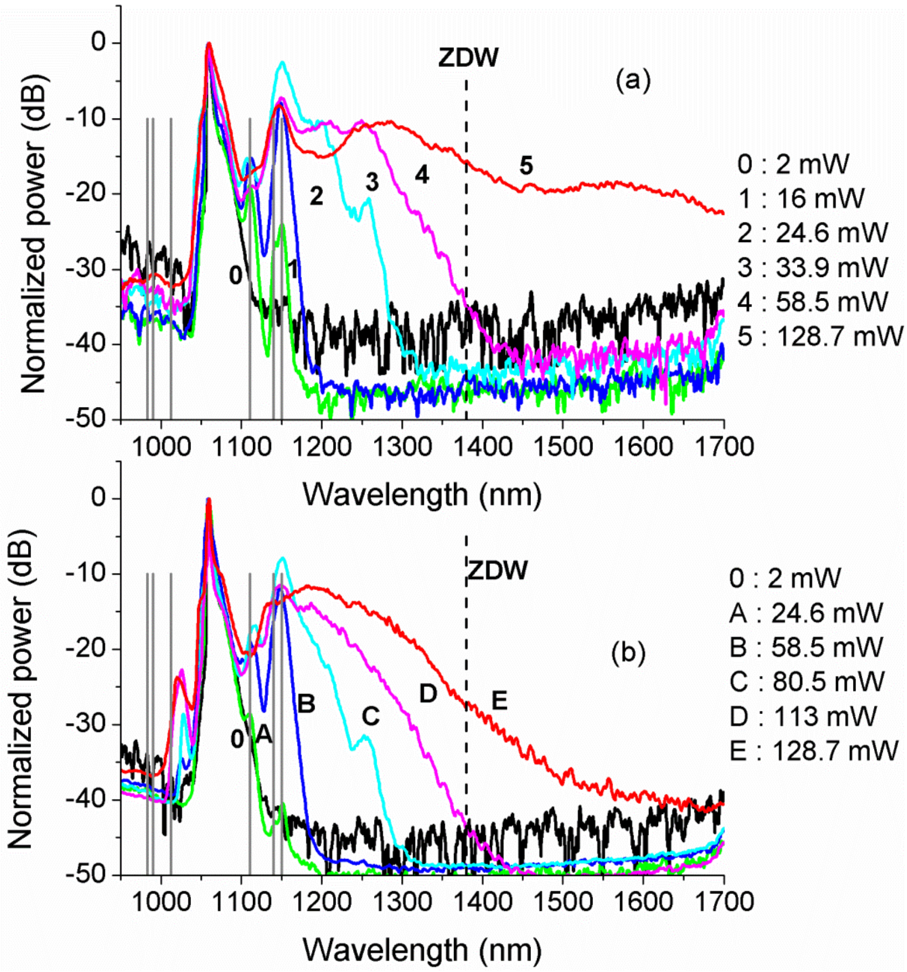

Fig. 4-6 Observed Raman-assisted SCG spectra from tellurite glass PCF with a length of (a) 1.35 m and (b) 0.50 m at varied incident average pump powers, respectively.

Fig. 4-6 (a) and (b) illustrate the evolution of Raman-assisted SCG with the increase of the incident average pump powers, from the fibres with the length of 1.35 m and 0.5 m, respectively. The dashed vertical lines at ~1.38 µm in Fig. 4-6 (a) and (b) indicate the ZDW of the fibre. The grey solid vertical lines represent the individual first-order Raman anti-Stokes at ~983 nm, ~990 nm and ~1013 nm and first-order Raman Stokes at ~1111 nm, ~1140 nm and

~1150 nm, corresponding to the Raman bands of tellurite glass shown in Fig. 4-2 with the Raman shift of 433 cm^{-1}, 665 cm^{-1} and 741 cm^{-1}, respectively.

For the PCF with 1.35 m length, the first-order Raman Stokes emerges when the incident average pump power is above 9.8 mW, corresponding to a peak power of ~34 W. When the incident average pump power increases to 16 mW, the shape of the Raman spectrum, trace 1 in Fig. 4-6 (a) is substantially distinct, and it has an identical profile to that of the bulk glass. In the case of 0.50 m-long fibre, the launched average pump power needs to be as high as ~24.6 mW to reach the threshold for first-order Raman Stokes (as trace A in Fig. 4-6 (b)), due to the smaller Raman gain in the shorter length fibre.

The second-order Raman Stokes from the 1.35 m-long fibre is generated and the spectrum extends beyond ~1200 nm, when the incident average pump power increases to ~33.9 mW and above (as the traces 3 and 4 in Fig. 4-6 (a)). In the case of 0.50 m-long fibre, at the average pump power of ~58.5 mW, two peaks belonging to the first order Raman Stokes can be seen from the trace B in Fig. 4-6 (b), but the spectrum does not extend across ~1180 nm. Additionally, a broadening of the spectrum on both sides of the pump is observed at this power level, due to the SPM effect. Also as seen from the trace C in Fig. 4-6 (b), the second-order Raman Stokes appears at the incident average pump power of ~80.5 mW.

As also seen in Fig. 4-6, for both 1.35 m-long and 0.50 m-long fibres, when the incident average pump power further increases, the relative intensity of the Stokes peak at 741 cm^{-1} keeps growing but the peak at 433 cm^{-1} appears saturated. This is because in the Raman process, the Stokes components at the higher frequency always act as the new pump for generating the lower frequency Stokes components. This is in agreement with the observation in silica glass fibres [65]. Furthermore, the first order Raman anti-Stokes appears at ~1020 nm, rather than the calculated ~1013 nm, in the case of 0.5 m long fibre, but it does not show up at all for the 1.35 m long fibre. This is mainly because (i) the higher total propagation loss in the longer fibre length case; and (ii) the Raman gain profile is asymmetric, which is very different from the FWM based symmetric parametric gain profile, so that the frequency components on the anti-Stokes side of the pump are in principle converted back to longer wavelengths by consecutive Raman process [193].

The further increase of the average incident pump power to ~128.7 mW, corresponding to a peak power of ~447 W, causes the formation of the higher-order Raman Stokes at the longer wavelengths and the flattened SC spectra can be clearly observed, as seen from traces 5 and E in Fig. 4-6. The 10 dB-bandwidth of the generated continuum spectra from 1.35 m-long (trace 5 in Fig. 4-6 (a)) and 0.5 m-long PCF (trace E in Fig. 4-6 (b)) are ~600 nm and ~200 nm, respectively. Note that the spectrum beyond 1700 nm could not be observed due to the limited range of the OSA. Such broadband SC observed in the longer PCF is because of the generated third-order Raman Stokes (around 1386 nm according to Raman shift of 741 cm^{-1}) is at a wavelength around ZDW (1380 nm), and subsequently acts as the pump for SC generation within the near zero dispersion/anomalous dispersion pump scheme. In this regime, a combination of nonlinear effects including FWM, modulation instability and soliton-related dynamics broaden the spectrum significantly [193, 194]. In particular, FWM process could broaden the spectrum towards both longer and shorter wavelength symmetrically by the ZDW of the fibre. Fig. 4-7 illustrates the wavelength relation of FWM with the ZDW of 1386 nm. It is clearly seen that if the SC extends to the shorter wavelength than the pump source (~1060 nm), the long wavelength edge of the SC should go beyond 2 μm. Within the pump power level in this experiment, the SC has not extended below the pump source, as shown in Fig. 4-6. This is due to the limitation of the pump power leading to the longest wavelength edge of the SC is between the 1700 nm and the 2000 nm only.

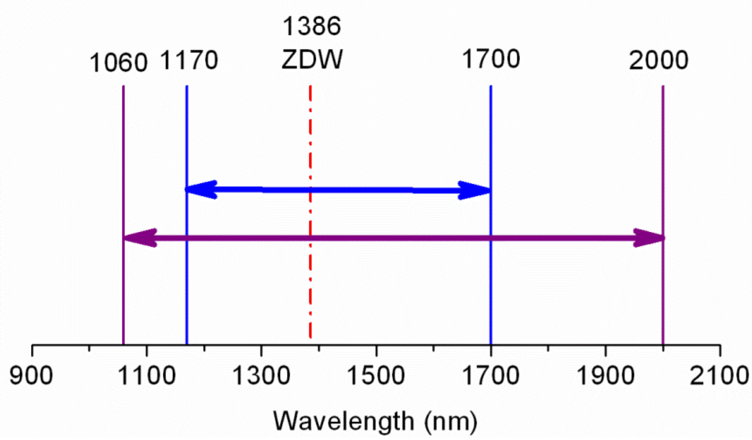

Fig. 4-7 Wavelength relation of FWM with ZDW at 1386 nm.

It is worth pointing out that the most efficient scheme for obtaining a broad SC is to pump the fibre within the anomalous dispersion regime [193, 195]. Accordingly, the pump wavelength has to be matched with the ZDW of the fibre or the ZDW of the fibre has to be tailored so as to meet the available pump source. The latter can frequently be realized by using the PCF technique [54]. For example, it has been shown that it is possible to engineer the ZDW of silica glass-based PCF over a very broad wavelength range (anywhere down to the green regions of the spectrum) via suitable control of the air-filling fraction and the lattice structure of the air holes in the micro-structured cladding. This is possible due to the wavelength-scale features of the micro-structured cladding and the large index contrast between the air and the background material. As a result, it becomes possible to fabricate a silica fibre with a ZDW slightly shorter than the wavelength of most common pump laser sources, for example, down to 1 μm to match the operating wavelength of the Yb-doped fibre laser which is merging as a pump laser of choice for many applications. However, note that in order to achieve a ZDW much shorter than the material dispersion wavelength, generally a fibre results in a very small core, because a large positive waveguide dispersion is needed in this case to compensate the large negative dispersion of the core material. Such DSFs are therefore generally quite nonlinear and the further the pump wavelength from the material ZDW the smaller the core and the more highly nonlinear and more prone to optical damage the fibre becomes. As the ZDW of the tellurite glass material is ~2.15 µm, micrometre or sub-micrometre core diameter is required for the tellurite glass PCF with the ZDW down to ~ 1 µm or even below [56]. Such a small core fibre will cause the difficulty of coupling the pump power into the core of the fibre and lead to a high coupling loss, which will damage the input end of the fibre easily.

However, the findings of this work have overcome the restrictions mentioned above. The broadband SC from the metre-length tellurite glass PCF by pumping in the normal dispersion region of the fibre is because of the high Raman gain coefficient and the multi-peak wide bandwidth of the Raman gain spectrum of the tellurite glass. At high pump powers, higher-order Raman Stokes lines appear when the Stokes power becomes large enough to pump the next-order Stokes. And the Raman Stokes spectrum flattens because of the broad bandwidth of the Raman gain of the tellurite glass. This cascaded effect occurs until the pump shifts into the anomalous dispersion regime. This feature is clearly identifiable from the experimental data as shown in Fig. 4-6. Note that only discrete Raman Stokes lines have been observed from 12 m-long chalcogenide fibres (As_2S_3) by pumping at the normal dispersion region of the fibre with a ns pump source at ~1550 nm [106]. In that work, although, the Raman gain coefficient of the chalcogenide fibre is ~89 times higher than silica fibre, only individual Stokes lines instead of a continuum spectrum was observed due to the narrow linewidth of the Raman gain spectrum of the chalcogenide glass. The mechanism for the spectrum broadening is applicable for *large mode area* (LMA) tellurite glass fibres, which have the material ZDW and could withstand high incident pump power before damage, to produce high energy SC. What is more, since the tellurite glass fibres are transparent in the mid-IR regime (to ~5 µm), the SC generated from tellurite glass fibre could easily extend into mid-IR with pump sources at 1550 nm or even 2 µm [153] when the peak pump power reaches the Raman threshold.

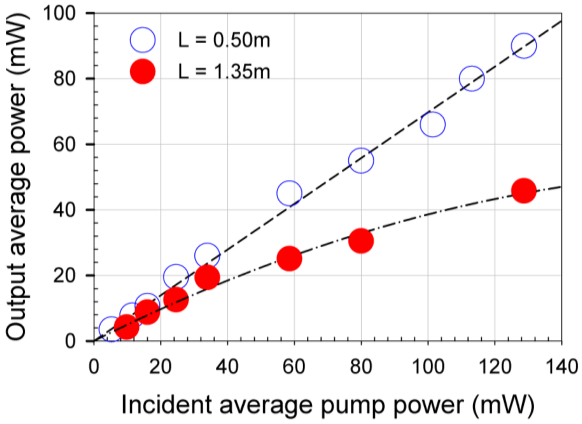

Fig. 4-8 Output average power against the incident average pump power. (L: the used fibre length).

The relation between the obtained output average power and the incident average pump power in the fibres with lengths of 1.35 m and 0.50 m is shown in Fig. 4-8. For the 0.50 m-long PCF, the output average power and the incident pump power show a good linear relationship with a nearly constant ~68% conversion efficiency. However, for the 1.35 m-long PCF, the pump-to-SC conversion efficiency appears nonlinear: at low pump power levels, i.e., when the incident average pump power is less than ~33.9 mW and the generated Raman Stokes is within the normal dispersion region, the slope of the conversion efficiency is ~50%; at high pump power range, where the generated SC extends across the ZDW of the fibre, the conversion efficiency decreases significantly, dropping to ~36% at an average pump power of ~128.7 mW. The decrease of the conversion efficiency of the 1.35 m-long fibre in comparison with the 0.50 m long fibre is probably because (1) there exists an additional propagation loss of ~1.8 dB (extra 0.85 m actual length) for the 1.06 μm pump in the longer fibre; and (2) the quantum defect from the pump photons to the generated photons significantly increases when the SC crosses the ZDW and extends towards much longer wavelengths. By contrast, for the 0.50 m long fibre the spectrum is essentially composed of SRS peaks between 1.15-1.20 μm so that the quantum defect is low.

4.2.4.2 Numerical simulation of SRS and SCG in tellurite glass PCF

In order to verify the understanding on the above experimental results, numerical simulations of SRS and SCG in the tellurite glass ASC PCF have been conducted. The simulations were developed by Dr. Peter Horak in ORC. The simulations solve the generalized nonlinear Schrödinger Equation using a split-step Fourier technique. A sufficiently large number of discretization points are chosen to ensure appropriate coverage of the large temporal and spectral windows. The measured Raman gain (see Table 4-2), Raman gain spectrum (see Fig. 4-2), fibre mode area (see Fig. 4-3), fibre dispersion profile (see Fig. 4-4), and input pump spectrum (see Fig. 4-6, trace 0) are used as the inputs of the model. In the time domain the pump pulses are modeled with a Gaussian shape of ~20 ps pulse duration according to the experimental results [192].

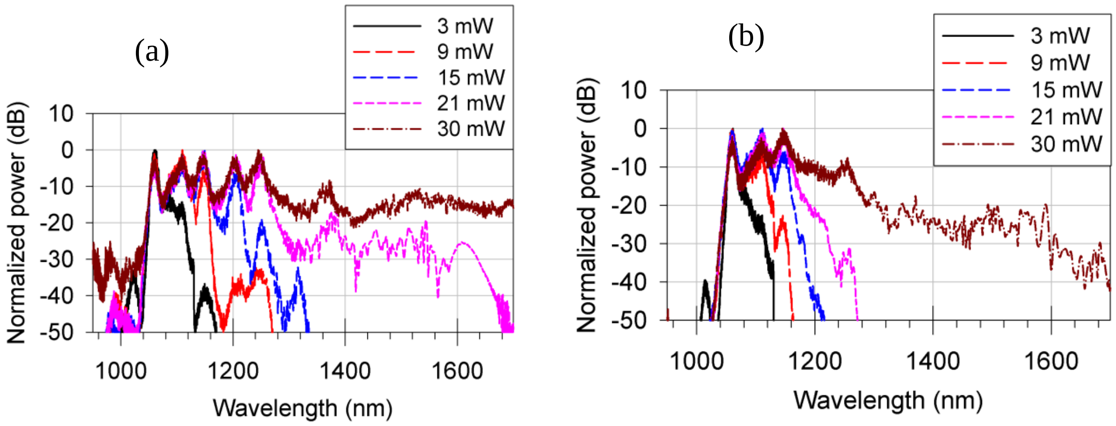

Fig. 4-9 Simulated SRS and SC generated in tellurite glass PCF with lengths of (a) 1.35 m and (b) 0.50 m, for incident average pump powers of 3 mW, 9 mW, 15 mW, 21 mW, and 30 mW, respectively.

Fig. 4-9 illustrates the calculated SRS and SC generated from the 1.35 m-long (a) and 0.50 m-long (b) fibre, under the average pump power of 3 mW, 9 mW, 15 mW, 21 mW, and 30 mW, corresponding to the peak power of 10 W, 30 W, 50 W, 70 W, and 100 W, respectively. The simulated spectra show more pronounced peaks than the measured curves, but overall the spectral profiles correspond well with the experimental results. However, it can be noticed that the powers used in the experiment are about 3-4 times higher than the powers obtained from the simulation for generating similar spectra. This discrepancy is mainly due to the idealized Gaussian pulse shape chosen in the simulation, which neglects pulse distortions prior to the fibre launching and for example any long temporal pedestals. The significantly enhanced undepleted pump power in the output spectra observed in the experiments compared to the simulations supports this argument.

In addition, an extra simulation has been run to investigate the impact of SPM effect in comparison with the SRS effect on the SCG in the fibre under the experimental conditions. Generally, it is not possible to separate, for example, SPM from FWM in the simulation. Instead, the SRS effect in the simulation is intentionally switched OFF in the model. This leaves all the Kerr nonlinearities (including SPM, FWM, and so on) intact. So under an average pump power of 30 mW (corresponding to a peak power of 100 W), for the 1.35 m long fibre, the outcome trace is very similar to the original pump and the broadening of the spectrum is minor due to the high normal dispersion at the pump wavelength. It strongly suggests that at the initial broadening stage of the spectrum when the generated SC is within the highly normal dispersion regime, no significant broadening occurs without the assistance of the Raman effect. Therefore, the SPM effect does not play a significant role in such a situation. Of course, once the SC is close to and/or crosses the ZDW, all the nonlinear effects contribute significantly to the SC.

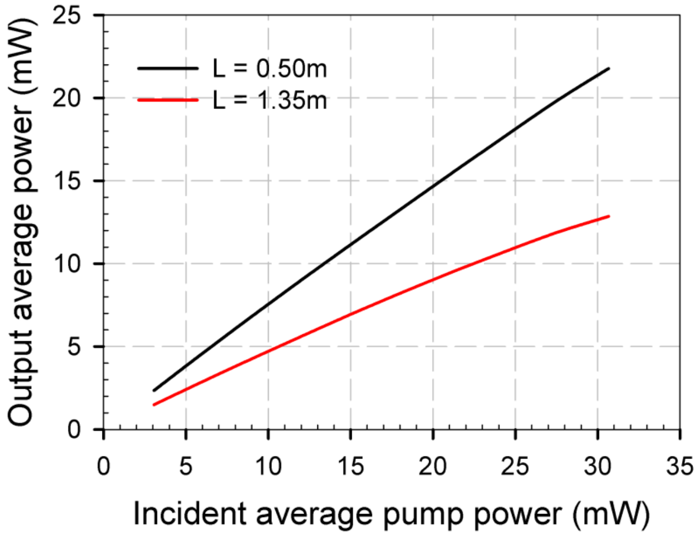

Fig. 4-10 Calculated output average powers vs incident average pump powers.

Fig. 4-10 shows the calculated output average SC power with respect to the incident average pump power for the fibre lengths of 0.5 m and 1.35 m. When the incident average pump power increases from 3 mW to 30 mW, the conversion efficiency (the output average SC power with respect to the incident average pump power) in the 0.50 m-long fibre decreases from ~77% to ~71%, while for the 1.35 m-long fibre the conversion efficiency decreases from ~49% to ~42%. These numbers match well with the experimental results, considering the differences in launched pump power as discussed above.

4.2.4.3 Perspective of power scaling for high power SC applications

SC source with higher output power could not be achieved in the experiment due to damage of the input facet of the PCF when the incident average pump power reaches ~140 mW (corresponding to a peak power of ~487 W). Fig. 4-11 shows optical photographs of the cross section of the tellurite glass ASC PCF before and after the facet damage. It can be seen that in the damaged fibre the ASC has disappeared but the three supporting spokes still exist. Such damage has been observed repeatedly under the same launched average pump power level. The damage intensity is estimated to be ~18.7 GW/cm^2. The surface damage threshold of tellurite bulk glasses has been reported to be ~15-20 GW/cm^2 using a Nd:YAG laser at 1064 nm with a similar pulse duration of ~25 ps [148]. Note that the reported damage threshold of tellurite bulk glass was measured before the light was launched into the glass so that the combined Fresnel reflection loss, which is ~20% given the light beam is at near-normal incident to the interface, was not taken into account. Even though, the damage threshold obtained from this experiment is still comparable to the reported value of the bulk glass.

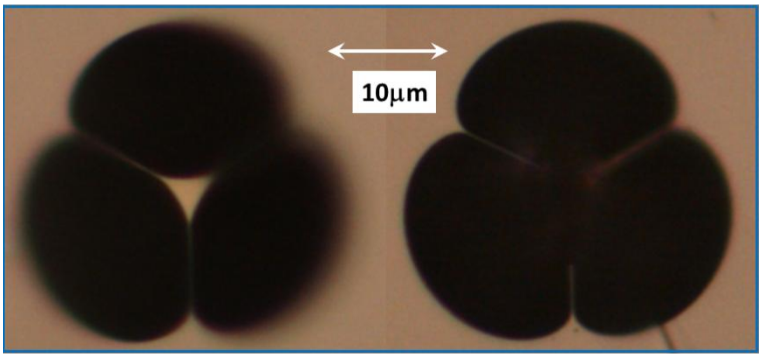

Fig. 4-11 Optical microscopic images at the input end of the tellurite ASC PCF before (left) and after (right) the damage.

Power scaling is always desirable for a laser source for practical purposes such as industrial and defence usage. For RE doped fibre lasers or Raman fibre lasers, power scaling of the laser can be achieved by scaling up the core diameter of the fibre. However, for a fibre-based SC source realized through pumping near the ZDW, the dispersion profile plays a dominant role for the SC spectrum profile and the SC bandwidth. With such a pumping scheme, unfortunately scaling up the core diameter from micron-size to tens of microns reduces the waveguide dispersion and causes the red-shift of ZDW towards the ZDW of material [196]. From Fig. 4-4 one can see such a difference on the dispersion profile between a small-core tellurite fibre and a large-core tellurite fibre. As a result, for tellurite glass fibres, using the ZDW and anomalous dispersion pumping scheme, power scaling by the means of enlarging the core diameter means that the pump laser wavelength needs to chase the red-shift of the ZDW of fibre. Typically a practical SC fibre source will rely on a CW or pulsed high power fibre laser at ~1.06 or ~1.55 μm, which is the lasing wavelength of high power Yb^{3+} and Yb^{3+}/Er^{3+} doped fibre laser. Note that the core diameter is required to be close to 1 μm for the tellurite glass fibre with ZDW at around 1.06 μm [56]. Therefore, the commonly available high power fibre lasers (at ~1.06 or ~1.55 μm) will be in the normal dispersion region of the tellurite glass fibre with a larger core diameter.

On the other hand, using the normal dispersion pumping scheme, the dispersion of the fibre becomes less problematic. If a large-core tellurite fibre is applied, more cascaded Raman Stokes orders are required before they reach and cross the ZDW (~2 μm) of the fibre, nevertheless the general mechanisms for generating a broadband SC are the same as in the small-core fibre, as shown in this experiment in Fig. 4-6. Additionally, in such a case, a much higher output power can be obtained without fibre damage. For example, when a large-core tellurite fibre with a LMA (A_{eff}) of 500 μm^2 at 1060 nm is considered, it can be deduced that the incident average pump power causing facet damage will be as high as ~27 W. Note that the fabrication of a very LMA tellurite PCF with A_{eff} of 3000 μm^2 has even been demonstrated [196].

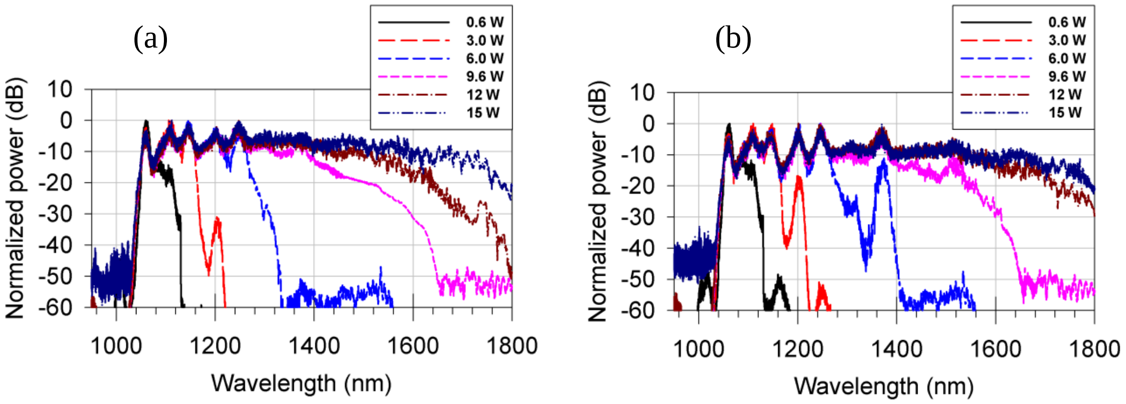

Fig. 4-12 Simulated SC generated in LMA (A_{eff} = 500 μm^2) tellurite PCF with lengths of (a) 1 m and (b) 2 m for launched average pump powers of 0.6 W, 3.0 W, 6.0 W, 9.6 W, 12 W, and 15 W.

Numerical simulations have been carried out to confirm the power scalability of SC in a tellurite glass fibre with a LMA of 500 μm^2. The simulations were developed by Dr. Peter Horak in ORC. Fig. 4-12 shows the simulation results for a 1 m-long (a) and 2 m-long (b) tellurite LMA fibre with A_{eff} = 500 μm^2. The fibre loss is assumed to be 1 dB/m at 1.06 μm and the dispersion is assumed to follow the bulk material dispersion with a ZDW of ~2.15 μm. The same pump source properties are chosen as for the simulations in Fig. 4-9 but have been scaled to higher powers. The launched average powers are set as 0.6 W, 3.0 W, 6.0 W, 9.6 W, 12 W and 15 W, corresponding to the peak powers of 2 kW, 10 kW, 20 kW, 32 kW, 40 kW and 48 kW, respectively. Fig. 4-12 shows the output spectra at these incident pump powers from 1 m-long and 2 m-long LMA tellurite fibres. The evolution of the spectrum broadening is very similar to that from the small-core tellurite glass ASC PCF, as illustrated in Fig. 4-9. With the increase of the incident pump power, the output spectrum extends to the longer wavelength with the assistance of the SRS. For the incident average pump power of 15 W, the broadband SC spanning from 1.1 μm to 1.7 μm, with 10 dB bandwidth, is respectively generated from 1 m-long and 2 m-long LMA tellurite fibres. At this point, it can be seen that there is no significant advantage by using 2 m-long fibre over using 1 m-long fibre, because of the walk-off effect. In the presence of the bulk dispersion profile, with Equation (4-3), the walk-off length is calculated to be ~0.63 m between the pump source (1060 nm) and the first-order Raman Stokes wave (~1150 nm).

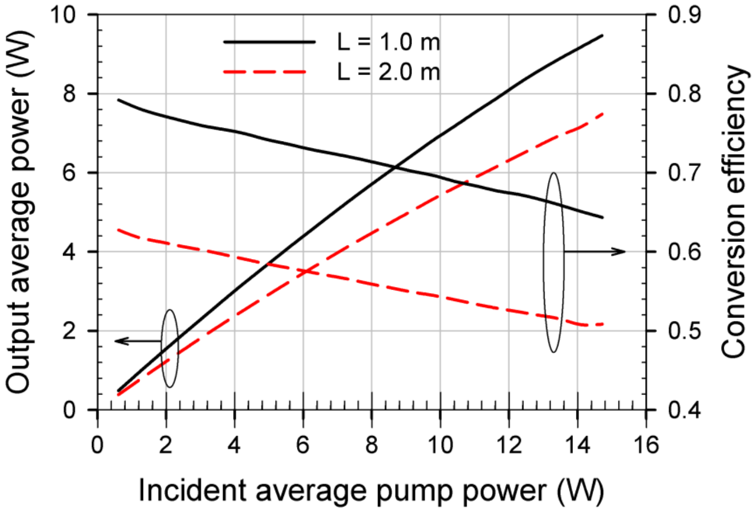

Fig. 4-13 Calculated output average powers vs incident average pump powers (left axis) and conversion efficiency vs incident average pump powers (right axis) with the 1 m-, and 2 m- long , LMA (A_{eff} = 500 μm^2) tellurite fibres, respectively.

Fig. 4-13 shows the calculated average output power and conversion efficiency as a function of the incident average pump powers for 1 m-, and 2 m- long LMA tellurite fibres. It can be noted that the generated SC output power as well as the conversion efficiency is higher from the shorter length (1 m) fibre than that from the 2 m-long fibre, due to the higher loss in the longer fibre. More than 60% conversion efficiency can be expected in a 1 m-long fibre when the average launched power increases up to 15 W. In other words, a SC from 1.1-1.7 μm, i.e., with a 10 dB-bandwidth of ~600 nm and with an average output power of 9.5 W, corresponding to a mean spectral density of ~15.8 mW/nm, can be achieved in a 1 m-long LMA tellurite fibre. Hence, a LMA tellurite fibre is a promising candidate for generating watt-level near-IR SC using the normal dispersion pumping scheme. Though the SC bandwidth using the normal dispersion pumping scheme here is not as great as the one obtained from the 1550 nm anomalous dispersion pumping (from ~0.9 μm to ~2.5 μm) [197], the high average power of SC output, the high spectral intensity, and the high pump-to-SC conversion efficiency in this work indicate the promise of generating a high average power SC source.

4.3 Fusion splicing non-silica glass fibres with standard silica fibres

In reality, it is necessary to integrate the above non-silica glass HNLF into the existing silica fibre based telecommunication system by joining these two different types of optical fibres together. In comparison with other alternatives like connectors or free-space coupling, splicing (mechanical splicing and fusion splicing) is a key technology to achieve compact and robust integrated fibre based devices. Also, low splicing loss is always desirable for connecting two fibres together. Reducing splice loss between two dissimilar fibres is fundamentally limited by the mismatch of the NA and the effective mode area of the two fibres [198, 199]. Apart from these intrinsic reasons, the quality of the fibre cleaved facets and the splice processing parameters are also important for obtaining low splice loss [199].

In a mechanical splice, two cleaved fibres are mechanically aligned to each other and then the index matching gel is positioned between the fibre tips to minimise the Fresnel reflection loss. Inasmuch as the connection loss due to the mismatch of MFD of the two fibres cannot be avoided, mechanical splicing is often applied to join two fibres with similar MFDs together. In addition, mechanical splicing is often carried out at room temperature and consequently it is ideal for joining silica fibre with non-silica glass fibre, which possesses very different thermal properties from the silica counterparts. For instance, a low splicing loss of ~0.3 dB per point has been reported by NTT (Japan) between a high-NA small-core tellurite glass fibre and a high-NA silica fibre, by means of the mechanical splicing method [149]. However, the mechanical splicing loss will be significantly enhanced for two fibres with different MFDs. Besides, the refractive index of most index matching compounds unfortunately varies with temperature, so that the performance of a mechanical splice can be very sensitive to the working temperature. Consequently, the main drawback of the mechanical splicing is that it cannot sustain laser powers above watt-level. This makes mechanical splicing less competitive than fusion splicing for high power applications. For example, in the case of connecting standard silica fibres with small-core non-silica HNLFs for FWM-based nonlinear applications, the required average power level of the pump laser (CW or pulsed) launched into the small-core HNLF is typically ~1-10 W [200]. Under such a high power level, a high mechanical splice loss will easily heat up the connection joint leading to burning the splice.

Compared to the mechanical splicing, the fusion splicing is to melt or fuse the ends of two fibres together using localized heat. As a result, the light passing through the fibres will not have been scattered or reflected back by the splice and so the splice and the region surrounding it are almost as strong as the virgin fibre itself, which is robust to environmental perturbations. Electric arc fusion splicing is commonly used and the splicing loss of conventional silica fibres can be reduced to ~0.01 dB per joint. In addition, the MFD of a fibre could also be expanded under heating [201], and low-loss (less than 1 dB/joint) fusion splicing small-core PCFs with standard silica fibres have been demonstrated via multi-arcing technique [202]. Besides, connecting high-index bismuth glass fibre with silica fibre has been realized via the fusion splicing approach as well and less than 0.5 dB/joint splice loss has been achieved [62, 203]. Therefore, fusion splicing is obviously a better solution than the mechanical splicing to obtain long-term and reliable splices with low connection loss between silica fibres and non-silica glass HNLFs.

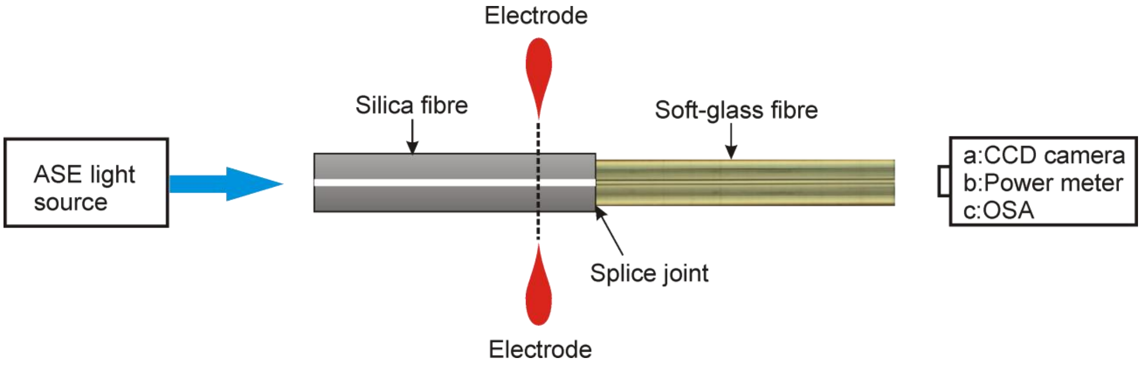

Fig. 4-14 Schematic diagram of arc-fusion splicing the soft-glass fibre with the silica fibre.

In this work, a commercial arc-fusion splicer (Model: Ericsson FSU 975) has been employed to splice the commercial silica fibres with home-made soft-glass HNLFs. Fig. 4-14 illustrates the experimental setup of splicing the two types of dissimilar glass fibres. After the fibre facets have been perpendicularly cleaved, they are mounted onto the V-grooves of the splicer. With a C-band ASE light source (FL7010), the two fibre tips are manually aligned through monitoring the output from the soft-glass fibre with a CCD camera to ensure the light has been guided only in the core of the fibre. The power in the core should be maximized by careful alignment. In order to form a fusion splice, the glass fibre must be softened with the corresponding viscosity reduced down to a level of 10^5 poise[2] [199]. For achieving this viscosity on the glass fibre, the temperature on the silica fibre should reach above 2000 ºC, whilst the lead silicate glass (Schott SF57 or SF6 for example) should be heated to just ~700-800 ºC and the tellurite (e.g., TZN) glass fibre should be heated to only about 400 ºC, respectively. Such a large thermal mismatch between the silica and non-silica fibre requires that the arc-electrode of the splicer (see the dashed line in Fig. 4-14), i.e., the heat source, has to be moved away from the splice joint position, to establish an offset splicing configuration as shown in Fig. 4-14. Additionally, the electric current (i.e., the actual temperature applied to the splice position) in the splicing process programme has to be lowered down to a specific level to match the low melting temperature of the soft-glass fibre. Ideally, the heat from the arc-electrode will be conducted through the silica fibre towards the splice joint position. The final temperature at the splice joint between the silica fibre and non-silica fibre should be just above the temperature for the non-silica glass fibre reaching the viscosity of 10^5 poise, to form a good splice.

For example, Fig. 4-15 (a) illustrates the outcome of the photograph after splicing with a high current of ~6 mA, at which temperature the soft-glass fibre tip is melted into a micro-

---

[2] Water has a viscosity of 0.00899 Poise at 25 ºC and a pressure of 1 atomsphere.

sphere. On the contrary, if the current is lowered down to ~4 mA, a good splice is formed, as seen in Fig. 4-15(b). Note that the offset distance between the soft-glass fibre tip and the electrode depends on the fibre diameter and the composition of soft-glass fibres. In this work, the offset distance is typically between 300-500 µm.

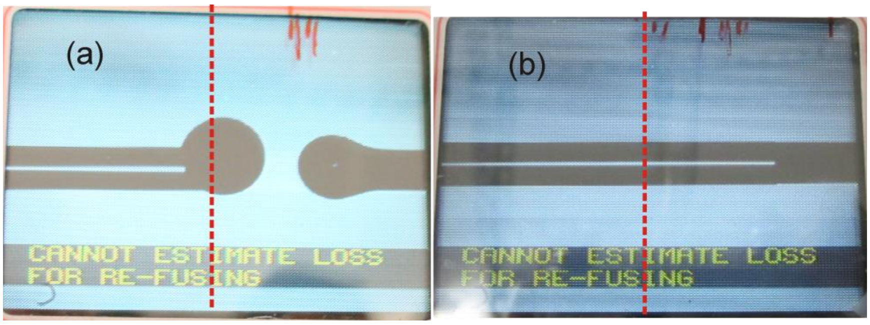

Fig. 4-15 Photograph of the spliced high-NA silica fibre (Nufern UHNA3) (left) and a lead silicate glass fibre (right) with a high current (a) and a proper low current (b). The dashed red line indicates the position of the arc-electrode.

Several small-core lead silicate glass fibres and a LMA tellurite glass fibre have been successfully fusion spliced with standard silica fibres. In practice, in order to obtain low splicing loss, a high-NA silica fibre, UHNA3 (from Nufern) is used as the bridge fibre between the conventional silica fibre (i.e., SMF28) and the small core non-silica glass fibres, whilst PS980 (from Fibrecore, Ltd) is used as the bridge fibre between the LMA tellurite glass fibre and SMF28 fibre. Note that <0.5 dB/joint splicing loss between the bridge fibre UHNA3 (MFD: 4.1 ± 0.3 µm @1550 nm) with Corning SMF28 (MFD: 10.7 ± 0.5 µm @1550nm) fibre has been obtained via symmetric, multi-arcing technique [202].

Table 4-3 summarises the outcome of fusion splicing two types of soft-glass fibre samples with silica fibres. Note that the splicing loss is obtained as the average joint loss of the input and output splicing joints (both ends of the soft-glass fibre are spliced with silica fibre). For each type of fibre, several splicing samples have been made and the splicing loss between the soft-glass fibre and the silica glass fibre is within the range listed in the Table 4-3.

For 1D MOF fibre, the lowest splicing loss is ~0.6 dB/joint. For W-type fibre-2, the best splicing loss is ~1.6 dB/joint. Also for W-type fibre-1, the best coupling efficiency through the free space lens coupling method has been reported to be ~25% [179], i.e., ~6 dB/joint. However, with fusion splicing, the connection loss is about 4 dB/ joint, which has been improved by ~2 dB/joint. Note that the variation of the splicing loss (referred to as the repeatability of splicing) is due to the quality of the cleaved fibre tips, the alignment, the stability of the heating temperature, the uniformity of the fibre and the mismatches of the refractive index, NA and MFD of the two fibres. Such a variation should be ultimately overcome by using high-precision apparatuses and high-quality uniform fibres.

Table 4-3 Summary of the fusion splicing results.

Silica glass fibre	Soft-galss fibre	Key parameters[3]	Splicing loss (dB/joint)
UHNA3 (Nufern) MFD: 4.1 μm @1.55 μm OD: 125 μm	1D MOF [61] (Lead silicate glass)	Core dia : 3.9 μm; OD: 150 μm A_{eff} = 6.7 μm^2	0.6 – 2.2 @1550 nm
	W-type fibre-1 [179] (Lead silicate glass)	Core dia: ~1.7 μm; OD: 115 μm A_{eff} = ~2 μm^2	3.5 – 4.5 @1550 nm
	W-type fibre-2 (Lead silicate glass)	Core dia: ~1.65μm; OD: 93μm A_{eff} = ~2 μm^2	1.6 – 4.0 @1550 nm
	W-type fibre-3 (Lead silicate glass)	Core dia: ~1.7 μm; OD: 115 μm A_{eff} = ~2 μm^2	2.5 – 5.0 @1550 nm
PS980 (fibre core) MFD: 6μm @0.98 μm OD: 125 μm	LMA fibre (Tellurite glass)	Core dia: ~13 μm; OD: 146 μm	8.4 @1047 nm

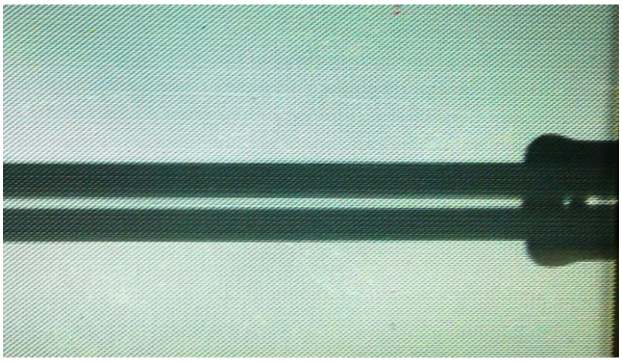

Fig. 4-16: Photograph of the spliced silica fibre (PS980) (left) and a tellurite LMA fibre (right) after fusion splicing.

Apart from the lead silicate glass fibres, a LMA tellurite glass fibre has also been tried to be spliced with a PS980 silica fibre and Fig. 4-16 shows the splice joint. The average splicing loss is ~8.4 dB/joint. Such a high loss value is believed to be due to the large mismatch of the MFD,

---

[3] In this column, Core dia represents core diameter and OD stands for outer (cladding) diameter.

NA and refractive indices between the two types of fibres. The different refractive indices results Fresnel reflection loss at the connection joint, which can be evaluated as $-10 * log_{10}[1 - \left(\frac{n_0^{LMA} - n_0^{PS980}}{n_0^{LMA} + n_0^{PS980}}\right)^2]$ [76]. Also, the connection loss caused by coupling light from large MFD (i.e., D_l) to small MFD (i.e., D_s) fibre can be calculated as $-10 * log_{10}(D_s/D_l)^2$ [198]. Likewise, there is connection loss when launching light from large NA (i.e., NA_l) to small NA (i.e., NA_s) and is usually estimated as $-10 * log_{10}(NA_s/NA_l)^2$. Otherwise, the connection loss could be ignored when coupling light from small MFD and NA to large MFD and NA. Table 4-4 shows the losses due to the Fresnel reflection, mismatch of the MFD and NA. When splicing the LMA fibre with PS980 at both ends, the average loss of the input and output splice joint can be calculated by Loss_n_0 + (Loss_MFD + Loss_NA)/2 = 5.9 dB, as shown in Table 4-4. However, the experimental splice loss (8.4 dB/joint) is higher than the calculation (5.9 dB/joint), which could be due to the core offset during splicing process (e.g., during pushing the fibre tips together), under-estimated the fibre propagation loss and uncertainties in the MFD of the fibres. The connection loss can be reduced by matching the MFD and NA of the two fibres.

Table 4-4 Refractive index, MFD, NA and calculated connection loss of the PS980 and LMA fibres.

Fibre	n_0	Loss_n_0 (dB)	MFD (μm)	Loss_MFD (dB)	NA	Loss_NA (dB)	Loss_avg (dB)
PS980	1.45	0.11	~6	6.72	~0.14	4.86	5.9
LMA	2		~13		~0.08		

Furthermore, the reliability as well as the stability of the splice joint with respect to the input pump power is very important for practical applications. Fig. 4-17 (a) shows the evolution of the splicing loss with the increase of the input pump power (CW, at 1550 nm). It is evident that the splicing loss remains constant at 2.74 ± 0.25 dB (per joint) with the pump power going up to 3.8 W. Note that the maximum input pump power is limited by the output of the 1550 nm laser source. Fig. 4-17 (b) shows the stability of the output power at the maximum input pump power of 3.8 W within 10 minutes at room temperature. It indicates that the splice is robust for continuous operation of at least 10 mins without any observable degradation on the output power. With the active cooling technique applied at the splice joint, it can be deduced that the splice joint is able to stand with an even higher pump power and last for an even longer operation time.

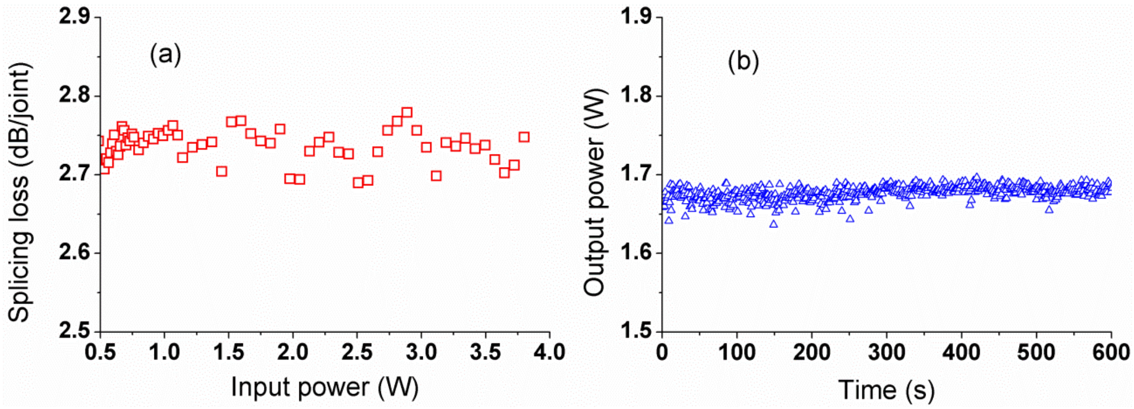

Fig. 4-17 Evolution of (a) the splicing loss vs the input power at 1550 nm and (b) the stability of the splicing at the input power of 3.8 W at room temperature.

4.4 Photosensitivity of high-index non-silica glass fibres

Directly writing FBGs into the core of non-silica glass fibres to form laser cavities will eliminate the splicing-induced connection loss at each pass of the signal in the fibre laser applications. Also, integrating the FBGs into the HNLFs will produce a number of compact fibre devices, such as all-optical switching devices and wavelength converters.

This section presents the study of inscription FBGs into the non-silica glass fibres, including (1) a review of the photosensitivity and Bragg gratings in fluoride, lead silicate, Bi_2O_3-, TeO_2- and chalcogenide glasses and their fibres; (2) experimental data of the photosensitivity of lead silicate and tellurite glasses; and (3) the challenges of writing FBGs into non-silica glass fibres.

4.4.1 Review of the photosensitivity properties of fluoride, lead silicate, bismuth, tellurite and chalcogenide glasses and fibres

Material photosensitivity refers to a permanent change of the refractive index or opacity induced in the material by exposure to light radiation [5, 11]. It is the foundation to fabricate fibre gratings, which is the main objective of this work. The mechanism of photosensitivity in germanosilicate optical fibres has been widely studied in the past two decades [4, 5, 204]. Novel photonic materials with higher photosensitivity are sought, such as lead silicate glass [205] and chalcogenide glass [206], and they have been receiving more and more attention as promising candidates as the host materials of special optical fibres to produce FBG-assisted optical fibre devices.

4.4.1.1 Fluoride glass (ZBLAN)

The fluorozirconate glass based on the composition of ZrF_4-BaF_2-LaF_3-AlF_3-NaF (ZBLAN), is the most thermally stable representative of the fluoride glass host for an optical fibre. It has been proven to have much more promising optical properties than silica-based glasses as the fibre host material, in terms of extremely low attenuation (<50 dB/km) in the 0.5–3.5 μm region and low phonon energy [207].

Previous studies show that undoped ZBLAN glass exhibits almost no UV photosensitivity at 248 nm, whilst small index change ~ 2.6 x 10^{-6} (@1550 nm) is observed in ZBLAN glass with radiation at 193 nm [208]. However, with the rare-earth dopants, ZBLAN glasses are found to be photosensitive to the UV radiation at round 248 nm [209, 210]. In particular, permanent Bragg gratings with an index change in the order of 10^{-5} (@633 nm or 1560 nm) have been reported in Ce-doped ZBLAN glasses and optical fibres by Taunay et al. [210]. In that work, a pulsed UV laser around 248 nm (from 235 nm to 250 nm) with a fluence of ~250 mJ/cm^2 per pulse was used as the pump source, because of the strong absorption of the Ce-doped ZBLAN at this wavelength band, as seen in Fig. 4-18. The mechanism for the photosensitivity of RE-doped ZBLAN glass and fibre has not yet been fully understood, but it is believed that it arises from the two-photon absorption of 248 nm light [209, 210]. The thermal stability of the Bragg gratings in Ce-doped ZBLAN glasses was measured by annealing up to 200ºC and the refractive index change was found to be reduced by a factor of 3 compared with the initial value [210]. In addition, the index change in other rare-earth, i.e., Tb-, Pr- and Tm-doped ZBLAN has been found to be more than 2 orders of magnitude smaller than that in Ce-doped ZBLAN glass [209].

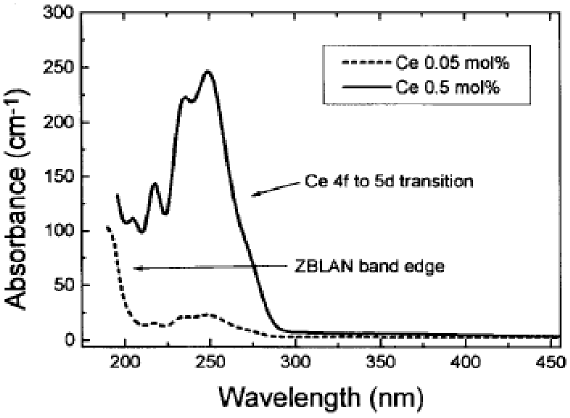

Fig. 4-18 Absorption spectra of Ce-doped ZBLAN glasses. (After Ref. [209]).

4.4.1.2 Lead silicate glasses (SiO_2-PbO glasses)

Lead silicate glasses, e.g., Schott commercial flint glass (with the codes of F, SF, and ZF, etc) have been found to be photosensitive across a wide spectral region range, including 193 nm (excimer ArF laser) [205], 244 nm (frequency doubled of Ar-ion laser) [211], 248 nm (excimer KrF laser) [205, 211], 266 nm (frequency quadrupled of Q-switched Nd:YAG laser) [205, 212, 213] and 308 nm (excimer XeCl laser) [214]. Even though, color centres were formed in lead silicate glasses via two-photon absorption of 532 nm from a Nd:YAG laser, no photosensitivity was observed in these glasses at laser intensities up to its damage threshold [215].

A large photo-induced refractive-index change (Δn) with a value of 0.21 (@633 nm) was first reported in SF59 glass (with 57 mol% PbO) with the radiation of 266 nm UV laser at a fluence of 25 mJ/cm^2 per pulse by X. C Long [212]. However, a negative index change with a value of -0.25 (@633 nm) in lead silicate glasses with 50 mol% PbO was observed by exposuring the glasses to the 266 nm laser with an energy density of 50 mJ/cm^2 [216]. Also, channel waveguides with Δn of 2.9 x 10^{-2} were written in SF57 glass with 244 nm laser with power level above 50 mW [211]. The index change was thermally stable up to the glass transition temperature [205, 211, 212, 216]. The mechanism of the photosensitivity in lead silica glasses has not been understood completely, but it is believed that bond breaking and structure changes play the key role [205, 216]. In addition, it has been found that Δn increases exponentially with the PbO concentration [205, 216] and photo-induced structural changes of lead silicate glasses are related to the UV laser energy density [216].

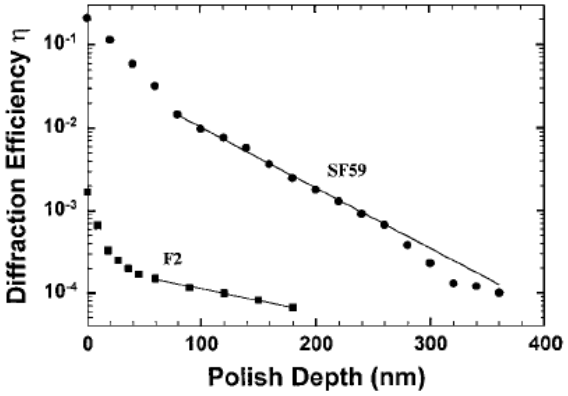

Fig. 4-19 Depth profile of the diffraction efficiency for 248 nm-laser induced grating on SF59 and F2. (After Ref. [212])

However, such strong UV laser induced gratings or waveguides on lead silicate glasses are only possible within the depth in the order of 100 nm because of the high absorption coefficient (>1 µm^{-1}) of glass at the UV wavelength. Fig. 4-19 shows the relation between the diffraction efficiency and the polish depth of lead silicate glasses of SF59 and F2 [212]. It is evident that the amplitude of the index modulation drops sharply after the ~100 nm thickness on the exposed SF59 glass surface is removed. This indicates that it is indeed difficult to write Bragg gratings into the core of the lead silicate glass fibres (the diameter of the cladding is at the order of 100 µm) with 244 nm or 248 nm UV laser due to the high UV absorption, if the cladding glass is of similar composition to the core glass.

4.4.1.3 Tellurite (TeO_2-based) glasses

Tellurite glasses have attracted great attention because of the attractive optical properties, such as a wide transmission window (0.35-5 µm), good glass stability, high solubility for rare-earths, and high nonlinear refractive index [217]. They are promising host materials for optical fibres for advanced nonlinear applications [59, 149, 187, 189]. The UV-absorption edge of tellurite glass is related to the glass composition and also to the impurity dopants, e.g., transition metal and RE ions [217-219]. A channel waveguide was formed on the surface of tellurite glass with 244 nm radiation and the index change was estimated to be ~1x10^{-3} [220]. In addition, a negative index change was observed in Er-doped tellurite glass with radiation at 308 nm [218] and CoO-doped tellurite glass irradiated by a green light-beam spot at 532 nm [221, 222]. The mechanism of changing the refractive index of tellurite glass by UV-radiations is not yet clarified at present either. But it has been suggested that the index change mainly originates from the thermal relaxation on glass structures caused by laser heating/cooling of the glass.

4.4.1.4 Chalcogenide glasses (chalcogen S, Se, Te based)

Chalcogenide glasses are well-known for the excellent transparency in mid-IR region, and possess high linear and nonlinear refractive indices. Thus, they are considered as promising host materials for mid-IR optical fibre devices [50, 223]. The optical bandgap edge of the chalcogenide glass is typically located in the visible region and thus the glass exhibits high absorption in the visible region and typically shows the colour of red or black. FBGs at 1543 nm with average index changes as large as ~4.7x10^{-3} have been demonstrated in As_2Se_3 fibres via the transverse holographic method by Brawley et al. [224]. In that work, the pump source was CW operation with 5 mW output power at 785 nm, at which the absorption of As_2Se_3 glass was around 25.5 cm^{-1} and also the photo-induced index change was observed to be negative. With the exposure laser at 800 nm, surface relief gratings were observed on As_2Se_3 glasses [225]. In addition, FBGs in As_2S_3-based glass fibres have been reported with the exposure of a CW He-Ne laser at 633 nm, at which the absorption coefficient was around 30 cm^{-1} [48]. The photosensitivity of As_2S_3-based glass with the radiation of 780-800 nm has been observed by C. Meneghini and A. Villeneuve [226], in which the photo-induced index change is believed to be due to two-photon absorption. It has also been predicted that the penetration depth at ~800 nm is as deep as ~2 cm, which strongly suggests that FBGs could be fabricated in As_2S_3-based glass fibres with 800 nm light source.

4.4.1.5 FBGs inscription in non-silica glass fibres with fs laser sources

The fs-IR inscription technique for FBGs can overcome the limitation of the UV transparency or UV photosensitivity. It is a powerful and versatile approach to write gratings into a wide range of optical fibres, i.e., Ge-free silica fibres [86, 227] and non-silica glass fibres such as phosphate, fluoride, tellurite, bismuth oxide and chalcogenide glass fibres [46, 47, 49, 227-230]. In those works, an ultrafast (125 fs) Ti:Sapphire laser operating at 800 nm with the pulse energies ranging from 0.2 to 2 mJ/pulse and the repetition rates of 1 to 1000 Hz, was used as the pump source to write FBGs. Phase masks are often used to form the interference patterns into the core of fibres. Even though a phase mask possesses poor zero-order suppression, pure two-beam interference gratings with fs-IR lasers can be established at a distance d normal to the phase mask, as illustrated in Fig. 4-20 [229]. This is due to the walk-off effect of the diffracted order beams. Besides the phase-mask method, the point-by-point technique has also been employed to write FBGs with fs-laser sources [7, 231]. The mechanism of the index change during the fs-IR irradiation differs from the UV-photon induced index change and it is likely to be due to the multi-photon absorption and ionization process [229].

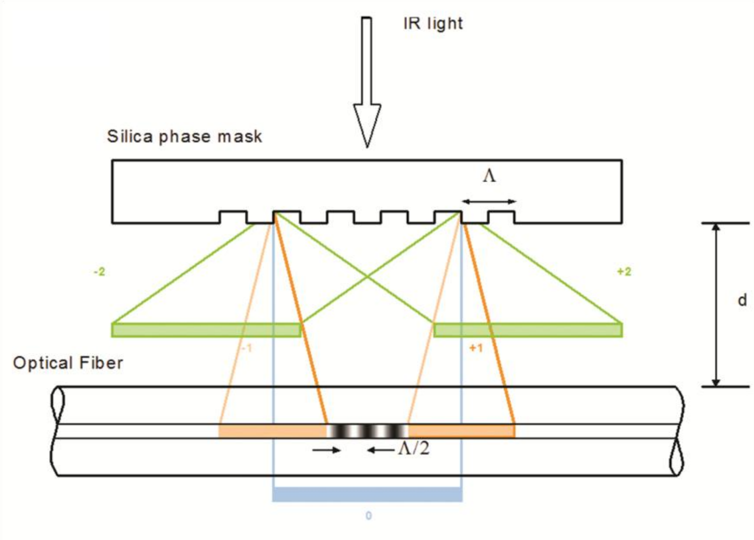

Fig. 4-20 Schematic diagram of diffractive order walk-off for a phase mask with IR light irradiation. (After Ref. [229])

4.4.2 Experimental studies of the photosensitivity of lead silicate and tellurite glasses

Some attempts have been done in order to write FBGs into the home-made lead silicate glass and tellurite glass-based fibres with the phase-mask method via UV light irradiation. The lead silicate glass fibres are made of Schott glasses, i.e., the core of the fibre is made of SF57 and the cladding is made of LLF1 or LLF1/F2. The refractive indices of them have been listed in the Appendix C. The tellurite glass has the same composition of TZN as discussed in Section 4.2.

Fig. 4-21 illustrates the UV-visible wavelength absorption trends of Schott high-index SF57, SF6 (see Appendix C for the refractive index) and TZN glasses (melted in Pt and Au crucibles), respectively. They are measured by using a Cary 500 Scan UV-Vis-NIR Spectrophotometer. The absorption coefficient is calculated by assuming uniform absorption along the thickness of the glasses, which are indicated in Fig. 4-21. The absorption profiles of these glasses are similar to the preceding work. Note that the saturation at the short wavelength is due to the thickness of the glass, which can be seen from the results of SF57 with various thicknesses. Therefore, these glasses exhibit huge absorption at the UV wavelengths shorter than their bandgap edges, (i.e.,

~340 nm for SF57 and 355 nm for tellurite glass), at which the penetration depth should be restricted of the order of micro-/sub-micro-metres only. By balancing the photosensitivity and the UV penetration depth, the UV light at the wavelength near the band-edge is likely to be suitable for writing FBGs into the non-silicate glass fibres.

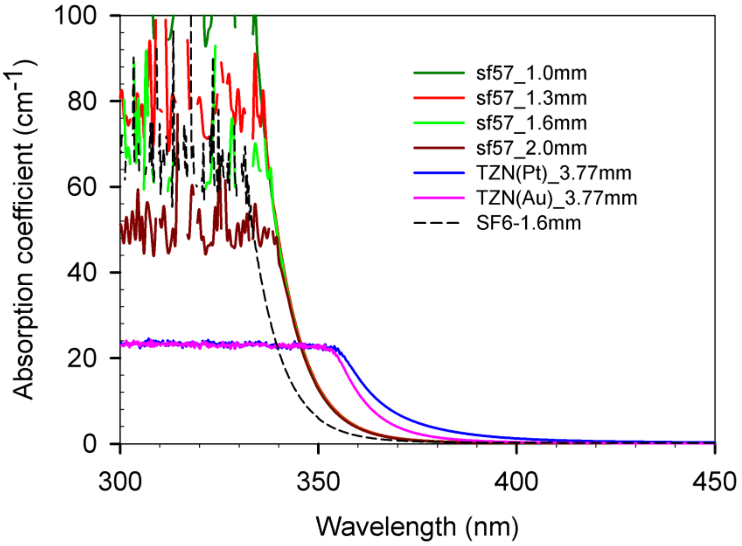

Fig. 4-21 Absorption coefficients of bulk samples of lead silicate and tellurite glasses.

The photosensitivity of these high-index non-silica glass bulk samples have been studied with a CW 325 nm HeCd laser, and a pulsed 355 nm frequency tripled Nd:YAG laser with a pulse duration of 5-6 ns and a repetition rate of 15 Hz , respectively.

Bragg gratings in bulk SF57 and tellurite glasses are observed with UV 325 nm laser exposure with the power of ~35 mW. The gratings are formed with the two-beam holographic method with a pitch of ~1.12 µm. A 633 nm He-Ne laser is probed onto the grating and a small portion of the light is diffracted according to the grating conditions. The diffraction efficiency is as small as ~9 x 10^{-5}. Due to the unknown of the absorption depth in the bulks, the index change cannot be calculated at the point of this work. However, the results indicate that the lead silicate and tellurite glasses are photosensitive to 325 nm. In addition, ~90% and ~70% light at 325 nm has been transmitted through 1.6 mm-thick LLF1 and F2 glass samples, respectively. This indicates that 325 nm light can be transmitted through the cladding (with the thickness of less than 60 µm formed by LLF1 and/or F2) of lead silicate glass fibres without attenuation to reach the core of the fibres.

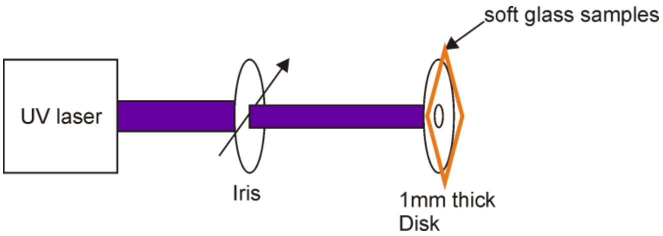

Fig. 4-22 Schematic diagram of the experimental setup for UV exposure.

With the pulsed 355 nm irradiation, the absorption spectrum of SF57 glass is measured before and after irradiation. Fig. 4-22 shows the experimental setup, in which an iris is used to reduce the size of the laser beam. On the 1 mm-thick metal disc, a pinhole is machined with a diameter of 1.5 mm, the same as the diameter of UV beam exposure to the bulk samples. The soft glass samples are mounted on the disc. After the exposure, the visible absorption spectra are measured with a sample-holder integrated with a 1 mm hole by the Cary 500 Scan. The UV-induced index change can be estimated via Kramers-Kronig relations as Equation (4-4) by using the measured absorption change of the glass samples before and after UV laser irradiation [11].

$$\Delta n(\lambda) = \frac{1}{(2\pi)^2}\int_{\lambda_1}^{\lambda_2} \frac{\Delta\alpha(\lambda')}{(1-(\lambda'/\lambda)^2)}d\lambda' \tag{4-4}$$

where $\Delta\alpha$ is the measured absorption change at wavelength of λ', which is in the range of $\lambda_1 < \lambda' < \lambda_2$.

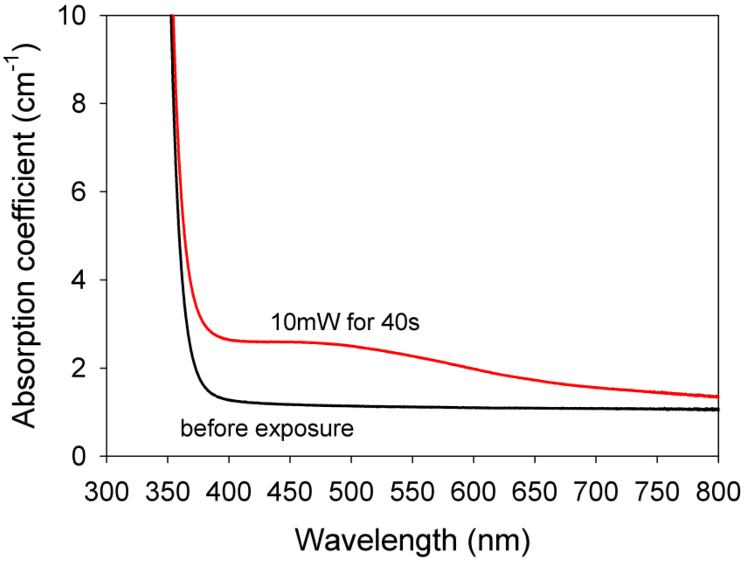

Fig. 4-23 Absorption spectra of SF57 glass before and after exposure with 355 nm with an average power of 10 mW for 40 s.

Surface damage has been observed on the SF57 glass samples when the average power of 355 nm is higher than 44 mW. Fig. 4-23 shows the absorption spectra of SF57 glass sample before and after exposure with 355 nm at an average power of 10 mW for 40 seconds, corresponding to a pulse fluence of 37.7 mJ/cm^2. It is seen that, from the UV absorption edge (~325 nm) of the SF57 glass to 800 nm, the absorption coefficient increases by at least 0.5 cm^{-1} and it increases to a maximum at around 450 nm. Fig. 4-24 shows the absorption coefficient change at 450 nm with respect to the exposure time. The uncertainty is observed by conducting the experiment several times and is due to the non-uniformity distribution of the laser intensity, the fluctuation of laser power and alignment errors when measuring the absorption by the Cary 500 Scan. The absorption coefficient change reaches saturation after the irradiation for ~60 s. According to Equation (4-4), the refractive index change at 1.3 µm is calculated (integrating from 355.2 nm to 800 nm) to be in the order of 10^{-6} after irradiation for 30 s with the average power of 10 mW. Such an index change will result in a coupling coefficient of ~2.4 /m at 1.3 µm given the effective index of the lead silicate glass ~1.8. Accordingly, in order to obtain a uniform FBG grating with reflectivity of 50%, the FBG needs to be ~37 mm long.

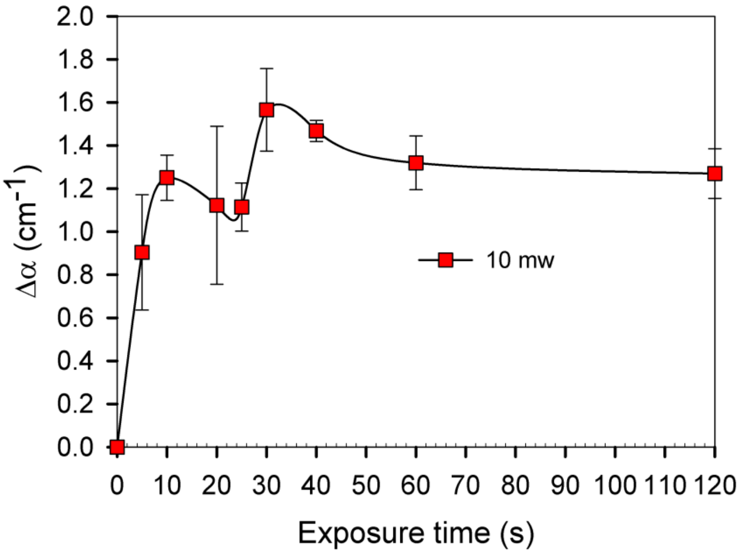

Fig. 4-24 Absorption change at 450 nm vs exposure time at the average power of 10 mW of 355 nm.

4.4.3 Challenges of inscribing FBGs into high-index non-silica glass fibres

With the evidence that non-silica glass is photosensitive to 325 nm and 355 nm UV light, it has been tried to write FBGs into these non-silica glass fibres using UV sources within this wavelength range. Fig. 4-25 shows the experimental setup for inscribing the FBGs into non-silica glass fibres. The collimated UV beam is focused with a cylindrical lens with a focal length of 20/40 cm, after which the beam is focused at the y axis, indicated by the coordinates in Fig. 4-25. A 10 mm long phase-mask, which is optimized for 355 nm and has a pitch of 726 nm, is used to induce the interference pattern into the fibres. Less than 5% UV light is diffracted by the zero-order of the phase-mask either with the 325 nm or 355 nm light source. The fibre sample is mounted straight with two clamps and placed close to the phase mask but without physically contact. Since the beam width (x-axis) is around 1 mm and less than the length of the phase-mask, both of the phase-mask and fibre are fixed on a translation stage and moved simultaneously along x-axis during the fabrication process. The non-silica fibre is spliced to standard silica fibres at both ends and the formation of the FBGs are monitored *in-situ* with a SC source (Fianium SC400). As the effective refractive index of the lead silicate glass fibre within the core is around 1.74, the predicted Bragg wavelength will be around 1263.2 nm with this phase-mask. At the time of the experiment, wide-band 3 dB coupler or circulator around 1.25 µm was not available. Therefore, a 10/90 coupler at 1117 nm was used instead to measure the reflection spectrum of the FBGs.

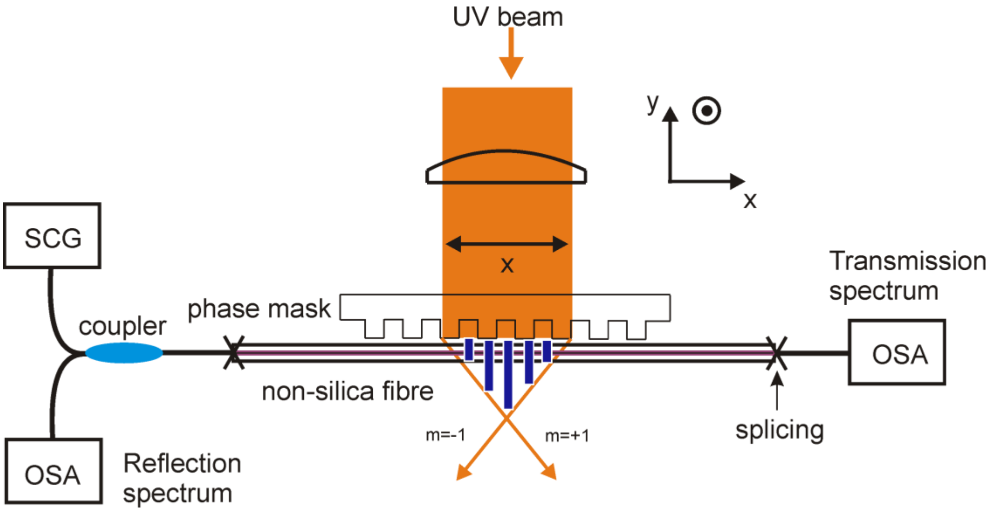

Fig. 4-25 Schematic diagram of the FBGs fabrication setup with UV source in non-silica glass fibres.

So far, solid core lead silicate glass fibres [61] with core/cladding of SF57/LLF1 have been used to write FBGs with the setup of Fig. 4-25. The experimental parameters of the UV sources adapted are summarised in Table 4-5, including the focus area (A_{focus}), the average power (P_{ave}), the peak intensity (I_{peak}), the total fluence of the UV sources before phase-mask and the velocities of the translation stage during the fabrication process. The 344 nm light source is a frequency tripled 1030 nm laser (from Fianium) with a pulse duration of 20 ps and a repetition rate of 50 MHz. Unfortunately no FBG with the detectable index change in the order of $\sim 10^{-5}$ (limited by the maximum length of phase-mask) has been observed from lead silicate glass fibres, with the experimental parameters listed in Table 4-5.

Table 4-5 Summary of the primary parameters for the FBGs fabrication.

UV source	P_{ave} (mW)	A_{focus} (cm^2)	I_{peak} (W/cm^2)	Fluence (J/cm^2)	$V_{translation}$ (mm/s)
355nm ***(5-6 ns)***	~4	~0.004 - 0.01	~4.2×10^6 – 12×10^6	~345 - 1000	0.002
325nm ***CW***	~37.5	~1.4×10^{-4} - 1.56×10^{-4}	~267-241	~1.23×10^4 - 1.23×10^5	0.002 - 0.02
344nm ***(20 ps)***	~120-380	~1.5×10^{-4}	~7.8×10^5 - 2.5×10^6	~1.6×10^5 – 5×10^6	0.001 - 0.01

However, by replacing the non-silica glass fibre with PS980 or UHNA3/7 fibres, uniform FBGs at ~1.05 µm with reflectivity as high as 60% have been successfully written with similar parameters in Table 4-5. Hence the failure to write FBGs into the lead silicate glass fibres, is mainly due to the weak UV photosensitivity properties of the lead silicate glass fibres at these UV source wavelengths.

It is indeed a great challenge to write FBGs into non-silica glass fibres with UV light sources, because (1) non-silica glasses exhibit high absorption at the UV wavelength range shorter than their cutoff wavelengths (see Section 4.4.1), which restrict the penetration depth in the order of sub-micrometres; (2) the mechanism of the UV-photosensitivity of the non-silica glasses is different from that of Ge-doped silica fibres, and is not yet well understood; (3) commonly, most of reported non-silica glass HNLFs are either made of a single material for PCFs, or similar compositions for solid core/cladding fibres. Thus both of the cladding and the core are similarly photosensitive to the UV light source such that it becomes problematic whether the UV light could reach the core but still with enough power to induce the index change; and (4) the quality of the non-silica glass fibres, in terms of the uniformity, linear propagation loss, mode confinement and so on, is not as good as the silica glass fibres and this could increase the difficulty of writing FBGs into the fibres.

However, there are several solutions to overcome these limitations: (1) using a light source at longer wavelength, e.g., visible or infrared light source, as demonstrated in chalcogenide glass fibres with 633 nm or 785 nm [48]; (2) using fs-IR laser source, which has been demonstrated in several non-silica glass fibres; and (3) doping RE ions into the core of the non-silica glass fibres to increase the absorption coefficient at specific bands, such as Ce^{3+} ion will increase the absorption at ~ 250 nm as seen in Fig. 4-18.

4.5 Conclusions

In summary, the nonlinearities of several high-index non-silica glass fibres, i.e., ZBLAN, lead silicate, tellurite, bismuth oxide and chalcogenide glass fibres, have been studies and their effective nonlinear coefficients (γ_{eff}) are found to be ~10^3-10^4 times higher than the conventional silica fibre (SMF28).

With the exception of the high γ_{eff}, the Raman gain coefficient of tellurite glass fibre is measured to be ~x35 higher than that of silica fibre. A wideband SRS-assisted SC has been observed from a metre-long ASC tellurite glass fibre by pumping at 1.06 µm, which is located in the highly normal dispersion range of the fibre. The spectral broadening is mainly attributed to the high Raman gain coefficient and the broad Raman gain bandwidth of the tellurite glass. With this normal dispersion pumping scheme, power scaling should be possible to generate a broadband infrared 1.1-1.7 µm SC with output average power as high as 10 W, corresponding to a mean spectral density of 15 mW/nm, from a ~1 m long LMA tellurite glass fibre with a mode area of 500 μm^2.

In order to improve the compatibility of the non-silicate glass fibres with the existing silica fibres, two types of non-silica glass fibres, i.e., lead silicate and tellurite glass fibres produced in-house, have been connected to standard/high NA silica fibres via the fusion splicing technique. The splicing loss between the non-silica glass fibres and silica glass fibres has been investigated and shows that less than 1 dB/joint can be achieved. It is a promising value for integrating the non-silica glass fibres into traditional silica fibre systems.

Finally, the feasibility of writing FBGs into the non-silica glass fibres with UV light sources at 325 nm, 344 nm and 355 nm has been investigated, respectively. The non-silica glasses show fairly reasonable UV photosensitivity, although, no FBG with the index change higher than 10^{-5} (limited by the sensitivity of the measurement) has been observed with the phase mask method. Alternatively, it might be a solution to write FBGs into the non-silica glass fibres by using a longer wavelength light source, e.g., visible light source or fs-IR laser sources.

Chapter 5 Concatenating PPSFs

The main purpose of this chapter is to demonstrate the feasibility of concatenating PPSFs so as to improve the overall conversion efficiency. At this point, the PPSFs used for this work were fabricated and characterised by the physical optics group in ORC [118]. The PPSFs can be fusion spliced together, but a connection loss is unavoidable. The influence of the splicing loss on the overall SHG conversion efficiency in concatenation PPSFs has been numerically studied in this work. Two similar PPSFs have been experimentally concatenated by thermal heating the interconnection section. It has been found that the overall conversion efficiency has been improved more than 2.86 times upon that of each single PPSF sample.

5.1 Numerical studies of the overall conversion efficiency of concatenation PPSFs

In this model, for simplification, it is assumed that the PPSFs are single mode and polarization maintained for both the SH wave and the fundamental wave. SEVA is applied onto the amplitudes of the SH wave ($A_{2\omega}$) and fundamental wave (A_{ω}). A CW fundamental wave is considered and undepleted during the SHG process in the PPSF. By recalling the amplitude coupled mode equations between the SH and fundamental waves, the amplitude evolution of the SH wave $A_{2\omega}(z)$ propagating along the PPSF device (z) can be expressed as [65, 71, 118]:

$$\frac{dA_{2\omega}(z)}{dz} = \frac{i\omega}{2n_{2\omega}c} A_{\omega}(0)^2 \chi^{(2)}(z) \cdot \exp{(-i\Delta kz)} \tag{5-1}$$

where ω is the fundamental frequency and c is the velocity of light in vacuum; $n_{2\omega}$ is the refractive index of the SH wave in the fibre; $A_{\omega}(0)$ is the fundamental input amplitude; $\chi^{(2)}$ is the effective second-order susceptibility induced through the thermal poling technique; Δk is the phase-mismatch between the fundamental and SH waves.

A QPM grating with a period of Λ is fabricated into the poled fibre by means of point-by-point erasure with a UV light (244 nm) to compensate the phase mismatch. The relationship between the phase mismatch (i.e. Δk, as indicated in Equation (2-32)) and the grating pitch is:

$$\Delta k = \frac{4\pi\Delta n}{\lambda_{\omega}} = \frac{2\pi}{\Lambda} \tag{5-2}$$

in which λ_{ω} is the fundamental wavelength and Δn is the index difference of the *second-harmonic wave* (SHW) and fundamental wave, which is noted as *fundamental-harmonic wave* (FHW) in the following content. Fig. 5-1 shows the schematic diagram of the core structure of the PPSF device after periodic UV erasure. The duty cycle is assumed to be 50% and the effective $\chi^{(2)}$ is assumed to be completely erased by UV exposure. For instance, as seen in Fig. 5-1, the effective $\chi^{(2)}$ is unity in the poled region and returned to zero after UV erasure. Therefore the coherence length is found to be half of the pitch, i.e., $l_c = \Lambda/2$.

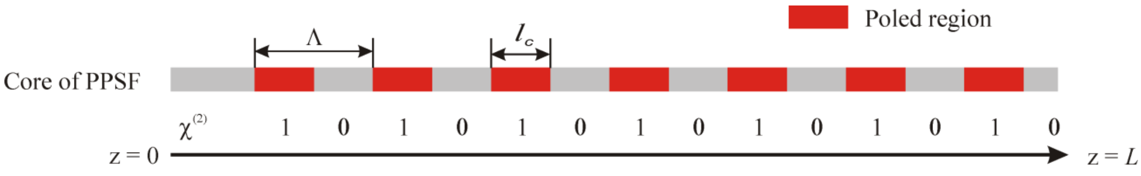

Fig. 5-1 Schematic diagram of the core structure of the PPSF after periodic UV erasure.

From Equation (5-1), the amplitude of SHW at the output of L-long PPSF can be obtained as:

$$A_{2\omega}(L) = \frac{i\omega A_{\omega}(0)^2}{2n_{2\omega}c}\int_0^L \chi^{(2)}(z)\cdot \exp\left(-i\Delta kz\right) dz$$
$$= \frac{i\omega A_{\omega}(0)^2}{2n_{2\omega}c}\sum_{j=1}^{N}\int_{l_{c(j-1)}}^{l_{cj}}\left|\frac{1-(-1)^j}{2}\chi^{(2)}(z)\right| \exp\left(-i\Delta kz\right)dz \tag{5-3}$$

in which the subscript j is the number of the coherence length along the fibre and $l_{c0} = 0, l_{cN} = L$. Consequently, the output SHW power can be calculated by:

$$P_{2\omega}(L) = \frac{1}{2}\varepsilon_0 c n_{2\omega} A_{eff} A_{2\omega}(L) A_{2\omega}{}^{*}(L) \tag{5-4}$$

where ε_0 is the vacuum permittivity ($\varepsilon_0 = 8.8542\times10^{-12}F/m$) and the A_{eff} is the effective area for SHW. Therefore, the overall normalized conversion efficiency, η, with the incident fundamental power of $P_{\omega}(0)$, can be evaluated.

$$\eta = \frac{P_{2\omega}(L)}{P_{\omega}(0)^2}\ W^{-1} \tag{5-5}$$

Practical parameters for PPSFs are used for simulation. The length of PPSF is ~20 cm with the $A_{eff} = 50\ \mu m^2$ for SHW. The fundamental wavelength is selected as ~1541 nm, and the coherence length is ~33.2 μm based on the experimental results [118]. The refractive index for SHW is assumed to be 1.45 and the effective $\chi^{(2)} = 0.14\ pm/V$. By combining the Equations of (5-3), (5-4) and (5-5), the normalized conversion efficiency for single PPSF is calculated to be ~0.083 %W^{-1}.

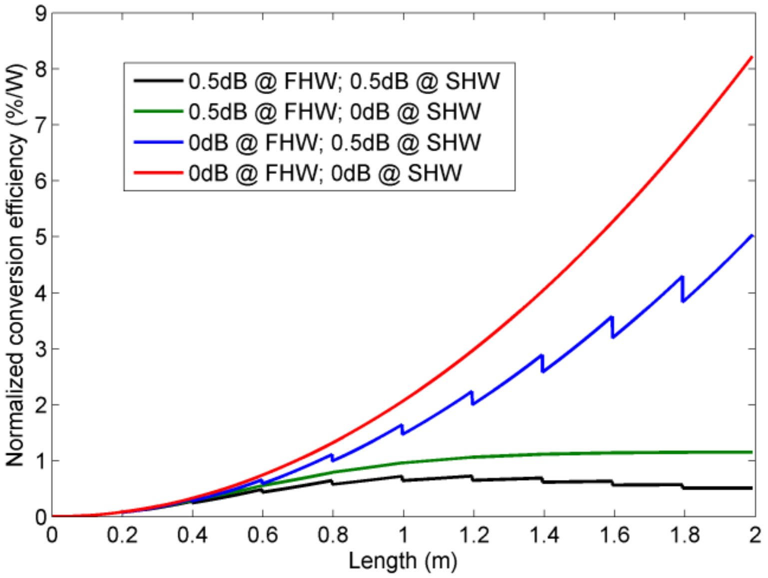

Fig. 5-2 Normalized overall conversion efficiency vs the overall length of concatenation PPSFs; The loss indicated in the figure denotes the splicing loss at the FHW and SHW.

Fig. 5-2 illustrates the growth of the overall normalized conversion efficiency after concatenating 10s of PPSFs with varied splicing loss at the connection points both for FHW and SHW, as indicated in the figure. As seen clearly in Fig. 5-2, the connection loss limits the increase of the η even though extending the interaction length of PPSFs. Specifically, in the ideal case of no connection loss (the red trace in Fig. 5-2), η increases as the quadratic of the concatenation PPSFs length and it reaches ~2.05 %/W by concatenating 5 PPSFs together to form an effective 1-m long PPSF device. With this conversion efficiency, watt-level visible light can be easily achieved with ~50 W fundamental input power. However, in reality, the connection loss is unavoidable. For instance, when the splicing loss is 0.5 dB for both FHW and SHW (the black curve in Fig. 5-2), η increases to the maximum of ~0.72 %/W with 5 PPSFs, which is about one third of that in the ideal case, but the η decreases from that point onwards. By considering the splicing loss at FHW only with a value of 0.5 dB, the η increases with the extension the PPSFs length to ~1.2 m and rolls off afterwards, as indicated by the green trace in Fig. 5-2. On the contrary, for the case of connection loss at SHW only with a value of 0.5 dB, as seen the blue trace in Fig. 5-2, the η keeps growing with the increase of the length of PPSFs, but the final η is still less than that in the ideal lossless case.

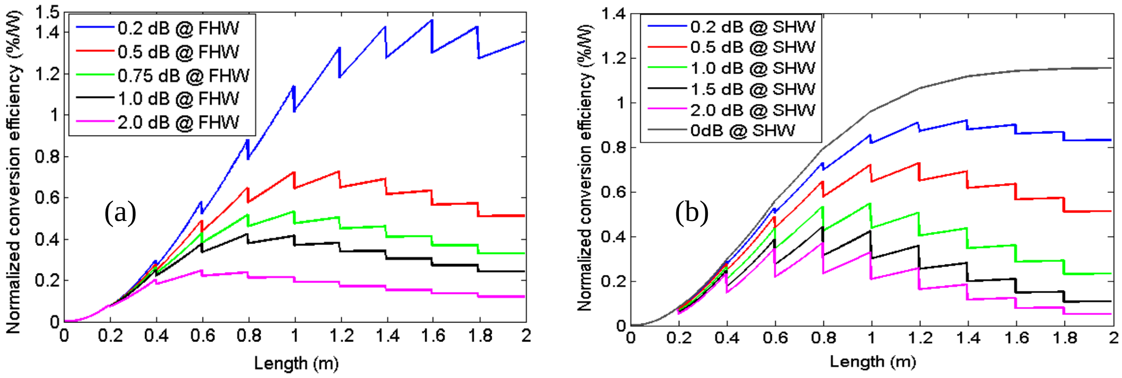

Fig. 5-3 Evolution of normalized conversion efficiency with (a) varied splicing loss at FHW but with a constant splicing loss of 0.5 dB at SHW and (b) varied splicing loss at SHW but with a constant splicing loss of 0.5 dB at FHW.

Furthermore, the effects of the splicing losses at the FHW and SHW on the normalized conversion efficiency have been simulated separately. Fig. 5-3 (a) shows the trend of η with varied splicing loss from 0.2 dB to 2.0 dB at the FHW but with constant splicing loss of 0.5 dB at SHW. The maximum η decreases as the increase of the splicing loss, and the maximum η is reduced from ~1.46%/W to ~0.10%/W, corresponding to concatenating 8 samples (0.2 dB @ FHW) and 2 samples of PPSFs (2.0 dB @ FHW). In terms of the effects of the splicing loss at the SHW, Fig. 5-3 (b) shows the trend of η by varying the splicing loss from 0 dB to 2.0 dB at the SHW but with fixed splicing loss of 0.5 dB at FHW. It behaves in a similar manner to Fig. 5-3 (a) and the maximum η is reduced from ~1.15%/W to ~0.37%/W, corresponding to concatenating 10 samples (0 dB @ SHW) and 4 samples of (2.0 dB @ SHW) PPSFs. From the results above, it can be deduced that the connection loss at the FHW degrades the improvement of the η more severely than that at SHW in the concatenation process.

5.2 Experimental setup for concatenating two PPSFs

In order to verify the performance of the simulation, the experiment work of concatenating two PPSFs together has been carried out. Fig. 5-4 shows the experimental setup, which is made up of a TLS, a PC with an insertion loss of ~0.3 dB, a power meter and thermal controller stages which are based on Peltier cooling effects. The power is measured using a silicon detector head (Newport 818-SL) and power meter (Newport 2936-C). Two samples of PPSF (PPSF1 and PPSF2) used for concatenation is obtained by cutting a single PPSF (PPSF0) into two parts of similar length. Then the concatenated sample of PPSF1&2 is obtained by fusion splicing the PPSF1 and PPSF2 together using the blank (un-poled) end of the samples. In order to ensure a uniform temperature distribution along the device, the two PPSFs are mounted on the left and right copper plates (CPL and CPR), where the temperatures are well controlled by the *temperature controllers* (TCs), (i.e., TC1 and TC2 respectively). The connection section (as indicated as B in Fig. 5-4) is mounted on an individual copper plate (CPM) and the temperature is controlled by the TC3. The temperatures of CPL and CPR can be continuously tuned from15℃ to 32℃ while the CPM has a larger temperature tunable range from 10℃ to 60℃. Additionally, a Labview programme developed by Dr. Canagasabey [118], is used to change the wavelength of the tunable laser source with a resolution of ~0.05 nm and read the corresponding SHG power from the power meter. All the spectra of SHG output with respect to fundamental wavelengths herein are obtained from this Labview programme. In the experiment, the fundamental wavelength is ~1541.9 nm for the initial PPSF0 and the corresponding SHG wavelength is ~770.95 nm.

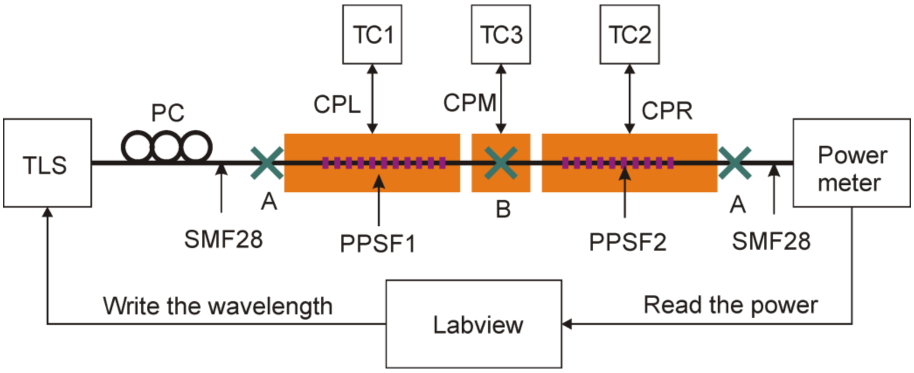

Fig. 5-4 Schematic diagram of the experimental setup. A and B denote splicing joints.

5.3 Experimental results of concatenation two PPSFs

5.3.1 *Phase-matching via thermal tuning technique*

The optimized SH wavelength is sensitive to the temperature applied on the PPSF, because of the thermal sensitivity of the QPM grating [72]. Also, the conversion efficiency of the concatenation PPSFs can only be improved when the two PPSFs are in phase. In this part, the quantity of the temperature tuning required for maximizing the conversion efficiency of concatenation two PPSFs is discussed.

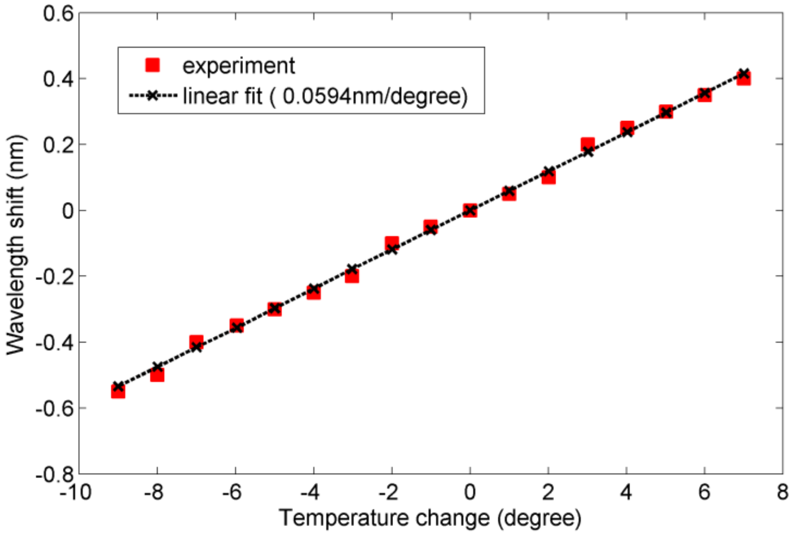

Fig. 5-5 Fundamental wavelength shift of PPSF vs the temperature change.

Fig. 5-5 shows the relationship between the wavelength shift, i.e., $\Delta\lambda_\omega$, which is measured at the optimized fundamental wavelength for SHG, and the temperature change ΔT applied on the PPSF with the TC, indicated in Fig. 5-4. From the experimental data, $\Delta\lambda_\omega$ is linearly proportional to the ΔT as:

$$\Delta\lambda_\omega = 0.059 \cdot \Delta T - 0.0024 \tag{5-6}$$

From Equation (5-6), the coefficient of the wavelength thermal effect can be expressed as:

$$\delta_\lambda = \frac{\Delta\lambda_\omega}{\lambda_\omega \cdot \Delta T} \cong \frac{0.059}{1541} = 3.83 \times 10^{-5}\ /℃ \tag{5-7}$$

As from Equation (5-2), the fundamental wavelength can be determined by the pitch of the QPM grating, Λ, and the index difference (Δn), as $\lambda_\omega = 2 \cdot \Delta\mathrm{n} \cdot \Lambda$. As the thermal response is 95% dominated by refractive index thermal expansion, dn/dT [15] in silica fibres, the thermo-optic coefficient of the PPSF device can be estimated as:

$$\delta_{\Delta n} = \frac{\delta_\lambda \cdot \lambda_\omega}{2\Lambda}\ /℃ \tag{5-8}$$

Substituting Equation (5-8) into the Equation (5-2), the thermal-phase difference coefficient with a thermal tuning length of L_{tt} of PPSF can be obtained as:

$$\delta_{\Delta\emptyset} = \frac{4\pi \cdot L_{tt} \cdot \delta_{\Delta n}}{\lambda_\omega} = \frac{2\pi \cdot L_{tt} \cdot \delta_\lambda}{\Lambda}\ /℃ \tag{5-9}$$

Therefore, the temperature tuning range required to compensate a phase-mismatch of $\Delta\phi$ can be calculated as:

$$\Delta T = \frac{\Delta\phi}{\delta_{\Delta\Phi}} = \frac{\Delta\phi \cdot \Lambda}{2\pi \cdot L_{tt} \cdot \delta_{\lambda}} \ ^{\circ}\mathrm{C} \tag{5-10}$$

The PPSFs used in the experiment have the $\Lambda = \sim 66.4$ μm and the L_{tt} is selected to be 20 mm and 40 mm. By substituting Equation (5-7) into Equation (5-10), the relationship between the tuned temperature and the compensated phase can be obtained and is illustrated in Fig. 5-6. It is found that π phase can be compensated by tuning 43.16 ℃ and 21.58 ℃ with thermal tuning lengths of 20 mm and 40 mm, respectively.

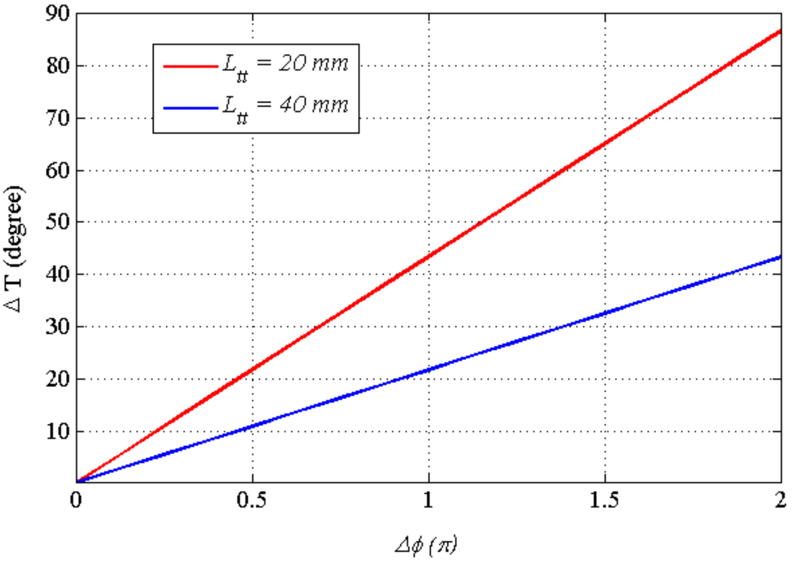

Fig. 5-6 Tuned temperature vs compensated phase.

5.3.2 *Measurement of the splicing loss at the FHW*

It has been discussed above that the splicing loss is crucial for the improvement of the conversion efficiency. The splicing losses at connection A and B have been measured at the FHW by using the TLS at ~1541 nm with an output of ~3 dBm. In the measurement, the splicing losses at the input and output ends of the PPSFs are assumed identical and the propagation loss through the PPSFs are ignored, which is fair for such a short length (<32 cm). Table 5-1 summarises the output power from the PPSF samples and the corresponding insertion loss, which is the power difference between the TLS and the incident FHW power of PPSFs (the total loss between the tunable laser source and joint A indicated in Fig. 5-4). The variation of the insertion losses is due to the varied splicing loss between the PPSF sample and SMF. For the concatenated sample of PPSF1&2, the insertion loss is measured to be 0.8 dB, including the insertion loss (~0.3 dB) of the PC and splicing loss (~0.5 dB) at the input end of the sample (as indicated as A in Fig. 5-4). As a result, the connection loss between the PPSF samples at point B is ~0.34 dB at the FHW. Because the visible laser source at SHW was not available when the work was carried out, the connection loss at the SHW has not yet been measured.

Table 5-1 Insertion loss of PPSF samples measured at the FHW.

PPSF samples	Source power (dBm)	Output power (dBm)	Insertion loss (dB)
PPSF0	3	1.74 ± 0.05	0.78 ± 0.05
PPSF1	3	1.72 ± 0.05	0.79 ± 0.05
PPSF2	3	1.58 ± 0.05	0.86 ± 0.05
PPSF1&2	3	1.36 ± 0.05	0.80 ± 0.05

5.3.3 Concatenation results

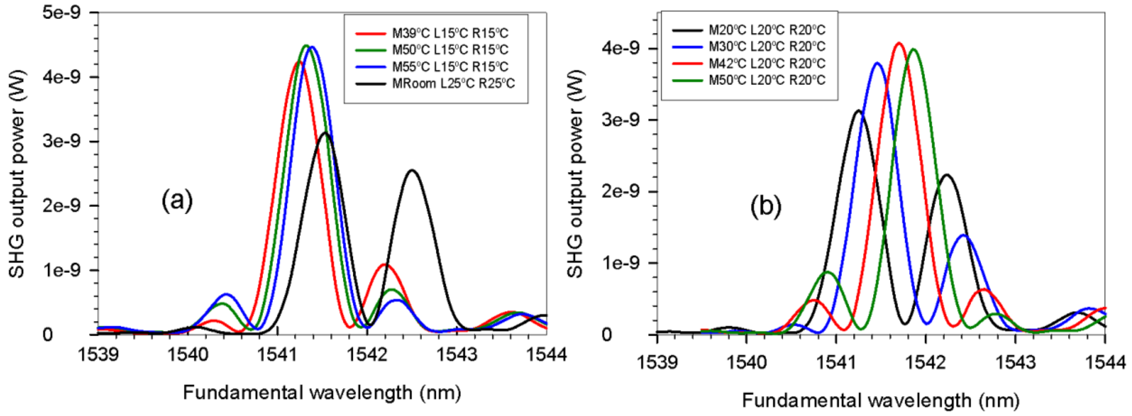

Fig. 5-7 The evolution of SHW output profiles by thermal tuning with (a) $L_{tt} = 20\ mm$ and (b) $L_{tt} = 40\ mm$. M/L/R represent middle/left/right copper plates indicated in Fig. 5-4, respectively.

Fig. 5-7 shows the evolution of SHG output by tuning the temperature with $L_{tt} = 20\ mm$ and $L_{tt} = 40\ mm$, respectively. All the traces are obtained with ~9.54 dBm of the TLS and the SHW output power has been maximised by tuning the PC. In the case of $L_{tt} = 20\ mm$, as seen in Fig. 5-7 (a), the SHG output trace has a deep dip close to ~1542 nm in the room temperature (black line). This indicates that the phase-mismatch between PPSF1 and PPSF2 after concatenation is $\sim\pi$ or odd integer multiple of π. According to the estimation in Fig. 5-6, it requires about ~43℃ temperature difference to compensate the phase mismatch with the $L_{tt} = 20mm$. Consequently, the side plates (L/R) are cooled down to ~15℃ but the middle plate (M) is heated up to increase the temperature difference. With the increase of the temperature of the middle plate, the right sidelobe of the output spectrum decreased while the left one increased significantly, as seen as the red, green and blue curves in Fig. 5-7 (a). When the middle temperature is tuned to ~55℃ , the SHG output profile is almost identical to a single SHG device. In this situation, the temperature difference is 40℃ and is in good agreement with the numerical calculation. On the other hand, when the $L_{tt} = 40mm$, the same evolution has been demonstrated as shown in Fig. 5-7(b).

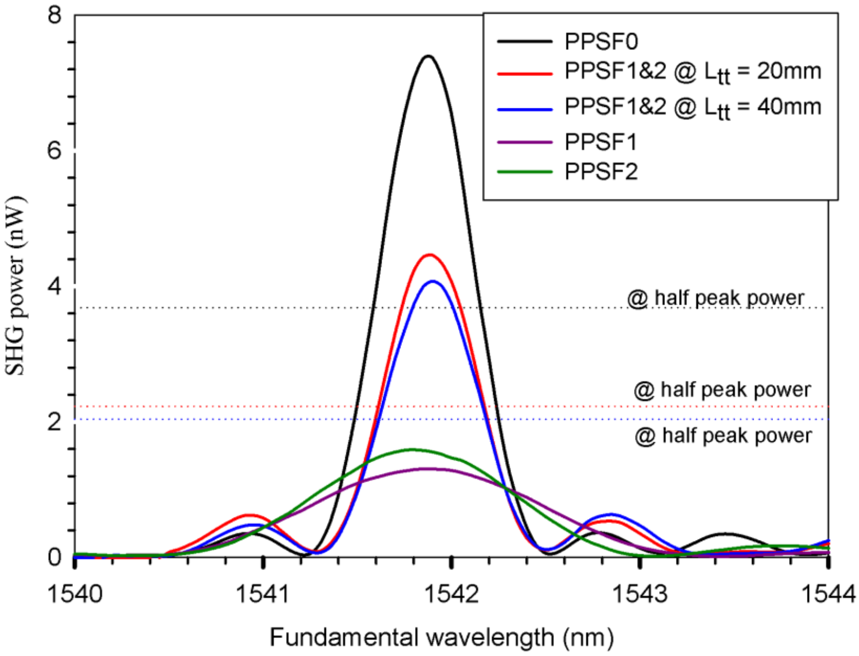

Fig. 5-8 Overlap of the SHG output profiles

Fig. 5-8 predicts the comparison of the SHG output profiles before and after concatenation. It can be seen clearly that after concatenation, the SHG output profiles are very close to that of single uniform device. Hence, thermal tuning of the middle section has achieved the phase matching for PPSF1 and PPSF2, and made them into one effective single device.

Table 5-2 summarises the experimental data of the concatenation PPSFs. The incident fundamental wave power is calculated to be ~8.74 dBm with the correction of ~0.8 dB insertion loss. The error of the wavelength and the FWHM bandwidth is due to the resolution of the wavelength scan programme (0.05 nm). Regarding the temperature, PPSF0, PPSF1 and PPSF2 are measured in the room temperature, which is about 23.5 ℃ with ~1 ℃ perturbation due to the variation of the air. During concatenation, the PPSF samples are mounted on the stages, which are controlled by TCs and with ~1% accuracy relates to the absolute temperature. After concatenation, the centre fundamental wavelength is down-shifted due to the cooling of the samples. In the case of PPSF1&2 @ $L_{tt} = 20\ mm$, the temperature on the PPSF samples have been cooled down by ~8.5 ℃ from the room temperature of ~23.5℃, which induces ~0.5 nm wavelength down-shift according to Equation (5-6). This is in good agreement with the experimental result of ~0.4 nm within the measurement uncertainty. This trend is similar in the situation of PPSF1&2 @ $L_{tt} = 40\ mm$.

Table 5-2 Experimental data of the concatenation PPSFs.

PPSF samples	SHG output power (dBm)	Centre wavelength (± 0.05 nm)	Temperature (℃)	Measured length (± 0.5cm)	Effective interaction length (cm)	FWHM (± 0.05nm)	η (%/W)
PPSF0	-51.33	1541.9	23.5 ± 1	28	22.65 ~ 26.76	0.6	0.0132
PPSF1	-58.83	1541.9	23.5 ± 1	13.5	10.51 ~11.32	1.4	0.0023
PPSF2	-57.99	1541.8	23.5 ± 1	13.5	11.32 ~11.78	1.3	0.0028
PPSF1&2 @ $L_{tt} = 20mm$	-53.51	1541.4	15 ± 0.2	24.5	22.65 ~26.76	0.6	0.0080
PPSF1&2 @ $L_{tt} = 40mm$	-53.89	1541.7	20 ± 0.2	24.5	22.65 ~26.76	0.6	0.0073
Reference	--	--	--	--	32	0.46	--

As discussed at the beginning of this chapter, the interaction length of PPSF is a key component for the SHG conversion efficiency. However, the start and end of QPM grating are uncertain on the initial single device (PPSF0) due to the loss of markers. As a result, the length of the interaction length for SHG cannot be measured directly with ruler. Fortunately, the effective interaction length is inversely scaled to the FWHM bandwidth [71, 118], and so it can be calculated back from its corresponding FWHM. Table 5-2 has shown the estimated interaction length of each sample referring to a given sample of 32 cm with 0.46 nm of FWHM bandwidth. It turns out that the effective interaction length after concatenation is almost identical to the original single sample of PPSF0, which is because of the almost identical FWHM bandwidth of the concatenated PPSF1&2 and PPSF0, as seen in Fig. 5-8.

In terms of the normalized conversion efficiency, η, the maximum η of PPSF1&2 is obtained as ~0.008%/W with the $L_{tt} = 20\ mm$, which is ~60.60% of the η of original PPSF0 and x3.48 and x2.86 times of that of PPSF1 and PPSF2, respectively. Even though the interactive length of PPSF1&2 and PPSF0 are identical, the η of PPSF1&2 is less than that of PPSF0, because of the extra-splicing losses at the concatenation joint both for the FHW and

SHW. This is also proven by the simulation results discussed above. Since the connection splicing loss at FHW is ~0.36 dB, with the aid of simulation, the connection splicing loss at SHG is estimated to be ~1.69 dB.

5.4 Conclusions

In summary, concatenating PPSFs together to extending the interaction length for SHG, so as to improve the SHG conversion efficiency, has been both numerically and experimentally investigated in this work. The results show that the losses induced by the connection (splicing loss) limit the improvement of the normalized conversion efficiency as well as the maximum number of PPSFs for concatenation. The simulations also show that the lower connection loss, the higher SHG conversion efficiency can be achieved by concatenating a greater number of PPSF samples in series. Furthermore, the higher connection loss at the FHW will decrease the conversion efficiency more quickly than that of the SHW. This is because the SHG power is quadratically proportional to the FHW power,

In experiment, two PPSFs have been successfully concatenated to form an effective uniform single PPSF device by thermal tuning the connection section. Even though the effective length of concatenated device (PPSF1&2), is about twice that of each single PPSFs (PPSF1 and PPSF2), the overall normalized conversion efficiency of PPSF1&2 have been enhanced to ~x3.48/x2.86 times that of PPSF1/PPSF2. The improvement factor is less than 4 which is for ideal incurred with no connection loss. This is evident due to the splicing loss occurred at the connection joint for the FHW and SHW, which is in good agreement with the simulation results.

Therefore, in order to overcome the practical length limitations of the poling and grating fabrication stages, concatenating 2 or 3 devices together to extend the interaction length for SHG by thermal tuning method will be an effective way to enhance the SHG conversion efficiency.

Chapter 6 Conclusions and future works

6.1 The thesis

The thesis is devoted to exploring advanced applications of periodic fibre devices, i.e., fibre gratings, with the combination of the nonlinearities of optical fibres, including $\chi^{(3)}$-based nonlinearities of Kerr effects, stimulated Raman scattering (SRS) and four-wave mixing (FWM), and $\chi^{(2)}$-based nonlinearity of frequency-doubling in periodic poled silica fibres (PPSFs).

First of all, Raman distributed-feedback (R-DFB) fibre lasers have been comprehensively studied in this work. The concept of R-DFB fibre laser was first proposed by Perlin and Winful in 2001 [68]. However, until 2009 when this work was initiated, no practical demonstration of R-DFB fibre laser had then been reported except a couple of works on numerical simulations of π phase-shifted R-DFB fibre lasers by Hu and Broderick [141]. According to the theory, the configuration of the DFB grating, including the coupling coefficient, DFB grating length and the phase-shift position, and the nonlinearities of the host fibres, are essential to the R-DFB fibre lasers. Therefore, this work began with simulating R-DFB fibre lasers with the target of finding out the parameters of the DFB grating for further experimental demonstration.

The simulation model of the R-DFB fibre laser is described by the nonlinear coupled mode equations (NLCMEs), which are solved numerically with C-language by using an implicit fourth-order Runge-Kutta algorithm proposed by de Sterke [143]. From a centre π phase-shifted R-DFB model, the results have shown that such a R-DFB fibre laser is very resilient against (root-mean-square) rms phase and amplitude errors (with random noise distribution) up to ~5%, with negligible deterioration of the pump threshold and slope-efficiency [73]. The simulation results have also shown that the lasing build-up time of the R-DFB fibre laser is of the order of a few micro-seconds, which is very useful for future demonstrations with a pulsed pump source. When the π phase-shift is placed at the middle of the DFB grating with a length of 30 cm, it reveals that the threshold pump power can be reduced from ~40 W to ~5.2 W by increasing the coupling coefficient (i.e., κ) to be higher than 35 m^{-1} whilst the total slope efficiency is found to be decreased from ~60% to ~31%. Therefore, it is a trade-off between the threshold pump power and the slope conversion efficiency, to choose a DFB grating with a moderate strength.

Moreover, the threshold pump power (CW) of the R-DFB fibre lasers with respect to the coupling coefficient of DFB grating (κ), the effective core area of the optical fibre (A_{eff}), Raman gain coefficient (g_r), propagation loss of the optical fibre (α), DFB grating length (L) and the phase-shift position, have been numerically analysed. The simulation results have revealed that (i) the threshold pump power is approximately proportional to the A_{eff} but inversely proportional to the g_r; and (ii) a longer length of DFB grating built into the host fibre with lower background loss is always helpful for having a R-DFB fibre laser with lower threshold. In particular, the simulation results have predicted that ultra-short (a few cms) R-DFB fibre laser with sub-watt lasing threshold can be achieved in a tellurite glass holey fibre provided the background loss is less than 20 dB/km [42].

Apart from the centre π phase-shifted R-DFB model, a novel step-like offset π phase-shifted R-DFB model has also been proposed and examined. The simulation results indicate that the threshold pump power can be further reduced by placing the π phase-shift at 20% offset from the centre whilst maintaining the grating strength identical for both sides of the π phase-shift. Even though the mechanism for such phenomenon has not yet been wholly understood at this stage, the threshold of R-DFB fibre laser is believed to be relative to the effective cavity length and the intensity distribution profile within the cavity.

In reality, the longest DFB grating that can be made in the group is 30 cm at the time this work was carried out. The threshold pump power for 30 cm long centre π phase-shifted R-DFB laser in silica fibres is predicted at the watt-level low power region from the simulation. In order to realize the R-DFB fibre laser in lab, two CW high-power Yb-doped fibre MOPA systems at ~1.06 µm have been set up as the pump sources for R-DFB fibre laser generation. One is unpolarised with a maximum output power of 20 W and another is a linearly polarised with a maximum output power of ~5 W.

Based on these pump sources, two types of commercially available non-PM silica fibres, i.e., PS980 (from Fibercore Ltd.) and UHNA4 (from Nufern), which are single-mode at the projected Raman Stokes wavelengths (~1.11 µm), were selected as the host fibres for DFB gratings. In both fibres the cores are heavily doped with germanium, which not only increases the photosensitivity of the core to the 244 nm UV light but also largely enhances Raman gain coefficient. In addition, these two fibres have low propagation loss ($\leq 20\ dB/km$ around 1-1.2 µm region). So they are both suitable host media for R-DFB fibre lasers. In each fibre sample, 30 cm long DFB gratings with centre π phase-shift have been directly written into the core with the continuous grating writing technique radiation at 244 nm CW UV light in-house. No hydrogen loading was applied before writing the FBGs. The wavelengths of the set of DFB gratings have been measured at ~1117 nm and ~1109 nm in PS980 and UHNA4, respectively.

The coupling coefficients of the gratings are estimated to be in the range of ~30 m^{-1} to ~37 m^{-1}, resulting in the amplitude of the refractive index modulation is in the order of 10^{-5}.

All-fibre R-DFB fibre laser systems have then been setup and high-power (>1.6 W for total R-DFB output power) R-DFB fibre lasers in PS980 and UHNA4 fibres have been demonstrated, respectively [39, 42]. To the best knowledge, this is the first time of showing a DFB fibre laser with watt-level output power. With the un-polarised pump source, the threshold pump power, the conversion efficiencies with respect to the incident pump power and absorbed pump power have been revealed to be ~0.98 W, 13% and 93% in UHNA4 fibre whilst ~2 W, 13% and 74% in PS980 fibre, respectively. The lower threshold in the UHNA4 R-DFB fibre laser than that in the PS980 is due to the higher Raman gain coefficient and smaller mode field diameter in the former fibre as a result of the higher concentration of Ge in the former fibre. By replacing the un-polarised pump laser with a linearly polarised PM pump source, the threshold pump powers of the R-DFB fibre lasers have been reduced with a factor of 2 and ~440 mW threshold has been demonstrated in UHNA4 DFB gratings [40]. This can be expected since the Raman effect is highly polarization dependent. What is more, a truly uni-directional output R-DFB fibre laser has been observed in the PS980 DFB grating samples with a centre π phase-shift but linearly tapered index modulation along the grating [74]. The power ratio of the output power from two sides is extraordinarily high since the R-DFB signal has been only detected from one side of the DFB grating, which can undoubtedly be proven from the output spectra from both ends of the R-DFB fibre laser.

Furthermore, the linewidth measurement of the R-DFB fibre lasers has been conducted with a delayed self-heterodyne interferometer method using a delay line of ~29.75 km, which gives a nominal resolution of ~2.5 kHz [158]. The beat spectra of the R-DFB fibre lasers have shown clearly the fact of single-frequency oscillation and the effects of the long coherence length of the R-DFB signals. Thus, the linewidth of the R-DFB fibre lasers are believed to be less than 2.5 kHz [40, 74]. Besides, the beat profile of the R-DFB signal has demonstrated a good approximation to the Lorentzian distribution, indicating that the thermal effect in this laser is negligible. This is consistent with the fact that the laser wavelength has been well stabilized at all power levels.

Highly efficient and broadband wavelength conversion by using the FWM in the R-DFB fibre lasers has been observed either in the single DFB grating (PS980 or UHNA4), in cascaded DFB gratings, or integrating with a tunable laser source at 1.06 µm [75]. In the FWM process, the R-DFB signal at ~1109 nm (for UHNA4 DFB gratings) or ~1117 nm (for PS980 DFB gratings) acts as the pump wave whilst the 1.06 µm wave represents the probe for the FWM process. Accordingly, the conjugate wave at ~1158 nm (for UHNA4 DFB gratings) or ~1176 nm (for PS980 DFB gratings) has been generated. The FWM conversion efficiency has been found to be ~ -25 dB for such a wide FWM generation. With the tunable laser source ranging from ~1040 nm to ~1080 nm and given the FWM conversion efficiency is above -37 dB, the wavelength conversion range, which is the wavelength separation between the conjugate wave and its original wave, has been obtained as ~113 nm from UHNA4 R-DFB fibre lasers and ~167 nm from PS980 R-DFB fibre lasers, respectively. In order to understand the mechanisms for the FWM in R-DFB fibre lasers, a theoretical model has been established and simulations have been conducted by solving the amplitude mode equations for a degenerated FWM process. The simulation results have demonstrated that the high intensity at the phase-shift position and the steep change of the dispersion at the pass-band of the DFB grating are likely to be the main reasons for the highly efficient FWM in 30 cm long R-DFB fibre lasers.

In order to achieve a R-DFB fibre laser with even lower threshold pump power, high-index non-silica glass fibres with high nonlinearity as well as high Raman gain coefficients, such as tellurite glass fibres [59] and chalcogenide glass fibres, are promising candidates as the host fibres for R-DFB generation. The Raman gain coefficient of the tellurite glass sample with the composition of 75TeO_2-20ZnO-5Na_2O (mol.%) (TZN) (made in-house), has been measured and the peak Raman gain coefficient is calculated to be ~35 times higher than the fused silica with a pump source at 1.06 µm. Using a metre-length (1.35 m) tellurite glass air-suspended-core fibre based on the same composition, a SRS-assisted broadband SC (from ~1.1 µm to ~1.7 µm, limited only by the detectable of OSA), has been demonstrated by pumping at the normal dispersion region of the fibre at 1.06 µm [59]. The combination of the high Raman gain coefficient, the high nonlinearity and the broadband Raman gain spectrum of the tellurite glass plays the key role in the process of spectral broadening.

Fusion splicing has been considered as an effective means to integrate the non-silica glass fibres into the conventional telecom optical fibres. Two types of home-made high-index non-silica glass fibres (lead silicate and tellurite glass fibres) have been fusion spliced with standard silica glass fibres with a connection loss ranging from ~0.6 dB/joint to ~8.4 dB/joint. The fusion splice loss depends on the mismatch of the NA and effective mode area between the two fibres being splicing.

Preliminary investigations of writing FBGs into the high-index non-silica glass fibres have been presented. The UV absorption profiles of the high-index non-silica glasses, including lead silicate glass and tellurite glass, have been measured and it is found that they are highly photosensitive to the UV light with the wavelength shorter than 350 nm. Consequently, experiments of writing FBGs into the lead silicate glass fibres (produced in-house) have been carried out with UV light sources at 325 nm (CW), 344 nm (CW) and 355 nm (pulsed), respectively. However, as yet no observable FBG has been detected on the spectrum. But the experimental data have indicated that the wavelength of the UV light source is a primary parameter to inscribe FBGs into the core of the non-silica glass fibres. It requires more future works to fully understand the mechanism of creating FBGs into the high-index non-silica glass fibres. Apart from these, the quality of the non-silica glass fibres, for example the uniformity of the fibre diameter along the length, is equally important for establishing a FBG in the core.

Finally, the inducible second-order nonlinearity in PPSFs is of the order of ~0.1 *pm/V* [118], but the frequency-doubling conversion efficiency can be enhanced by extending the interaction length of PPSFs. Concatenating two or more PPSFs together has been demonstrated as an economic and simple route to improve the conversion efficiency. However, the splice losses occurring at the connection joints will degenerate the overall conversion efficiency. Simulation results have shown that the connection loss limits the improvement of the conversion efficiency as well as the maximum number of PPSFs for concatenation. In addition, two PPSFs with similar length have been experimentally concatenated via thermal heating method and the overall conversion efficiency has been increased to 2.86 times of that of the single PPSF device.

6.2 Future works

Since the field of R-DFB fibre laser is at the very beginning stage, the future works are very obvious and promising. The following are just a few examples.

6.2.1 Lower threshold R-DFB fibre lasers

As the oscillation wavelength of R-DFB fibre laser depends on the pump source, it will be desirable if the threshold of R-DFB fibre lasers can be lowered down to the range of a few milli-watts to hundreds of milli-watts, which is the typical output power range from commercially available fibre-pigtailed single-mode laser diodes operating from ~400 nm to mid-IR region.

The most evident route to lower the threshold of the R-DFB fibre lasers is either enhancing the Raman gain coefficient of the host fibres or extending the length of the DFB gratings. The former can be achieved by using highly nonlinear fibres based on non-silica glasses, e.g., tellurite glass, which possess the Raman gain coefficients ~35 times higher than silica glass fibres [59], and chalcogenide glass, whose Raman gain coefficient is almost two orders of magnitude higher than that of silica [232]. To do this, high-quality DFB gratings have to be formed into the non-silica glass fibres first and therefore, continuous efforts are required to target this. On the other hand, there is no seen technical difficulty in writing a DFB grating longer than 30 cm using the continuous writing technique, since 1 m long chirped FBG was reported 15 years ago [25]. Or similar to the technique of cascading PPSFs, longer DFB gratings can be formed by stitching several uniform FBGs together and thereupon inducing the π phase-shift by localized thermal heating [27].

6.2.2 Mid-IR R-DFB fibre lasers

R-DFB fibre lasers have shown several excellent properties of (1) single-frequency operation, (2) ultra-narrow linewidth, (3) continuous tunablity, and (4) can virtually be generated at any wavelength given a proper pump source. These performances have made R-DFB fibre lasers to be ideal laser sources for the applications of remote sensing, e.g., LIDAR and precision molecule spectroscopy. In particular, mid-IR spectral region (2-20 µm) is a domain of interest for these applications. Two important windows, i.e., 3-5 µm and 8-13 µm, can be exploited to detect small traces of environmental and toxic vapours down to sensitivities of parts-per-billion in a variety of atmospheric, security and industrial applications, because of the relative transparent atmosphere in these regions [233]. Fig. 6-1 illustrates absorption spectra of various gaseous molecules in the wavelength region of 2-12 µm [233]. Many molecules undergo fundamental fingerprint vibrational transitions in this domain, which renders mid-IR spectroscopy a crucial means to identify and quantify molecular species in a given environment.

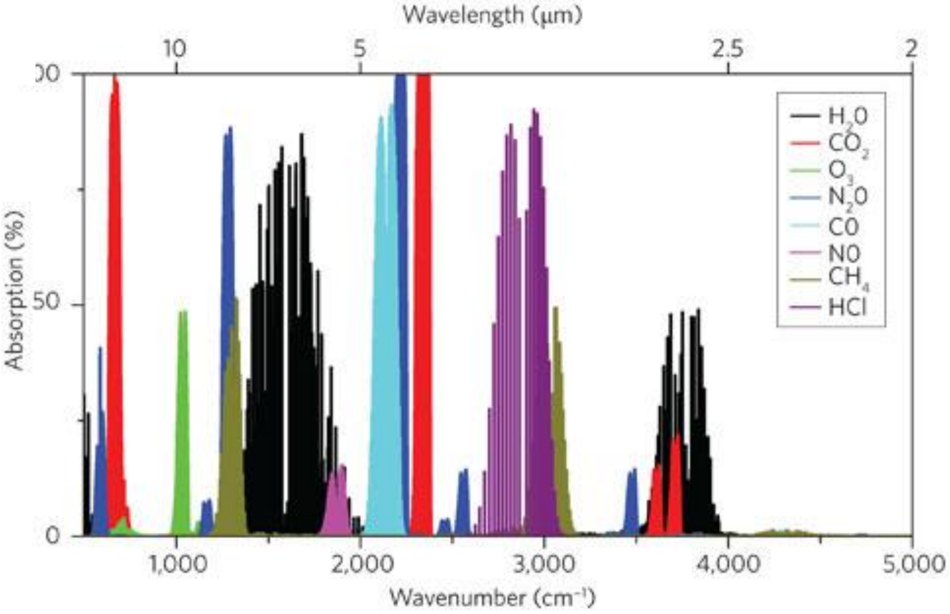

Fig. 6-1 Absorption of various gaseous molecules in the mid-infrared region. (After Ref. [233])

It is well established that the chalcogenide glass fibres possess much higher nonlinearities and Raman gain coefficient than that of silica fibres. Additionally, they are transparent in the mid-IR region (2-12 µm) with typical losses about 0.1-0.8 dB/m depending upon composition [232]. Therefore, it is feasible to demonstrate mid-IR R-DFB fibre lasers by incorporating DFB gratings into the chalcogenide glass fibres, since FBGs have been fabricated in this type of fibre already [48, 206].

6.2.3 ***Pulsed R-DFB fibre lasers***

This thesis focuses on the CW pumping operation, in which the GVD effects can be ignored. However, it will be very interesting to generate a pulsed R-DFB fibre laser, which will have a much higher peak power than that of CW counterparts, for nonlinear applications, e.g., frequency-doubling and FWM. Note that the pulse duration of the pump source should be larger than the lasing build-up time of the R-DFB fibre laser, which is in the order of μs indicated from the simulation in the silica glass fibre case.

Appendix A Raman threshold of forward and backward SRS in single mode silica fibre

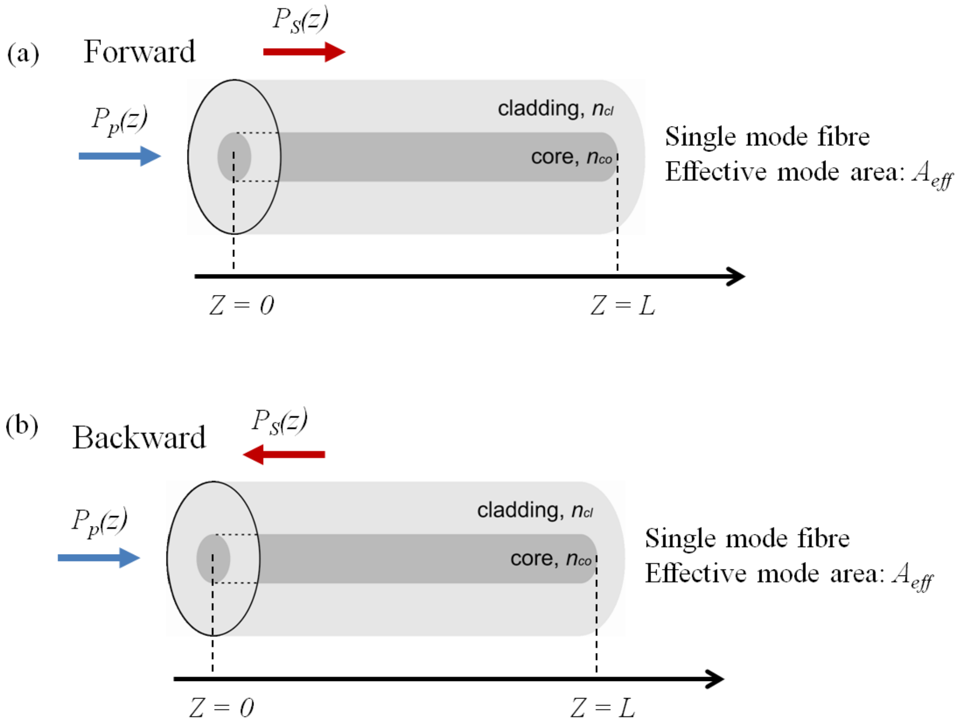

Fig. A-1 Schemetic of (a) forward and (b) backward Raman scattering process in SMF.

(1) Raman threshold in forward Raman scattering process

In the case of forward Raman scattering process, as shown in Fig. A-1 (a), the pump propagates along the fibre can be expressed as:

$$P_p(z) = P_p(0)\exp\left(-\alpha_p z\right) \tag{A-1}$$

The differential equation for a forward Raman Stokes is then given by [103]:

$$\frac{dP_s(z)}{dz} = \frac{g_r}{A_{eff}} P_p(z) P_s(z) - \alpha_s P_s(z) \tag{A-2}$$

In the above equations,

α_p: fibre attenuation at pump (in m^{-1});

α_s: fibre attenuation at Stokes (in m^{-1});

$P_p(z)$: pump power (in W) at position z;

$P_p(0)$: incident pump power at the input (z=0, in W);

$P_s(z)$: Stokes power (in W) at position z;

A_{eff}: effective mode area of single mode Raman fibre (in m^{-2}), assuming that they are the same at pump frequency and Stokes frequency);

L: total length of the SMF (in m);

g_r: frequency-dependent Raman gain coefficient (in m/W).

For simplification, it is assumed that the pump power is attenuated not by the nonlinear Raman process (e.g., the pump power is undepleted) but only by the linear attenuation of the fibre medium. By substituting Equation (A-1) into Equation (A-2), it is obtained as:

$$\frac{dP_s(z)}{dz} = \frac{g_r}{A_{eff}} P_p(z) P_s(0) exp\,(-\alpha_p z) - \alpha_s P_s(z) \qquad \text{(A-3)}$$

The solution to the ordinary differential equation (A-3) is:

$$P_s(z) = P_s(0) exp\,\{-\alpha_s z + \frac{g_r}{\alpha_p A_{eff}} P_p(0)\left[1 - exp\left(-\alpha_p z\right)\right]\} \qquad \text{(A-4)}$$

At the output end of the fibre (e.g., Z=L) and noting $L_{eff} = (1 - \exp\,(-\alpha_p z))/\alpha_p$, Equation (A-4) becomes

$$P_s(L) \cong P_s(0) \exp\,[-\alpha_s L + \frac{g_r \cdot L_{eff} \cdot P_p(0)}{A_{eff}}] \qquad \text{(A-5)}$$

Equation (A-5) is actually based on the assumption that there is a Stokes small signal injected at the input end of the fibre (z=0). However, in the reality, it is not true. The Raman Stokes occurs at the output end of fibre due to the amplified spontaneous Stokes scattering through the length of the Raman fibre medium. In Ref. [103], it was assumed that at the input end (z=0), the injected Stokes flux is equal to one photon per mode (longitudinal and transverse) of the fibre. For a single mode fibre, the total Stokes flux at the output end (z=L) should then be expressed as the integration of the Equation (A-5) for all the Stokes frequencies:

$$P_s(L) = \int (hv)\, \exp\,(-\alpha_s L + \frac{g_r(\upsilon) \cdot L_{eff} \cdot P_p(0)}{A_{eff}}]\mathrm{d}\upsilon \qquad \text{(A-6)}$$

where $g_r(\upsilon)$ is frequency dependent Raman gain profile. Assuming that $g_r(\upsilon)$ has a Lorentzian lineshape with FWHM of $\Delta\upsilon_{FWHM}$ and the peak Raman gain coefficient $g_{r,peak}$ is large, Equation (A-6) becomes as:

$$P_s(L) = (hv_s)\ \Delta\upsilon_{eff}\ exp[-\alpha_s L + \frac{g_{r,peak} \cdot L_{eff} \cdot P_p(0)}{A_{eff}}] \qquad \text{(A-7)}$$

in which $\Delta\upsilon_{eff}$ is the effective bandwidth or number of longitudinal modes, and it is expressed as:

$$\Delta\upsilon_{eff} = \frac{\sqrt{\pi}}{2} \frac{\Delta\upsilon_{FWHM}}{(\frac{g_{r,peak} \cdot L_{eff} \cdot P_p(0)}{A_{eff}})^{1/2}} \qquad \text{(A-8)}$$

The effective input Stokes power can be expressed as:

$$P_s(0)_{eff} = (hv_s)\Delta\upsilon_{eff} = \frac{\sqrt{\pi}}{2}(hv_s)\frac{\Delta\upsilon_{FWHM}}{(\frac{g_{r,peak} \cdot L_{eff} \cdot P_p(0)}{A_{eff}})^{1/2}} \qquad \text{(A-9)}$$

The Raman threshold P_{th} is defined as the input pump power $P_p(0)$ at which Stokes power $P_s(L)$ becomes equal to the pump power $P_p(L)$ at the fiber output ($z=L$) [103], i.e.,

$$P_s(L) = P_p(L) \qquad \text{(A-10)}$$

Hence, combining Equations (A-1), (A-7) and (A-10), it is obtained as:

$$P_s(0)_{eff}\exp\,(-\alpha_s L + \frac{g_r(\upsilon) \cdot L_{eff} \cdot P_{th}}{A_{eff}}] = P_{th}\exp\,(-\alpha_p L) \qquad \text{(A-11)}$$

Assuming $\alpha_p = \alpha_s$ and substituting Equation (A-7) into Equation (A-11), the Raman threshold P_{th} is determined as [103]:

$$\begin{aligned} &\frac{\sqrt{\pi}}{2}(hv_s)(\frac{g_{r,peak} \cdot L_{eff}}{A_{eff}})\Delta\upsilon_{FWHM} \\ &= (\frac{g_{r,peak} \cdot L_{eff} \cdot P_{th}}{A_{eff}})^{3/2}\exp\,(-\frac{g_{r,peak} \cdot L_{eff} \cdot P_{th}}{A_{eff}}) \end{aligned} \qquad \text{(A-12)}$$

(2) Raman threshold in backward Raman scattering process

In the case of backward Raman scattering process, as shown in Fig. A-1 (b), it is assumed that the incident pump wave travels from $z=0$ to $z=L$, the same as Equation (A-1), while the Stokes wave travels backward, i.e., in the –*z* direction. Therefore, the differential equation for the backward Raman Stokes is expressed as:

$$-\frac{dP_S(z)}{dz} = \frac{g_r}{A_{eff}} P_p(\mathrm{z}) P_S(\mathrm{z}) - \alpha_{\mathrm{s}} P_S(\mathrm{z}) \qquad \text{(A-13)}$$

Please note that in Equation (A-13), because the Stokes wave travels opposite to the pump along the fibre, the left term has the minus sign, which is different from the case of forward Raman scattering process (see Equation (A-2)).

With the same assumption as the forward Raman process discussed above, by substituting Equation (A-1) into Equation (A-13), obtain:

$$\frac{dP_S(z)}{dz} = -\frac{g_r}{A_{eff}} P_p(0) P_S(z) \exp\left(-\alpha_p z\right) + \alpha_{\mathrm{s}} P_S(\mathrm{z}) \qquad \text{(A-14)}$$

The Raman threshold P_{th} for the backward is defined as the input pump power $P_p(0)$ at which backward Stokes power $P_S(0)$ becomes equal to the pump power $P_p(0)$ at the fiber input [103]. As similar derivation as for the forward Stokes, as discusses above, the Raman threshold P_{th} in the backward scattering process can be obtained from Equation (A-14) as:

$$\frac{\sqrt{\pi}}{2}(h\upsilon_s)(\frac{g_{r,peak} \cdot L_{eff}}{A_{eff}})\Delta\upsilon_{FWHM} = (\frac{g_{r,peak} \cdot L_{eff} \cdot P_{th}}{A_{eff}})^{5/2} \exp\,(-\frac{g_{r,peak} \cdot L_{eff} \cdot P_{th}}{A_{eff}}) \qquad \text{(A-15)}$$

Threshold Equations (A-12) (for forward Raman Stokes) and (A-15) (for backward Raman Stokes) can be solved numerically. For example, Table A-1 summarises the Raman threshold for the forward and backward Stokes process with varied $\Delta\upsilon_{FWHM}$ (from 10 cm^{-1} to 200 cm^{-1}) in a SMF with $g_{R,peak}$ of $5\mathrm{x}10^{-12}$ m/W, $\alpha_{p,s}$ of $5\mathrm{x}10^{-}3$ m^{-1} (i.e., 20 dB/km), A_{eff} of $10^{-11}\mathrm{m}^2$. It can be seen clearly that the product of $\frac{g_{r,peak} \cdot L_{eff} \cdot P_{th,forward}}{A_{eff}}$ (for forward Raman Stokes) is around 16 whilst $\frac{g_{r,peak} \cdot L_{eff} \cdot P_{th,backward}}{A_{eff}}$ (for backward Raman Stokes) is around 20, when the linewidth of Raman gain profile is as narrow as 10 cm $^{-1}$.

In conclusion, first, because the forward Raman Stokes wave and the backward Raman Stokes waves travel in the different direction compared to the pump wave, the pump and the Stokes waves interact differently and consequently the Raman threshold of the backward Stokes is greater than that of the forward Stokes roughly by 20-25%. Second, the ratios of 16 and 20 given in Ref.[103] are approximation values and they vary slightly with the parameters of Raman fibre and the linewidth of Raman gain profile.

Table A-1 Comparison of Raman threshold P_{th} between forward and backward Raman scattering process

$\Delta\upsilon_{FWHM}$ (cm^{-1})	$P_{th,forward}$ (W)	$\frac{g_{r,peak} \cdot L_{eff} \cdot P_{th,forward}}{A_{eff}}$	$P_{th,backward}$ (W)	$\frac{g_{r,peak} \cdot L_{eff} \cdot P_{th,backward}}{A_{eff}}$	$\frac{P_{th,backward}}{P_{th,forward}}$
200	0.130	13.0	0.161	16.1	1.24
100	0.138	13.8	0.169	16.9	1.22
50	0.146	14.6	0.177	17.7	1.21
10	0.164	16.4	0.196	19.6	1.20

Appendix B F factor calculation

Factor F is calculated with the method presented in Ref. [155].

$$F = F_L F_C F_{out} F_V \qquad \text{(A-1)}$$

in which $F_L = (1 - {R_{SiO_2}}^2)/(1 - {R_{TZN}}^2)$, takes into account the difference in exciting radiation power inside the samples at its constant input value for each sample and $R = (1 - n_0)^2/(1 + n_0)^2$ (n_0 is the linear refractive index of the sample).

The second factor in Equation (A-1), $F_C = {n_{TZN}}^2/{n_{SiO_2}}^2$, allows for the difference in a solid angle of radiation falling into the spectrometre and scattered from the samples, with equal thickness and various linear refractive index values n_0.

The third factor, $F_{out} = (1 - R_{SiO_2})/(1 - R_{TZN})$, accounts for the reflection of radiation scattered from the surface, through which this radiation is collected in the spectrometre.

The last factor, $F_V = 1$, at a 90º scattering geometry and for samples with small thickness (which depends on the scattering volume).

Appendix C Refractive indices of Schott glasses

Refractive indices of commercial Schott glasses of SF57, SF6, LLF1 and F2 from the Schott Optical Glass catalogue 2000.

λ (nm)	**Refractive index**			
	SF57	SF6	LLF1	F2
1970.1	1.76539	1.75813	1.52354	1.58958
1529.6	1.80187	1.76444	1.52884	1.59513
1060.0	1.81185	1.77380	1.53470	1.60190
1014.0	1.81335	1.77517	1.53541	1.60279
632.8	1.83957	1.79884	1.54566	1.61651
480.0	1.87425	1.82970	1.55725	1.63310
365.0	1.95131	1.89703	1.57932	1.66623

Bibliography

[1] K. O. Hill, *et al.*, "Photosensitivity in optical fiber waveguides: Application to reflection filter fabrication," *Applied Physics Letters,* vol. 32, pp. 647-649, 1978.

[2] G. Meltz, *et al.*, "Formation of Bragg gratings in optical fibers by a transverse holographic method," *Optics Letters,* vol. 14, pp. 823-825, 1989.

[3] K. O. Hill, *et al.*, "Bragg gratings fabricated in monomode photosensitive optical fiber by UV exposure through a phase mask," *Applied Physics Letters*, vol. 62, pp. 1035-1037, 1993.

[4] K. O. Hill and G. Meltz, "Fiber Bragg grating technology fundamentals and overview," *Lightwave Technology, Journal of,* vol. 15, pp. 1263-1276, 1997.

[5] A. Othonos, "Fiber Bragg gratings," *Review of Scientific Instruments,* vol. 68, pp. 4309-4341, 1997.

[6] B. Malo, *et al.*, "Point-by-point fabrication of micro-Bragg gratings in photosensitive fibre using single excimer pulse refractive index modification techniques," *Electronics Letters,* vol. 29, pp. 1668-1669, 1993.

[7] G. D. Marshall, *et al.*, "Point-by-point written fiber-Bragg gratings and their application in complex grating designs," *Optics Express,* vol. 18, pp. 19844-19859, 2010.

[8] P. S. J. Russell, *et al.*, "Fibre grating," *Physics World,* pp. 41-46, 1993.

[9] T. Erdogan, "Fiber grating spectra," *Lightwave Technology, Journal of,* vol. 15, pp. 1277-1294, 1997.

[10] C. R. Giles, "Lightwave applications of fiber Bragg gratings," *Lightwave Technology, Journal of,* vol. 15, pp. 1391-1404, 1997.

[11] R. Kashyap, *Fiber Bragg Gratings*, Second ed.: Elsevier Inc., 2010.

[12] J. L. Archambault and S. G. Grubb, "Fiber gratings in lasers and amplifiers," *Lightwave Technology, Journal of,* vol. 15, pp. 1378-1390, 1997.

[13] Y. J. Rao, "Recent progress in applications of in-fibre Bragg grating sensors," *Optics and Lasers in Engineering,* vol. 31, pp. 297-324, 1999.

[14] G. A. Ball, *et al.*, "Standing-wave monomode erbium fiber laser," *Photonics Technology Letters, IEEE,* vol. 3, pp. 613-615, 1991.

[15] A. D. Kersey, *et al.*, "Fiber grating sensors," *Lightwave Technology, Journal of,* vol. 15, pp. 1442-1463, 1997.

[16] J. Canning, "Fibre gratings and devices for sensors and lasers," *Laser & Photonics Review,* vol. 2, pp. 275-289, 2008.

[17] G. A. Cranch, *et al.*, "Distributed Feedback Fiber Laser Strain Sensors," *Sensors Journal, IEEE,* vol. 8, pp. 1161-1172, 2008.

[18] H. G. Winful, "Pulse compression in optical fiber filters," *Applied Physics Letters,* vol. 46, pp. 527-529, 1985.

[19] B. J. Eggleton, *et al.*, "Bragg Grating Solitons," *Physical Review Letters,* vol. 76, p. 1627, 1996.

[20] N. G. R. Broderick, *et al.*, "The optical pushbroom in action," presented at the BGPP, 1997.

[21] J. T. Mok, *et al.*, "Dispersionless slow light using gap solitons," *Nature Physics,* vol. 2, pp. 775-780, 2006.

[22] J. T. Mok, *et al.*, "Delay-tunable gap-soliton-based slow-light system," *Optics Express,* vol. 14, pp. 11987-11996, 2006.

[23] J. T. Mok, *et al.*, "Dispersionless slow light with 5-pulse-width delay in fibre Bragg grating," *Electronics Letters,* vol. 43, p. 1418, 2007.

[24] W. H. Loh, *et al.*, "10 cm chirped fibre Bragg grating for dispersion compensation at 10 Gbit/s over 400 km of non-dispersion shifted fibre," *Electronics Letters,* vol. 31, pp. 2203-2204, 1995.

[25] M. Ibsen, *et al.*, "Long continuously chirped fibre Bragg gratings for compensation of linear- and 3rd -order- dispersion," in *Integrated Optics and Optical Fibre Communications, 11th International Conference on, and 23rd European Conference on Optical Communications (Conf. Publ. No.: 448),* 1997, pp. 49-52 vol.2.

[26] P. Gunning, *et al.*, "Picosecond pulse generation of <5 ps from gain-switched DFB semiconductor laser diode using linearly step-chirped fibre grating," *Electronics Letters,* vol. 31, pp. 1066-1067, 1995.

[27] J. T. Kringlebotn, *et al.*, "Er^{3+}: Yb^{3+}-codoped fiber distributed-feedback laser," *Optics Letters,* vol. 19, pp. 2101-2103, 1994.

[28] A. Asseh, *et al.*, "10 cm Yb^{3+} DFB fibre laser with permanent phase shifted grating," *Electronics Letters,* vol. 31, pp. 969-970, 1995.

[29] M. Sejka, *et al.*, "Distributed feedback Er^{3+}-doped fibre laser," *Electronics Letters,* vol. 31, pp. 1445-1446, 1995.

[30] W. H. Loh and R. I. Laming, "1.55 μm phase-shifted distributed feedback fibre laser," *Electronics Letters,* vol. 31, pp. 1440-1442, 1995.

[31] L. B. Fu, *et al.*, "977-nm all-fiber DFB laser," *Photonics Technology Letters, IEEE,* vol. 16, pp. 2442-2444, 2004.

[32] C. A. Codemard, *et al.*, "400-mW 1060-nm ytterbium-doped fiber DFB laser," 2004, pp. 56-63.

[33] H. N. Poulsen, *et al.*, "1607 nm DFB Fibre Laser for Optical Communication in the L-band," *ECOC'99,* vol. Tech. Digest, p. B2.1, 1999.

[34] N. Y. Voo, *et al.*, "345-mW 1836-nm single-frequency DFB fiber laser MOPA," *Photonics Technology Letters, IEEE,* vol. 17, pp. 2550-2552, 2005.

[35] Z. Zhang, *et al.*, "High-power Tm-doped fiber distributed-feedback laser at 1943 nm," *Optics Letters,* vol. 33, pp. 2059-2061, 2008.

[36] P. Westbrook, *et al.*, "A seven core fiber DFB," 2012, p. BW3E.4.

[37] P. S. Westbrook, *et al.*, "Demonstration of a Raman fiber distributed feedback laser," presented at the OSA/CLEO, 2011.

[38] P. S. Westbrook, *et al.*, "Raman fiber distributed feedback lasers," *Optics Letters,* vol. 36, pp. 2895-2897, 2011.

[39] J. Shi, *et al.*, "High Power, Low Threshold, Raman DFB Fibre Lasers," in *Proceedings of the International Quantum Electronics Conference and Conference on Lasers and Electro-Optics Pacific Rim 2011,* Sydney, Austrain, 2011, p. C1174.

[40] J. Shi, *et al.*, "Sub-watt threshold, kilohertz-linewidth Raman distributed-feedback fiber laser," *Optics Letters,* vol. 37, pp. 1544-1546, 2012.

[41] K. S. Abedin, *et al.*, "Single-frequency Brillouin distributed feedback fiber laser," *Optics Letters,* vol. 37, pp. 605-607, 2012.

[42] J. Shi, *et al.*, "Highly efficient Raman distributed feedback fibre lasers," *Optics Express,* vol. 20, pp. 5082-5091, 2012.

[43] X. Feng, *et al.*, "Nonsilica glasses for holey fibers," *Lightwave Technology, Journal of,* vol. 23, pp. 2046-2054, 2005.

[44] J. Y. Leong, *et al.*, "A Lead Silicate Holey Fiber with ? = 1820 W-1km-1 at 1550 nm," 2005, p. PDP22.

[45] I. V. Kabakova, *et al.*, "Bragg grating-based optical switching in a bismuth-oxide fiber with strong $\chi^{(3)}$-nonlinearity," *Optics Express,* vol. 19, pp. 5868-5873, 2011.

[46] R. Suo, *et al.*, "Fiber Bragg gratings inscribed using 800nm femtosecond laser and a phase mask in singleand multi-core mid-IR glass fibers," *Optics Express*, vol. 17, pp. 7540-7548, 2009.

[47] D. Grobnic, *et al.*, "Femtosecond IR Laser Inscription of Bragg Gratings in Single- and Multimode Fluoride Fibers," *Photonics Technology Letters, IEEE*, vol. 18, pp. 2686-2688, 2006.

[48] M. Asobe, *et al.*, "Fabrication of Bragg grating in chalcogenide glass fibre using the transverse holographic method," *Electronics Letters*, vol. 32, pp. 1611-1613, 1996.

[49] D. Grobnic, *et al.*, "Bragg Gratings Made in Highly Nonlinear Bismuth Oxide Fibers With Ultrafast IR Radiation," *Photonics Technology Letters, IEEE*, vol. 22, pp. 124-126, 2010.

[50] T. M. Monro, *et al.*, "Chalcogenide holey fibres," *Electronics Letters*, vol. 36, pp. 1998-2000, 2000.

[51] X. Feng, *et al.*, "Dispersion controlled highly nonlinear fibers for all-optical processing at telecoms wavelengths," *Optical Fiber Technology*, vol. 16, pp. 378-391, 2010.

[52] T. M. Monro and H. Ebendorff-Heidepriem, "Progress in Microstructured Optical Fibers," *Annual Review of Materials Research*, vol. 36, pp. 467-495, 2006.

[53] J. C. Knight, *et al.*, "All-silica single-mode optical fiber with photonic crystal cladding," *Optics Letters*, vol. 21, pp. 1547-1549, 1996.

[54] P. S. J. Russell, "Photonic-Crystal Fibers," *Lightwave Technology, Journal of*, vol. 24, pp. 4729-4749, 2006.

[55] N. Sugimoto, *et al.*, "Bismuth-based optical fiber with nonlinear coefficient of 1360 W/sup -1/ km/sup -1," in *Optical Fiber Communication Conference, 2004. OFC 2004*, 2004, p. 3 pp. vol.2.

[56] M. Liao, *et al.*, "Tellurite microstructure fibers with small hexagonal core for supercontinuum generation," *Optics Express*, vol. 17, pp. 12174-12182, 2009.

[57] T. N. Nguyen, *et al.*, "Ultra highly nonlinear asse chalcogenide holey fiber for nonlinear applications," in *Optical Communication, 2009. ECOC '09. 35th European Conference on*, 2009, pp. 1-2.

[58] X. Feng, *et al.*, "Broadband Supercontinuum Using Single-Mode/Dual-Mode Tellurite Glass Holey Fibers with Large Mode Area," 2008, p. CMDD7.

[59] S. Jindan, *et al.*, "1.06 μm Picosecond Pulsed, Normal Dispersion Pumping for Generating Efficient Broadband Infrared Supercontinuum in Meter-Length Single-Mode Tellurite Holey Fiber With High Raman Gain Coefficient," *Lightwave Technology, Journal of*, vol. 29, pp. 3461-3469, 2011.

[60] S. Asimakis, *et al.*, "Towards efficient and broadband four-wavemixing using short-length dispersion tailored lead silicate holey fibers," *Optics Express*, vol. 15, pp. 596-601, 2007.

[61] X. Feng, *et al.*, "Dispersion-shifted all-solid high index-contrast microstructured optical fiber for nonlinear applications at 1.55µm," *Optics Express*, vol. 17, pp. 20249-20255, 2009.

[62] P. Periklis, *et al.*, "A spliced and connectorized highly nonlinear and anomalously dispersive bismuth-oxide glass holey fiber," 2004, p. CTuD3.

[63] X. Feng, *et al.*, "Fusion-Spliced Highly Nonlinear Soft-glass W-type Index Profiled Fibre with Ultra-flattened, Low Dispersion Profile in 1.55µm Telecommunication Window," 2011, p. We.10.P1.05.

[64] K. O. Hill, *et al.*, "Low-threshold cw Raman Laser," *Applied Physics Letters*, vol. 29, pp. 181-183, 1976.

[65] G. Agrawal, "Nonlinear Fiber Optics," Third ed: Springer Berlin / Heidelberg, 2000.

[66] B. A. Cumberland, *et al.*, "2.1 µm continuous-wave Raman laser in GeO_2 fiber," *Optics Letters*, vol. 32, pp. 1848-1850, 2007.

[67] A. Siekiera, *et al.*, "Short 17-cm DBR Raman Fiber Laser With a Narrow Spectrum," *Photonics Technology Letters, IEEE*, vol. 24, pp. 107-109, 2012.

[68] V. E. Perlin and H. G. Winful, "Distributed feedback fiber Raman laser," *Quantum Electronics, IEEE Journal of*, vol. 37, pp. 38-47, 2001.

[69] P. G. Kazansky, *et al.*, "Blue-light generation by quasi-phase-matched frequency doubling in thermally poled optical fibers," *Optics Letters*, vol. 20, pp. 843-845, 1995.

[70] V. Pruneri and P. G. Kazansky, "Frequency doubling of picosecond pulses in periodically poled D-shape silica fibre," *Electronics Letters,* vol. 33, pp. 318-319, Feb 1997.

[71] C. Corbari, "Development of Non-Linear Waveguide Devices for Optical Signal Processing," 2005.

[72] A. Canagasabey, *et al.*, "High-average-power second-harmonic generation from periodically poled silica fibers," *Optics Letters*, vol. 34, pp. 2483-2485, 2009.

[73] J. Shi and M. Ibsen, "Effects of Phase and Amplitude Noise on π Phase-Shifted DFB Raman Fibre Lasers," in *Bragg Gratings, Photosensitivity, and Poling in Glass Waveguides*, 2010, p. JThA30.

[74] J. Shi*, et al.*, "Raman DFB Fiber Laser with Truly Unidirectional Output," 2012, p. BW3E.6.

[75] J. Shi, *et al.*, "Ultra-Wide Range Wavelength Conversion Using FWM in a Raman DFB Fiber Laser," 2012, p. BW3E.7.

[76] B. E. A. Saleh and M. C. Teich, *Fundamentals of Photonics* 2nd ed.: John Wiley & Sons, Inc., Hoboken, New Jersey, 2007.

[77] C. K. Kao, "Nobel Lecture: Sand from centuries past: Send future voices fast," *Reviews of Modern Physics,* vol. 82, pp. 2299-2303, 2010.

[78] J. A. Buck, "Fundamentals of Optical Fibers," *John Wiley & Sons, Inc.,* 1995.

[79] J. L. Y. Yeen, "FABRICATION AND APPLICATIONS OF LEAD-SILICATE GLASS HOLEY FIBRE FOR 1-1.5MICRONS: NONLINEARITY AND DISPERSION TRADE OFFS," PhD, ORC, University of Southampton, Southampton, 2007.

[80] X. Feng, *et al.*, "Extruded singlemode, high-nonlinearity, tellurite glass holey fibre," *Electronics Letters,* vol. 41, p. 835, 2005.

[81] A. othonos and K. Kalli, "Fiber Bragg Gratings, Fundamentals and Applications in Telecommunications asn Sensing," *Artech House, Inc.,* 1999.

[82] V. C. Lauridsen, *et al.*, "Design of DFB fibre lasers," *Electronics Letters,* vol. 34, pp. 2028-2030, 1998.

[83] M. Ibsen, *et al.*, "Robust high power (>20 mW) all-fibre DFB lasers with unidirectional and truly single polarisation outputs," in *Lasers and Electro-Optics, 1999. CLEO '99. Summaries of Papers Presented at the Conference on*, 1999, pp. 245-246.

[84] M. Ibsen, *et al.*, "8- and 16-channel all-fiber DFB laser WDM transmitters with integrated pump redundancy," *Photonics Technology Letters, IEEE,* vol. 11, pp. 1114-1116, 1999.

[85] M. Ibsen, *et al.*, "Sinc-sampled fibre Bragg gratings for identical multiple wavelength operation," *Photonics Technology Letters, IEEE,* vol. 10, pp. 842-4, 1998.

[86] S. J. Mihailov, *et al.*, "Fiber Bragg gratings made with a phase mask and 800-nm femtosecond radiation," *Optics Letters,* vol. 28, pp. 995-997, 2003.

[87] Y. Lai, *et al.*, "Point-by-point inscription of first-order fiber Bragg grating for C-band applications," *Optics Express,* vol. 15, pp. 18318-18325, 2007.

[88] T. Geernaert, *et al.*, "Point-by-point fiber Bragg grating inscription in free-standing step-index and photonic crystal fibers using near-IR femtosecond laser," *Optics Letters,* vol. 35, pp. 1647-1649, 2010.

[89] Y. Lai, *et al.*, "Microchannels in conventional single-mode fibers," *Optics Letters,* vol. 31, pp. 2559-2561, 2006.

[90] F. El-Diasty, *et al.*, "Analysis of Fiber Bragg Gratings by a Side-Diffraction Interference Technique," *Applied Optics,* vol. 40, pp. 890-896, 2001.

[91] A. Carballar and M. A. Muriel, "Phase reconstruction from reflectivity in fiber Bragg gratings," *Lightwave Technology, Journal of,* vol. 15, pp. 1314-1322, 1997.

[92] R. Billington, "A report of four-wave mixing in optical fibre and its metrological applications," *National Physical Laboratory (NPL) Report* vol. COEM 24, p. PDB: 1549, 1999.

[93] J. Hansryd, *et al.*, "Fiber-Based Optical Parametric Amplifiers and Their Applications," *IEEE Journal of Selected Topics in Quantum Electronics,* vol. 8, pp. 506-520, 2002.

[94] S. Radic, "Parametric amplification and processing in optical fibers," *Laser & Photon. Rev.,* vol. 2, pp. 498-513, 2008.

[95] W. Weishu, *et al.*, "Phase conjugation by four-wave mixing in single-mode fibers," *Photonics Technology Letters, IEEE,* vol. 6, pp. 1448-1450, 1994.

[96] R. W. Hellwarth, "Theory of Stimulated Raman Scattering," *Physical Review,* vol. 130, p. 1850, 1963.

[97] Y. R. Shen and N. Bloembergen, "Theory of Stimulated Brillouin and Raman Scattering," *Physical Review,* vol. 137, p. A1787, 1965.

[98] R. H. Stolen and E. P. Ippen, "Raman gain in glass optical waveguides," *Applied Physics Letters,* vol. 22, pp. 276-278, 1973.

[99] R. H. Stolen, *et al.*, "Development of the stimulated Raman spectrum in single-mode silica fibers," *Journal of the Optical Society of America B,* vol. 1, pp. 652-657, 1984.

[100] S. G. Grubb, *et al.*, "High-Power 1.48 µm Cascaded Raman Laser in Germanosilicate Fibers," 1995, p. SaA4.

[101] T. T. Basiev and R. C. Powell, "Introduction," *Optical Materials,* vol. 11, pp. 301-306, 1999.

[102] E. M. Dianov, "Advances in Raman Fibers," *Journal of lightwave technology,* vol. 20, pp. 1457-1462, 2002.

[103] R. G. Smith, "Optical Power Handling Capacity of Low Loss Optical Fibers as Determined by Stimulated Raman and Brillouin Scattering," *Applied Optics,* vol. 11, pp. 2489-2494, 1972.

[104] F. L. Galeener and G. Lucovsky, "Longitudinal Optical Vibrations in Glasses: GeO_{2} and SiO_{2}," *Physical Review Letters,* vol. 37, pp. 1474-1478, 1976.

[105] K. K. Chen, *et al.*, "Excitation of individual Raman Stokes lines in the visible regime using rectangular-shaped nanosecond optical pulses at 530 nm," *Optics Letters,* vol. 35, pp. 2433-2435, 2010.

[106] O. P. Kulkarni, *et al.*, "Third order cascaded Raman wavelength shifting in chalcogenide fibers and determination of Raman gain coefficient," *Optics Express,* vol. 14, pp. 7924-7930, 2006.

[107] J. W. Nicholson, *et al.*, "Raman fiber laser with 81 W output power at 1480 nm," *Optics Letters,* vol. 35, pp. 3069-3071, 2010.

[108] B. Min, *et al.*, "Compact, fiber-compatible, cascaded Raman laser," *Optics Letters,* vol. 28, pp. 1507-1509, 2003.

[109] M. M. Fejer, *et al.*, "Quasi-phase-matched second harmonic generation: tuning and tolerances," *Quantum Electronics, IEEE Journal of,* vol. 28, pp. 2631-2654, 1992.

[110] U. Österberg and W. Margulis, "Experimental studies on efficient frequency doubling in glass optical fibers," *Optics Letters,* vol. 12, pp. 57-59, 1987.

[111] R. H. Stolen and H. W. K. Tom, "Self-organized phase-matched harmonic generation in optical fibers," *Optics Letters,* vol. 12, pp. 585-587, 1987.

[112] R. Kashyap, "Phase-matched periodic electric-field-induced second-harmonic generation in optical fibers," *Journal of the Optical Society of America B,* vol. 6, pp. 313-328, 1989.

[113] R. Kashyap, "Phase-matched second-harmonic generation in periodically poled optical fibers," *Applied Physics Letters,* vol. 58, pp. 1233-1235, 1991.

[114] R. A. Myers, *et al.*, "Large second-order nonlinearity in poled fused silica," *Optics Letters,* vol. 16, pp. 1732-1734, 1991.

[115] V. Pruneri, *et al.*, "Greater than 20%-efficient frequency doubling of 1532-nm nanosecond pulses in quasi-phase-matched germanosilicate optical fibers," *Optics Letters,* vol. 24, pp. 208-210, 1999.

[116] G. Bonfrate, *et al.*, "Periodic UV erasure of the nonlinearity for quasi-phase-matching in optical fibres," in *Lasers and Electro-Optics (CLEO 2000)*, San Francisco, CA, 2000, p. 73.

[117] C. Corbari, *et al.*, "All-fibre frequency conversion in long periodically poled silica fibres," in *Optical Fiber Communication Conference, 2005. Technical Digest. OFC/NFOEC*, 2005, p. 3 pp. Vol. 6.

[118] A. Canagasabey, "Development of Frequency Converters with Extended Functionalities in Periodically Poled Silica Fibres," *Thesis*, 2009.

[119] J. E. Carroll, *et al.*, *Distributed feedback semiconductor lasers*, 1998.

[120] R. Erlend, "Frequency and Intensity Noise of Single Frequency Fiber Bragg Grating Lasers," *Optical Fiber Technology,* vol. 7, pp. 206-235, 2001.

[121] N. Y. Voo, "Development, characterisation and analysis of narrow linewidth, single-frequency DFB fibre lasers in the 1.5 µm - 2 µm region," Phd. thesis, 2006.

[122] M. Ibsen, *et al.*, "Broad-band continuously tunable all-fiber DFB lasers," *Photonics Technology Letters, IEEE,* vol. 14, pp. 21-23, 2002.

[123] O. Hadeler, *et al.*, "Distributed-feedback fiber laser sensor for simultaneous strain and temperature measurements operating in the radio-frequency domain," *Applied Optics,* vol. 40, pp. 3169-3175, 2001.

[124] M. Ibsen, *et al.*, "Broadly tunable DBR fibre laser using sampled fibre Bragg gratings," *Electronics Letters,* vol. 31, pp. 37-38, 1995.

[125] Y. Zhang, *et al.*, "Ultra-short distributed Bragg reflector fiber laser for sensing applications," *Optics Express,* vol. 17, pp. 10050-10055, 2009.

[126] G. A. Ball and W. W. Morey, "Continuously tunable single-mode erbium fiber laser," *Optics Letters,* vol. 17, pp. 420-422, 1992.

[127] Y. Lai, *et al.*, "Distributed Bragg reflector fiber laser fabricated by femtosecond laser inscription," *Optics Letters,* vol. 31, pp. 1672-1674, 2006.

[128] C. Spiegelberg, *et al.*, "Low-Noise Narrow-Linewidth Fiber Laser at 1550 nm (June 2003)," *Lightwave Technology, Journal of,* vol. 22, pp. 57-62, 2004.

[129] P. S. Christine, "Compact 100 mW fiber laser with 2 kHz linewidth," 2003, p. PD45.

[130] J. Canning, *et al.*, "All-fibre photonic crystal distributed Bragg reflector (PC-DBR) fibre laser," *Optics Express,* vol. 11, pp. 1995-2000, 2003.

[131] P. Varming, *et al.*, "Design and fabrication of Bragg grating based DFB fiber lasers operating above 1610 nm," in *Optical Fiber Communication Conference, 2000*, 2000, pp. 17-19 vol.3.

[132] S. Agger, *et al.*, "Single-frequency thulium-doped distributed-feedback fiber laser," *Optics Letters,* vol. 29, pp. 1503-1505, 2004.

[133] S. Furst and M. Sorel, "Cavity-Enhanced Four-Wave Mixing in Semiconductor Ring Lasers," *Photonics Technology Letters, IEEE,* vol. 20, pp. 366-368, 2008.

[134] M. Ams, *et al.*, "Ultrafast laser written active devices," *Laser & Photonics Review,* vol. 3, pp. 535-544, 2009.

[135] S. A. Babin, *et al.*, "Single frequency single polarization DFB fiber laser," *Laser Physics Letters,* vol. 4, pp. 428-432, 2007.

[136] W. H. Loh, *et al.*, "Intensity profile in a distributed feedback fiber laser characterized by a green fluorescence scanning technique," *Applied Physics Letters,* vol. 69, pp. 3773-3775, 1996.

[137] W. H. Loh, *et al.*, "High Performance Single Frequency Fiber Grating-Based Erbium:Ytterbium-Codoped Fiber Lasers," *Lightwave Technology, Journal of,* vol. 16, p. 114, 1998.

[138] Y. Feng, *et al.*, "150 W highly-efficient Raman fiber laser," *Optics Express,* vol. 17, pp. 23678-23683, 2009.

[139] R. Engelbrecht, *et al.*, "Characterization of Short PM Raman Fiber Lasers with a Small Spectral Bandwidth," presented at the OFC/NFOEC Los Angeles, CA, USA, 2011.

[140] H. Kogelnik and C. V. Shank, "Coupled Wave Theory of Distributed Feedback Lasers," *Journal of Applied Physics,* vol. 43, pp. 2327-2335, 1972.

[141] Y. Hu and N. G. R. Broderick, "Improved design of a DFB Raman fibre laser," *Optics Communications,* vol. 282, pp. 3356-3359, 2009.

[142] V. Perlin and H. Winful, "Stimulated Raman scattering in nonlinear periodic structures," *Physical Review A*, vol. 64, p. 043804, 2001.

[143] C. M. d. Sterke, *et al.*, "Nonlinear coupled-mode equations on a finite interval: a numerical procedure," *Journal of the Optical Society of America B,* vol. 8, pp. 403-412, 1991.

[144] G. P. Agrawal, "Nonlinear fiber optics," *2nd Editon (Academic Press),* 1995.

[145] F. L. Galeener, *et al.*, "The relative Raman cross sections of vitreous SiO_2, GeO_2, B_2O_3, and P_2O_5," *Applied Physics Letters,* vol. 32, pp. 34-36, 1978.

[146] "http://www.rp-photonics.com/threshold_pump_power.html," *Encyclopedia of Laser Physics and Technology,*.

[147] R. Stolen, "Polarization effects in fiber Raman and Brillouin lasers," *Quantum Electronics, IEEE Journal of,* vol. 15, pp. 1157-1160, 1979.

[148] R. Stegeman, *et al.*, "Tellurite glasses with peak absolute Raman gain coefficients up to 30 times that of fused silica," *Optics Letters,* vol. 28, pp. 1126-1128, 2003.

[149] A. Mori, *et al.*, "Ultra-Wide-Band Tellurite-Based Fiber Raman Amplifier," *Lightwave Technology, Journal of,* vol. 21, p. 1300, 2003.

[150] K. Yelen, *et al.*, "A new design approach for fiber DFB lasers with improved efficiency," *Quantum Electronics, IEEE Journal of,* vol. 40, pp. 711-720, 2004.

[151] M. Ibsen and R. I. Laming, "Fibre non-uniformity caused Bragg grating imperfections," in *Optical Fiber Communication Conference, 1999, and the International Conference on Integrated Optics and Optical Fiber Communication. OFC/IOOC '99. Technical Digest*, 1999, pp. 2-4 vol.4.

[152] D. J. Richardson, *et al.*, "High power fiber lasers: current status and future perspectives (Invited)," *Journal of the Optical Society of America B,* vol. 27, pp. B63-B92, 2010.

[153] C. Guo, *et al.*, "High-power and widely tunable Tm-doped fiber laser at 2 μm," *Chinese Optics Letters,* vol. 10, pp. 91406-91408, 2012.

[154] C. Fukai, *et al.*, "Effective Raman gain characteristics in germanium- and fluorine-dopedoptical fibers," *Optics Letters,* vol. 29, pp. 545-547, 2004.

[155] V. G. Plotnichenko, *et al.*, "Raman band intensities of tellurite glasses," *Optics Letters,* vol. 30, pp. 1156-1158, 2005.

[156] Y. Kang, "Calculations and Measurements of Raman Gain Coefficients of Different Fiber Types," Master of Science, 2002.

[157] G. Qin, *et al.*, "Zero-dispersion-wavelength-decreasing tellurite microstructured fiber for wide and flattened supercontinuum generation," *Optics Letters,* vol. 35, pp. 136-138, 2010.

[158] D. Derickson, "Fiber Optic Test and Measurement," *Prentice Hall PTR,* 1998.

[159] T. Okoshi, *et al.*, "Novel method for high resolution measurement of laser output spectrum," *Electronics Letters,* vol. 16, pp. 630-631, 1980.

[160] P. Horak and W. H. Loh, "On the delayed self-heterodyne interferometric technique for determining the linewidth of fiber lasers," *Optics Express,* vol. 14, pp. 3923-3928, 2006.

[161] A. Canagasabey, *et al.*, "A Comparison of Delayed Self-Heterodyne Interference Measurement of Laser Linewidth Using Mach-Zehnder and Michelson Interferometers," *Sensors*, vol. 11, pp. 9233-9241, 2011.

[162] X. Chen, "Ultra-Narrow Laser Linewidth Measurement," PhD thesis, Virginia Polytechnic Institute and State University, 2006.

[163] K. Inoue, "Four-wave mixing in an optical fiber in the zero-dispersion wavelength region," *Lightwave Technology, Journal of*, vol. 10, pp. 1553-1561, 1992.

[164] T. Simoyama, *et al.*, "High-efficiency wavelength conversion using FWM in an SOA integrated DFB laser," *Photonics Technology Letters, IEEE*, vol. 12, pp. 31-33, 2000.

[165] Z. Jianhui, *et al.*, "Four-wave mixing wavelength conversion efficiency in semiconductor traveling-wave amplifiers measured to 65 nm of wavelength shift," *Photonics Technology Letters, IEEE*, vol. 6, pp. 984-987, 1994.

[166] F. Girardin, *et al.*, "Low-noise and very high-efficiency four-wave mixing in 1.5-mm-long semiconductor optical amplifiers," *Photonics Technology Letters, IEEE*, vol. 9, pp. 746-748, 1997.

[167] H. Kuwatsuka, *et al.*, "Nondegenerate four-wave mixing in a long-cavity λ/4-shifted DFB laser using its lasing beam as pump beams," *Quantum Electronics, IEEE Journal of*, vol. 33, pp. 2002-2010, 1997.

[168] H. Kuwatsuka, *et al.*, "THz frequency conversion using nondegenerate four-wave mixing process in a lasing long-cavity λ/4-shifted DFB laser," *Electronics Letters*, vol. 31, pp. 2108-2110, 1995.

[169] B. E. Little, *et al.*, "Nondegenerate four-wave mixing efficiencies in DFB laser wavelength converters," *Photonics Technology Letters, IEEE*, vol. 10, pp. 519-521, 1998.

[170] H. Fukuda, *et al.*, "Four-wave mixing in silicon wire waveguides," *Optics Express*, vol. 13, pp. 4629-4637, 2005.

[171] H. Hu, *et al.*, "Wavelength Conversion with Large Signal-Idler Separation using Discrete Four-Wave Mixing in a Silicon Nanowire," in *CLEO: Science and Innovations (CLEO: S and I)*, San Jose, California, 2012, p. CW1A.2.

[172] K. Inoue and H. Toba, "Wavelength conversion experiment using fiber four-wave mixing," *Photonics Technology Letters, IEEE*, vol. 4, pp. 69-72, 1992.

[173] O. Aso, *et al.*, "Broadband four-wave mixing generation in short optical fibres," *Electronics Letters*, vol. 36, pp. 709-711, 2000.

[174] K. Inoue, "Arrangement of fiber pieces for a wide wavelength conversion range by fiber four-wave mixing," *Optics Letters*, vol. 19, pp. 1189-1191, 1994.

[175] A. Zhang and M. S. Demokan, "Broadband wavelength converter based on four-wave mixing in a highly nonlinear photonic crystal fiber," *Optics Letters*, vol. 30, pp. 2375-2377, 2005.

[176] D. Méchin, *et al.*, "180-nm wavelength conversion based on Bragg scattering in an optical fiber," *Optics Express*, vol. 14, pp. 8995-8999, 2006.

[177] R. Hui, *et al.*, "Optical frequency conversion using nearly degenerate four-wave mixing in a distributed-feedback semiconductor laser: theory and experiment," *Journal of Lightwave Technology*, vol. 11, pp. 2026-2032, 1993.

[178] Z. Qingsheng, "Dispersive properties in phase-shifted Bragg grating filters," in *Antennas and Propagation Society International Symposium, 1998. IEEE*, 1998, pp. 1060-1063 vol.2.

[179] A. Camerlingo, *et al.*, "Wavelength Conversion in a Short Length of a Solid Lead–Silicate Fiber," *Photonics Technology Letters, IEEE*, vol. 22, pp. 628-630, 2010.

[180] I. V. Kabakova, *et al.*, "Performance of field-enhanced optical switching in fiber Bragg gratings," *Journal of the Optical Society of America B*, vol. 27, pp. 1343-1351, 2010.

[181] T. Kremp, *et al.*, "Simulation of two-photon absorption in Raman DFB lasers," 2012, p. BW3E.5.

[182] M. P. Fok, *et al.*, "Dual-Pump Four-Wave Mixing in Bismuth-Oxide Highly Nonlinear Fiber for Wide-Band DPSK Wavelength Conversion," in *Optical Fiber Communication and the National Fiber Optic Engineers Conference, 2007. OFC/NFOEC 2007. Conference on*, 2007, pp. 1-3.

[183] V. Finazzi, *et al.*, "Small-core silica holey fibers: nonlinearity and confinement loss trade-offs," *Journal of the Optical Society of America B,* vol. 20, pp. 1427-1436, 2003.

[184] J. Y. Y. Leong, *et al.*, "High-Nonlinearity Dispersion-Shifted Lead-Silicate Holey Fibers for Efficient 1-µm Pumped Supercontinuum Generation," *Lightwave Technology, Journal of,* vol. 24, p. 183, 2006.

[185] H. Ebendorff-Heidepriem, *et al.*, "Fluoride glass microstructured optical fiber with large mode area and mid-infrared transmission," *Optics Letters,* vol. 33, pp. 2861-2863, 2008.

[186] H. Ebendorff-Heidepriem, *et al.*, "Bismuth glass holey fibers with high nonlinearity," *Optics Express,* vol. 12, pp. 5082-5087, 2004.

[187] X. Feng, *et al.*, "Developing single-mode tellurite glass holey fiber for infrared nonlinear applications," *Advances in Science and Technology,* vol. 55, pp. 108-117, 2008.

[188] D.-I. Yeom, *et al.*, "Low-threshold supercontinuum generation in highly nonlinear chalcogenide nanowires," *Optics Letters,* vol. 33, pp. 660-662, 2008.

[189] G. S. Murugan, *et al.*, "Tellurite glasses for ultrabroadband fiber Raman amplifiers," *Applied Physics Letters,* vol. 86, p. 161109, 2005.

[190] A. Mori, *et al.*, "Ultra-wideband tellurite-based Raman fibre amplifier," *Electronics Letters,* vol. 37, pp. 1442-1443, 2001.

[191] R. Shuker and R. W. Gammon, "Raman-Scattering Selection-Rule Breaking and the Density of States in Amorphous Materials," *Physical Review Letters,* vol. 25, p. 222, 1970.

[192] K. K. Chen, *et al.*, "Polarisation maintaining 100W Yb-fiber MOPA producing µJ pulses tunable in duration from 1 to 21 ps," *Optics Express,* vol. 18, pp. 14385-14394, 2010.

[193] J. M. Dudley and S. Coen, "Supercontinuum generation in photonic crystal fiber," *Reviews of Modern Physics,* vol. 78, pp. 1135-1184, 2006.

[194] A. K. Abeeluck and C. Headley, "Continuous-wave pumping in the anomalous- and normal-dispersionregimes of nonlinear fibers for supercontinuum generation," *Optics Letters,* vol. 30, pp. 61-63, 2005.

[195] J. K. Ranka, *et al.*, "Visible continuum generation in air-silica microstructure optical fibers with anomalous dispersion at 800 nm," *Optics Letters,* vol. 25, pp. 25-27, 2000.

[196] X. Feng, *et al.*, "Single-mode tellurite glass holey fiber with extremely large mode area for infrared nonlinear applications," *Optics Express,* vol. 16, pp. 13651-13656, 2008.

[197] T. Delmonte, *et al.*, "Generation of Mid-IR continuum using tellurite microstructured fiber," in *Lasers and Electro-Optics, 2006 and 2006 Quantum Electronics and Laser Science Conference. CLEO/QELS 2006. Conference on*, 2006, pp. 1-2.

[198] J. Crisp, *Introduction to Fiber Optics*, 2nd ed.: Newnes, 2001.

[199] A. D. Yablon, *Optical Fiber Fusion Splicing*: Springer Berlin Heidelberg New York, 2005.

[200] A. Camerlingo, *et al.*, "Near-zero dispersion, highly nonlinear lead-silicate W-type fiber for applications at 1.55µm," *Optics Express,* vol. 18, pp. 15747-15756, 2010.

[201] M. Kihara, *et al.*, "Characteristics of thermally expanded core fiber," *Lightwave Technology, Journal of,* vol. 14, pp. 2209-2214, 1996.

[202] L. Xiao, *et al.*, "Fusion splicing small-core photonic crystal fibers and single-mode fibers by repeated arc discharges," *Optics Letters,* vol. 32, pp. 115-117, 2007.

[203] N. Sugimoto, "Erbium doped fiber and highly non-linear fiber based on bismuth oxide glasses," *Journal of Non-Crystalline Solids,* vol. 354, pp. 1205-1210, 2008.

[204] R. M. Atkins and R. P. Espindola, "Photosensitivity and grating writing in hydrogen loaded germanosilicate core optical fibers at 325 and 351 nm," *Applied Physics Letters,* vol. 70, pp. 1068-1069, 1997.

[205] X.-C. Long and S. R. J. Brueck, "Large photosensitivity in lead-silicate glasses," *Applied Physics Letters,* vol. 74, pp. 2110-2112, 1999.

[206] R. Ahmad, *et al.*, "Fabrication of Bragg gratings in subwavelength diameter As_2Se_3 chalcogenide wires," *Optics Letters,* vol. 36, pp. 2886-2888, 2011.

[207] S. Tokita, *et al.*, "Stable 10 W Er:ZBLAN fiber laser operating at 2.71-2.88µm," *Optics Letters,* vol. 35, pp. 3943-3945, 2010.

[208] M. Zeller, *et al.*, "UV-induced index changes in Undoped Fluoride glass," *Lightwave Technology, Journal of,* vol. 23, pp. 624-627, 2005.

[209] G. M. Williams, *et al.*, "Photosensitivity of rare-earth-doped ZBLAN fluoride glasses," *Lightwave Technology, Journal of,* vol. 15, pp. 1357-1362, 1997.

[210] T. Taunay, *et al.*, "Ultraviolet-induced permanent Bragg gratings in cerium-doped ZBLAN glasses or optical fibers," *Optics Letters,* vol. 19, pp. 1269-1271, 1994.

[211] C. Contardi, *et al.*, "Study of UV-written channels in lead silicate glasses," *Journal of Non-Crystalline Solids,* vol. 291, pp. 113-120, 2001.

[212] X.-C. Long and S. R. J. Brueck, "Composition dependence of the photoinduced refractive-index change in lead silicate galsses," *Optics Letters,* vol. 24, pp. 1136-1138, 1999.

[213] H. Jia, *et al.*, "UV–visible absorption changes of lead silicate glasses after UV laser irradiation," *Journal of Non-Crystalline Solids,* vol. 319, pp. 322-326, 2003.

[214] S. Radic, *et al.*, "Photorefraction in lead tin-fluorophosphate glasses," *Optics Letters,* vol. 23, pp. 1730-1732, 1998.

[215] K. W. DeLong, *et al.*, "Color-center dynamics in a lead glass fiber," *Journal of the Optical Society of America B,* vol. 7, pp. 2210-2216, 1990.

[216] H. Jia, *et al.*, "Refractive index and absorption spectra changes induced by UV irradiation in lead silicate glasses," *Journal of Non-Crystalline Solids,* vol. 347, pp. 220-223, 2004.

[217] J. S. Wang, *et al.*, "Tellurite glass: a new candidate for fiber devices," *Optical Materials,* vol. 3, pp. 187-203, 1994.

[218] T. Fujiwara, *et al.*, "Refractive index change induced by ultraviolet laser irradiations in erbium-doped tellurite glasses," *Electronics Letters,* vol. 39, pp. 1576-1577, 2003.

[219] R. Elmallawany, *et al.*, "New tellurite glass: Optical properties," *Materials Chemistry and Physics,* vol. 109, pp. 291-296, 2008.

[220] E. Chierici, *et al.*, "Direct writing of channel waveguide on a tellurite glass using a focused ultraviolet laser beam," in *Fibre and Optical Passive Components, 2002. Proceedings of 2002 IEEE/LEOS Workshop on*, 2002, pp. 24-28.

[221] Inoue and S., "Correlation between specific heat and change of refractive index formed by laser spot heating of tellurite glass surfaces," *Journal of Non-Crystalline Solids,* vol. 324, pp. 133-141, 2003.

[222] S. Inoue, *et al.*, "Refractive-Index Patterning of Tellurite Glass Surfaces by Laser Spot Heating," *Applied Optics,* vol. 37, pp. 48-53, 1998.

[223] A. Zakery and S. R. Elliott, "Optical properties and applications of chalcogenide glasses: a review," *Journal of Non-Crystalline Solids,* vol. 330, pp. 1-12, 2003.

[224] G. A. Brawley, *et al.*, "Strong photoinduced Bragg gratings in arsenic selenide optical fibre using transverse holographic method," *Electronics Letters,* vol. 44, pp. 846-847, 2008.

[225] C. Florea, *et al.*, "Surface relief gratings in AsSe glass fabricated under 800-nm laser exposure," *Materials Letters,* vol. 61, pp. 1271-1273, 2007.

[226] C. Meneghini and A. Villeneuve, "As_2S_3 photosensitivity by two-photon absorption: holographic gratings and self-written channel waveguides," *Journal of the Optical Society of America B,* vol. 15, pp. 2946-2950, 1998.

[227] D. Grobnic, *et al.*, "Femtosecond Laser Induced Bragg Gratings in Silica and Exotic Optical Fibers Applications," 2010, p. BWA1.

[228] D. Grobnic, *et al.*, "Bragg Gratings Made With a Femtosecond Laser in Heavily Doped Er–Yb Phosphate Glass Fiber," *Photonics Technology Letters, IEEE,* vol. 19, pp. 943-945, 2007.

[229] S. J. Mihailov, *et al.*, "Bragg grating inscription in various optical fibers with femtosecond infrared lasers and a phase mask," *Opt. Mater. Express,* vol. 1, pp. 754-765, 2011.

[230] D. Grobnic, *et al.*, "Fiber Bragg gratings made in highly nonlinear bismuth oxide fibers using IR ultrafast radiation," in *Optical Communication, 2009. ECOC '09. 35th European Conference on*, 2009, pp. 1-2.

[231] A. Martinez, *et al.*, "Direct writing of fibre Bragg gratings by femtosecond laser," *Electronics Letters,* vol. 40, p. 1170, 2004.

[232] J. S. Sanghera, *et al.*, "Chalcogenide Glass-Fiber-Based Mid-IR Sources and Applications," *Selected Topics in Quantum Electronics, IEEE Journal of,* vol. 15, pp. 114-119, 2009.

[233] A. Schliesser, *et al.*, "Mid-infrared frequency combs," *Nature Photonics,* vol. 6, pp. 440-449, 2012.

List of Publications

Journal articles:

J. Shi, S. Alam, M. Ibsen, "Sub-Watt Threshold, Kilohertz-Linewidth Raman Distributed-Feedback Fiber Laser", Optics Letters 37(9), 1544-1546 (2012).

J. Shi, S. Alam, M. Ibsen, "Highly Efficient Raman Distributed Feedback Fiber Lasers", Optics Express 20(5), 5082–5091 (2012).

J. Shi, X. Feng, P. Horak, K. Chen, P. S. Teh, S. Alam, W. H. Loh, D. J. Richardson, M. Ibsen, "1.06 µm picosecond pulsed, normal dispersion pumping for generating efficient broadband infrared supercontinuum in metre-length single-mode tellurite holey fiber with high Raman gain coefficient", Journal of Lightwave Technology 29(22), 3461-3469 (2011).

M. A. Ettabib, L. Jones, J. Kakande, R. Slavík, F. Parmigiani, X. Feng, F. Poletti, G. M. Ponzo, **J. Shi**, M. N. Petrovich, W. H. Loh, P. Petropoulos, D. J. Richardson, "Phase sensitive amplfication in a highly nonlinear lead-silicate fiber," Optics Express 20, 1629-34 (2012).

X. Feng, F. Poletti, A. Camerlingo, F. Parmigiani, P. Petropoulos, P. Horak, G. M. Ponzo, M. Petrovich, **J. Shi**, W. H. Loh, D. J. Richardson, "Dispersion controlled highly nonlinear fibers for all-optical processing at telecoms wavelengths", Optical Fiber Technology 16(6), 378-391 (Invited) (2010).

Conferences:

X. Feng, **J. Shi**, C. C. Huang, P. S. The, S. Alam, M. Ibsen, W. Loh, "Laser-Induced Crystalline Optical Waveguide on Glass Fibre," ECOC 2012, Amsterdam, 16-20 September, Mo.2.F.4 (2012) (Accepted)

J. Shi, S. Alam, M. Ibsen, "Raman DFB Fiber Laser with Truly Unidirectional output," BGPP 2012, Colorado, 17-21 June, BW3E.6 (2012).

J. Shi, S. Alam, M. Ibsen, "Ultra-Wide Range Wavelength Conversion Using FWM in a Raman DFB Fiber Laser," BGPP 2012, Colorado, 17-21 June, BW3E.7 (2012).

J. Shi, S. Alam, M. Ibsen, "Single-frequency Raman Distributed-feedback Fiber Laser," CLEO/QELS 2012 San Jose 6-11 May, CF3N.6 (2012).

J. Shi, S. Alam, M. Ibsen, "High power, low threshold, Raman DFB fibre lasers," IQEC/CLEO Pacific Rim Sydney, Australia, 28 Aug - 1 Sep, C1174 (2011) (Postdeadline).

X. Feng, **J. Shi**, G. M. Ponzo, F. Poletti, M. N. Petrovich, N. White, P. Petropoulos, M. Ibsen, W. H. Loh, D. J. Richardson, “Fusion-spliced highly nonlinear soft-glass W-type index profiled fibre with ultra-flattened, low dispersion profile in 1.55µm telecommunication window,” ECOC Geneva, Switzerland 18-22 September, We.10.P1 (2011).

M. A. Ettabib, L. Jones, J. Kakande, R. Slavík, F. Parmigiani, X. Feng, F. Poletti, G. M. Ponzo, **J. Shi**, M. N. Petrovich, P. Petropoulos, W. H. Loh, D. J. Richardson, “Phase sensitive amplification in a highly nonlinear lead-silicate fibre,” ECOC Geneva, Switzerland 18-22 September, Th.11.LeCervin.3 (2011).

J. Shi, X. Feng, K. K. Chen, P. S. Teh, P. Horak, D. Lin, S. -U. Alam, W. H. Loh, D. J. Richardson, M. Ibsen, “Efficient near-infrared supercontinuum generation in tellurite holey fiber pumped 320nm within the normal dispersion regime” ACP2010, Shanghai, 8-12 Dec, pp.493-494 (2010).

J. Shi, M. Ibsen, “Effects of phase and amplitude noise on pi phase-shifted DFB Raman fibre lasers,” BGPP 2010, Karlsruhe Germany, 21-24 Jun, JThA30 (2010).